



Transonic Boundary Layer Transition Prediction over Wing Sections with Embedded DG Spectral/*hp* Discretisations

by

Ganlin Lyu

In partial fulfillment of the requirements for the degree of
Doctor of Philosophy of Imperial College London

Department of Aeronautics
Imperial College London
United Kingdom

September 2023

Statement of originality

This is to certify that this thesis is the product of my own work completed at Department of Aeronautics, Imperial College London. Any ideas or quotations from the work of other people, published or otherwise, are fully acknowledged in accordance with the standard referencing practices of the discipline.

Ganlin Lyu
September 2023

Copyright Declaration

The copyright of this thesis rests with the author. Unless otherwise indicated, its contents are licensed under a Creative Commons Attribution-Non Commercial 4.0 International Licence (CC BY-NC). Under this licence, you may copy and redistribute the material in any medium or format. You may also create and distribute modified versions of the work. This is on the condition that: you credit the author and do not use it, or any derivative works, for a commercial purpose. When reusing or sharing this work, ensure you make the licence terms clear to others by naming the licence and linking to the licence text. Where a work has been adapted, you should indicate that the work has been changed and describe those changes. Please seek permission from the copyright holder for uses of this work that are not included in this licence or permitted under UK Copyright Law.

Acknowledgement

I would like to express my gratitude to my PhD supervisor, Prof. Spencer Sherwin, who provided me with this great opportunity at Imperial College London to continue the research journey of exploring and understanding in the world of Computational Fluid Dynamics. I have learned a lot from his high-level systematic understanding across different scientific areas as well as approaches to developing research ideas. Along the journey he has offered me not only inspiring discussions but also the freedom of research, without which this thesis would not have been possible.

My sincere thanks go to my co-supervisor, Dr. Shahid Mughal. He generously shared his time and expertise in the discussions, which significantly boosted the progress of the research. I have been impressed by his strictness and attitude of excellence. Special thanks go to my co-supervisors Dr. Chris Cantwell and Dr. Yongyun Hwang, for all the technical assistance in the computing system and my first lesson in the field of flow instability, respectively.

I would like to acknowledge the scholarship provided by COMAC - Imperial Research Centre for Wing Technology of Commercial Aircraft and the Department of Aeronautics, which enabled me to conduct the simulations and conference travellings necessary for this study, as well as have a comfortable life in London without financial burdens.

I must also express my appreciation to all my dear friends, lab mates, and colleagues in the community, for whom the list is too long to enumerate. Their company, support, and the joyful moments we spend together are indeed treasures of my life.

Lastly, my deepest gratitude goes to my parents and family for their unwavering love and support throughout my past thirty years of life, which has been my source of strength to keep marching.

This wonderful journey will always be shining in my memory.

Abstract

The prediction of laminar boundary layer transition is still under intensive investigations in the fluid instability community, particularly when complicated factors (e.g. realistic geometries) are involved. In this thesis we introduce an open-source and unified framework for boundary layer transition analysis at transonic conditions and over wing sections where surface irregularities may present. Different computational tools are integrated in the framework, and therefore overcomes the difficulties of two separate and usually quite disparate processes, i.e. the computation of baseflow and disturbances, when using e^N transition prediction method.

To reduce the computational cost, a near-body reduced domain is adopted with boundary conditions enforced to be compatible with a computationally cheaper three-dimensional (3D) RANS simulation. It is desirable to enforce a consistent pressure distribution. However, the pressure compatibility is not typically the case when using the standard Riemann inflow boundary condition, while not all modified boundary condition enforcements lead to a stable simulation. We therefore revisit the Riemann problem adopted in many DG-based high-fidelity formulations and develop a useful analysis approach to construct boundary conditions for the inviscid term based on a linearized one-dimensional model. In-depth analysis and results are also presented.

We next apply this analysis framework to investigate the transition performance using a wing section of CRM-NLF model for both clean and gapped geometries. In 3D gapped case, we find self-sustained oscillations in the small-sized gap which excites travelling waves. An incompressible swept plate flow is simulated to investigate the hydrodynamic instability that drives the oscillation inside the gap. It is found that the traveling waves correspond to a BiGlobal mode inside the gap and possess a convective nature. This new discovery suggests the presence of different physics compared with a gapped non-swept case, and thus motivates our in-depth investigations in future works.

Contents

I Introduction and computational methods	16
1 Introduction	17
1.1 The call for sustainable aviation	17
1.2 Boundary layer transition over wings	18
1.2.1 Laminar boundary layer transition	18
1.2.2 Boundary layer instabilities	19
1.2.2.1 Tollmien-Schlichting (TS) instability	19
1.2.2.2 Crossflow instability	19
1.2.2.3 Other instabilities	20
1.2.3 Effect of real geometries	21
1.3 Transition prediction	22
1.3.1 Linear stability analysis	22
1.3.2 e^N transition model	25
1.4 Motivation and main objectives	26
1.5 Outline of the thesis	27
1.6 List of publications and conference presentations	28
1.6.1 Publications	28
1.6.2 Conference presentations	28
2 Governing equations and numerical methods	30
2.1 Governing equations	30
2.1.1 Navier-Stokes (NS) equations	30
2.1.2 Non-dimensionalization of the Navier-Stokes equations	31
2.1.3 Euler equations	32
2.2 Spectral/ hp element method and Discontinuous Galerkin (DG) formulation	33
2.3 DG formulation of a model problem	34
2.3.1 Elemental and flux/primal formulation	34
2.3.2 Global formulation	36
2.3.3 Advection operator	37
2.3.4 Diffusion operator	38
2.4 DG formulation of the NS equations	39
2.4.1 Formulation	39
2.4.2 Advection term: Riemann problem	41
2.5 Boundary conditions	42
2.5.1 Farfield	43
2.5.1.1 Advection term: low viscous effect region	43
2.5.1.2 Advection term: high viscous effect region	45

2.5.1.3	Diffusion term	46
2.5.2	Viscous wall	46
2.5.2.1	Advection term	46
2.5.2.2	Diffusion term: isothermal wall	47
2.5.2.3	Diffusion term: adiabatic wall	47
2.5.2.4	Numerical blowing-suction on the wall	47
2.6	Discretisations in space and time	47
2.6.1	Spatial discretisation	48
2.6.2	Time integration	49
2.6.3	Jacobian-free Newton-Krylov (JNFK) method	50
2.7	Other numerical methods	52
2.7.1	Selective frequency damping	52
2.7.2	Absorption layer	52
2.8	Nektar++	54

II Numerical method developments 55

3	Framework for transonic laminar boundary layer natural transition analysis over complex geometries	56
3.1	Introduction	56
3.2	Pipeline for transition prediction	57
3.3	Methods to reduce wave contamination	59
3.4	One-dimensional data filtering	61
3.4.1	Chebyshev polynomials	62
3.4.2	Least squares approximation	63
3.5	Precision requirement and linear growth limit for instability study . .	64
3.6	Framework verification: TS wave development in 2D transonic flat plate boundary layer	66
4	Stable Riemann boundary condition for embedded DG compressible flow simulations	71
4.1	Introduction	71
4.2	Boundary conditions linear stability analysis	75
4.2.1	Linearized DG approximation for 1D Euler equations	75
4.2.2	Analysis for Riemann boundary condition	80
4.3	Stability analysis for pressure compatible subsonic Riemann inflow boundary conditions	82
4.3.1	Entropy-pressure compatible inflow	83
4.3.2	Velocity-pressure compatible inflow	83
4.3.3	Momentum-pressure compatible inflow	84
4.4	Other types of stable subsonic inflows	85
4.4.1	Entropy-velocity compatible inflow	86
4.4.2	Entropy-total enthalpy compatible inflow	86
4.5	Stability analysis of inflow entropy modification	87
4.6	Further discussion	88
4.6.1	Physical explanation of unstable Riemann boundary condition	88
4.6.2	Applicability: local analysis vs. global analysis	89

4.7	Ill-posedness for entropy-pressure inflow at the presence of a stagnation point	92
4.7.1	Linearized DG approximation for 2D Euler equations	92
4.7.2	Analysis in the stagnation point region	95
4.8	Results	96
4.8.1	CRM-NLF	96
4.8.2	DLR-F5	100
4.9	Conclusion	101
III	Laminar boundary layer natural transition studies	104
5	Transitional analysis on the wing section of CRM-NLF model	105
5.1	Introduction	105
5.2	Geometries and conditions for simulations	105
5.2.1	Sizes of surface irregularities on the wings	105
5.2.2	CRM-NLF geometry, scaling, and settings	107
5.3	Challenges in baseflow computation	108
5.4	Baseline for two-dimensional analysis	110
5.5	Effect of different wall boundary conditions	113
5.6	The influence of a gap irregularity	115
5.7	Effects of three-dimensionality and swept geometry	119
6	Incompressible laminar boundary layer flow over a quasi-3D gapped swept plate	125
6.1	Introduction	125
6.2	Quasi-3D boundary layer flow over a swept plate with gap	127
6.3	Discussion on the origin of the downstream waves	130
6.4	Conclusion	138
IV	Conclusions and future works	140
7	Conclusions and future works	141
7.1	Conclusions	141
7.2	Future works	144
7.2.1	Operator speedup in Nektar++	144
7.2.2	Gapped swept plate flow at medium Reynolds numbers	144
Bibliography		146
V	Appendix	160
A	DG formulations	161
A.1	DG with different forms of interior penalty	161
A.2	DG formulation of NS equations	163

B Linearized DG approximation for Euler equations	164
B.1 Linearized DG approximation for 1D Euler equations	164
B.2 Linearized DG approximation for 2D Euler equations	165
B.3 Global linear system for the three-element model problem	167
C CRM-NLF	168
C.1 Convergence check	168
D Self-similar solution of boundary layer equations	170
D.1 2D compressible boundary layers	170
D.1.1 Governing equations	170
D.1.2 Solving	172
D.2 3D incompressible boundary layers with crossflow	173
D.2.1 Governing equations	173
D.2.2 Solving	175

List of Figures

1.1	Different paths for laminar flow transition to turbulence [15].	19
1.2	Illustration for streamline and boundary-layer velocity profile near the leading edge of a swept wing.	21
1.3	Wing of a Boeing 737-800 airliner from Norwegian Air Shuttle. Several sources of surface irregularities are labelled. Image by author. . .	22
2.1	Relation between spectral/ <i>hp</i> element method and finite difference method, spectral method, and finite element/finite volume Method. Reproduced from Ref. [78].	33
2.2	The blue element with solid edges is the element of interest, where the quantities are denoted by (−); the grey element with dashed edges is one of its neighbors, where the quantities are denoted by (+).	37
2.3	The Coordinate system to calculate Riemann solution at the element interface. $\mathbf{x} = (x_1, x_2, x_3)$ is the Cartesian coordinate system, and $\mathbf{y} = (y_1, y_2, y_3)$ shows the local coordinate system at a interface point.	41
2.4	The propagation of waves in the three-dimensional Riemann problem. The red dashed lines are nonlinear waves and the blue dotted line in the middle denotes three contact waves. In the brackets are the corresponding waves speed, where u is the normal velocity to the boundary.	42
2.5	A sketch of the states for boundary condition enforcement. The normal \mathbf{n} is outward-pointing.	43
2.6	Sketch of the sponge region and the corresponding local coordinate system $\mathbf{x}^* = (x_1^*, x_2^*, x_3^*)$	53
2.7	Damping coefficient distribution for the absorption layer.	53
3.1	Pipeline for transonic boundary layer natural transition analysis.	58
3.2	Sketch of the wave reflection at a inflow boundary and at a forward-facing step. The long dashed line represents the extra wave caused by the blowing-suction, the short dashed line represents the reflection wave at the inflow boundary, and the dotted line represents the reflection wave at the step.	59
3.3	Comparison of the disturbances in the streamwise component of the velocity field (u') in TS wave excitation over an airfoil in the reduced domain: (a) contaminated TS wave packet because of the wave reflection, and (b) clear resolved wave packet with the adoption of a sponge region.	61
3.4	Disturbance in the streamwise component of the velocity field (u') showing the TS wave reflection at a forward-facing step.	62

3.5	Reflected waves in the slice passing $Re_x = 2.4177 \times 10^6$ on the wall and of 15 deg with respect to the y -axis. (The forward-facing step is located at $Re_x = 2.45 \times 10^6$, and detailed settings are provided in Section 3.6. The vertical coordinate is represented by Re_y to follow the convention used in Ref. [110].)	62
3.6	Comparison of raw data and the filtered results. The raw data is the amplification curve of 2D TS instability of $f = 19$ kHz over the flat plate with a forward-facing step. $N = 20$ is used to filter the data in the Re_x interval $[3.45 \times 10^5, 2.06 \times 10^6]$. Comparison of two sets of raw data and the filtered results. The first set of raw data (red line) includes oscillation because of the acoustic reflection at the forward-facing step. The second set of raw data (black line) is oscillation-free since it is obtained before the TS wavefront hits the step. The filtered data removes the oscillation using modified Chebyshev polynomials.	63
3.7	The first four Chebyshev polynomials.	64
3.8	Comparison of scaled TS wave growth curves of the five cases in Table 3.1. The relative difference for each curve in (b) is computed using the adjacent two cases in Table 3.1. The data in the latter case in the legend is used as the reference to compute the relative difference.	66
3.9	Precision verification: (a) the computational errors are $O(10^{-12})$ to $O(10^{-11})$; (b) the baseflow converges to $O(10^{-11})$.	67
3.10	TS wave result of Case 1 in Table 3.1 around $Re_x = 8.35 \times 10^5$ in the presence of reflected waves. The plot shows the disturbance of the streamwise component of the velocity field (u'). The y -axis is scaled by a factor of 5.	67
3.11	Schematic representation of the flow problem. The dashed line represents the wall for the clean geometry, and the dotted line represents the wall for the stepped geometry.	68
3.12	Baseflow of the flat plate cases. Streamwise component of the velocity u is displayed.	69
3.13	Frequency scans at an upstream position and a downstream position.	69
3.14	N -factors for the two flat plate cases.	70
3.15	Wall pressure distribution comparison.	70
4.1	Illustrations of subsonic compressible flow simulations with specific physical quantities to be enforced at inflow boundary: (a) pressure along the inflow boundary is expected to be enforced; (b) the inflow velocity is to be enforced to guarantee the desired AoA. The dashed line in (b) denotes periodic boundary conditions.	74
4.2	1D solution domain and associated conservative states. The red region represents the inner state and blue regions represent the ghost state on each side where the solution domain boundaries are provided.	76
4.3	Steady state and perturbation in 1D cases: (a) Perturbation on the internal state; (b) perturbation on the reference state. The dashed lines represent the steady state.	78
4.4	Characteristic lines for a subsonic boundary.	80
4.5	Variation of $\lambda_{2,3}^{MP}$ for subsonic flows.	85

4.6	Normalized real part of $\lambda_{2,3}$ changing with parameter d at different three Mach numbers: $Ma = 0.3$ (black), 0.6 (red), and 0.9 (blue). The solid line represents λ_2 and the dashed line represents λ_3	89
4.7	Global analysis and local analysis.	91
4.8	Eigenvalues at $Ma = 0.3, 0.6, 0.9$ for global analysis of the three-element system with entropy-pressure compatible inflow and pressure outflow.	92
4.9	Baseflow and boundary conditions for 2D stability analysis near to a wall: (a) with a stagnation point and (b) without a stagnation point.	93
4.10	Pressure distribution in the RANS simulation over the full CRM-NLF model.	97
4.11	Boundary conditions for the reduced domain in the CRM-NLF simulation. The periodic boundary condition is adopted in the x_3 -direction for the 3D simulation.	98
4.12	Pressure contours comparison for using different boundary conditions.	98
4.13	Comparison for C_p distributions of the CRM-NLF case. The result by entropy-invariant compatible inflow is not plotted in (b) for its significant deviation as indicated in (a).	99
4.14	Pressure distribution in the RANS simulation over the DLR-F5 model.	100
4.15	Pressure and density contours comparisons for using the entropy-pressure compatible inflow boundary condition.	101
4.16	Comparison for C_p distributions of the DLR-F5 case. (b) shows the zoomed-in view of (a).	102
5.1	Coordinate systems and computational meshes in the $x - y$ plane.	109
5.2	Density fields ρ showing the development of disturbances after turning-off the artificial viscosity, and effects of different damping methods. The flow travels from left to right. From top to bottom in each subfigure shows three representative snapshots in time order. The snapshots are dumped from 2D simulations but are visualized in 3D where the vertical axis also shows the density.	111
5.3	C_p comparison of the background RANS data and 2D embedded simulation.	112
5.4	Boundary layer profile comparisons of using a 3rd-order expansion (P3), a 4th-order expansion (P4), and the CoBL solver for the 2D clean CRM-NLF case.	112
5.5	Streamwise component of the velocity disturbance fields u' of fully developed TS waves over the 2D clean CRM-NLF case. The four snapshots from top to bottom show the disturbance fields with frequencies $f = 30, 40, 50$, and 60 kHz.	113
5.6	Disturbance amplitude profile comparisons of using 3rd-order (P3) and 4th-order (P4) expansions. The frequency of the disturbance is 50 kHz. The profiles for velocity disturbance amplitudes $ u' $ and $ v' $ are scaled by the maximum on the streamwise velocity disturbance amplitude profile $ u' _{max}$, and the temperature disturbance amplitude profile $ T' $ is scaled by its maximum.	114

5.7	<i>N</i> -factor of the 2D clean CRM-NLF case. The component <i>n</i> -factors correspond to the highest frequency of 100 kHz and the lowest frequency of 30 kHz.	114
5.8	Boundary layer profile comparisons for using adiabatic and isothermal temperature boundary condition.	116
5.9	Disturbance amplitude profile comparisons of using adiabatic wall and isothermal wall boundary conditions. The frequency of the disturbance is 50 kHz.	116
5.10	<i>N</i> -factor comparisons for using adiabatic wall and isothermal wall boundary condition. The four curves in (a) from right to left correspond to disturbance frequencies $f = 30, 40, 50, 60$ kHz.	117
5.11	Baseflow in the gap region.	118
5.12	Comparison of TS waves of 60 kHz frequency in the gap region.	119
5.13	Amplitude of velocity components.	120
5.14	<i>N</i> -factor comparisons of the clean case and the gapped case.	120
5.15	Gap induced oscillations of the velocity in the x -direction.	122
5.16	3D boundary layer profile comparisons of the initial and reduced simulations.	122
5.17	Pressure distribution comparison of the initial (Mesh 2 in Fig. 5.1(b)) and reduced (Mesh 3 in Fig. 5.1(c)) simulations.	122
5.18	Gap induced receptivity at $\beta = 2.4 \times 10^4 \text{ m}^{-1}$. Flow from left to right. (b) shows the $z = 0$ plane in 3D, where the additional axis represents the disturbance of the x -component of the velocity.	124
5.19	Time history and FFT analysis results inside and outside the gap at sampling points $(0.339, 0.0895, 0)$ and $(0.355, 0.0928, 0)$, respectively. In (a) the first two convective time scales out of twelve are shown for clarity. The maximum single-sided amplitude in (b) reaches 6×10^{-3} but it is not shown for clarity. The symbol $(\cdot)'$ denotes the disturbance of the corresponding field.	124
6.1	Configuration of the computational domain over the swept plate.	127
6.2	Computational mesh and expanded view in the gap region.	129
6.3	Averaged modal energy of the Fourier modes. The bottom subplot shows the expanded view of the top subplot. Local peaks are highlighted by red dots.	129
6.4	Chordwise velocity (u) contours of the self-sustained oscillation of the first ten Fourier modes. All the plots use the same scale.	131
6.5	Top view of the wall shear stress magnitude. The white arrows show the freestream direction. The color is adjusted to better visualize the streaks.	131
6.6	Vorticity field (z -component) and streamlines in the gap. Freestream comes from left to right.	131
6.7	Wall pressure in the x -direction.	132
6.8	Boundary layer velocity profiles and differences with respect to the rotated Blaius profile.	133

6.9	Disturbance frequency spectra (frequency vs. amplitude) at different sampling locations. The spectra are computed by FFT. The highest peak in each sub-plot except (a)(b)(d)(g) corresponds to a non-dimensional frequency of 0.325.	134
6.10	Eigenspectrum of the LST at different locations.	136
6.11	Comparisons of the LST eigenfunctions and shape of DNS waves at different locations.	136
6.12	Chordwise component of velocity comparison of the DNS wave and BiGlobal mode.	137
6.13	Comparisons of the BiGlobal mode and shape of DNS waves at different locations.	137
6.14	Scaled structural sensitivity, s , of the swept plate with a gap.	138
C.1	N -factor comparisons for P3 and P4 expansions of the 2D clean CRM-NLF case. The four curves from right to left shows the disturbance frequencies $f = 30, 40, 50, 60$ kHz.	168
C.2	N -factor comparisons for using different parameters of the 2D clean CRM-NLF case. P3 expansion is used.	169
C.3	N -factor comparisons for P3 and P4 expansions of the 2D gapped CRM-NLF case. The four curves from right to left shows the disturbance frequencies $f = 30, 40, 50, 60$ kHz.	169
D.1	2D compressible flat plate boundary layer self-similar profiles using the definition $g = h_t/h_{te}$. The Prandtl number $Pr = 0.71$. (a) uses iso-thermal wall where $T_{wall} = T_\infty$	173
D.2	3D incompressible Falkner-Skan-Cooke (FSC) profiles.	175

List of Tables

2.1	Types of boundary conditions.	43
3.1	Initial disturbance scaled by the freestream velocity.	65
3.2	Parameters for the forward-facing step on the plate.	67
4.1	Definitions of different states.	76
4.2	Stability for different inflow boundary conditions	87
4.3	Freestream conditions for the RANS simulation of the CRM-NLF model.	97
4.4	Freestream conditions for the RANS simulation of the DLR-F5 model [136].	100
5.1	Skin thickness of airplanes. Unit [mm].	106
5.2	Trailing-edge thickness reduction using PIP [140]. Unit [mm].	106
5.3	Spoiler trailing edge gap reduction using PIP [141]. Unit [mm].	106
5.4	Mean aerodynamic chords of typical commercial airplanes. Unit [m].	107
5.5	Scaled gap on the CRM-NLF model. Unit [m].	107
5.6	Freestream conditions for experiment #2524 of CRM-NLF model.	107
5.7	Types of boundary conditions.	108
6.1	Re_x at key positions.	128
6.2	Locations of the sampling points on the $z = 0$ plane.	135
6.3	Eigenvalues and wave angles from sectional stability analysis.	136
A.1	Interior penalty numerical diffusion fluxes.	162

Part I

Introduction and computational methods

Chapter 1

Introduction

1.1 The call for sustainable aviation

Aviation is considered one of the greatest achievements in human history that brings global connectivity physically and efficiently. The growth of passengers in commercial aviation has been remarkable over the past few decades. However, side effects come along with the prosperity. Although the average fuel consumption has significantly decreased since 1968 [1, 2], this growing demand keeps consuming more fuel in total [3] and generating more waste emissions including CO₂, NO_x, and etc. [4] (at least before the COVID-19 pandemic while the aviation sector recovers quickly according to the International Air Transport Association (IATA) [5]). As climate change has become an increasingly pressing concern in recent years, finding solutions to address this issue has gained widespread recognition and urgency. This leads to a growing call for sustainability in the aviation sector. Massive investment is made in new technologies to reduce the environmental footprint of aviation, including sustainable fuel [6, 7], hydrogen turbofan [8, 9], battery/fuel cells [10], full electrification [9], light-weight composite [11], and etc.

In spite of the above new contributions towards sustainable aviation, however, it is also of great significance to seek for improvement by revisiting its fundamental: aerodynamics. One of the main goals of this subject is to harvest certain lift more efficiently, i.e. with lower drag and consequently lower fuel consumption by the engines. The drag of an commercial airliner have several sources, where the friction drag typically accounts for approximately 50% of the total drag [12, 13]. Aerodynamic designs with lower skin friction are therefore a topic of interest.

Over the long history of aerodynamics, scientists have already developed an in-depth understanding in macroscopic level from low speed to high speed flows. Nevertheless, many detailed mechanisms are not yet fully clear and more importantly, utilizable, which prevents engineers further optimizing the designs. Specifically, in terms of the the friction drag, it can be five times higher after the smooth laminar boundary flows loose their stability and evolve to chaotic turbulence [14], known as laminar flow transition. A good aerodynamic design of an airliner is therefore closely dependent on the correct prediction of transition onset of external boundary layer flows and subsequent turbulence features. However, the numerous mechanisms and their complex interactions behind flow transition are still the topic of intensive research in the community.

1.2 Boundary layer transition over wings

1.2.1 Laminar boundary layer transition

Laminar boundary layer transition initiates with a receptivity process where environmental disturbances get into boundary layer. The environmental disturbances can come from both the freestream and wall. For compressible flows, sources of freestream disturbances include acoustic waves, vorticity waves (or turbulence), and entropy waves [15, 16]. These waves are associated with different fluctuations. The acoustic waves come from pressure fluctuations and travel at the speed of sound with respect of the flow. The freestream turbulent velocity fluctuations are accounted for in the vorticity waves, and the entropy waves include temperature and density fluctuations at a constant pressure. Both vorticity waves and entropy waves travel with the flow [17, 18]. As for the disturbances from the wall, they can be generated either dynamically or statically. The dynamic disturbances come from mechanical motion, such as vibration and blowing-suction, while surface irregularities, either discrete or distributed, are considered as a kind of static disturbance. The aforementioned disturbances excite disturbances inside the boundary layer through different and complex mechanisms. It is discovered that the dynamic wall disturbances directly resonate with the boundary layer instabilities due to its broad wavenumber spectrum, while the freestream disturbances energize the boundary layer in the region with large streamwise variation, e.g. near leading edge or surface irregularities [15].

According to different environmental disturbance conditions the transition process can vary from gradual to abrupt. Fig. 1.1 summarizes five transition paths and related mechanisms. In transition path A the initial disturbances first experience linear growth, which is typically weak and well described by Linear Stability Theory (LST) of primary modes [15]. It is then followed by rapid non-linear growth through secondary mechanisms, where three-dimensional effects play a role and spanwise vorticities are formed. The disturbances breakdown shortly downstream. Compared with the linear growth region, the non-linear region is much shorter in the streamwise direction. This enables the transition prediction based on the computation of the linear growth of disturbances. A requirement for boundary layer transition following path A is low environmental disturbance level. The transition process following path A is referred to as natural transition. On the other hand, if the environmental disturbances are strong enough, the linear growth stage will be bypassed. The receptivity stage can also be followed by the breakdown to turbulence, which is depicted by path E. This process is known as bypass transition. In the middle of paths A and E are path B, C, and D, which are characterized by transient growth of disturbances. The transient growth is caused by the interaction of two non-orthogonal, stable modes, leading to an algebraic growth and exponential decay. Having experienced the transient mechanisms, the transition process can keep following the linear growth, or directly be led to the non-linear growth stage or the breakdown stage depending on the strength of the environmental disturbances.

At the typical cruise condition of a commercial airliner, the atmosphere is steady and quiet. The environmental disturbances is so weak (i.e. the freestream turbulence intensity is less than 1% [19]) that the boundary layer transition over the wings usually follows the natural transition in path A [20]. In the linear growth stage, the disturbances develop in form of primary modes (or instabilities), whose detailed description are given in the next section.

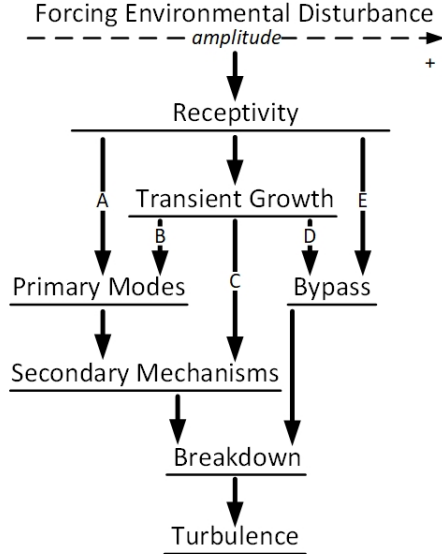


Figure 1.1: Different paths for laminar flow transition to turbulence [15].

1.2.2 Boundary layer instabilities

Laminar boundary layer natural transition follows path A in Fig. 1.1. This process is dominated by the linear growth stage, where small disturbances exponentially grow as primal modes of instability. In this section four critical instabilities are introduced, including Tollmien-Schlichting instability, crossflow instability, attachment line instability, and centrifugal instability.

1.2.2.1 Tollmien-Schlichting (TS) instability

The well-known Tollmien-Schlichting (TS) instability is named after the two main contributors for their first prediction. However, this instability has not come into observation until Schubauer and Skramstad's experiment in 1943 [21, 22]. The TS instability is a kind of viscous instability, where the viscosity destabilizes the flow rather than having a stabilizing effect. The TS instability occurs when the flows exhibit 2D characteristics, such as a boundary layer over a straight wing or at the mid-chord region over a swept wing [23]. In the linear growth stage, the TS instability generates TS waves, which are unsteady vortices with spanwise pointing axes. As the 3D disturbance develops through the secondary mechanisms, A vortices occur and become hairpin vortices downstream [23]. The hairpin vortices are followed by turbulent spots. Finally the flow develops to fully turbulent shortly after the turbulent spots merge [24]. The above transition process is named TS transition, as a certain type of natural transition.

1.2.2.2 Crossflow instability

Swept wings are widely adopted for the transonic aircrafts to increase the critical Mach number and reduce the wave drag. The swept setting together with the airfoil geometries makes the flows over the wings show three-dimensional (3D) features. When the flow passes the upper surface of a swept wing, for inviscid flow outside the boundary layer, the spanwise velocity component parallel to the leading-edge

basically retains its value. However, the chordwise component normal to the leading-edge first decelerates when approaching the wing. Then it experiences acceleration before passing the minimum pressure point and decelerates again due to the adverse pressure gradient. The above processes finally generate an S-shaped inviscid streamline [25] as illustrated in Fig. 1.2(a). As to the fields inside the boundary layer, the velocity decreases rapidly while the pressure approximately keeps the value in the wall-normal direction. Therefore the pressure gradient inside the boundary layer also remains the same in the crossflow (CF) direction, i.e. z_t in the Fig. 1.2, which is defined as normal to the plane spanned by the inviscid streamline direction x_t and the wall normal direction. On the S-shaped inviscid streamline outside the boundary layer, the pressure gradient balances the centripetal acceleration. However, the reduced velocity inside the boundary layer breaks this balance, which finally leads to the crossflow in z_t direction, which a typical secondary flow [26].

An illustration of the 3D boundary layer velocity profile with crossflow is given in Fig. 1.2(b). The crossflow velocity component is exactly zero at the wall, and the profile's curvature in the vicinity is negative due to the viscosity nature. On the other hand, when approaching the edge of the boundary layer the crossflow velocity recovers zero asymptotically, which results in positive curvature in this region. Therefore an inflection point exists leading to the crossflow instability. Unlike the TS instability caused by viscosity's destabilization, the crossflow instability is based on the inflection point so it is an inviscid instability. Another significant difference to the TS instability is that the TS instability is stabilized by a favorable pressure gradient and destabilized by adverse pressure gradient while both pressure gradients destabilize the crossflow instability [26, 27]. The corresponding crossflow waves has the form of co-rotating vortices whose axis direction are only a few degrees deviating from the local inviscid streamline direction [26].

The crossflow waves can be either traveling or stationary. For civil airliners cruising in the steady atmosphere, the stationary instability is the dominant [26]. The stationary vortices can modify the baseflow, modulating the instability development [28]. Thus, extra care should be taken in computation studies. In addition, the stationary crossflow instability can generate secondary instability, which can easily cause breakdown shortly downstream [26]. Flow transition caused by crossflow instability will show a saw-tooth pattern, for which a good visualization is provided in Ref. [29].

1.2.2.3 Other instabilities

In addition to the TS instability and crossflow instability, other major instabilities include attachment line instability and centrifugal instability. The attachment line instability arises on the swept wings. Because of the swept geometry, there is a crossflow component along the attachment line, where the flow hits the wing and bifurcates to cover the upper and lower sides of the wing. The disturbances can develop along this line and drive the flow to turbulence. An associated concept is attachment line contamination, where the turbulent boundary layer arising from the fuselage sweeps over the wing along the attachment line. In general, the wings with large leading-edge radii is more sensitive to the attachment line transition and contamination [26]. The turbulence attachment line invalidates the streamwise analysis for TS instability and crossflow instability as well as corresponding flow controls since the local boundary layer of interest is already turbulence. To obtain

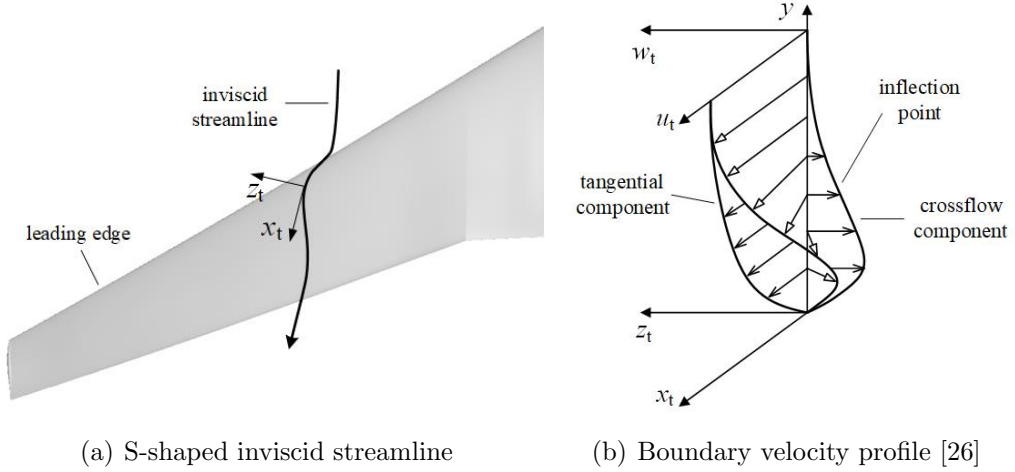


Figure 1.2: Illustration for streamline and boundary-layer velocity profile near the leading edge of a swept wing.

a laminar attachment line, attachment line control and relaminarisation methods have been developed [30].

In the boundary layers over a concave surface, the centrifugal force stabilizes 2D disturbances while destabilizing the 3D disturbances, leading to centrifugal instability (also known as Görtler instability) [23]. The adjacent Görtler vortices rotate in counter directions with respect to streamwise aligned axes. On a swept wing geometry the crossflow waves typically suppress the Görtler vortices [31], such vortices are therefore not typically observed near the leading edge of the wing.

1.2.3 Effect of real geometries

An airliner in the physical world is never as clean as a CAD model. In the manufacturing of an airliner, different parts are assembled to enclose the outer surface, which typically leaves the junctions imperfectly matched but within an accepted tolerance. This can lead to several types of surface irregularities. Fig. 1.3 shows a photograph of the left-wing of a well-known Boeing 737-800 airliner. It is clear that the wing surface is filled with several types of irregularities. Apart from the designed vortex generators, the most evident irregularity in the upstream region is the step/gap at the trailing-edge of the slat even when it is closed. A similar step/gap irregularity also presents at the junction of two skin panels in the middle of the main wing. These irregularities span almost over the full wing, showing a quasi-3D feature. Note that in the above the irregularities are denoted by “step/gap” because the detailed type depends on the local geometry, where a mixed type is also possible. Moreover, although covered by paint, macroscopic indentations are present at the rivets on both main wing and slat. Since the rivets are in array, periodicity is also expected.

In the chordwise direction these surface irregularities are typically small in size, which can be comparable with the local boundary layer thickness. For the irregularities located upstream of the flow, e.g. the step/gap at the slat trailing edge, they will typically interact with and amplify the disturbances inside the laminar boundary layer, and finally cause early flow transition. This destabilization effect has been studied in many scenarios including forward-facing step/backward-facing

step (FFS/BFS) [32–35], gap [36], etc. However, opposite to the destabilization effect, surfaces irregularities can also surprisingly stabilize the boundary layer. Wu and Hogg [37] numerically discovered a 2D hump may stabilize the TS waves when the size is small enough. Local or downstream stabilization have also been reported through numerical simulations by Xu et al. for TS waves over smooth FFS [38] and indentations [39], and by Casacuberta et al. [40] for crossflow waves over FFS. The stabilizing effect on the crossflow waves by FFS was also investigated and showed in the experiments by Rius-Vidales and Kotsonis [41].

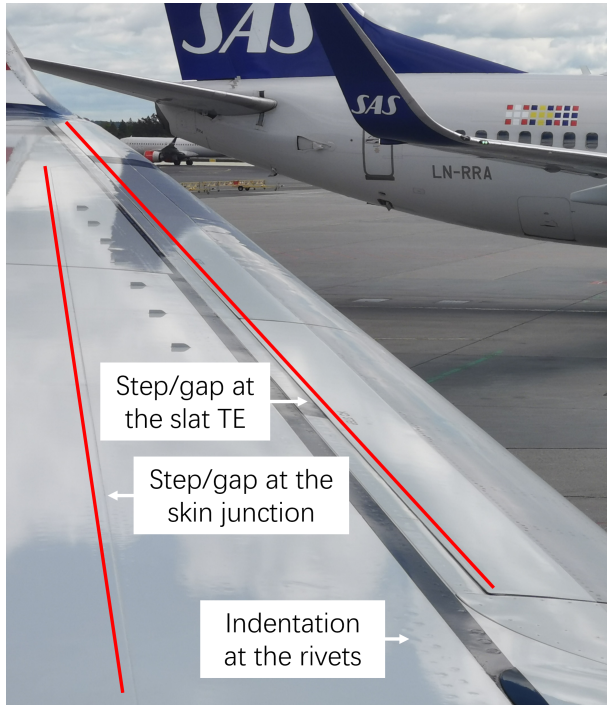


Figure 1.3: Wing of a Boeing 737-800 airliner from Norwegian Air Shuttle. Several sources of surface irregularities are labelled. Image by author.

1.3 Transition prediction

The prediction of laminar boundary layer natural transition helps to provide drag estimations in the design stage of airliners, and therefore is of interest. The natural transition process is characterized by a dominant streamwise linear growth stage of instabilities. This physical setting makes the e^N method a common and suitable tool for the transition prediction. Since the e^N method is developed based on the linear stability analysis, the fundamentals of this analysis are first introduced in this section.

1.3.1 Linear stability analysis

To understand the process of laminar flow transition to turbulence, researchers have developed various approaches to analyze the stability performances of the flows. It is not surprising that the first established and the most well-known approach is the Linear Stability Theory (LST) since, despite the additional assumptions in this

theory, in general the linearization is a conventional approach to deal with complex problems and its mathematical foundation has the best level of maturity in all tools we have even so far. The LST has a long history of development dating back to late 19th century [42]. As implied by the terminology, the basic idea of the LST is to study the development of small disturbances on top of a steady, undisturbed baseflow [27] as

$$\mathbf{q}(x, y, z, t) = \underbrace{\bar{\mathbf{q}}(x, y, z)}_{\text{Baseflow}} + \underbrace{\mathbf{q}'(x, y, z, t)}_{\text{Disturbance}}, \quad (1.1)$$

where \mathbf{q} is the vector of state variables that can take different forms for incompressible or compressible flows, (\cdot) denotes the baseflow and $(\cdot)'$ denotes the disturbance. Before we adopt additional assumptions, the above decomposition in Eq. (1.1) is general and independent of coordinate system, x , y , and z are the coordinates of an arbitrary Cartesian coordinate system. However, the LST further assumes parallel baseflow where only the variations in the wall-normal direction play significant roles. To discriminate the coordinates in the context of LST, we perform the analysis in a local coordinate system (denoted by $(\cdot)^{\text{loc}}$) with its origin on the wall, and we let $x = x^{\text{loc}}$, $y = y^{\text{loc}}$, and $z = z^{\text{loc}}$ be the local coordinates in the wall-tangential direction, wall-normal direction, and spanwise direction with respect to a given surface or channel in Eq. (1.1). (Note the wall-tangential direction is defined to be orthogonal to the wall-normal and spanwise directions.) As the LST also assumes the wall-normal baseflow velocity component is zero, the baseflow velocity therefore reads

$$\bar{\mathbf{u}} = \begin{pmatrix} \bar{u} \\ \bar{v} \\ \bar{w} \end{pmatrix} = \begin{pmatrix} \bar{u}(y^{\text{loc}}) \\ 0 \\ \bar{w}(y^{\text{loc}}) \end{pmatrix}, \quad (1.2)$$

where \bar{u} is the baseflow velocity component in the wall-tangential direction, \bar{v} in the wall-normal direction, and \bar{w} in the spanwise direction. The parallel assumption is well satisfied in many typical flows, e.g. laminar boundary layer downstream of the leading edge of a wing.

On the other hand, in the local coordinate system the LST considers disturbances of the form

$$\mathbf{q}'(x^{\text{loc}}, y^{\text{loc}}, z^{\text{loc}}, t) = \hat{\mathbf{q}}_{1D}(y^{\text{loc}})e^{i\theta_{1D}} + c.c., \quad \theta_{1D} = \alpha x^{\text{loc}} + \beta z^{\text{loc}} - \omega t, \quad (1.3)$$

where $\hat{\mathbf{q}}_{1D}(y^{\text{loc}})$ is the shape function of the disturbances varying only in the wall-normal direction while homogeneity is assumed in the other two directions parallel with the surface of interest. Therefore wall-tangential and spanwise wavenumbers α and β appear in the complex phase function θ_{1D} , where ω is the angular frequency. In the above, *c.c.* denotes the complex conjugate leading to a real $\mathbf{q}'(x^{\text{loc}}, y^{\text{loc}}, z^{\text{loc}}, t)$ in Eq. (1.3).

By substituting the above Eqs. (1.1), (1.2), and (1.3) into the governing Navier-Stokes equations (e.g. the compressible form (2.1)), we have a relation between temporal frequency and spatial wavenumbers, known as the dispersion relation [42]

$$\phi(\omega, \alpha, \beta) = 0,$$

which is an eigenvalue problem of the frequency or wavenumber in form of an Ordinary Differential Equation (ODE) of the shape function. The dispersion relation is the core of the LST and it can be solved either spatially or temporally where further

assumptions are included. For example, temporal analysis solves for the complex frequency $\omega = \omega_r + i\omega_i$ with prescribed real wavenumbers α and β . More systematic reviews can be found in Mack [42], Schmid and Henningson [43], and many other monographs such as Ref. [44].

As mentioned above, the classic LST only considers the nonhomogeneous spatial variation in the wall-normal direction for both baseflow and disturbance. It is therefore a one-dimensional analysis [45] or local stability analysis. It is sometimes also referred to as sectional stability analysis as the analysis outputs the stability propriety of a certain cross-section of the baseflow [46]. However, the parallel flow assumption deviates from the physical settings behind rapid changing baseflows where multi-dimensional features are dominant, e.g. laminar boundary layer flow with recirculation bubble or over surface irregularities. More general models/tools are therefore required. One successful extension of the LST is the Parabolised Stability Equations (PSE) approach where the wall-normal baseflow velocity components is taken into account. However, since the chordwise variation is still assumed to be mild, the PSE is considered as a quasi-two-dimensional analysis approach [45].

Another branch of the extensions is global stability analysis [45, 47], where the spatial variations in two or three directions are modelled in the shape function rather than in the exponent, indicating nonhomogeneous variation. Specifically, wall-tangential and/or spanwise variation(s) can be modelled in the shape function, and the local coordinate system as in the above LST is not adopted. This leads to the disturbances of the form

$$\mathbf{q}'(x, y, z, t) = \begin{cases} \widehat{\mathbf{q}}_{2D}(x, y)e^{i\theta_{2D,z}} + c.c., & \theta_{2D,z} = \beta z - \omega t, \\ \widehat{\mathbf{q}}_{2D}(y, z)e^{i\theta_{2D,x}} + c.c., & \theta_{2D,x} = \alpha x - \omega t, \\ \widehat{\mathbf{q}}_{3D}(x, y, z)e^{i\theta_{3D}} + c.c., & \theta_{3D} = -\omega t, \end{cases} \quad \begin{array}{l} \text{BiGlobal analysis } (x-y) \\ \text{BiGlobal analysis } (y-z), \\ \text{TriGlobal analysis} \end{array} \quad (1.4)$$

where the terminology “BiGlobal” denotes two-dimensional and “TriGlobal” denotes three-dimensional [47], and in the BiGlobal analysis we can model the shape function in either $x-y$ or $y-z$ planes. Accordingly, the global stability analysis, i.e. BiGlobal or TriGlobal analysis, is performed with the baseflow varying in the same spatial direction(s) as the disturbances. The replacement of Eq. (1.4) to Eq. (1.3) still leads to an eigenvalue problem.

Moreover, it should be highlighted on the computational side that global stability analysis is much more demanding compared with local stability analysis. This is because the global stability analysis becomes a Partial Differential Equation (PDE) problem and the more degrees of freedom (DOFs) cause much higher memory consumption and longer solution period, known as the curse of dimensionality, an estimation of which has been performed by Theofilis [47]. Therefore, the BiGlobal analysis has a wider application than the TriGlobal analysis. For the same reason, more advanced numerical methods, such as the iteration method based on Krylov subspace are necessary to find the global solutions.

Additionaly, here we also clarify terminology confusion about the “global method” and “local method” one would typically find in the numerical method for the local stability analysis. The global method refers to the direct solution of the eigenvalue problem such that the full eigenspectra and all eigenfunctions are obtained; its counterpart, local method typically means the iteration method eventually converging to a certain eigenmode, which has the advantage of better accuracy [43, 44, 48, 49].

This confusion does not appear in the global stability analysis probably because the direct solution is infeasible for a large, real problem.

Lastly, we consider the global stability analysis is an extension to but still lies in the scope of the “linear stability theory” since the fundamental idea of linearization is the same. However, the abbreviation “LST” still specifically refers to the local stability analysis in this work to follow the convention in the community.

1.3.2 e^N transition model

The e^N method, also known as the N -factor method, is developed by Smith and Gamberoni [50] and by van Ingen [51] through the local stability analysis. The basic idea is to compute the amplitude amplification of a spectrum of disturbances. The transition onset is predicted where the envelope of these amplification curves exceeds some prescribed threshold. In most cases, including both incompressible flows and compressible flows, this threshold is typically within the range of 6 to 11 while much larger threshold above 20 has also been reported with flight test data [52, 53]. An exact threshold depends on the freestream environment, i.e. freestream turbulence intensity of the case and therefore still needs calibration for more accurate prediction. The influence of the environmental condition can also be directly considered in a model, where Mack [54] first proposed an N -factor correction method according to the freestream turbulence intensity. In addition, based on the standard model introduced in the following, well-known variations include variable N -factor method [55] and two N -Factor methods [56].

In spatial analysis of the LST, a disturbance in Eq. (1.3) has complex wavenumbers, $\alpha = \alpha_r + i\alpha_i$ and $\beta = \beta_r + i\beta_i$. The corresponding eigenvalue problem solves for the spatial growth rate in the wall-tangential direction α_i and the eigenfunction $\hat{\mathbf{q}}(y)$ with further assumptions adopted for the spanwise wavenumber β , which will be introduced in the last paragraph. The amplification curve (n -factor) is defined by

$$n(x) = \ln \left(\frac{A(x)}{A_0} \right) = \int_{x_0}^x -\alpha_i dx^{\text{loc}}(x), \quad (1.5)$$

where the body-fitted local coordinate in the wall-tangential direction x^{loc} is a function of the global coordinate x , $A(x)$ is the amplitude of the mode $\hat{\mathbf{q}}(y)$

$$A(x) = \left\{ \max_y (|\hat{\mathbf{q}}(y)|) \right\}_x. \quad (1.6)$$

In the above Eq. (1.5), the subscript $(\cdot)_0$ denotes the position where the disturbance first starts to grow. Therefore x_0 is the point on left branch of the neutral stability curve (see Ref. [23]), and $A_0 = A(x_0)$. After generating a set of amplification curves for the disturbances of different frequencies, the N -factor envelope of the amplification curves is given by

$$N(x) = \max_{f,\beta} (n(x)), \quad (1.7)$$

where $f = \omega/(2\pi)$ is the disturbance frequency.

We note that in Eq. (1.5) that an amplification curve $n(x)$ can be computed using two approaches. One is based on the amplitude through scanning in the wall-normal direction in Eq. (1.6) and then in the chordwise direction to get an array of $A(x)$.

Another approach is amplitude-free by directly integrating the spatial growth rate $-\alpha_i$ of the eigenvalue problem. For a conventional LST analysis the latter approach is preferable for its simplicity while for analysis involving flow field simulations, such as DNS or LES, the former approach is more convenient due to the lack of growth rate information.

The above computation can be simplified for two-dimensional analysis since the spanwise wavenumber in Eq. (1.3) is zero. However, further assumptions for spanwise wavenumber are required for three-dimensional analysis. The available methods are saddle point, fixed wave angle, and fixed spanwise wavelength methods [44]. The current work adopts the fixed spanwise wavelength approach proposed by Mack [57], where the spanwise wavenumber β_r is considered as a constant for each simulation while the disturbance is assumed to grow only in wall-tangential direction so that β_i is set to be zero.

1.4 Motivation and main objectives

As is mentioned above, in aerospace applications the e^N method is a common and suitable method to predict transition for transonic external flows which experience a freestream with low turbulence intensity and background noise. The e^N method involves two major steps: the baseflow computation and the prediction of the disturbances' growth. Conventionally, the baseflow is computed by a boundary layer equations solver with a prescribed pressure distribution as input. Since the pressure distribution plays a significant role on the growth of the disturbances, this approach accurately predicts transition of ideal boundary layer flows where short scale rapid variations are not present. However, the underlying assumptions of boundary layer equations limit its application. The real geometry of the wing surface are not typically smooth but includes irregularities in the form of steps and gaps due to the manufacturing, operation, and maintenance. Such surface irregularities typically complicate the local flow by generating local recirculation, i.e. separation bubbles. Under this condition, the boundary layer equations fail to correctly describe the baseflow. A Navier-Stokes solver therefore needs to be used instead. The growth of disturbances is next computed to complete the analysis. It can be solved following different approaches such as LST, PSE [58, 59], Linear Harmonic Navier-Stokes (LHNS) [60–62], linearized Navier-Stokes, or full Navier-Stokes equations [36]. In the above, when different computational approaches are involved in this two main steps, new researchers in the field find it extremely difficult to start their investigation since developing each of the tools requires specific yet different knowledge. Moreover, a set of trusted and well documented software is still unavailable to the best of author's knowledge. Although different research groups have developed their own tools [63–68], relatively few, if any, are available to the wider community as open-source. A set of integrated tools is therefore desirable.

The current work is motivated by designing high fidelity simulation tools for both academia community and industry to study boundary layer transition at realistic Reynolds numbers and transonic conditions over wings, where the surface may not be smooth but contains irregularities. The simulation is expected to be efficient. Therefore a near wall, reduced computational domain is adopted over wing sections while a prescribed pressure distribution should be maintained. This must be achieved through appropriate boundary conditions when the baseflow is governed by

the Navier-Stokes equations. Unlike a supersonic flow where at the inflow boundary all the boundary data can be specified, a subsonic flow have more complicated characteristic propagation directions, which means only two conditions can be enforced in the normal direction at the inflow boundary [69]. An appropriate selection of the two conditions is critical not only to ensure well-posedness of the flow problem but also to produce a stable numerical solution. However, a challenge to achieve this is the lack of practical stability theory as guidance to design the boundary conditions for element-based discretisations (e.g. discontinuous Galerkin). We therefore revisit the fundamental setting of the numerical flux-based, weak boundary condition adopted in the solver. A simple yet practical stability theory is developed before we see how best to enforce pressure compatibility at the subsonic inflow boundary.

On the other hand, after completing the integrated tool for transition analysis, the transition performance on the imperfect surface and the underlying flow physics will be investigated. This is motivated by the fact that for the airliner design manufacturers, the cost to produce a high quality surface and the aerodynamic benefit in return is a balance for the lowest total cost, which must be decided based on thorough understandings of the effects by the surface irregularities [70]. According to our review, most studies focused on small forward/backward-facing steps (FFS/BFS) [32, 34, 35, 38, 40], smooth indentation [39], hump [71], large cavities [72–74], and 3D cylindrical roughness [75]. As typical surface irregularities, small sized gaps (in contrast to large sized cavities) widely exist on the wings of aircrafts at the skin panel junctions [34] and trailing-edge of the slat. However, the influence of the gaps on the transition performance has not been sufficiently documented in the literature, particularly in the conditions close to the real flows on the wings. Therefore in this work we also explore a physically motivated sized gap and its influence in the transition analysis. A survey of involved geometries is first performed to clarify the realistic sizes to be studied.

1.5 Outline of the thesis

This thesis is organized as follows. Chapter 2 introduces the governing equations and numerical methods adopted in this work, including the discontinuous Galerkin formulations for a model advection-diffusion problem and for the compressible Navier-Stokes equations, as well as the detailed boundary condition treatments for the latter of both advection and diffusion terms. Chapter 3 overviews the transition analysis pipeline that we have developed. The approach to avoid signal contamination in the disturbance field simulation is also presented. We verify this pipeline using the 2D transonic flat plate with a forward-facing step at Mach 0.8 and a Reynolds number of 4.9×10^6 based on the length of the domain. One of the critical techniques in this pipeline is the appropriate boundary condition enforcement to maintain pressure compatibility with the prescribed data. In Chapter 4 we demonstrate a practical analysis for designing stable boundary conditions of different kinds with rigorous mathematical proofs. We test both CRM-NLF and DLR-F5 models to show the effectiveness of the pressure compatible condition we design.

On the flow simulation side, as our goal is to investigate the transitional performance on the wing surfaces, a survey to determine realistic sizes of gap irregularities is first performed in Chapter 5. A geometry with such irregularities is then introduced onto the CRM-NLF model, and transition related aspects are analyzed

including the influence of different temperature boundary conditions on the wall. In the computation of 3D baseflow, self-sustained oscillation is observed. To better understand the underlying physics, a smaller computational domain on a swept plate model problem focused on the gap region is set and direct numerical simulations are performed in Chapter 6. Finally, Chapter 7 summarizes the thesis work and includes a few future focuses of study.

In addition, the appendices provide the more details of formulation, analysis algorithms, boundary condition settings, and intermediate results from the above chapters.

We note that Chapters 3 and 4 are reproduced and extended from the two publications listed in Section 1.6.1. These works are developed by the author in collaboration with other researchers so that “we” rather than “I” is used in this thesis.

1.6 List of publications and conference presentations

1.6.1 Publications

- **G. Lyu**, C. Chen, X. Du, and S.J. Sherwin. Stable, entropy-pressure compatible subsonic Riemann boundary condition for embedded DG compressible flow simulations. *Journal of Computational Physics*, vol. 476, p. 111896, 2023. DOI: 10.1016/j.jcp.2022.111896.
- **G. Lyu**, C. Chen, X. Du, M. S. Mughal, and S.J. Sherwin. Open-source framework for transonic boundary layer natural transition analysis over complex geometries in Nektar++, *AIAA Paper*, p. 4032, 2022. DOI: 10.2514/6.2022-4032.

1.6.2 Conference presentations

- **G. Lyu**, C. Chen, X. Du, S.J. Sherwin. Stable Riemann inflow boundary conditions for embedded DG compressible flow simulations. *International Conference on Spectral and High Order Methods (ICOSAHOM 2023)*, Seoul, South Korea, 14–18 August, 2023.
- **G. Lyu**, C. Chen, S. Mughal, X. Du, S.J. Sherwin. Transonic boundary layer natural transition analysis over a gapped wing section. *15th ERCOFTAC SIG 33 Workshop, Progress in Flow Instability, Transition and Control*, Alghero, Italy, 28–30, June, 2023.
- **G. Lyu**, C. Chen, S. Mughal, X. Du, S.J. Sherwin. Studies of disturbance growth in transonic boundary layer s over complex geometries using embedded DG simulations. *9th International Symposium on Bifurcations and Instabilities in Fluid Dynamics (BIFD 2022)*, Groningen, The Netherlands, 16–19 August, 2022.

- **G. Lyu**, C. Chen, X. Du, M. S. Mughal, and S.J. Sherwin. Open-source framework for transonic boundary layer natural transition analysis over complex geometries in Nektar++, *AIAA AVIATION Forum*, Chicago, USA, 27 June–1 July 2022.
- **G. Lyu**, C. Chen, S. Mughal, X. Du, S.J. Sherwin. Studies of disturbance growth in transonic boundary layers over complex geometries using embedded DG simulations. *14th ERCOFTAC SIG 33 Workshop, Progress in Flow Instability, Transition and Control*, Cádiz, Spain, 15–17 June, 2022.
- **G. Lyu**, C. Chen, X. Du, S.J. Sherwin. Stable, entropy-pressure compatible subsonic Riemann boundary condition for embedded DG compressible flow simulations. *8th European Congress on Computational Methods in Applied Sciences and Engineering (ECCOMAS CONGRESS 2022)*, Oslo, Norway, 6–9 June, 2022.
- D. Lindblad, **G. Lyu**, S. Sherwin, C. Cantwell, A. Proença, J. Lawrence, M.M. Ginard. Influence of boundary layer tripping on the flow and sound field produced by a turbulent jet. *8th European Congress on Computational Methods in Applied Sciences and Engineering (ECCOMAS CONGRESS 2022)*, Oslo, Norway, 6–9 June, 2022.
- **G. Lyu**, S.J. Sherwin, S. Mughal, C. Chen, X. Du. Understanding appropriate boundary conditions for embedded high order method into RANS. *PRISM Residential Workshop*, Milton Keynes, United Kingdom, 10–12 January, 2022.
- **G. Lyu**, S.J. Sherwin, S. Mughal, C. Chen, X. Du, High-fidelity modeling of laminar flow transition to turbulence. COMAC-Imperial Research Centre - Technical Workshop, London, United Kingdom, 28 June, 2021.
- S. Sherwin, Z. Yan, Y. Pan, **G. Lyu**, and J. Peiró. Development and application of a spectral/hp element, implicit compressible solver using the JFNK approach. *7th International Conference on Numerical Methods for Hyperbolic Problems (NumHyp 2021)*, Trento, Italy, 26–30 July, 2021.
- **G. Lyu**, C. Chen, X. Du, S.J. Sherwin. Pressure-density compatible Riemann boundary condition for DG compressible flow simulations. *International Conference on Spectral and High Order Methods (ICOSAHOM 2020)*, Vienna, Austria, 12–16 July, 2021.

Chapter 2

Governing equations and numerical methods

2.1 Governing equations

2.1.1 Navier-Stokes (NS) equations

Compressible flows are simulated here by solving the conservative form of the Navier-Stokes (NS) equations, which in a Cartesian coordinate system read

$$\frac{\partial \mathbf{Q}}{\partial t} + \frac{\partial \mathbf{F}_1}{\partial x_1} + \frac{\partial \mathbf{F}_2}{\partial x_2} + \frac{\partial \mathbf{F}_3}{\partial x_3} = \frac{\partial \mathbf{G}_1}{\partial x_1} + \frac{\partial \mathbf{G}_2}{\partial x_2} + \frac{\partial \mathbf{G}_3}{\partial x_3}, \quad (2.1)$$

where x_i denotes the x , y , and z -directions for $i = 1, 2, 3$, respectively, \mathbf{Q} is the vector of conservative variables, $\mathbf{F}_i = \mathbf{F}_i(\mathbf{Q})$ and $\mathbf{G}_i = \mathbf{G}_i(\mathbf{Q}, \nabla \mathbf{Q})$ are vectors of inviscid fluxes and viscous flux, respectively

$$\mathbf{Q} = \begin{pmatrix} \rho \\ \rho u \\ \rho v \\ \rho w \\ E \end{pmatrix}, \quad \mathbf{F}_i = \begin{pmatrix} \rho u_i \\ \rho u_1 u_i + p \delta_{1i} \\ \rho u_2 u_i + p \delta_{2i} \\ \rho u_3 u_i + p \delta_{3i} \\ u_i(E + p) \end{pmatrix}, \quad \mathbf{G}_i = \begin{pmatrix} 0 \\ \tau_{1i} \\ \tau_{2i} \\ \tau_{3i} \\ u_j \tau_{ji} + \kappa \partial T / \partial x_i \end{pmatrix}, \quad (2.2)$$

where ρ is the density, u_i is the velocity component in the x_i -direction, p is the pressure, δ_{ij} is the Kronecker delta function, E is the total energy per unit volume, T is the temperature, κ is the thermal conductivity, and τ_{ij} are the components of the stress tensor

$$\tau_{ij} = \mu \left(\frac{\partial u_i}{\partial x_j} + \frac{\partial u_j}{\partial x_i} \right) - \frac{2}{3} \mu \frac{\partial u_k}{\partial x_k} \delta_{ij}, \quad (2.3)$$

where μ is the dynamic viscosity computed by Sutherland's law

$$\mu = \mu_0 \left(\frac{T}{T_0} \right)^{3/2} \frac{T_0 + C}{T + C}, \quad (2.4)$$

where the calibrated values used are $\mu_0 = 1.716 \times 10^{-5}$ kg/ms, $T_0 = 273.15$ K, and $C = 110.4$ K for air.

We consider air to be perfect gas, for which the pressure is related to the total energy per unit volume through the relations:

$$E = \frac{p}{\gamma - 1} + \frac{1}{2} \rho (u_1^2 + u_2^2 + u_3^2), \quad (2.5)$$

$$p = \rho R T, \quad (2.6)$$

where γ is the specific heats ratio and R is the specific gas constant.

In Eq. (2.2), the thermal conductivity is computed by

$$\kappa = \frac{\mu c_p}{Pr}, \quad (2.7)$$

where c_p is the specific heat at constant pressure, and Pr is the Prandtl number. Since c_p can be rewritten as

$$c_p = \frac{\gamma}{\gamma - 1} R, \quad (2.8)$$

the expression for thermal conductivity becomes

$$\kappa = \frac{\gamma}{\gamma - 1} \frac{\mu R}{Pr}. \quad (2.9)$$

For simplicity of the expressions, the vectors for inviscid and viscous fluxes are abridged as [76]

$$\mathbf{F} = \begin{pmatrix} \mathbf{F}_1 \\ \mathbf{F}_2 \\ \mathbf{F}_3 \end{pmatrix}, \quad \mathbf{G} = \begin{pmatrix} \mathbf{G}_1 \\ \mathbf{G}_2 \\ \mathbf{G}_3 \end{pmatrix}, \quad (2.10)$$

and the NS equations take the form

$$\frac{\partial \mathbf{Q}}{\partial t} + \nabla \cdot \mathbf{H} = \mathbf{0}, \quad (2.11)$$

where $\mathbf{H}(\mathbf{Q}, \nabla \mathbf{Q}) = \mathbf{F}(\mathbf{Q}) - \mathbf{G}(\mathbf{Q}, \nabla \mathbf{Q})$.

2.1.2 Non-dimensionalization of the Navier-Stokes equations

In numerical simulations, it is not the original NS equations but their non-dimensional form that is usually solved. A proper non-dimensionalization scales the flow variables to the order of $O(1)$, which could improve accuracy and convergence during numerical calculations [77]. Moreover, the equations are usually solved with stabilization methods, where some stabilization parameters are case dependent but typically calibrated for non-dimensionalized flows, and therefore they can be directly used to set up non-dimensionalized simulations. In other words, the setting process will be simplified if the flow problem is non-dimensionalized from the beginning.

To non-dimensionalize the NS equations the freestream quantities are often chosen as the references. Let L_{ref} be a reference length, U_∞ be a reference velocity, $t_{\text{ref}} = L_{\text{ref}}/U_\infty$ be a reference time, ρ_∞ be a reference density, T_∞ be a reference temperature, μ_∞ be a reference viscosity, and denote the non-dimensionalized parameters by an overbar, we have

$$\begin{aligned} t &= \frac{L_{\text{ref}}}{U_\infty} \bar{t}, & x_i &= L_{\text{ref}} \bar{x}_i, & u_i &= U_\infty \bar{u}_i, & \rho &= \rho_\infty \bar{\rho}, \\ p &= \rho_\infty U_\infty^2 \bar{p}, & E &= \rho_\infty U_\infty^2 \bar{E}, & T &= T_\infty \bar{T}, & \mu &= \mu_\infty \bar{\mu}, \\ Re &= \frac{\rho_\infty U_\infty L_{\text{ref}}}{\mu_\infty}, & \kappa &= \frac{\mu_\infty U_\infty^2}{T_\infty} \frac{\bar{\mu}}{(\gamma - 1) Pr Ma_\infty^2} = \frac{\mu_\infty U_\infty^2}{T_\infty} \bar{\kappa}, \end{aligned} \quad (2.12)$$

where Re is the Reynolds number, Ma_∞ is the freestream Mach number, and the last equation is derived using thermodynamic relations. By substituting the expressions in Eq. (2.12) into Eq. (2.1), the non-dimensionalized NS equations take the form

$$\frac{\partial \bar{\mathbf{Q}}}{\partial \bar{t}} + \frac{\partial \bar{\mathbf{F}}_1}{\partial \bar{x}_1} + \frac{\partial \bar{\mathbf{F}}_2}{\partial \bar{x}_2} + \frac{\partial \bar{\mathbf{F}}_3}{\partial \bar{x}_3} = \frac{1}{Re} \left(\frac{\partial \bar{\mathbf{G}}_1}{\partial \bar{x}_1} + \frac{\partial \bar{\mathbf{G}}_2}{\partial \bar{x}_2} + \frac{\partial \bar{\mathbf{G}}_3}{\partial \bar{x}_3} \right). \quad (2.13)$$

It is noticed that Eq. (2.13) is different with Eq. (2.1) due to the presence of the coefficient $1/Re$ in front of the viscous fluxes. By absorbing $1/Re$ into the viscosity and thermal conductivity as $\bar{\mu} = \bar{\mu}/Re$ and $\bar{\kappa} = \bar{\kappa}/Re$, the form of non-dimensionalized NS equations recover that of the original NS equations in Eq. (2.1). However, in a non-dimensional case, the specific gas constant needs to be specified as

$$\bar{R} = \frac{\bar{p}}{\bar{\rho}\bar{T}} = \frac{1}{\gamma Ma_\infty^2}. \quad (2.14)$$

Recall the viscosity, $\bar{\mu} = \bar{\mu}/Re$, it can be checked that the form of thermal conductivity is also consistent with the dimensional from in Eq. (2.9), as well as the stress tensor components

$$\bar{\kappa} = \frac{\bar{\kappa}}{Re} = \frac{\bar{\mu}}{(\gamma - 1) Pr Ma^2} = \frac{\gamma}{\gamma - 1} \frac{\bar{\mu} \bar{R}}{Pr}. \quad (2.15)$$

As for the Sutherland's law, it is non-dimensionalized by dividing Eq. (2.4) by Sutherland's relation at freestream

$$\frac{\mu_\infty}{\mu_0} = \left(\frac{T_\infty}{T_0} \right)^{3/2} \frac{T_0 + C}{T_\infty + C}. \quad (2.16)$$

The expression then reads

$$\frac{\mu}{\mu_\infty} = \left(\frac{T}{T_\infty} \right)^{3/2} \frac{T_\infty + C}{T + C}. \quad (2.17)$$

Finally, the non-dimensional viscosity takes the form

$$\bar{\mu} = \frac{\bar{T}^{3/2}}{Re} \frac{1 + C/T_\infty}{\bar{T} + C/T_\infty}. \quad (2.18)$$

Since the non-dimensionalized NS equations and original NS equations have exactly the same form when using the non-dimensionalized expressions for Sutherland's law and specific gas constant, the two sets of equations are not further distinguished in the following chapters, and the overbars on the non-dimensional quantities are dropped for simplicity.

2.1.3 Euler equations

Although it is the NS equations that are solved in the boundary layer related simulation, their inviscid counterparts, the Euler equations are also used in this work to construct stable Riemann inflow boundary conditions in the following chapters, and therefore are provided.

The expression of the Euler equations can be obtained by dropping the viscous terms on the right-hand-side of Eq. (2.1), and takes the form

$$\frac{\partial \mathbf{Q}}{\partial t} + \frac{\partial \mathbf{F}_1}{\partial x_1} + \frac{\partial \mathbf{F}_2}{\partial x_2} + \frac{\partial \mathbf{F}_3}{\partial x_3} = \mathbf{0}, \quad (2.19)$$

or can be compactly denoted by

$$\frac{\partial \mathbf{Q}}{\partial t} + \nabla \cdot \mathbf{F} = \mathbf{0}. \quad (2.20)$$

2.2 Spectral/*hp* element method and Discontinuous Galerkin (DG) formulation

Spectral/*hp* element method is a state-of-the-art numerical technique for solving partial differential equations (PDEs). It combines the geometrical flexibility and adaptivity (i.e. applicability on unstructured meshes) of the finite element/volume method (FEM/FVM) with the high spatial accuracy of the spectral method, as shown in Fig. 2.1, which enables the high-order solution to be computed in individual element from the domain decomposition (or mesh generation).

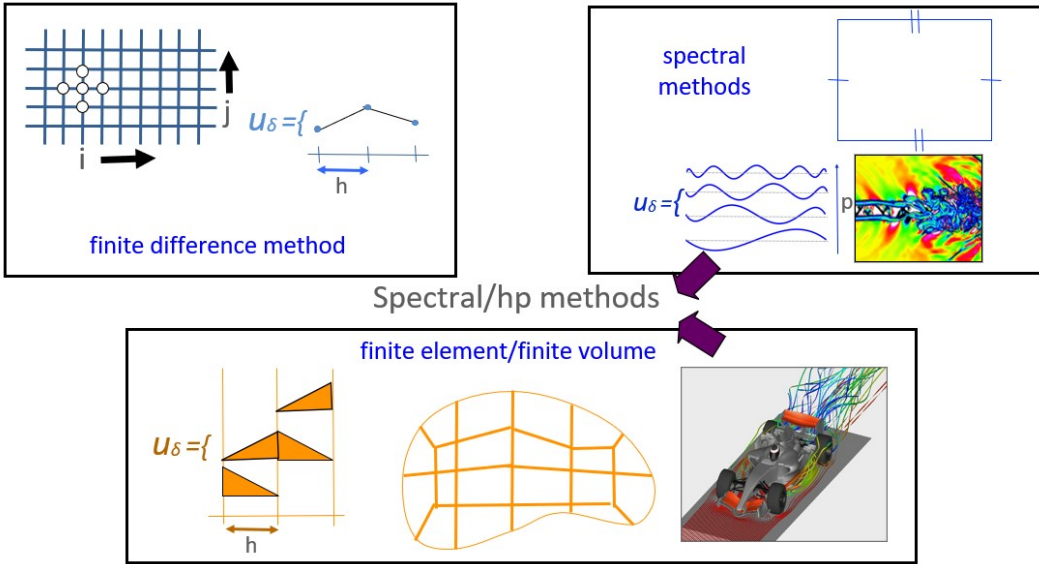


Figure 2.1: Relation between spectral/*hp* element method and finite difference method, spectral method, and finite element/finite volume Method. Reproduced from Ref. [78].

The spectral/*hp* element method can be applied to a wide variety of elements, including one-dimensional (1D) segments, two-dimensional (2D) quadrilaterals and triangles, as well as three-dimensional (3D) hexahedra, tetrahedra, and pyramids. The flexible choice of element together with the well-established automatic unstructured mesh generation technique makes the spectral/*hp* element method a friendly approach to be applied in engineering applications involving complicated geometries involved, e.g. the full geometry of a road car [79], where structured mesh generation is challenging and therefore the conventional finite difference method is difficult to be applied.

Within each element of the computational domain, the spectral/ hp method solution is represented by an expansion of high-order basis functions, which is similar to the spectral method while more high-order elements are involved rather than the whole computational domain being represented by a single spectral element as shown in Fig. 2.1. The use of high-order basis functions results in exponential convergence in smooth solutions. The basis functions in the spectral/ hp element method are typically high-order polynomials, where the commonly used ones are Lagrange polynomials and modified Jacobi polynomials. The choice of Lagrange polynomials leads to nodal expansion since the coefficient of each basis function is equal to the represented value at the very point the Lagrange polynomial is set. On the other hand, the adoption of the modified Jacobi polynomials makes modal or hierarchical expansion, where a lower order basis function set are included in a higher order basis function set. It is noted that the polynomial degree or the number of basis functions used within an element can be chosen independently, allowing for greater flexibility and adaptivity than traditional linear finite element methods.

To produce the global solution over the whole computational domain, the solutions in the spectral/ hp elements are joined together, where different approaches can be followed. If the the solutions are forced to be C^0 continues across the elements, the approach is known as continuous Galerkin (CG) formulation. Due to its continuity property, CG formulation is often employed to solve elliptic problems such as incompressible flows and structural dynamics. In contrast to the CG formulation, discontinuous Galerkin (DG) formulation relaxes the continuity requirement. The solutions are therefore only continues within the elements and experience jumps when moving to the neighbors. As a consequence, in the DG formulation the solutions in the elements are weakly coupled through numerical flux rather than strongly coupled, at the cost that more degrees of freedom are introduced than in the CG formulation. This weakly coupling accelerates a DG based solver as the global matrix is no longer generated and the problems are solved locally, which brings additional benefits for the vectorized operator implementations for better utilising modern CPU/GPU hardware. For the hyperbolicity dominated compressible flows governed by Eq. (2.1) or Eq. (2.19), a DG based solver can well preserve the conservation law and therefore is a suitable choice.

In the following sections we introduce the numerical methods adopted in this thesis. To begin with, in Section 2.3.1 a model scalar problem is used to describe the idea of the DG formulation.

2.3 DG formulation of a model problem

2.3.1 Elemental and flux/primal formulation

We consider a model problem of time dependent linear advection-diffusion in the d -dimensional space ($d = 2$ or 3):

$$\begin{cases} \frac{\partial u}{\partial t} + \nabla \cdot (\mathbf{a}u) - \nabla \cdot (b\nabla u) = f, \\ u(\mathbf{x}, 0) = u_0(\mathbf{x}), \end{cases} \quad (2.21a)$$

$$(2.21b)$$

where $u(\mathbf{x}, t)$ is a scalar function, $\mathbf{a} = (a_1, \dots, a_d)$ is the constant advection velocity, b is the constant diffusion coefficient, and f is a source term. The above problem

is assumed to be defined on a squared (or cubic) computational domain Ω , and periodic boundary conditions are applied.

The DG discretisation of the above equation initiates with the computational domain Ω being decomposed into N_e non-overlapping elements (subdomains) Ω_e ($e = 1, 2, \dots, N_e$)

$$\Omega = \bigcup_{e=1}^{N_e} \Omega_e, \quad \Omega_e \bigcap_{e \neq j} \Omega_j = \Gamma_{ej}, \quad (2.22)$$

where Γ_{ej} denotes the common edge (or face) shared by element Ω_e and Ω_j .

Before generating the weak form of Eq. (2.21a), it is first transformed into a system of first-order equations to deal with the second-order term by introducing an auxiliary variable $\boldsymbol{\sigma} = \nabla u$ as follows

$$\frac{\partial u}{\partial t} + \nabla \cdot (\mathbf{a}u) - \nabla \cdot (b\boldsymbol{\sigma}) = f, \quad (2.23a)$$

$$\boldsymbol{\sigma} = \nabla u. \quad (2.23b)$$

We then introduce the piecewise continuous polynomials space \mathbb{V}^P , in which the solution is sought, as well as the d -dimensional piecewise continuous polynomials space \mathbb{W}^P for the derivation in the following

$$\mathbb{V}^P = \left\{ v \in L^2(\Omega) : v|_{\Omega_e} \in \mathbb{P}^P(\Omega_e), \forall \Omega_e \in \Omega \right\}, \quad (2.24a)$$

$$\mathbb{W}^P = \left\{ \tau \in [L^2(\Omega)]^d : \tau|_{\Omega_e} \in [\mathbb{P}^P(\Omega_e)]^d, \forall \Omega_e \in \Omega \right\}, \quad (2.24b)$$

where \mathbb{P}^P is the space of polynomial functions of order P . By the ansatz of the Galerkin method, both the basis and test functions are selected from the same space, i.e. \mathbb{V}^P . The space \mathbb{W}^P is required due to the introduction of auxiliary variable $\boldsymbol{\sigma}$.

We derive the elemental DG formulation by multiplying Eqs. (2.23a) and (2.23b) by test functions $v \in \mathbb{V}^P$ and $\boldsymbol{\tau} \in \mathbb{W}^P$ respectively, and integrating over an element by parts. This converts the volume integrals of divergence terms into boundary integrals of fluxes while the fluxes are not well-defined because of the jump across the elements. These fluxes are therefore replaced by numerical fluxes (denoted by $(\hat{\cdot})$ and (\cdot) for advection and diffusion fluxes respectively), which are defined separately due to their different natures. We obtain the following formation

$$\begin{aligned} \int_{\Omega_e} b\boldsymbol{\sigma} \cdot \nabla v d\Omega_e &= \int_{\Omega_e} v f d\Omega_e - \frac{\partial}{\partial t} \int_{\Omega_e} v u d\Omega_e \\ &\quad + \int_{\Omega_e} \nabla v \cdot \mathbf{a} u d\Omega_e - \int_{\Gamma_e} v (\mathbf{a} \hat{u} \cdot \mathbf{n}) d\Gamma_e + \int_{\Gamma_e} v (b \hat{\boldsymbol{\sigma}} \cdot \mathbf{n}) d\Gamma_e, \end{aligned} \quad (2.25a)$$

$$\int_{\Omega_e} \boldsymbol{\sigma} \cdot \boldsymbol{\tau} d\Omega_e = \int_{\Gamma_e} \hat{u} (\boldsymbol{\tau} \cdot \mathbf{n}) d\Gamma_e - \int_{\Omega_e} u \nabla \cdot \boldsymbol{\tau} d\Omega_e, \quad (2.25b)$$

where \mathbf{n} is the outward pointing normal on the boundary. Eq. (2.25) is called the flux formulation [80]. With appropriate definitions of numerical fluxes, Eq. (2.25b) is solved first for $\boldsymbol{\sigma}$ and then Eq. (2.25a) can be dealt with [81, 82]. This procedure suits well for an explicit solver while for an implicit solver the solution of Eqs. (2.25a) and (2.25b) need to be coupled and complicated strategies are involved. Moreover, the introduction of auxiliary variable leads to a larger system and consequently less efficient.

The primal formulation solves this problem by eliminating the auxiliary variable. Substitute the second term on the right-hand-side of Eq. (2.25b) with the identity of integration by parts

$$\int_{\Omega_e} u \nabla \cdot \boldsymbol{\tau} d\Omega_e = \int_{\Gamma_e} u (\boldsymbol{\tau} \cdot \mathbf{n}) d\Gamma_e - \int_{\Omega_e} \nabla u \cdot \boldsymbol{\tau} d\Omega_e, \quad (2.26)$$

and let $\boldsymbol{\tau} = \nabla v$, Eq. (2.25b) takes the form

$$\int_{\Omega_e} \boldsymbol{\sigma} \cdot \nabla v d\Omega_e = \int_{\Gamma_e} (\hat{u} - u) (\nabla v \cdot \mathbf{n}) d\Gamma_e + \int_{\Omega_e} \nabla u \cdot \nabla v d\Omega_e \quad (2.27)$$

Next we combine Eq. (2.27) with Eq. (2.25a), and obtain the primal formulation

$$\begin{aligned} & \underbrace{\frac{\partial}{\partial t} \int_{\Omega_e} v u d\Omega_e - \int_{\Omega_e} \nabla v \cdot \mathbf{a} u d\Omega_e + \int_{\Gamma_e} v (\mathbf{a} \hat{u} \cdot \mathbf{n}) d\Gamma_e}_{\text{Advection operator}} \\ & + \underbrace{\int_{\Omega_e} b \nabla u \cdot \nabla v d\Omega_e + \int_{\Gamma_e} b (\hat{u} - u) (\nabla v \cdot \mathbf{n}) d\Gamma_e - \int_{\Gamma_e} v (b \hat{\boldsymbol{\sigma}} \cdot \mathbf{n}) d\Gamma_e}_{\text{Diffusion operator}} = \int_{\Omega_e} v f d\Omega_e \end{aligned} \quad (2.28)$$

where only the unknown u presents while $\hat{\boldsymbol{\sigma}}$ is provided by numerical diffusion flux. In Eq. (2.28) the second and third term on the left-hand-side are computed in the advection operator and the forth to the sixth terms are computed in the diffusion operator. Note that although \hat{u} and \hat{u} are both numerical fluxes of u , they are treated differently because of different natures behind these terms.

Eq. (2.28) is our goal of elemental and primal DG formulation. However, its global formulation is also provided for better introduction of different treatments of diffusion flux. In addition, the global formulation is convenient for mathematical analysis, such as stability analysis and error estimation, and therefore is more popular in the classical articles, e.g. Ref. [80, 83, 84]. The global formulation is described in the following.

2.3.2 Global formulation

If we sum Eq. (2.28) over all the elements [85], and follow the notion in Fig. 2.2, we obtain the global formulation

$$\begin{aligned} & \frac{\partial}{\partial t} \int_{\Omega} v u d\Omega - \int_{\Omega} \nabla v \cdot \mathbf{a} u d\Omega + \int_{\Gamma_I} \left([\![\mathbf{a} \hat{u}]\!] \cdot [\![v]\!] + [\![\mathbf{a} \hat{u}]\!] [\![v]\!] \right) d\Gamma_I \\ & + \int_{\Omega} b \nabla u \cdot \nabla v d\Omega + \int_{\Gamma_I} b ([\![\nabla v]\!] \cdot [\![\hat{u} - u]\!] + [\![\nabla v]\!] [\![\hat{u} - u]\!]) d\Gamma_I \\ & - \int_{\Gamma_I} b ([\![\hat{\boldsymbol{\sigma}}]\!] \cdot [\![v]\!] + [\![\hat{\boldsymbol{\sigma}}]\!] [\![v]\!]) d\Gamma_I = \int_{\Omega} v f d\Omega \end{aligned} \quad (2.29)$$

where Γ_I is the internal boundary set (without repeat)

$$\Gamma_I = \bigcup_{e=1}^{N_e} \partial\Omega_e = \bigcup_{e=1}^{N_e} \Gamma_e.$$

In the above Eq. (2.29), the average operator $\{\cdot\}$ and jump operator $[\![\cdot]\!]$ at an internal boundary for a scalar q and a vector valued function ϕ are defined as

$$\begin{aligned}\{\!\{q\}\!\} &= \frac{1}{2}(q^- + q^+), & [q] &= q^- \mathbf{n}^- + q^+ \mathbf{n}^+, \\ \{\!\{\phi\}\!\} &= \frac{1}{2}(\phi^- + \phi^+), & [\![\phi]\!] &= \phi^- \cdot \mathbf{n}^- + \phi^+ \cdot \mathbf{n}^+, \end{aligned}\quad (2.30)$$

where the jump of a scalar is a vector while the jump of a vector is a scalar. The derivation of Eq. (2.29) takes advantage of the following identity, and the proof of which is provided in Ref. [85].

$$\sum_{\Omega_e} \int_{\Gamma_e} \phi^- \cdot \mathbf{n}^- q^- d\Gamma_e = \int_{\Gamma_I} (\{\!\{\phi\}\!\} \cdot [q] + [\![\phi]\!] \{\!\{q\}\!\}) d\Gamma_e. \quad (2.31)$$

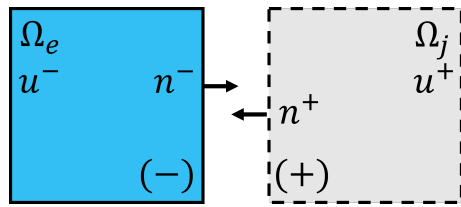


Figure 2.2: The blue element with solid edges is the element of interest, where the quantities are denoted by $(-)$; the grey element with dashed edges is one of its neighbors, where the quantities are denoted by $(+)$.

In general, a well defined numerical flux is continuous across an internal edge such that its jump is zero and its average equals to itself [80, 85]. Eq. (2.29) is therefore simplified as

$$\begin{aligned}\frac{\partial}{\partial t} \int_{\Omega} v u d\Omega - \int_{\Omega} \nabla v \cdot \mathbf{a} u d\Omega + \int_{\Gamma_I} (\mathbf{a} \hat{u} \cdot [v]) d\Gamma_I + \int_{\Omega} b \nabla u \cdot \nabla v d\Omega \\ + \int_{\Gamma_I} b (-\{\!\{\nabla v\}\!\} \cdot [u] + [\![\nabla v]\!] \{\!\{\hat{u} - u\}\!}) d\Gamma_I - \int_{\Gamma_I} b \hat{\sigma} \cdot [v] d\Gamma_I = \int_{\Omega} v f d\Omega. \end{aligned}\quad (2.32)$$

By specifying appropriate numerical fluxes, i.e. \hat{u} , $\hat{\sigma}$, and \hat{u} , different DG schemes are derived. We introduce detailed numerical flux treatments in the following subsections.

2.3.3 Advection operator

The treatment of advection operator considers that the advection related information comes from upstream. The numerical inviscid flux in Eqs. (2.28) and (2.32) therefore depends on the local advection velocity, i.e. $\mathbf{a} \cdot \mathbf{n}$

$$\hat{u} = \begin{cases} u^+, & \mathbf{a} \cdot \mathbf{n} \leq 0 \\ u^-, & \mathbf{a} \cdot \mathbf{n} > 0 \end{cases}, \quad (2.33)$$

which is known as upwind scheme, and stabilize the simulations.

2.3.4 Diffusion operator

There are different approaches to define the numerical fluxes in the diffusion operator in Eq. (2.28), including interior penalty (IP) method [86, 87], Bassi-Rebay (BR) method [81], local DG (LDG) method [82], and etc. These approaches are proposed to solve different problems while Arnold et al. [80] first developed an unified analysis based on the global primal formulation. In this work we are using a symmetric type interior penalty flux, and the method is known as symmetric interior penalty Galerkin (SIPG) method. This method was introduced by Wheeler in 1978 [86] and by Arnold in 1979 [87]. For a more detailed review, see Ref. [80, 88]. We are interested in the SIPG method for its compact stencil, where only the direct neighbours of the target element are included in an implicit solver [89].

In the SIPG method, the numerical fluxes in the diffusion operator take the form

$$\hat{u} = \{u\}, \quad \hat{\sigma} = \{\nabla u\} - \eta[u],$$

where η is the penalty coefficient. It must be sufficiently large to stabilize the numerical simulation [83], but excessive penalty coefficient increases ill-conditioning of the system to be constructed and solved [90]. Substituting the above numerical fluxes into Eq. (2.28) and Eq. (2.32), the elemental and global formulations take the expressions

$$\begin{aligned} & \frac{\partial}{\partial t} \int_{\Omega_e} vud\Omega_e - \int_{\Omega_e} \nabla v \cdot \mathbf{a}ud\Omega_e + \int_{\Gamma_e} v(\mathbf{a}\hat{u} \cdot \mathbf{n})d\Gamma_e \\ & + \int_{\Omega_e} b\nabla u \cdot \nabla vd\Omega_e + \int_{\Gamma_e} b(\{u\} - u)(\nabla v \cdot \mathbf{n})d\Gamma_e - \int_{\Gamma_e} bv(\{\nabla u\} - \eta[u]) \cdot \mathbf{n}d\Gamma_e \\ & = \int_{\Omega_e} vfd\Omega_e, \end{aligned} \tag{2.34}$$

and

$$\begin{aligned} & \frac{\partial}{\partial t} \int_{\Omega} vud\Omega - \int_{\Omega} \nabla v \cdot \mathbf{a}ud\Omega + \int_{\Gamma_I} (\mathbf{a}\hat{u} \cdot [v]) d\Gamma_I \\ & + \int_{\Omega} b\nabla u \cdot \nabla vd\Omega + \int_{\Gamma_I} b(-\{\nabla u\} \cdot [v] - \{\nabla v\} \cdot [u] + \eta[u] \cdot [v]) d\Gamma_I = \int_{\Omega} vfd\Omega, \end{aligned} \tag{2.35}$$

respectively. Eq. (2.34) is the form we need to develop a solver while Eq. (2.35) is convenient for analysis. In Eq. (2.35), the diffusion operator is written as the bilinear form

$$\mathcal{B}_v^{SIPG}(u, v) = \int_{\Omega} b\nabla u \cdot \nabla vd\Omega + \int_{\Gamma_I} b(\underbrace{-\{\nabla u\} \cdot [v]}_{\text{Consistency term}} - \underbrace{\{\nabla v\} \cdot [u]}_{\text{Symmetry term}} + \underbrace{\eta[u] \cdot [v]}_{\text{Penalty term}}) d\Gamma_I, \tag{2.36}$$

which is symmetric, $\mathcal{B}_v^{SIPG}(u, v) = \mathcal{B}_v^{SIPG}(v, u)$, and adjoint consistent, leading to the optimal order of convergence [83]. (See Ref. [91] for more details.) If the negative sign of the symmetry term in Eq. (2.36) is replaced by a positive sign or 0, the method becomes non-symmetric interior penalty Galerkin (NIPG) or incomplete interior penalty Galerkin (IIPG). The NIPG and IIPG methods are typically derived by specifying appropriate numerical fluxes in Eq. (2.32). However, in Appendix A we present a different derivation for the NIPG and IIPG while keeping the same numerical fluxes as in SIPG.

2.4 DG formulation of the NS equations

Having derived the DG formulation for the linear advection-diffusion problem in Section 2.3, we next follow a similar approach to obtain the DG formulation for the NS equations.

2.4.1 Formulation

The DG formulation for the NS equations is much more involved than that for the model problem. The additional complexity arises not only from the higher dimensionality of the NS equations but mainly from the treatment of the viscous flux and the related tensor operations. Since integration by parts is used in the derivation while the gradient of the field variables is implicitly contained in the viscous flux, i.e. the block vector \mathbf{G} in Eq. (2.10), the viscous flux is first rewritten for explicit separation as

$$\mathbf{G}_i(\mathbf{Q}, \nabla \mathbf{Q}) = \mathbf{K}_{ij}(\mathbf{Q}) \frac{\partial \mathbf{Q}}{\partial x_j}, \quad \mathbf{G} = \begin{pmatrix} \mathbf{G}_1 \\ \mathbf{G}_2 \\ \mathbf{G}_3 \end{pmatrix} = \begin{pmatrix} (\mathbf{K}_{11}, \mathbf{K}_{12}, \mathbf{K}_{13}) \cdot \nabla \mathbf{Q} \\ (\mathbf{K}_{21}, \mathbf{K}_{22}, \mathbf{K}_{23}) \cdot \nabla \mathbf{Q} \\ (\mathbf{K}_{31}, \mathbf{K}_{32}, \mathbf{K}_{33}) \cdot \nabla \mathbf{Q} \end{pmatrix} = \mathbf{K} \nabla \mathbf{Q}, \quad (2.37)$$

where the indices follow the summation convention. The \mathbf{K}_{ij} are square matrices, and \mathbf{K} is a fourth-order tensor, which can also be considered as a block matrix

$$\mathbf{K} = \{\mathbf{K}_{ij}\} = \begin{pmatrix} \mathbf{K}_{11} & \mathbf{K}_{12} & \mathbf{K}_{13} \\ \mathbf{K}_{21} & \mathbf{K}_{22} & \mathbf{K}_{23} \\ \mathbf{K}_{31} & \mathbf{K}_{32} & \mathbf{K}_{33} \end{pmatrix}. \quad (2.38)$$

In the above, the detailed expressions for \mathbf{K}_{ij} are provided by Dolejší and Feistauer [92] for the 3D NS equations while those for the 2D NS equations are given by Hartmann and Houston [83].

The derivation of the DG formulation for the 3D NS equations also starts from the introduction of an auxiliary variable $\boldsymbol{\sigma}$, leading to

$$\frac{\partial \mathbf{Q}}{\partial t} + \nabla \cdot \mathbf{F} - \nabla \cdot \boldsymbol{\sigma} = \mathbf{0}, \quad (2.39a)$$

$$\boldsymbol{\sigma} = \mathbf{G}(\mathbf{Q}, \nabla \mathbf{Q}). \quad (2.39b)$$

We then multiply Eqs. (2.39a) and (2.39b) by test functions \mathbf{v} and $\boldsymbol{\tau} = (\boldsymbol{\tau}_1, \boldsymbol{\tau}_2, \boldsymbol{\tau}_3)$, and integrate in an element, providing

$$\int_{\Omega_e} \frac{\partial \mathbf{Q}}{\partial t} \cdot \mathbf{v} d\Omega_e + \int_{\Omega_e} (\nabla \cdot \mathbf{F}) \cdot \mathbf{v} d\Omega_e - \int_{\Omega_e} (\nabla \cdot \boldsymbol{\sigma}) \cdot \mathbf{v} d\Omega_e = 0, \quad (2.40a)$$

$$\int_{\Omega_e} \boldsymbol{\sigma} : \boldsymbol{\tau} d\Omega_e = \int_{\Omega_e} \nabla \mathbf{Q} : (\mathbf{K}^T \boldsymbol{\tau}) d\Omega_e. \quad (2.40b)$$

where the test functions are from the piecewise continuous finite element spaces

$$\bar{\mathbb{V}}^P = \left\{ \mathbf{v} \in [L^2(\Omega)]^5 : \mathbf{v}|_{\Omega_e} \in [\mathbb{P}^P(\Omega_e)]^5, \forall \Omega_e \in \Omega \right\}, \quad (2.41a)$$

$$\bar{\mathbb{W}}^P = \left\{ \boldsymbol{\tau} \in [L^2(\Omega)]^{3 \times 5} : \boldsymbol{\tau}|_{\Omega_e} \in [\mathbb{P}^P(\Omega_e)]^{3 \times 5}, \forall \Omega_e \in \Omega \right\}, \quad (2.41b)$$

and (\cdot) is the double index contraction which results to a scalar here

$$\boldsymbol{\sigma} : \boldsymbol{\tau} = \sigma_{ij}\tau_{ij} \quad i = 1, 2, 3 \quad j = 1, 2, \dots, 5.$$

Additionally, in Eq. (2.40b) we used the following identity

$$\begin{aligned} \boldsymbol{\sigma} : \boldsymbol{\tau} &= \begin{pmatrix} \boldsymbol{\sigma}_1 \\ \boldsymbol{\sigma}_2 \\ \boldsymbol{\sigma}_3 \end{pmatrix} : \begin{pmatrix} \boldsymbol{\tau}_1 \\ \boldsymbol{\tau}_2 \\ \boldsymbol{\tau}_3 \end{pmatrix} = \boldsymbol{\sigma}_i \cdot \boldsymbol{\tau}_i = \left(\mathbf{K}_{ij} \frac{\partial \mathbf{Q}}{\partial x_j} \right) \cdot \boldsymbol{\tau}_i = \frac{\partial \mathbf{Q}}{\partial x_j} \cdot (\mathbf{K}_{ij}^T \boldsymbol{\tau}_i) \\ &= \begin{pmatrix} \partial \mathbf{Q} / \partial x_1 \\ \partial \mathbf{Q} / \partial x_2 \\ \partial \mathbf{Q} / \partial x_3 \end{pmatrix} : \begin{pmatrix} \mathbf{K}_{11}^T \boldsymbol{\tau}_1 + \mathbf{K}_{21}^T \boldsymbol{\tau}_2 + \mathbf{K}_{31}^T \boldsymbol{\tau}_3 \\ \mathbf{K}_{12}^T \boldsymbol{\tau}_1 + \mathbf{K}_{22}^T \boldsymbol{\tau}_2 + \mathbf{K}_{32}^T \boldsymbol{\tau}_3 \\ \mathbf{K}_{13}^T \boldsymbol{\tau}_1 + \mathbf{K}_{23}^T \boldsymbol{\tau}_2 + \mathbf{K}_{33}^T \boldsymbol{\tau}_3 \end{pmatrix} = \nabla \mathbf{Q} : (\mathbf{K}^T \boldsymbol{\tau}), \end{aligned} \quad (2.42)$$

where $(\mathbf{K}^T)_{ij} = (\mathbf{K}_{ji})^T$. More details of their derivation are provided in Appendix A.

After integrating by parts and substituting the boundary fluxes by numerical fluxes, Eq. (2.40) is transformed to be

$$\begin{aligned} \int_{\Omega_e} \frac{\partial \mathbf{Q}}{\partial t} \cdot \mathbf{v} d\Omega_e + \int_{\Gamma_e} (\hat{\mathbf{F}} \cdot \mathbf{n}) \cdot \mathbf{v} d\Gamma_e - \int_{\Omega_e} \mathbf{F} : \nabla \mathbf{v} d\Omega_e \\ - \int_{\Gamma_e} (\hat{\boldsymbol{\sigma}} \cdot \mathbf{n}) \cdot \mathbf{v} d\Gamma_e + \int_{\Omega_e} \boldsymbol{\sigma} : \nabla \mathbf{v} d\Omega_e = 0, \end{aligned} \quad (2.43a)$$

$$\int_{\Omega_e} \boldsymbol{\sigma} : \boldsymbol{\tau} d\Omega_e = \int_{\Gamma_e} \hat{\mathbf{Q}} \cdot ((\mathbf{K}^T \boldsymbol{\tau}) \cdot \mathbf{n}) d\Gamma_e - \int_{\Omega_e} \mathbf{Q} \cdot (\nabla \cdot (\mathbf{K}^T \boldsymbol{\tau})) d\Omega_e, \quad (2.43b)$$

where the integration by parts formulation for (\cdot) reads

$$\int_{\Omega_e} \nabla \mathbf{Q} : (\mathbf{K}^T \boldsymbol{\tau}) d\Omega_e = \int_{\Gamma_e} \mathbf{Q} \cdot ((\mathbf{K}^T \boldsymbol{\tau}) \cdot \mathbf{n}) d\Gamma_e - \int_{\Omega_e} \mathbf{Q} \cdot (\nabla \cdot (\mathbf{K}^T \boldsymbol{\tau})) d\Omega_e. \quad (2.44)$$

We next perform the integration by parts again in Eq. (2.43b) using Eq. (2.44) to obtain

$$\int_{\Omega_e} \boldsymbol{\sigma} : \boldsymbol{\tau} d\Omega_e = \int_{\Omega_e} \nabla \mathbf{Q} : (\mathbf{K}^T \boldsymbol{\tau}) d\Omega_e + \int_{\Gamma_e} (\hat{\mathbf{Q}} - \mathbf{Q}) \cdot ((\mathbf{K}^T \boldsymbol{\tau}) \cdot \mathbf{n}) d\Gamma_e \quad (2.45)$$

Finally we let $\boldsymbol{\tau} = \nabla \mathbf{v}$, and substitute Eq. (2.45) into Eq. (2.43a) to have the primal formulation

$$\begin{aligned} &\underbrace{\int_{\Omega_e} \frac{\partial \mathbf{Q}}{\partial t} \cdot \mathbf{v} d\Omega_e - \int_{\Omega_e} \mathbf{F} : \nabla \mathbf{v} d\Omega_e + \int_{\Gamma_e} (\hat{\mathbf{F}} \cdot \mathbf{n}) \cdot \mathbf{v} d\Gamma_e}_{\text{Advection operator}} \\ &+ \underbrace{\int_{\Omega_e} \mathbf{G} : \nabla \mathbf{v} d\Omega_e - \int_{\Gamma_e} (\hat{\boldsymbol{\sigma}} \cdot \mathbf{n}) \cdot \mathbf{v} d\Gamma_e + \int_{\Gamma_e} (\hat{\mathbf{Q}} - \mathbf{Q}) \cdot ((\mathbf{K}^T \nabla \mathbf{v}) \cdot \mathbf{n}) d\Gamma_e}_{\text{Diffusion operator}} = 0 \end{aligned} \quad (2.46)$$

where the substitution $\nabla \mathbf{Q} : (\mathbf{K}^T \boldsymbol{\tau}) = \mathbf{G} : \nabla \mathbf{v}$ is used for clarity.

Eq. (2.46) gives the general elemental and primal DG formulation of the NS equations. The normal numerical inviscid flux, i.e. $\hat{\mathbf{F}} \cdot \mathbf{n}$, is computed by a Riemann solver $\mathcal{H}(\mathbf{Q}^-, \mathbf{Q}^+, \mathbf{n}^-, \mathbf{n}^+)$, which can be either exact or approximate. In the diffusion operator, the SIPG method adopts the following numerical viscous fluxes

$$\hat{\mathbf{Q}} = \{\mathbf{Q}\}, \quad \hat{\boldsymbol{\sigma}} = \{\mathbf{G}\} - \eta \{\mathbf{K}\} \llbracket \mathbf{Q} \rrbracket, \quad (2.47)$$

where different forms of the penalty coefficient η are given in Ref. [84, 89, 93], and in addition to the jump and average operators defined in Eq. (2.30), a new operator $\llbracket \cdot \rrbracket$ for vector-valued operands is used here

$$\llbracket \mathbf{Q} \rrbracket = \mathbf{Q}^- \otimes \mathbf{n}^- + \mathbf{Q}^+ \otimes \mathbf{n}^+, \quad (2.48)$$

where \otimes is the tensor product operator. Note on the edges where $\mathbf{n}^+ = -\mathbf{n}^-$, we have $\llbracket \mathbf{Q} \rrbracket \cdot \mathbf{n}^- = \mathbf{Q}^- - \mathbf{Q}^+$, which is independent from the normal vector \mathbf{n} .

Therefore the final formulation takes the form

$$\begin{aligned} & \int_{\Omega_e} \frac{\partial \mathbf{Q}}{\partial t} \cdot \mathbf{v} d\Omega_e - \int_{\Omega_e} \mathbf{F} : \nabla \mathbf{v} d\Omega_e + \int_{\Gamma_e} \mathcal{H} \cdot \mathbf{v} d\Gamma_e \\ & + \int_{\Omega_e} \mathbf{G} : \nabla \mathbf{v} d\Omega_e - \int_{\Gamma_e} (\llbracket \mathbf{G} \rrbracket \cdot \mathbf{n}) \cdot \mathbf{v} d\Gamma_e + \int_{\Gamma_e} (\llbracket \mathbf{Q} \rrbracket - \mathbf{Q}) \cdot ((\mathbf{K}^T \nabla \mathbf{v}) \cdot \mathbf{n}) d\Gamma_e \\ & + \int_{\Gamma_e} \eta (\llbracket \mathbf{K} \rrbracket \llbracket \mathbf{Q} \rrbracket \cdot \mathbf{n}) \cdot \mathbf{v} d\Gamma_e = 0. \end{aligned} \quad (2.49)$$

2.4.2 Advection term: Riemann problem

At each quadrature point on the element interface, the numerical inviscid flux is specified from a Riemann solution, through which the information is propagated across the elements. The Riemann problem is an initial value problem (IVP) governed by conservation law, and studies the evolution of the initial jump. For instance, Riemann problem for the one-dimensional Euler equations has the following initial condition

$$\mathbf{Q}(x, 0) = \begin{cases} \mathbf{Q}_L = (\rho, \rho u, E)_L, & x < 0, \\ \mathbf{Q}_R = (\rho, \rho u, E)_R, & x \geq 0, \end{cases}$$

and the jump at $x = 0$ can be considered as the the interface of two elements where the solution is discontinuous. A Riemann solver calculates this IVP, and the solution at the initial jump interface, i.e. $x/t = 0$ is used as the numerical flux.

For a multi-dimensional compressible flow problem, a Riemann solver calculates the numerical flux at a interface quadrature point in a local coordinate system, where only the numerical flux in the normal direction (e.g. y_1 -direction in Fig. 2.3) is calculated, and therefore it recovers a one-dimensional flux. The associated Riemann problem is composed of two nonlinear waves (dashed line) and three contact waves (dotted line) as shown in Fig.2.4, and the nonlinear waves can be either shock waves or rarefaction waves.

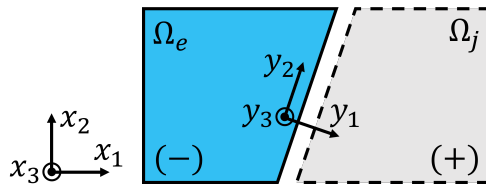


Figure 2.3: The Coordinate system to calculate Riemann solution at the element interface. $\mathbf{x} = (x_1, x_2, x_3)$ is the Cartesian coordinate system, and $\mathbf{y} = (y_1, y_2, y_3)$ shows the local coordinate system at a interface point.

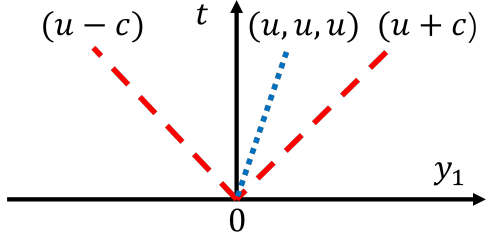


Figure 2.4: The propagation of waves in the three-dimensional Riemann problem. The red dashed lines are nonlinear waves and the blue dotted line in the middle denotes three contact waves. In the brackets are the corresponding waves speed, where u is the normal velocity to the boundary.

In the normal direction of the local coordinate system, the Riemann problem can be solved using either exact or approximated approaches. The exact Riemann solver was developed by Godunov [94, 95] while popular approximated Riemann solvers include Roe, HLL, HLLC, etc, and their construction follows different simplifications. For more details about the Riemann solver, see Toro [96]. In this thesis the simulations are performed using Roe's Riemann solver.

2.5 Boundary conditions

The suitable boundary condition treatment is the next key aspect to enable a successful solver for a variety of simulations, which is the topic of the current section.

The boundary conditions for a flow solver can be applied through either strong enforcement or weak enforcement. The strong enforcement directly modifies the flow variables on the boundary \mathbf{Q}_b based on the target reference values \mathbf{Q}_{ref} and the internal state of the domain/element \mathbf{Q}_{int} , which is widely employed in Finite Difference and CG-based FEM solvers. On the other hand, the weak enforcement have a variety of approaches. The two approaches we are used in this work are Weak-Riemann and Weak-Prescribed, both of which dictate the flow field through numerical flux.

As shown in Table 2.1, in the Weak-Riemann approach we replace the external state, \mathbf{Q}_{ext} by an appropriate ghost state, \mathbf{Q}_{gho} , and the numerical flux at the quadrature points are computed through a Riemann solver \mathcal{H} . The Weak-Prescribed approach directly computes the numerical flux using the boundary value \mathbf{Q}_b , which is computed by the internal state and reference state. A sketch of the states is shown in Fig. 2.5. We remark that if the boundary value considers the characteristic treatment, the Weak-Prescribed approach is identical to Weak-Riemann approach where an exact Riemann solver is adopted [97].

For the advection term in the NS equations, the boundary conditions can be enforced through either Weak-Riemann approach or Weak-Prescribed approach, while only the Weak-Prescribed approach is used for the diffusion term in this work. In the rest of this section we introduce different types of boundary conditions for both advection and diffusion terms.

Table 2.1: Types of boundary conditions.

Strong enforcement	Weak enforcement	
	Riemann	Prescribed
$\mathbf{Q}_b = \mathbf{Q}_b(\mathbf{Q}_{\text{int}}, \mathbf{Q}_{\text{ref}})$	$\mathcal{H} = \mathcal{H}(\mathbf{Q}_{\text{int}}, \mathbf{Q}_{\text{gho}})$	$\mathcal{H} = \mathcal{H}(\mathbf{Q}_b)$

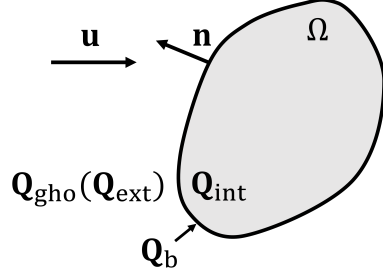


Figure 2.5: A sketch of the states for boundary condition enforcement. The normal \mathbf{n} is outward-pointing.

2.5.1 Farfield

2.5.1.1 Advection term: low viscous effect region

At the farfield boundary, the advection term is enforced by standard Riemann boundary condition, which directly uses the reference state \mathbf{Q}_{ref} as the ghost state in the Weak-Riemann approach

$$\mathbf{Q}_{\text{gho}} = \begin{pmatrix} \rho_{\text{gho}} \\ (\rho u_1)_{\text{gho}} \\ (\rho u_2)_{\text{gho}} \\ (\rho u_3)_{\text{gho}} \\ E_{\text{gho}} \end{pmatrix} = \begin{pmatrix} \rho_{\text{ref}} \\ (\rho u_1)_{\text{ref}} \\ (\rho u_2)_{\text{ref}} \\ (\rho u_3)_{\text{ref}} \\ E_{\text{ref}} \end{pmatrix} = \mathbf{Q}_{\text{ref}}, \quad (2.50)$$

and the numerical flux is computed by the Riemann solver $\mathcal{H}(\mathbf{Q}_{\text{int}}, \mathbf{Q}_{\text{ref}})$. In Eq. (2.50) and the rest of the work, the reference state indicates the target value we expect the field to reach. Therefore we have $\mathbf{Q}_{\text{ref}} = \mathbf{Q}_\infty$ at farfield.

On the other hand, the standard Riemann boundary condition can also be enforced through the Weak-Prescribed approach, which takes the form

$$\mathbf{Q}_b = \begin{pmatrix} \rho_b \\ (\rho u_1)_b \\ (\rho u_2)_b \\ (\rho u_3)_b \\ E_b \end{pmatrix}, \quad \mathcal{H} = \mathcal{H}(\mathbf{Q}_b), \quad (2.51)$$

where the entries of \mathbf{Q}_b are computed according to the characteristic relations. More details of the characteristic relations will be provided in Chapter 4 while in the current section we simply give the intermediate procedures and results.

When the local normal Mach number $Ma_n = (\mathbf{u}_{\text{int}}/c) \cdot \mathbf{n} \in (-\infty, -1]$, this boundary is an supersonic inflow, and all the information comes from the upstream flow. Similarly, a supersonic outflow ($Ma_n \geq 1$) finds all the information comes from the computational domain. We therefore have

$$\mathbf{Q}_b|_{Ma_n \leq -1} = \mathbf{Q}_{\text{ref}}, \quad \mathbf{Q}_b|_{Ma_n \geq 1} = \mathbf{Q}_{\text{int}}.$$

When the local normal Mach number sits in the ranges $(-1, 0]$ and $(0, 1)$, the boundary are subsonic inflow and subsonic outflow respectively. Under these conditions, the boundary state is no longer simply equal to a single sided state but depends on both internal state and the target reference states

$$\mathbf{Q}_b = \mathbf{Q}_b(\mathbf{Q}_{\text{int}}, \mathbf{Q}_{\text{ref}}).$$

In the following derivation we adopt a global coordinate system fixed to the ground. For the subsonic inflow, the characteristic relations are

$$\begin{aligned} R_b^+ &= u_{b,n} + \frac{2}{\gamma - 1} c_b = (-\mathbf{u}_{\text{ref}} \cdot \mathbf{n}) + \frac{2}{\gamma - 1} c_{\text{ref}}, \\ R_b^- &= u_{b,n} - \frac{2}{\gamma - 1} c_b = (-\mathbf{u}_{\text{int}} \cdot \mathbf{n}) - \frac{2}{\gamma - 1} c_{\text{int}}, \end{aligned} \quad (2.52)$$

where R_b^+ and R_b^- are the Riemann invariants corresponding to flow-direction and reverse-flow-direction, namely inward propagating and outward propagating Riemann invariants in this inflow scenario. $u_{b,n} = -\mathbf{u}_b \cdot \mathbf{n}$ is the (absolute) normal velocity pointing inward of the domain. Since the entropy information also comes from upstream, one finds that

$$S_b = \frac{p_b}{\rho_b^\gamma} = \frac{p_{\text{ref}}}{\rho_{\text{ref}}^\gamma}. \quad (2.53)$$

Accordingly, the flow variables for the boundary state are solved by

$$\left\{ \begin{array}{l} u_{b,n} = \frac{1}{2} (R_b^+ + R_b^-), \\ c_b = \frac{\gamma - 1}{4} (R_b^+ - R_b^-), \\ \mathbf{u}_b = \mathbf{u}_{\text{ref}} - (\mathbf{u}_{\text{ref}} \cdot \mathbf{n}) \mathbf{n} - u_{b,n} \mathbf{n}, \\ \rho_b = \left(\frac{c_b^2}{\gamma S_b} \right)^{1/(\gamma-1)}, \\ p_b = \frac{\rho_b c_b}{\gamma}. \end{array} \right. \quad (2.54)$$

Following the same procedures as in Eqs. (2.52) and (2.53), the boundary state for a subsonic outflow are calculated by

$$\left\{ \begin{array}{l} u_{b,n} = \frac{1}{2} (R_b^+ + R_b^-), \\ c_b = \frac{\gamma - 1}{4} (R_b^+ - R_b^-), \\ \mathbf{u}_b = \mathbf{u}_{\text{int}} - (\mathbf{u}_{\text{int}} \cdot \mathbf{n}) \mathbf{n} + u_{b,n} \mathbf{n}, \\ \rho_b = \left(\frac{c_b^2}{\gamma S_b} \right)^{1/(\gamma-1)}, \\ p_b = \frac{\rho_b c_b}{\gamma}, \end{array} \right. \quad (2.55)$$

where R_b^+ and R_b^- are the outward and inward propagating Riemann invariants,

$u_{b,n} = \mathbf{u}_b \cdot \mathbf{n}$ is the (absolute) normal velocity pointing outward of the domain, and

$$\begin{aligned} R_b^+ &= (\mathbf{u}_{\text{int}} \cdot \mathbf{n}) + \frac{2}{\gamma - 1} c_{\text{int}}, \\ R_b^- &= (\mathbf{u}_{\text{ref}} \cdot \mathbf{n}) - \frac{2}{\gamma - 1} c_{\text{ref}}, \\ S_b &= \frac{p_{\text{int}}}{\rho_{\text{int}}^\gamma}. \end{aligned} \quad (2.56)$$

Note that the treatment of standard Riemann boundary condition depends on local normal Mach number rather than local Mach number since the Mach number does not represent the direction selection property that the information propagation relies on (e.g. a supersonic flow can be subsonic in the normal direction), and the local normal Mach number is calculated based on the internal state.

In the above the explicit characteristic treatment in Weak-Prescribed approach is implicitly performed in the Weak-Riemann approach, and therefore both approaches lead to a non-reflective boundary. Since the standard Riemann boundary condition is developed by only considering the hyperbolic feature, it performs well particularly in the upstream farfield boundary. However, in the regions where viscous effect plays a significant role such as wakes region with vortical structures or near the outflow, this boundary condition can cause spurious reflections. This is because the current boundary condition treatment comes from the inviscid characteristic theory, which cannot capture the viscous effects [97]. Therefore in the region with high viscous effect different boundary conditions are necessary.

2.5.1.2 Advection term: high viscous effect region

In high viscous region, the boundary conditions are modified to impose the pressure rather than the velocity as done in the standard Riemann boundary condition [97].

We introduce the treatment using the Weak-Riemann approach. When the boundary is subsonic inflow, the pressure from internal state is extrapolated to the ghost state while reference state values are specified to other ghost state quantities. In contrast, for the subsonic outflow the pressure is enforced to the ghost state while other ghost state quantities are extrapolated from the internal state [97], which is also known as pressure outflow boundary condition. Moreover, when the local normal Mach number indicates supersonic in/outflow, the all information comes from upstream, and the Riemann solver leads to no adverse influence to the viscous effect. (This treatment is also known as do-nothing approach.) These treatments provide the following ghost state expressions

$$\begin{aligned} \mathbf{Q}_{\text{gho}}|_{Ma_n \leq -1} &= \mathbf{Q}_{\text{ref}}, & \mathbf{Q}_{\text{gho}}|_{Ma_n \geq 1} &= \mathbf{Q}_{\text{int}}, \\ \mathbf{Q}_{\text{gho}}|_{-1 < Ma_n \leq 0} &= \begin{pmatrix} \rho_{\text{ref}} \\ (\rho u_1)_{\text{ref}} \\ (\rho u_2)_{\text{ref}} \\ (\rho u_3)_{\text{ref}} \\ E_{\text{ref}} - \frac{p_{\text{ref}}}{\gamma - 1} + \frac{p_{\text{int}}}{\gamma - 1} \end{pmatrix}, & \mathbf{Q}_{\text{gho}}|_{0 < Ma_n < 1} &= \begin{pmatrix} \rho_{\text{int}} \\ (\rho u_1)_{\text{int}} \\ (\rho u_2)_{\text{int}} \\ (\rho u_3)_{\text{int}} \\ E_{\text{int}} - \frac{p_{\text{int}}}{\gamma - 1} + \frac{p_{\text{ref}}}{\gamma - 1} \end{pmatrix}. \end{aligned} \quad (2.57)$$

2.5.1.3 Diffusion term

As for the diffusion term treatment, it has a different form for each different spatial discretisation. In this IP method, the numerical flux at the farfield boundary reads [83, 84]

$$\hat{\mathbf{Q}} = \mathbf{Q}_b, \quad \hat{\boldsymbol{\sigma}} = \mathbf{G}(\mathbf{Q}_{\text{int}}, \nabla \mathbf{Q}_{\text{int}}) - \eta \mathbf{K}(\mathbf{Q}_b)(\mathbf{Q}_{\text{int}} - \mathbf{Q}_b) \otimes \mathbf{n} \quad (2.58)$$

where the viscous flux \mathbf{G} is evaluated at the internal state for both \mathbf{Q} and $\nabla \mathbf{Q}$, and the coefficient tensor \mathbf{K} is evaluated at the boundary state $\mathbf{Q}_b = \mathbf{Q}_b(\mathbf{Q}_{\text{int}}, \mathbf{Q}_{\text{ref}})$, which takes the expressions

$$\begin{aligned} \mathbf{Q}_b|_{Ma_n \leq -1} &= \mathbf{Q}_{\text{ref}}, & \mathbf{Q}_b|_{Ma_n \geq 1} &= \mathbf{Q}_{\text{int}} \\ \mathbf{Q}_b|_{-1 < Ma_n \leq 0} &= \begin{pmatrix} \rho_{\text{ref}} \\ (\rho u_1)_{\text{ref}} \\ (\rho u_2)_{\text{ref}} \\ (\rho u_3)_{\text{ref}} \\ E_{\text{ref}} - \frac{p_{\text{ref}}}{\gamma-1} + \frac{p_{\text{int}}}{\gamma-1} \end{pmatrix}, & \mathbf{Q}_b|_{0 < Ma_n < 1} &= \begin{pmatrix} \rho_{\text{int}} \\ (\rho u_1)_{\text{int}} \\ (\rho u_2)_{\text{int}} \\ (\rho u_3)_{\text{int}} \\ E_{\text{int}} - \frac{p_{\text{int}}}{\gamma-1} + \frac{p_{\text{ref}}}{\gamma-1} \end{pmatrix}, \end{aligned} \quad (2.59)$$

2.5.2 Viscous wall

For the NS equations the viscous wall enforces a no-slip condition. The reference state therefore has zero velocity components (for a fixed wall) while the density and total energy are not constrained

$$\mathbf{Q}_{\text{ref}} = (\cdot, 0, 0, 0, \cdot)^T.$$

The viscous wall has two types: isothermal wall and adiabatic wall, whose differences lie in the diffusion term treatment while the condition for the advection term are the same.

2.5.2.1 Advection term

In the Weak-Riemann approach, the viscous wall can be achieved by specifying the “mirror image” of the internal velocity on the ghost state, and the Riemann solver will obtain a contact wave of zero velocity. The density and energy component on the ghost state are extrapolated from the internal state so that

$$\mathbf{Q}_{\text{gho}} = \begin{pmatrix} \rho_{\text{gho}} \\ (\rho u_1)_{\text{gho}} \\ (\rho u_2)_{\text{gho}} \\ (\rho u_3)_{\text{gho}} \\ E_{\text{gho}} \end{pmatrix} = \begin{pmatrix} \rho_{\text{int}} \\ -(\rho u_1)_{\text{int}} \\ -(\rho u_2)_{\text{int}} \\ -(\rho u_3)_{\text{int}} \\ E_{\text{int}} \end{pmatrix}. \quad (2.60)$$

2.5.2.2 Diffusion term: isothermal wall

The boundary condition for diffusion term of the isothermal wall finds the boundary state of the following form

$$\mathbf{Q}_b = \begin{pmatrix} \rho_b \\ (\rho u_1)_b \\ (\rho u_2)_b \\ (\rho u_3)_b \\ E_b \end{pmatrix} = \begin{pmatrix} \rho_{int} \\ 0 \\ 0 \\ 0 \\ \frac{\rho_{int} R T_w}{\gamma - 1} \end{pmatrix}, \quad (2.61)$$

thereby we obtain the numerical diffusion flux using Eq. (2.58).

2.5.2.3 Diffusion term: adiabatic wall

In the adiabatic wall boundary condition, the boundary state uses both the density and the energy from the internal state and zero velocity components as in the reference state

$$\mathbf{Q}_b = \begin{pmatrix} \rho_b \\ (\rho u_1)_b \\ (\rho u_2)_b \\ (\rho u_3)_b \\ E_b \end{pmatrix} = \begin{pmatrix} \rho_{int} \\ 0 \\ 0 \\ 0 \\ E_{int} \end{pmatrix}, \quad (2.62)$$

In addition, when calculating the numerical flux in Eq. (2.58), the normal flux from the shear stress is extrapolated from the internal state while the normal flux from the thermal diffusion is set to be zero, i.e. $\kappa \nabla T \cdot \mathbf{n} = 0$ [98]. Therefore on the adiabatic wall the tensor $\mathbf{K}(\mathbf{Q}_{int})$ is modified to drop the thermal diffusion so that in Eq. (2.58) the viscous term satisfies

$$\mathbf{G}^{adia}(\mathbf{Q}_{int}, \nabla \mathbf{Q}_{int}) \cdot \mathbf{n} = \mathbf{K}_{ij}^{adia}(\mathbf{Q}_{int}) \frac{\partial \mathbf{Q}_{int}}{\partial x_j} n_i = \begin{pmatrix} 0 \\ \tau_{1i} n_i \\ \tau_{2i} n_i \\ \tau_{3i} n_i \\ u_j \tau_{ji} n_i \end{pmatrix}_{int}.$$

2.5.2.4 Numerical blowing-suction on the wall

The blowing-suction on the wall is adopted for simulations where disturbances need to be introduced into the boundary layers, e.g. the study of TS wave growth. The blowing-suction is performed numerically by breaking the zero velocity of the contact wave. In the Weak-Riemann approach this is achieved by superimposing a time dependent disturbance on to the ghost state of the advection term treatment of viscous wall boundary condition.

2.6 Discretisations in space and time

The analytical expressions of the DG formulation need to be discretised in space and time before we can solve them numerically on a computer. In this section the spatial discretisation and implicit time integration scheme, as well as the numerical methods to solve the nonlinear system arising from the implicit time integration, are introduced.

2.6.1 Spatial discretisation

We start introducing the spatial discretisation from the weak form of Eq. (2.11)

$$\int_{\Omega_e} \phi_p \frac{\partial \mathbf{Q}}{\partial t} d\Omega_e = \int_{\Omega_e} \nabla \phi_p \cdot \mathbf{H} d\Omega_e - \int_{\Gamma_e} \phi_p (\mathbf{H} \cdot \mathbf{n}) d\Gamma_e, \quad (2.63)$$

where $\phi_p \in \mathbb{V}^P$ is the test function. Within each spectral/ hp element Ω_e the vector of conservative variables \mathbf{Q} is approximated in the finite element space \mathbb{V}^P as

$$\mathbf{Q}(\mathbf{x}, t) \simeq \sum_{q=1}^{N_P} \tilde{\mathbf{Q}}_q(t) \phi_q(\mathbf{x}), \quad (2.64)$$

where N_P is the total degrees of freedom (DoFs) in an element for each field, $\tilde{\mathbf{Q}}_q(t)$ is the vector of time-dependent coefficients of the basis function $\phi_q(\mathbf{x})$ taking the form

$$\tilde{\mathbf{Q}}_q(t) = \left(\tilde{\rho}, \tilde{\rho u}_1, \dots, \tilde{\rho u}_d, \tilde{E} \right)_q^T$$

To calculate the integrals in Eq. (2.63), the domain of each element $\Omega_e(\mathbf{x})$ ($e = 1, 2, \dots, N_e$) is first mapped to a standard element $\Omega_s(\xi)$ where each local coordinate $\xi_j \in [-1, 1]$, $j = 1, 2, \dots, d$. Numerical quadrature is then performed on the standard element, leading to

$$\begin{aligned} & \sum_{i=1}^{N_Q} \sum_{q=1}^{N_P} \phi_p(\xi_i) w_i J_i \phi_q(\xi_i) \frac{d\tilde{\mathbf{Q}}_q}{dt} \\ &= \sum_{i=1}^{N_Q} \nabla \phi_p(\xi_i) w_i J_i \mathbf{H}(\xi_i) - \sum_{i=1}^{N_Q^\Gamma} \phi_p(\xi_i^\Gamma) w_i^\Gamma J_i^\Gamma \left(\hat{\mathbf{H}}(\xi_i^\Gamma) \cdot \mathbf{n}_i \right), \end{aligned} \quad (2.65)$$

where N_Q is the number of quadrature points inside an element, N_Q^Γ is the number of quadrature points on the boundary, w_i are the weights at the quadrature points, J_i are the Jacobians of the mapping

$$J = \det(\mathbf{J}), \quad \mathbf{J} = \frac{\partial(x_1, \dots, x_d)}{\partial(\xi_1, \dots, \xi_d)},$$

$\hat{\mathbf{H}}$ is the numerical flux evaluated at the element boundary, and w_i^Γ and J_i^Γ are the weights and Jacobians for boundary quadrature. In this work we are using Gauss-Lobatto-Legendre (GLL) quadrature, where the end points of the interval are included. However, note that the quadrature points on the element boundary are usually different to those in the element. For more details of the mapping and quadrature, see Karniadakis and Sherwin [99].

In Eq. (2.65), the evaluation at a quadrature point ξ_i , e.g. $\mathbf{H}(\xi_i)$, takes the form

$$\mathbf{H}(\xi_i) = \mathbf{H}(\mathbf{Q}(\xi_i)) = \mathbf{H} \left(\sum_{q=1}^{N_P} \tilde{\mathbf{Q}}_q(t) \phi_q(\xi_i) \right) = \mathbf{H} \left(\sum_{q=1}^{N_P} \mathbf{B}_{iq} \tilde{\mathbf{Q}}_q \right),$$

where \mathbf{B}_{iq} is the entry in the i -th row of the $N_Q \times N_P$ backward transformation matrix

$$\mathbf{B} = \begin{pmatrix} \phi_1(\xi_1) & \phi_2(\xi_1) & \cdots & \phi_{N_P}(\xi_1) \\ \phi_1(\xi_2) & \phi_2(\xi_2) & \cdots & \phi_{N_P}(\xi_2) \\ \vdots & \vdots & \ddots & \vdots \\ \phi_1(\xi_{N_Q}) & \phi_2(\xi_{N_Q}) & \cdots & \phi_{N_P}(\xi_{N_Q}) \end{pmatrix}. \quad (2.66)$$

If in Eq. (2.64) we use nodal expansions, i.e. ϕ_q are Lagrange polynomials, then the backward transformation matrix would be identity matrix when $N_P = N_Q$. In addition, the w_i and J_i can also be contained in a $N_Q \times N_Q$ diagonal weight matrix

$$\mathbf{W} = \text{diag}(w_i J_i), \quad (2.67)$$

and the $N_P \times N_P$ mass matrix for an element therefore reads

$$\mathbf{M} = \mathbf{B}^T \mathbf{W} \mathbf{B}. \quad (2.68)$$

Moreover, as shown in Eq. (2.11) since \mathbf{H} is a function of $\nabla \mathbf{Q}$, differentiation also needs to be evaluated numerically. For example, the derivative of \mathbf{Q} with respect to ξ_j is expressed by

$$\frac{\partial}{\partial \xi_j} \mathbf{Q}(\boldsymbol{\xi}_i, t) = \sum_{q=1}^{N_P} \tilde{\mathbf{Q}}_q(t) \frac{\partial \phi_q(\boldsymbol{\xi}_i)}{\partial \xi_j} = \sum_{q=1}^{N_P} (\mathbf{D}_j)_{iq} \tilde{\mathbf{Q}}_q,$$

where \mathbf{D}_j ($j = 1, \dots, d$) is the $N_Q \times N_P$ derivative matrix with respect to ξ_j

$$\mathbf{D}_j = \begin{pmatrix} \frac{\partial \phi_1(\boldsymbol{\xi}_1)}{\partial \xi_j} & \frac{\partial \phi_2(\boldsymbol{\xi}_1)}{\partial \xi_j} & \cdots & \frac{\partial \phi_{N_p}(\boldsymbol{\xi}_1)}{\partial \xi_j} \\ \frac{\partial \phi_1(\boldsymbol{\xi}_2)}{\partial \xi_j} & \frac{\partial \phi_2(\boldsymbol{\xi}_2)}{\partial \xi_j} & \cdots & \frac{\partial \phi_{N_p}(\boldsymbol{\xi}_2)}{\partial \xi_j} \\ \vdots & \vdots & \vdots & \vdots \\ \frac{\partial \phi_1(\boldsymbol{\xi}_{N_Q})}{\partial \xi_j} & \frac{\partial \phi_2(\boldsymbol{\xi}_{N_Q})}{\partial \xi_j} & \cdots & \frac{\partial \phi_{N_p}(\boldsymbol{\xi}_{N_Q})}{\partial \xi_j} \end{pmatrix}. \quad (2.69)$$

With the numerical differentiation technique, now the only unknown in Eq. (2.65) is the treatment of the numerical flux $\hat{\mathbf{H}}$, which is the combination of numerical inviscid and viscous fluxes. The inviscid flux is calculated as the Riemann solution while viscous flux is obtained according the the SIPG method as addressed in Section 2.4.

By using the matrices defined above, the discretisation in matrix form reads [100]

$$\mathbf{M} \frac{d\tilde{\mathbf{Q}}}{dt} = \sum_{j=1}^d \mathbf{B}^T \mathbf{D}_j^T \mathbf{W} \mathbf{H}_j(\mathbf{Q}) - (\mathbf{B}^\Gamma \mathbf{M}_c)^T \mathbf{W}^\Gamma \hat{\mathbf{H}}^n - \sum_{j=1}^d \mathbf{B}^T \mathbf{D}_j^T \mathbf{M}_q \mathbf{W}^\Gamma \hat{\mathbf{S}}_j^n \quad (2.70)$$

where \mathbf{M}_c is the mapping matrix between basis functions in the element and on the boundary, \mathbf{M}_q is the interpolation matrix from the elemental quadrature points to the boundary quadrature points of the same element, $\hat{\mathbf{H}}$ is the numerical flux vector containing the consistency term and penalty term, and $\hat{\mathbf{S}}^n$ is the vector for the symmetry term of the SIPG method. The superscript Γ denotes the corresponding matrix on the boundary. For further details of the matrix form, see Ref. [93, 100].

2.6.2 Time integration

The NS equations are solved through time integration in semi-discrete form

$$\frac{d\mathbf{Q}}{dt} = \mathcal{L}(\mathbf{Q}), \quad (2.71)$$

where, compared with the expression in Eq. (2.70), the tilde above \mathbf{Q} and mass matrix \mathbf{M} on the left-hand side (LHS) are dropped for clarity. Eq. (2.71) is considered as an ordinary differential equations (ODEs) system with respect to time

since the spatial terms are all grouped in $\mathcal{L}(\mathbf{Q})$ on the right-hand side (RHS). In the above, different time integration schemes can be applied to solve this system while the spatial discretisation performed on the RHS is used to compute the time derivatives.

In the flow simulations the time step is dictated by the Courant–Friedrichs–Lewy (CFL) number. The CFL number should be typically smaller than 1 for explicit schemes. However, when using the P -th order DG spatial discretisation the CFL number is scaled by P^2 for the advection term and by P^4 for the diffusion term [93, 99]

$$CFL_{\text{advection}} \sim \frac{\Delta t}{\Delta x} P^2, \quad CFL_{\text{diffusion}} \sim \frac{\Delta t}{\Delta x^2} P^4,$$

which suggests a significantly smaller time step Δt must be adopted for an explicit solver, particularly when the discretisation order is high. To enable larger time steps in the simulations and achieve potentially higher efficiency [100, 101], we therefore use an implicit solver in this work.

The implicit solver is based on singly diagonally implicit Runge-Kutta (SDIRK) schemes. Let superscript “ n ” denote the current time step, we have the initial condition for the time integration

$$\mathbf{Q}^{(0)} = \mathbf{Q}^n,$$

then the i -th stage of the m stage Runge-Kutta (RK) method reads

$$\mathbf{S}^{(i)} = \mathbf{Q}^n + \Delta t \sum_{j=0}^{i-1} a_{ij} \mathcal{L}(\mathbf{Q}^{(j)}), \quad (2.72a)$$

$$\mathbf{Q}^{(i)} = \mathbf{S}^{(i)} + \Delta t a_{ii} \mathcal{L}(\mathbf{Q}^{(i)}), \quad i = 1, 2, \dots, m, \quad (2.72b)$$

where $\mathbf{S}^{(i)}$ is explicitly calculated in Eq. (2.72a), and is the source term for Eq. (2.72b). The solution for the next time step is calculated as

$$\mathbf{Q}^{n+1} = \mathbf{Q}^n + \Delta t \sum_{i=1}^m b_i \mathcal{L}(\mathbf{Q}^{(i)}). \quad (2.73)$$

In the above Eqs. (2.72b) and (2.73), a_{ij} and b_i are coefficients of the scheme. For an implicit scheme where $a_{ii} \neq 0$, Eq. (2.72b) is a nonlinear system to be solved, and can be rewritten as

$$\mathbf{N}(\mathbf{Q}^{(i)}) = \mathbf{Q}^{(i)} - \mathbf{S}^{(i)} - \Delta t a_{ii} \mathcal{L}(\mathbf{Q}^{(i)}) = \mathbf{0}. \quad (2.74)$$

This nonlinear system is solved using Newton method.

2.6.3 Jacobian-free Newton-Krylov (JNFK) method

The Newton iteration to solve Eq. (2.74) starts from an initial guess, for which the already known source term $\mathbf{S}^{(i)}$ in Eq. (2.74) is a reasonable one

$$\bar{\mathbf{Q}}^0 = \mathbf{S}^{(i)},$$

where we denote the intermediate state vector involved in the Newton iteration by an overbar ($\bar{\cdot}$), and the superscript shows the current step. The formula for Newton iteration then reads

$$\left. \frac{\partial \mathbf{N}}{\partial \mathbf{Q}} \right|_{\bar{\mathbf{Q}}^k} (\bar{\mathbf{Q}}^{k+1} - \bar{\mathbf{Q}}^k) = -\mathbf{N}(\bar{\mathbf{Q}}^k), \quad k = 0, 1, 2, \dots \quad (2.75)$$

where $-\mathbf{N}(\bar{\mathbf{Q}}^k)$ acts as the residual. The iteration stops when the L_2 norm of the residual is smaller than 10^{-2} of the initial residual or drops below 10^{-10} as the absolute tolerance. Then the solution for the i -th stage of SDIRK scheme is $\mathbf{Q}^{(i)} = \bar{\mathbf{Q}}^{k+1}$.

In each step of the Newton iteration, a linear system needs to be solved. Since the Jacobian matrix, $\partial \mathbf{N} / \partial \mathbf{Q}$ typically has a large order and is not symmetrical, the restarted generalized minimal residual method (GMRES) is adopted. The GMRES is a Krylov subspace methods, which iteratively constructs an approximate solution by projecting the residual onto a higher dimensional subspace spanned by the coefficient matrix of the linear system and the current residual vector. The Arnoldi iteration is used to generate an orthonormal basis to span the subspace [102]. Note that since the GMRES solver is used within the Newton iteration loops, a slight loss in accuracy for better efficiency by using a larger tolerance is considered a reasonable choice. In this thesis we use a relative tolerance of 10^{-2} with respect to the initial residual.

Further, a challenge to adopt the GMRES solver is its massive storage requirement for the successively generated basis to minimise the residual [103]. The storage management is particularly challenging when the high-order DG spatial discretisation is used. For a compressible flow solver, the dimension of $\mathbf{Q}^{(i)}$ in an element is the number of field variables $d + 2$, multiplied by the DoFs for each field $(P + 1)^d$, where d is the dimension and P is the polynomial order of the expansion basis. This eventually leads to a large linear system. To reduce the computation and memory cost for the Jacobian matrix, a Jacobian-free method is adopted to evaluate the product of the Jacobian matrix and a vector via finite difference as

$$\frac{\partial \mathbf{N}}{\partial \mathbf{Q}} \mathbf{V} \simeq \frac{\mathbf{N}(\mathbf{Q} + \epsilon \mathbf{V}) - \mathbf{N}(\mathbf{Q})}{\epsilon}, \quad (2.76)$$

In the above \mathbf{V} is the target vector, ϵ is the scaled machine epsilon $\hat{\epsilon}$ by the L_2 norm of the local variable as [93]

$$\epsilon = \|\mathbf{Q}\|_2 \sqrt{\hat{\epsilon}}$$

which is a small value so that it enables a high accuracy of the Jacobian-free evaluation when the entries of \mathbf{Q} are in the similar order. In this way, only a residual $\mathbf{N}(\mathbf{Q} + \epsilon \mathbf{V})$ needs to be computed by storing $\mathbf{N}(\mathbf{Q})$ [93], and the difference can be performed with high efficiency in the software implementation.

In practice, the GMRES solver is assisted by preconditioners to achieve better efficiency. A preconditioner clusters the eigenvalues of the coefficient matrix of the linear system to accelerate convergence during iterations [103]. Eq. (2.75) is transformed to the preconditioned system with right preconditioner as

$$\left(\frac{\partial \mathbf{N}}{\partial \mathbf{Q}} \mathbf{P}^{-1} \right) (\mathbf{P} \Delta \bar{\mathbf{Q}}^k) = -\mathbf{N}(\bar{\mathbf{Q}}^k) \quad (2.77)$$

where $\Delta\bar{\mathbf{Q}}^k = \bar{\mathbf{Q}}^{k+1} - \bar{\mathbf{Q}}^k$, and \mathbf{P} is the preconditioning matrix. In this work the J step block relaxed Jacobi iterative preconditioner, BRJ(J), developed by Yan et al. [93] is used for its low memory cost.

2.7 Other numerical methods

In addition to the above mentioned numerical methods to solve the NS equations, other methods are also adopted to globally or locally damp the disturbances when performing transition analysis using the e^N model. In this section we introduce the Selective Frequency Damping to accelerate the calculation of a steady baseflow and the absorption layer to avoid wave reflection in the disturbance field simulations.

2.7.1 Selective frequency damping

In the current work, Selective Frequency Damping (SFD) is used to accelerate the convergence to a steady baseflow. The SFD is an effective method to numerically find the steady state of a dynamical system [104], where the basic idea is to continually damp the unsteady component through a low-pass filter until a user-prescribed tolerance, 10^{-10} in this thesis, is achieved. For a dynamical system of the form

$$\dot{q} = f(q), \quad (2.78)$$

the corresponding SFD system takes the form

$$\begin{cases} \dot{q} = f(q) - \chi(q - \bar{q}) \\ \dot{\bar{q}} = \frac{q - \bar{q}}{\Delta} \end{cases} \quad (2.79)$$

where \bar{q} is the target steady solution, χ is the control coefficient, and Δ is the filter width. The system in Eq. (2.79) can be marched in time with any appropriate scheme and be stopped when $|q - \bar{q}|$ becomes smaller than the prescribed tolerance. The implementation of the SFD is relatively simple since it is independent of specific equations and numerical methods. It can be directly used as an outer loop to wrap the existed NS equations solver as the inner loop.

2.7.2 Absorption layer

In the simulations of disturbance fields, a blowing-suction on the wall is typically adopted to excite the disturbances. However, the disturbances are usually not only generated inside the boundary layer but also outside. When a near wall computational domain is used and the boundaries are reflective, the solution in the boundary-layer region can be contaminated by the reflected waves. To minimize this adverse effect, we adopt an absorption layer (also known as sponge region) near the sensitive reflective boundaries, as sketched in Fig. 2.6, by adding a forcing term on the right-hand side of Eq. (2.11) [105], giving

$$\frac{\partial \mathbf{Q}}{\partial t} + \nabla \cdot \mathbf{H} = -\sigma(\mathbf{x}) (\mathbf{Q}_{\text{ref}} - \mathbf{Q}), \quad (2.80)$$

where $\sigma(\mathbf{x})$ is a positive damping coefficient and \mathbf{Q}_{ref} is the reference solution to damp the current simulation which can come from the average field, a low-resolution simulation, steady simulation, etc.

The damping coefficient typically has a smooth spatial distribution to avoid sharp variations. In this work we adopt the damping coefficient in the form of a fifth-order polynomial with respect to only one direction in the local coordinate system (as shown in Fig. 2.6):

$$\sigma(\mathbf{x}(\mathbf{x}^*)) = \begin{cases} 0, & \bar{x}_1^* < 0, \\ 6(\bar{x}_1^*)^5 - 15(\bar{x}_1^*)^4 + 10(\bar{x}_1^*)^3, & \bar{x}_1^* \in [0, 1], \\ 1, & \bar{x}_1^* > 1, \end{cases}$$

where $\bar{x}_1^* = (x_1^* - x_{1,1}^*)/(x_1^* - x_{1,2}^*)$ is a scaled local coordinate, $x_{1,1}^*$ and $x_{1,2}^*$ are the begin and end of the absorption layer in the selected direction x_1^* . The profile of the damping coefficient is given in Fig.2.7.

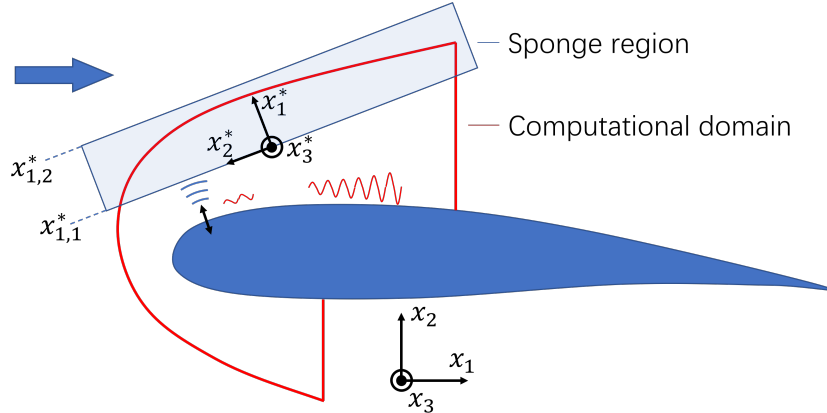


Figure 2.6: Sketch of the sponge region and the corresponding local coordinate system $\mathbf{x}^* = (x_1^*, x_2^*, x_3^*)$.

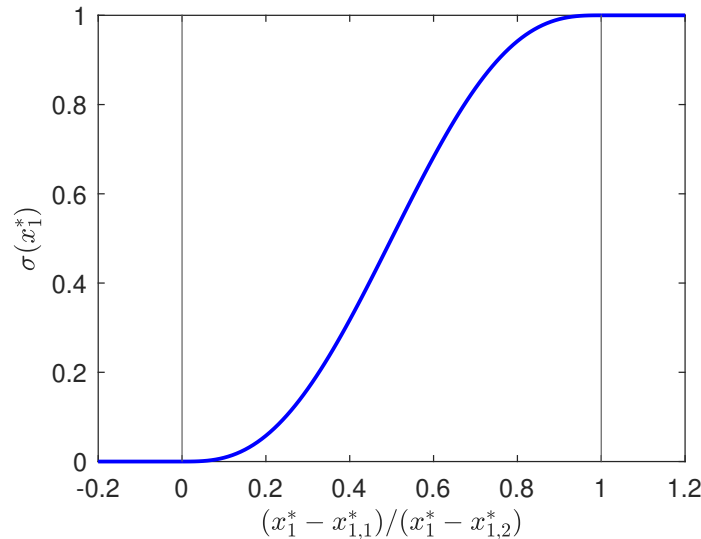


Figure 2.7: Damping coefficient distribution for the absorption layer.

2.8 Nektar++

High-order methods have been considered difficult to implement due to the complexity of algorithms, which limits the usage mostly within research groups for academic study and numerical analysis [106]. Nektar++ is a project aiming to bridge the gap between high-order method study and real applications, and is presented in form of open-source spectral/*hp* element method framework.

The Nektar++ framework is coded in object-oriented C++ and is organized by CMake building system, therefore has the merit of cross-platform. In this framework, both CG and DG discretisation are supported. On the mesh side, with the inherent mesh generator NekMesh, a set of high-order mesh can be either directly generated or converted from the linear mesh produced by other softwares such as Gmsh, Simcenter STAR-CCM+, Cadence Pointwise, and ANSYS ICEM. A variety of types of elements can be used, including 2D triangular, quadrilateral, and 3D hexahedron, prism, tetrahedron, pyramid, which enables high flexibility in mesh generation and significantly reduces the workload for the users. For more information see the website www.nektar.info [106, 107].

In this thesis work all the simulations are performed using the compressible and incompressible flow solvers in the Nektar++. On the other hand, the code developments by the author and collaborators on numerical methods and transitional analysis are fully implemented into Nektar++ framework, including

- 2D high-order mesh generation module;
 - stable subsonic Riemann inflow boundary conditions to enforce different quantities;
 - stabilization methods;
 - SFD for compressible flow simulations;
 - interactive data extraction module (in NekPy interface)
 - local stability analysis module;
 - numerical blowing-suction boundary condition on the wall;
 - coordinate transformation module;
 - disturbance amplitude calculation module;
 - Fourier mode operations module.
- .

Part II

Numerical method developments

Chapter 3

Framework for transonic laminar boundary layer natural transition analysis over complex geometries

This chapter is reproduced and extended from the following publication. Since this work is developed by the author in collaboration with other researchers so that “we” rather than “I” is used.

- **G. Lyu**, C. Chen, X. Du, M. S. Mughal, and S.J. Sherwin. Open-source framework for transonic boundary layer natural transition analysis over complex geometries in Nektar++, *AIAA Paper*, p. 4032, 2022. DOI: 10.2514/6.2022-4032.

3.1 Introduction

This thesis adopts the e^N method to analyse the laminar boundary layer natural transition. The use of this method involves two major steps: (i) the baseflow computation and (ii) the growth prediction of the disturbances. Since the disturbance development is sensitive to the baseflow profiles, accurate computation of the baseflow is critical to a successful transition prediction. On clean geometries the base flow can be computed by a computationally fast and cheap boundary layer solver. Then the disturbance fields are solved according to the Linear Stability Theory (LST) or Parabolized Stability Equations (PSE) [108], and the transition prediction analysis can then be undertaken. However, the baseflow over geometries with sufficiently large imperfections such as steps and gaps, cannot typically be computed through a boundary layer equations solver particularly in the presence of local recirculation, i.e. separation bubbles. Therefore, a Navier-Stokes solver needs to be used to obtain the baseflow. As for the disturbance fields, a linearised solver or full Navier-Stokes solver has to then be applied, since typically PSE models fail to correctly capture any rapid short scale variations in the baseflow; as well as some uncertainty of correctness of PSE modelling when dealing with large area of locally confined reversed flow.

When different computational tools are involved in these two main steps, data conversion issues can arise, typically involving difficulties interpolating and rescaling to alternative grids as accurately as possible. This causes losses in precision of

data and extra workload for researchers and engineers. A particular example would be that of an abrupt change in the vicinity of a localized stepped feature – interpolation using a standard cubic spline of the boundary layers for the consequent instability analysis may give rise to overshoots and unphysical flow gradients, which then impact the instability analysis. A set of integrated tools is therefore desirable. However, to the best of authors' knowledge although different research groups have developed their own tools for boundary layer analysis and flow transition prediction, relatively few, if any, are available as open-source to the wider community. Since developing each of the tools requires specific yet different knowledge, new researchers in the field find it extremely difficult, due to unavailability of trusted and well documented software, to start their investigation. Therefore, we have developed an open-source and unified framework which overcomes the difficulties of the two-stage process (i.e two separate and usually quite disparate baseflow and linear stability computations, and usually different numerical discretization strategies used in the base flow and instability tools). This chapter will describe a unified approach to modelling flow instabilities, which utilizes the spectral/hp element method framework Nektar++. (See Section 2.8 for more details). The high-order solvers in Nektar++ enable accurate boundary layer profile computations over complex geometries (which may well include locally reversed flows), as well as the ability to capture disturbance development with high accuracy.

This chapter is organized as follows. Section 3.2 introduces the pipeline for transition analysis. Section 3.3 discusses methods to reduce wave contamination for the disturbance field computation. A detailed one-dimensional signal filtering methods is provided in Section 3.4. When computing the disturbance fields using the Navier-Stokes solver, the accuracy and precision is a concern since the magnitude of disturbance fields is smaller than the baseflow for several orders. The ability to accurately capture disturbance development is then demonstrated in Section 3.5. For the verification of the framework, in Section 3.6 a two-dimensional transonic flat plate problem is solved with both clean and stepped geometries.

Moreover, in the baseflow and disturbance fields computation of the framework, pressure compatibility at the inflow boundary with the background results is desired. This must be achieved to through appropriate boundary condition, which is discussed in details in the next chapter.

For better demonstration purposes, some intermediate results from the flat plate case are used in early sections and are more completely discussed later.

3.2 Pipeline for transition prediction

The pipeline for transition prediction over a wing section is described in Fig. 3.1. To reduce the computational cost of high-fidelity simulation of boundary layer flows, we wish to use a near-body, reduced domain, whose outer boundary conditions are interpolated from a computationally cheaper three-dimensional (3D) Reynolds-Averaged Navier-Stokes (RANS) simulation. Taking advantage of its lower cost, the RANS simulation can be carried out over the full geometry such as a wing-fuselage configuration, and thus the three-dimensionality effects and the influence by the fuselage on the field distributions are automatically taken into account.

As a next step we compute the baseflow in the reduced domain, including the near wall laminar boundary layer. The matching of the outer RANS solution with

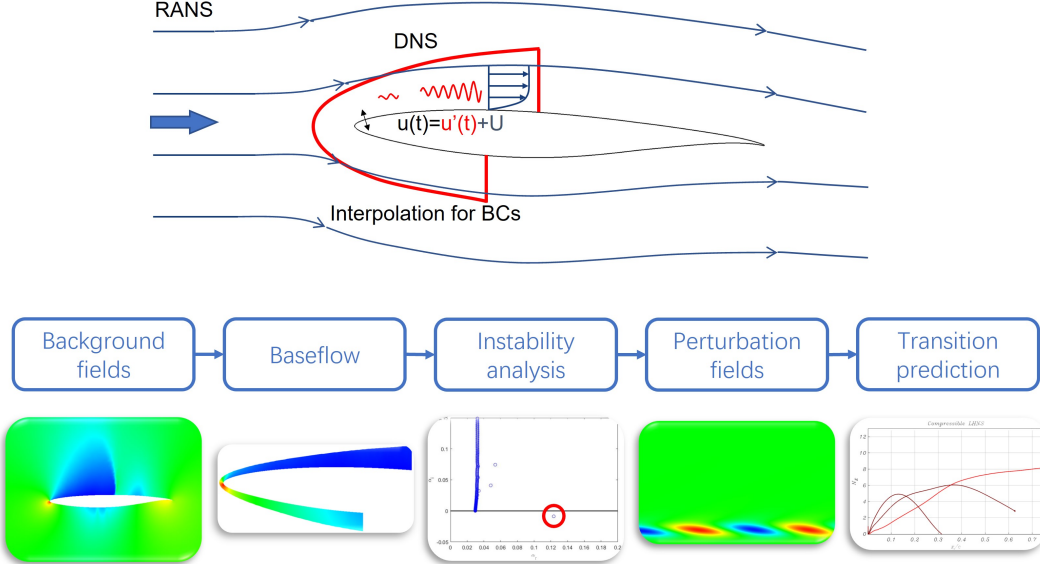


Figure 3.1: Pipeline for transonic boundary layer natural transition analysis.

the inner baseflow requires careful treatment of the inflow conditions. For a subsonic inflow condition in a Discontinuous Galerkin (DG) and Riemann-based solver, two conditions can be imposed in the normal direction to the boundary. As the standard condition in a DG solver, the incoming Riemann invariant and the measure of entropy are set, leading to a non-reflecting boundary. However, this does not adequately enforce a compatible pressure condition with the outer RANS simulation. This incompatibility in pressure distribution is undesirable since the pressure load is usually well captured by the Euler or RANS simulation (at least for lift prediction) and since the pressure distribution does not typically vary much over the boundary layer. Moreover, the disturbance development inside the boundary layer is significantly influenced by the pressure distribution. The above reasons therefore make pressure distribution a quantity of interest from the lower fidelity models and is an important property to maintain in the reduced domain, for the higher fidelity simulations that we hope to achieve with Nektar++. To best enforce the pressure compatibility, an entropy-pressure compatible inflow boundary conditions is considered for its linear stability, which is further discussed in the next chapter.

Before we solve the disturbance fields, sectional instability analysis (1D) is carried out along the boundary layer to ascertain and map out the instability parameter space, in terms of frequencies and spanwise wavenumbers of unstable disturbances, likely playing the most dominant role(s) in the transition process in the boundary layer. This is achieved through a local LST spatial instability analysis of boundary layer profiles at different streamwise positions. In this step accurate boundary layer profiles can be extracted interactively using the Nektar++ Python interface (NekPy), where the spatial analysis is undertaken using the LST module, using the open-source part of the CoPSE3d code [68, 109]. In the LST module the compressible LST equations are discretised with 4th-order finite differences. A generalized QZ method is used for eigenvalues and the discrete mode selected. This is then further refined using inverse Rayleigh iteration to get a highly accurate grid independent eigenvalue and eigenfunction.

Next, having identified the frequencies and spanwise wavenumbers of the most

dominant disturbances, the prescribed disturbances are then introduced in the reduced domain. To excite the disturbances, artificial receptivity is adopted by setting part of the wall near the leading edge as a blowing-suction interface, operating at the selected frequencies. Finally, the envelope (N -factor) of the growth curves of each disturbance (n -factors) can be generated, and the transition onset is considered at the position where the envelope exceeds a user prescribed threshold.

It is worth mentioning although the current work focuses on compressible flows, the aforementioned approach is also equivalently applicable to laminar boundary layer natural transition predictions for incompressible flows. The differences lie in the choices of solvers in Nektar++ to compute the baseflows and disturbance fields, as well as the necessity to reduce signal contamination by the wave reflections.

3.3 Methods to reduce wave contamination

Unlike incompressible flows where the speed of sound is assumed infinite so that the information of pressure and velocity influences the whole field instantaneously, the compressible flows update the fields through complex wave propagation due to its mixed parabolic-hyperbolic nature. The emergence of undesired waves may contaminate the disturbance signals of interest, such as the fields for Tollmien–Schlichting (TS) waves and crossflow waves. For the transonic boundary layer natural transition analysis over complex geometries, two main causes of wave contamination are:

- Waves generated by blowing-suction and reflected at the inflow boundaries;
- Reflected waves at the surface irregularities.

Both are related to the wave reflection at the boundaries of the domain, and a sketch of the reflections is shown in Fig. 3.2.

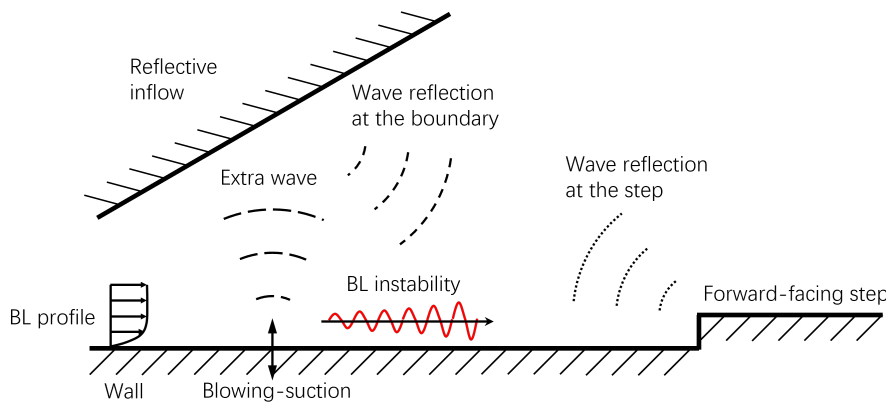


Figure 3.2: Sketch of the wave reflection at a inflow boundary and at a forward-facing step. The long dashed line represents the extra wave caused by the blowing-suction, the short dashed line represents the reflection wave at the inflow boundary, and the dotted line represents the reflection wave at the step.

To excite the boundary layer instabilities blowing and suction are introduced on the wall at prescribed frequencies. This boundary perturbation does not only excite the disturbance inside the boundary layer but also generate waves propagating in all directions. If the inflow boundary is reflective (e.g. the entropy-pressure compatible

inflow), the waves are reflected back to the wall. Fig. 3.3(a) shows this type of contamination in a reduced domain over a wing section of the CRM-NLF model, which is studied in detail in Chapter 5. In the case in Fig. 3.3, the blowing-suction is turned off after the first cycle to better trace the wave reflection between the wall and inflow boundary. It is apparent that the reflected waves are of similar magnitude to the target TS wave packet, and therefore the TS signals are difficult to be separated. A solution to this issue is to set up a sponge region, which adds additional forcing terms to damp the differences with respect to a mean or steady field. As shown in Fig. 3.3(b), the adoption of a sponge region effectively removes the wave reflection and the TS wave packet is clearly resolved. In addition to the sponge region, mesh coarsening [110] and lower order polynomials can be used for the spectral elements outside the boundary layer region to reduce the resolution and therefore smear the waves as they travel across this region, further damping the reflected waves.

As the excited waves travel downstream inside the boundary layer, they may be reflected if they experience a surface irregularity. This is the second source of contamination. Fig. 3.4 provides an example for wave reflection at a forward-facing step, which will be introduced in Section 3.6 as the verification of the framework. In general these reflected waves are much weaker than the disturbances of interest in most parts of the domain. However, since the disturbances grow over several orders of magnitude as they travel downstream, and since the adoption of the e^N method requires precise capture of the weakest amplitudes of the disturbances (which are used as the denominators in the calculation), the reflection waves can easily contaminate the results and lead to an incorrect N -factor.

To the best of the author's knowledge, few methods are available to clean a contaminated signal, especially when the two signals (i.e. the incident and reflected waves) have the same frequency. Schopper [111] spotted standing waves in the TS wave experiment and he explained the phenomenon as the superposition of the TS waves and freestream acoustic waves. He modelled the acoustic field to obtain cleaner TS wave signals, where proper adjustment was still needed. However, it can be expected that acoustic modelling at the surface irregularities is more difficult than that for the freestream acoustics. Moreover, in the TS wave study by Edelmann [110] the reflected waves were considered as acoustics whereas the profile of the reflected waves of the same case (see Section 3.6) in Fig. 3.5 indicates a more complicated condition. The reflected waves are acoustics (p') dominated but vorticity waves (u' and v') and entropy waves (T' and ρ') have comparable amplitude. Further u' has opposite phase to the others is also observed. These complicated waves make the general wave modelling more difficult and therefore not an ideal method to be adopted.

To obtain a clean TS wave packet signal Edelmann used a "Moving Tukey Window" for Fourier transform to obtained the amplitude [110]. However, the moving speed needs to be known in advance to apply the window, which restricts the application of this method. To enable the amplitude of disturbances to be obtained the current framework filters a signal by modified Chebyshev polynomials [112] to remove the influence of the reflected waves. Fig. 3.6 gives an example of the filtering, and compares the TS wave amplitude signal before reflection, with reflection, and the filtered result. The signal before reflection is taken before the TS wave reaches the step and therefore no reflected wave is generated. This signal can be

considered as the non-contaminated signal although it is only available in a limited region upstream of the step. The signal with reflection is taken after both TS waves and the physically reflected waves have become fully developed in the domain. The filtered signal is post-processed based on the signal with reflection. The comparison shows that the relative difference between the minimum amplitude of the filtered signal and the non-contaminated signal is only 2.68% while that between the contaminated signal and non-contaminated signal is 20.35%, indicating the filtering effectively removes 86.34% of contamination at the minimum amplitude point (which is the critical point since this amplitude will be used as the denominator to calculate N -factor) and recovers the signal to a low level. In the next section the filtering algorithms will be presented.

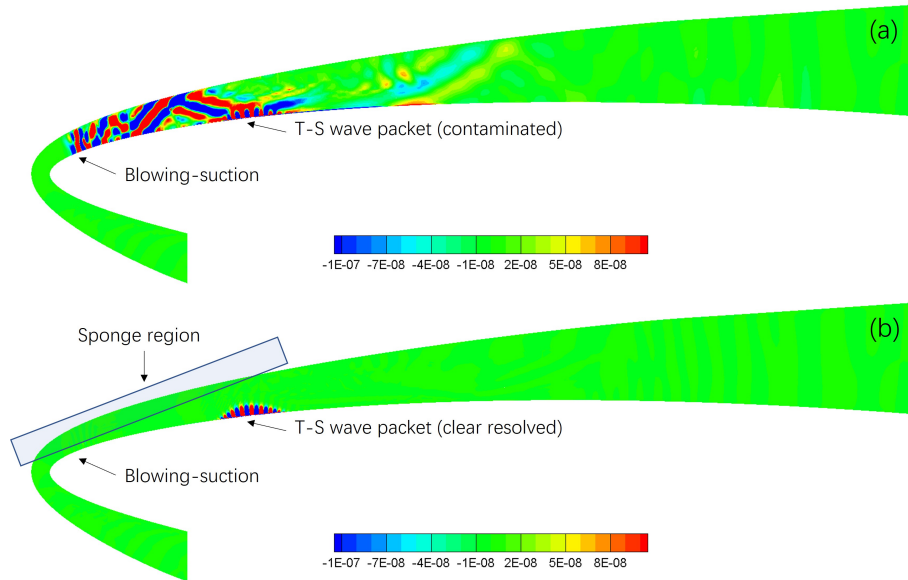


Figure 3.3: Comparison of the disturbances in the streamwise component of the velocity field (u') in TS wave excitation over an airfoil in the reduced domain: (a) contaminated TS wave packet because of the wave reflection, and (b) clear resolved wave packet with the adoption of a sponge region.

3.4 One-dimensional data filtering

To reduce the influence by the reflected waves mentioned above, as well as the noise in data sampling, the original one-dimensional data for the growth of disturbances is filtered before computing the n -factor. Since the reflected waves should have the same frequency as the incident TS waves or crossflow waves of our interest, direct signal decomposition is difficult. Therefore curve fitting is a practical solution to filter out the standing wave pattern which is featured by a high streamwise wavenumber. The basic idea is to expand the original one-dimensional data by several low order basis functions and then use the least squares approximation to determine the coefficients. The Chebyshev polynomials are used for filtering as basis functions for their strong ability in curve representation. Note that the data vary rapidly in the vicinity of the irregularities. This part of the data is left as is and only the smooth region will be filtered.

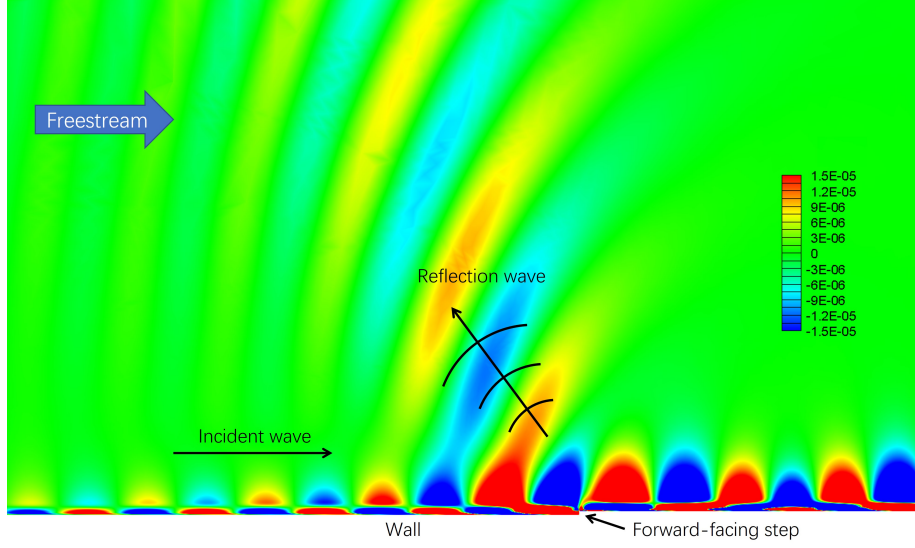


Figure 3.4: Disturbance in the streamwise component of the velocity field (u') showing the TS wave reflection at a forward-facing step.

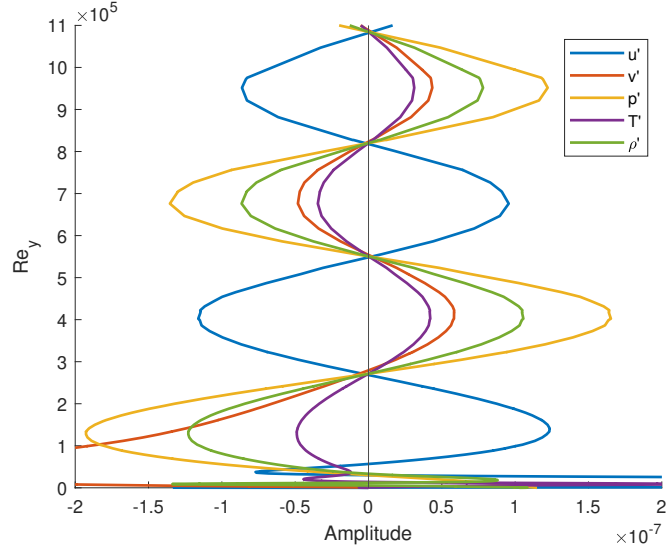


Figure 3.5: Reflected waves in the slice passing $Re_x = 2.4177 \times 10^6$ on the wall and of 15 deg with respect to the y -axis. (The forward-facing step is located at $Re_x = 2.45 \times 10^6$, and detailed settings are provided in Section 3.6. The vertical coordinate is represented by Re_y to follow the convention used in Ref. [110].)

3.4.1 Chebyshev polynomials

The Chebyshev polynomial of the first kind of order n is defined as

$$T_n(x) = \cos(n \arccos x), \quad x \in [-1, 1], \quad n = 0, 1, 2, \dots \quad (3.1)$$

which holds the following recurrence relation for $n \geq 1$

$$T_{n+1} = 2xT_n - T_{n-1}. \quad (3.2)$$

The first four Chebyshev polynomials take the explicit form

$$T_0(x) = 1, \quad T_1(x) = x, \quad T_2(x) = 2x^2 - 1, \quad T_3(x) = 4x^3 - 3x, \quad (3.3)$$

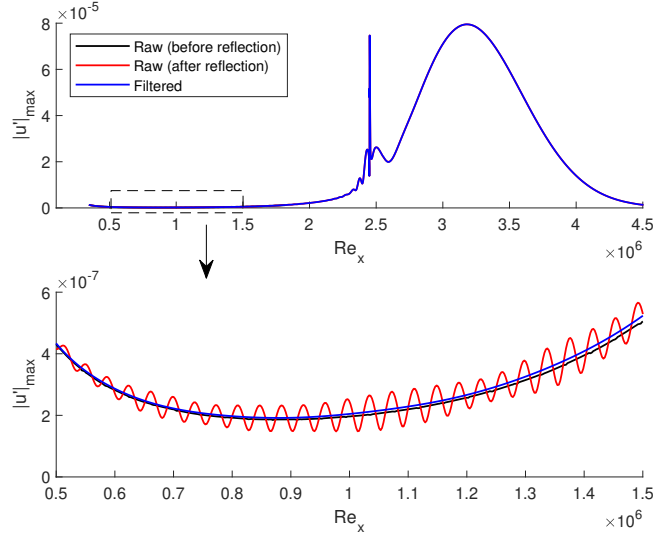


Figure 3.6: Comparison of raw data and the filtered results. The raw data is the amplification curve of 2D TS instability of $f = 19$ kHz over the flat plate with a forward-facing step. $N = 20$ is used to filter the data in the Re_x interval $[3.45 \times 10^5, 2.06 \times 10^6]$. Comparison of two sets of raw data and the filtered results. The first set of raw data (red line) includes oscillation because of the acoustic reflection at the forward-facing step. The second set of raw data (black line) is oscillation-free since it is obtained before the TS wavefront hits the step. The filtered data removes the oscillation using modified Chebyshev polynomials.

and plotted in Fig.3.7(a). These polynomials have non-zero end-point values. However, in the current work the end-point values of the sampled data are considered accurate and will be kept from changing. The data will be decomposed into a linear part and a homogeneous part, and only the homogeneous part will be filtered. The Chebyshev polynomials are therefore modified to have homogeneous boundary conditions as [112]

$$\begin{cases} \Phi_{2n-2} = T_{2n} - T_0 \\ \Phi_{2n-1} = T_{2n+1} - T_1 \end{cases}, \quad n = 1, 2, \dots \quad (3.4)$$

The first four modified Chebyshev polynomials are plotted in Fig.3.7(b) as examples, where $\Phi_n(\pm 1) = 0$ is always satisfied.

3.4.2 Least squares approximation

To filter out the noises and oscillations while holding the sampled boundary values of a one-dimensional data set, the independent variable is first mapped onto the standard interval $[-1, 1]$. For simplicity assume the independent variable x is already mapped in the following.) The original signal $f(x)$ is then decomposed into a linear part $f_l(x)$ and a homogeneous part $f_h(x)$, i.e. $f_h(\pm 1) = 0$

$$f(x) = f_l(x) + f_h(x). \quad (3.5)$$

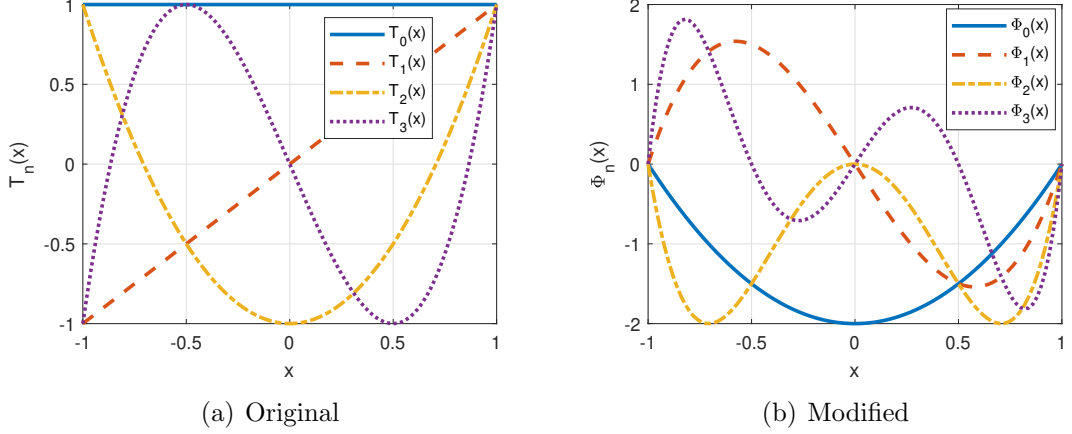


Figure 3.7: The first four Chebyshev polynomials.

The homogeneous part is then approximated using the modified Chebyshev polynomials in Eq. (3.4)

$$f_h(x) \approx \sum_{n=0}^{N-1} a_n \Phi_n(x) \quad (3.6)$$

Assuming the f_h is known at M different points $x_i, i = 0, 1, \dots, M-1$, where $M > N$, we have

$$\begin{pmatrix} f_h(x_0) \\ f_h(x_1) \\ \vdots \\ f_h(x_{M-2}) \\ f_h(x_{M-1}) \end{pmatrix}_M = \begin{pmatrix} \Phi_0(x_0) & \Phi_1(x_0) & \cdots & \Phi_{N-1}(x_0) \\ \Phi_0(x_1) & \Phi_1(x_1) & \cdots & \Phi_{N-1}(x_1) \\ \vdots & \vdots & \vdots & \vdots \\ \Phi_0(x_{M-2}) & \Phi_1(x_{M-2}) & \cdots & \Phi_{N-1}(x_{M-2}) \\ \Phi_0(x_{M-1}) & \Phi_1(x_{M-1}) & \cdots & \Phi_{N-1}(x_{M-1}) \end{pmatrix}_{M \times N} \begin{pmatrix} a_0 \\ a_1 \\ \vdots \\ a_{N-1} \end{pmatrix}_N, \quad (3.7)$$

which is written in matrix form as

$$\mathbf{f}_h = \mathbf{A}\mathbf{a}. \quad (3.8)$$

The above equation is unsolvable since $M > N$. Therefore a least-squares approximation is adopted as

$$\mathbf{a} = (\mathbf{A}^T \mathbf{A})^{-1} \mathbf{A}^T \mathbf{f}_h. \quad (3.9)$$

Finally the filtered signal is reconstructed by

$$\tilde{f}(x) = f_l(x) + \mathbf{A}\mathbf{a}. \quad (3.10)$$

3.5 Precision requirement and linear growth limit for instability study

In the e^N method an empirical threshold for transition sits in the range of 6–11 [52, 53, 56, 113–115]. This is not as trivial as it sounds since it means a disturbance can grow up to e^{11} ($\simeq 60000$) times and even higher whereas the amplitude of the disturbance still needs to be small enough so that the non-linearity can be neglected. Edelmann and Rist [32] obtained satisfactory results in DNS simulations by keeping

the disturbance amplitude below 10^{-4} of the freestream velocity in the whole domain, and a N -factor up to 9 is presented. This corresponds to the smallest amplitude of 1.2×10^{-8} of the freestream value. In the related work by Zahn and Rist [36], a maximum N -factor of 10.2 is reported and the amplitudes of disturbances are roughly 10^{-8} of the freestream value at introduction, which leads to a maximum non-dimensionalized amplitude of 2.7×10^{-4} .

However, the disturbance of order $O(10^{-4})$ may not be the limit to adopt the e^N method together with DNS simulations. To figure out the capability for simulating the linear growth of disturbance in the current framework, the comparisons are made by introducing disturbance of different strength into a two dimensional flat plate boundary layer with a forward-facing step (see 3.6 for the geometry and detailed settings). The freestream Mach number is 0.8 and the disturbance frequency of 19 kHz is used to obtain representative results.

Table 3.1: Initial disturbance scaled by the freestream velocity.

	Case 1	Case 2	Case 3	Case 4	Case 5
Initial disturbance	5×10^{-9}	1×10^{-7}	1×10^{-6}	1×10^{-5}	1×10^{-4}

We compare five cases as shown in Table 3.1, where the initial disturbances vary from weak to strong with approximate magnitudes of 5×10^{-9} , 10^{-7} , 10^{-6} , 10^{-5} , and 10^{-4} of the freestream value. Fig. 3.8(a) provides the scaled curves for maximum amplitude of streamwise velocity of the excited TS wave in the streamwise direction. It shows that all the cases have a good linear scaling relation except Case 5, which has a larger amplification than the others near the peak. This larger amplification is likely arising from non-linear effects. The relative differences for the adjacent two cases are plotted in Fig. 3.8(b), where the relative difference for Case a and Case b, for example, is computed by

$$\eta_{a,b} = \frac{|(|u'|_{max}^a - c_{a,b} \cdot |u'|_{max}^b)|}{c_{a,b} \cdot |u'|_{max}^b} \quad (3.11)$$

where $c_{a,b}$ is the scaling coefficient for the two cases, computed by the ratio of the maximum values of $|u'|_{max}^a$ and $|u'|_{max}^b$. It is shown that only the relative difference for Case 5 and Case 4 goes beyond 1% from $Re_x = 3.14 \times 10^6$, corresponding to a $|u'|_{max}$ of 7.9×10^{-3} of the freestream value in Fig. 3.8(a). Therefore 7.9×10^{-3} of the freestream value is considered as the estimated upper limit for linear growth.

On the other hand, an estimation for the lower limit is also needed since the disturbances whose amplitude smaller than the limit cannot not be well distinguished from the computational errors and undamped waves. The $|u'|$ -profiles of these cases at $Re_x = 8.35 \times 10^5$ are plotted in Fig. 3.9(a). This streamwise position is close to where the amplitudes of the disturbances reach their minimums. The figure shows that all of these profiles are well resolved and the computation errors cause a maximum relative error of 0.51% in the profile for Case 1. Since the amplitude of 10^{-9} is well captured (from Case 1, also see Fig. 3.10), this value can be used as the estimation for the lower limit. (Although the lower limit is not reached, for example, with respect to 1% relative error and smaller amplitude is still available, 10^{-9} is enough for the estimation.) Therefore, the disturbances whose amplitudes grow from 10^{-9} to 7.9×10^{-3} of the freestream value can be studied in a single

simulation (rather than divided into several) within the current framework. This gives the maximum N -factor of 15.9, covering the typical transitional value from 6 to 11. For extreme cases where a larger N -factor is needed, the amplification curve for certain disturbance can be generated in two runs by placing the blowing-suction in two different streamwise position, and then combine the result in post-processing.

The above estimation is about the disturbances, which are obtained by subtracting the steady baseflow from the perturbed fields, which are obtained by activating the blowing-suction on the wall and restarting from the steady baseflow. To make sure the disturbance of order of $O(10^{-9})$ is well resolved, the simulation of baseflow needs to converge to the order of $O(10^{-10})$ to $O(10^{-11})$. This can be achieved by direct time marching for a long time or using the Selective Frequency Damping (SFD) for higher efficiency. (See Section 2.7.1 for detailed descriptions of parameters.)

A convergence verification for the baseflow for cases in Table 3.1 is given in Fig. 3.9(b). With the control coefficient $\chi = 1$ the baseflow only converges to 10^{-10} since some TS wave-shaped structures continue to exist downstream of the step whereas 10^{-11} convergence is achieved by increasing the control coefficient to 4.

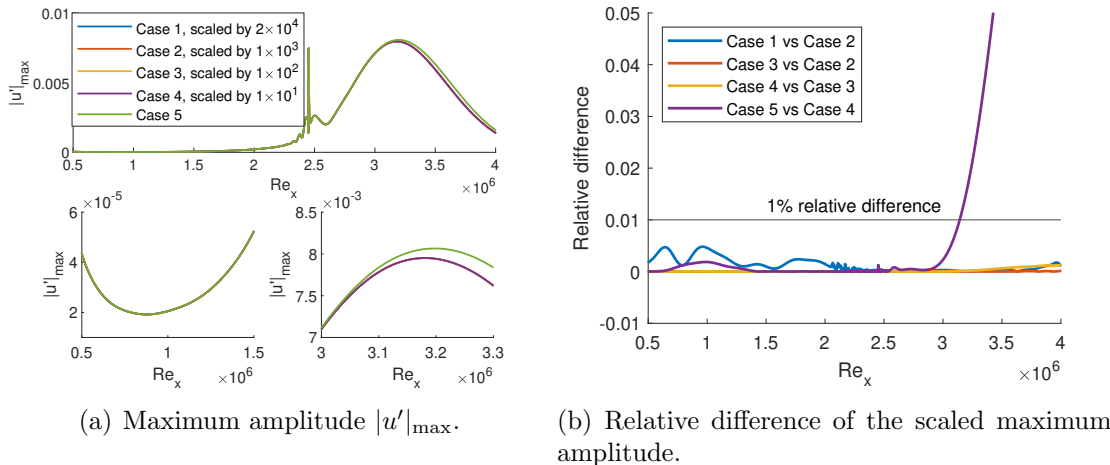


Figure 3.8: Comparison of scaled TS wave growth curves of the five cases in Table 3.1. The relative difference for each curve in (b) is computed using the adjacent two cases in Table 3.1. The data in the latter case in the legend is used as the reference to compute the relative difference.

3.6 Framework verification: TS wave development in 2D transonic flat plate boundary layer

In this section 2D TS wave development in two transonic flat plate boundary layer flows are simulated, and the N -factors are computed to verify the workflow. The two boundary layers considered are over a clean geometry and a geometry with a forward-facing step (FFS), respectively. These two cases have been studied by Edelmann and Rist [32] using DNS as well, and their results are used for comparisons.

Figure 3.11 shows the geometries and computational domains for the two cases. For the stepped case, detailed parameters of the step are given in Table 3.2, where Re_S is the Reynolds number based on the step position, Re_H is the Reynolds number

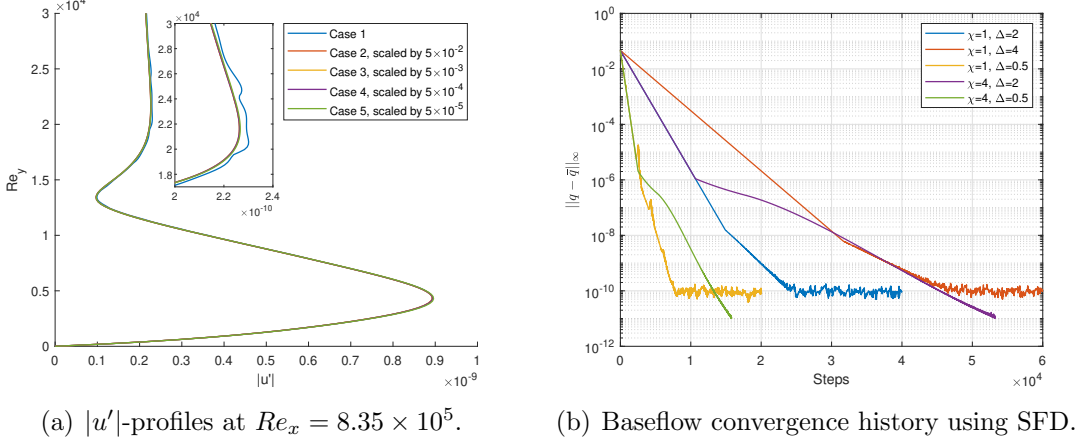


Figure 3.9: Precision verification: (a) the computational errors are $O(10^{-12})$ to $O(10^{-11})$; (b) the baseflow converges to $O(10^{-11})$.

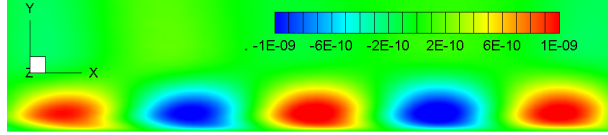


Figure 3.10: TS wave result of Case 1 in Table 3.1 around $Re_x = 8.35 \times 10^5$ in the presence of reflected waves. The plot shows the disturbance of the streamwise component of the velocity field (u'). The y -axis is scaled by a factor of 5.

based on the step height, H/θ is the step height over momentum thickness at the very position in the clean case, $Re_{H,H}$ is the Reynolds number based on step height and velocity at the step height in the clean case, L_1/H and L_2/H are the separation region length upstream and downstream of the step over the step height, respectively. In our simulations the flow conditions for the two cases are exactly the same. Both of them have a freestream Mach number $Ma = 0.8$, freestream temperature $T_\infty = 288$ K, and Prandtl number $Pr = 0.71$. The wall is iso-thermal with $T_{wall} = T_\infty$. A compressible boundary layer profile (see Appendix D for details) is weakly imposed at the inflow ($Re_x = 10^5$) while a pressure outflow with freestream value is adopted.

Table 3.2: Parameters for the forward-facing step on the plate.

Re_S	Re_H	H/θ	$Re_{H,H}$	L_1/H	L_2/H
2.45×10^6	2640	~ 2.4	~ 1350	~ 4.8	~ 0.9

Since the geometry is simple, the background field simulation in Fig. 3.1 is skipped. We directly compute steady baseflows using the compressible flow solver in Nektar++, and the results are shown in Fig. 3.12. To find an appropriate frequency range for the TS waves to be simulated, sectional instability analysis by LST is performed using the boundary layer profile of the clean case. The profiles at 10% and 90% streamwise positions are analyzed. Frequency scans, where the grow rate of TS waves with a range of frequencies are computed, are performed and the results are provided Fig. 3.13. It shows that the most amplified TS waves have the

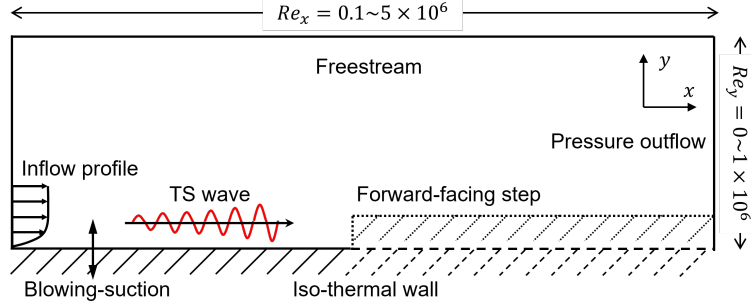
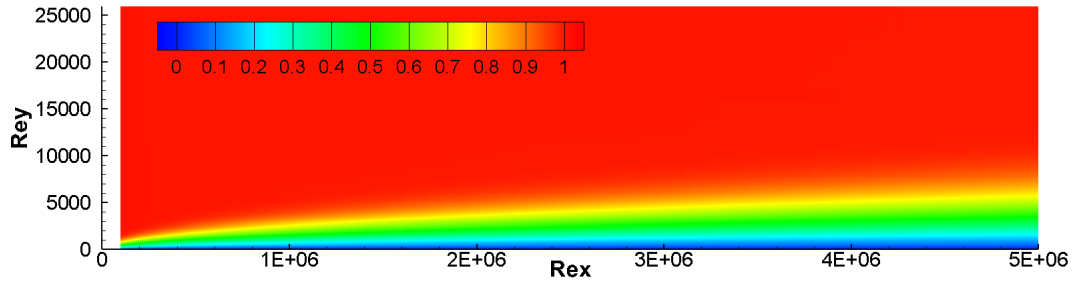


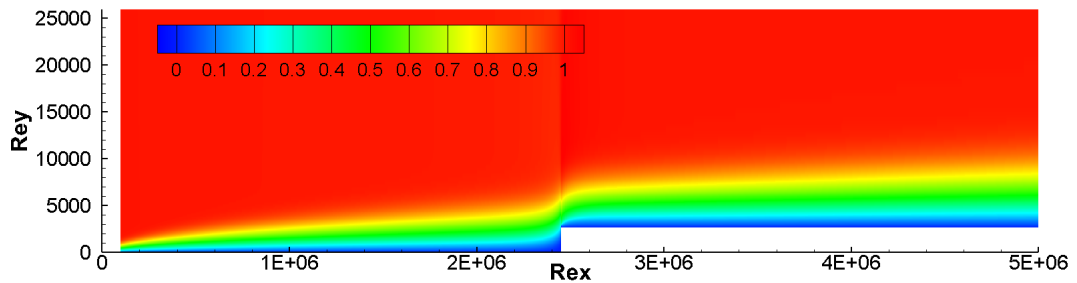
Figure 3.11: Schematic representation of the flow problem. The dashed line represents the wall for the clean geometry, and the dotted line represents the wall for the stepped geometry.

frequencies of approximately 42 kHz and 10 kHz at $x/L = 10\%$ and $x/L = 90\%$, respectively. Therefore, with these reference frequencies, TS waves of 16 different frequencies in the range [13, 45] kHz are selected for simulations. The same frequency range is used for both clean and stepped cases.

Figure 3.14(a) and 3.14(b) show the final N -factor curves for the two cases as well as the component n -factors. It is apparent that the N -factor for clean case well agrees with the data from the reference for $Re_x > 1.2 \times 10^6$. The discrepancy at low Re_x is due to the different domains size and treatments to high-frequency TS waves. The higher N -factor in the current work comes from further upstream domain being included in the simulations whereas it is assumed to be truncated in the reference work. As for the comparison for the stepped case, good agreement is achieved in the shape of the N -factor envelope, where the peaks and troughs of the oscillations near the FFS agree well with the reference. However, the absolute value of the N -factor in the current thesis is larger than the reference by 0.215. This is considered coming from the differences in the baseflow. As shown in Fig. 3.15, the wall pressure distributions in the current work and the reference work are not perfectly matched. This is because in the presence of the step, the baseflow is unavoidably modulated and the zero pressure gradient condition does not hold when using the same boundary conditions as the clean case, particularly when the inflow profile is weakly enforced. Compared with the reference, a larger adverse pressure gradient upstream of the step is observed while the pressure gradient downstream is slightly smaller. It is these different pressure gradients that leads to a larger growth in the N -factor in Fig. 3.14(b) since the development of TS wave is sensitive to pressure distribution and is destabilized by the adverse pressure gradient.



(a) Clean flat plate



(b) Flat plate with a forward-facing step

Figure 3.12: Baseflow of the flat plate cases. Streamwise component of the velocity u is displayed.

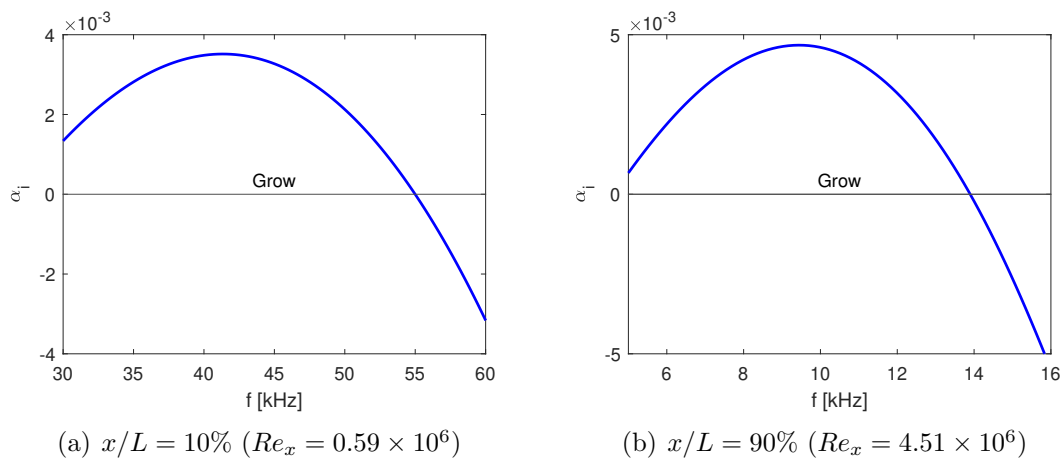
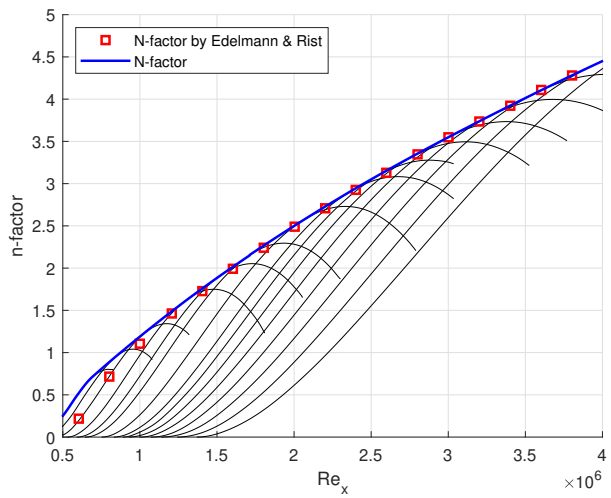
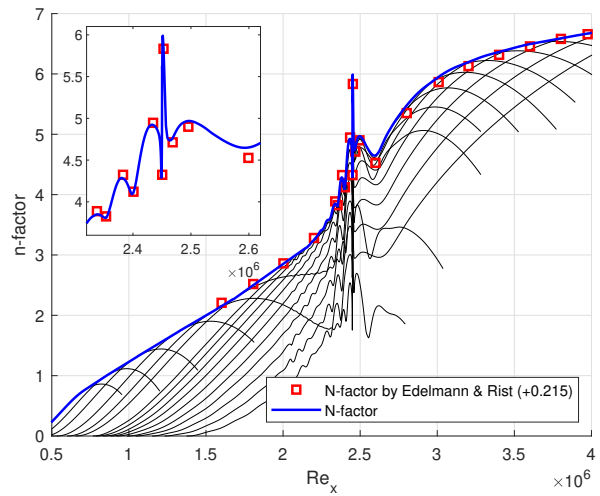


Figure 3.13: Frequency scans at an upstream position and a downstream position.



(a) Clean flat plate



(b) Flat plate with a forward-facing step

Figure 3.14: N -factors for the two flat plate cases.

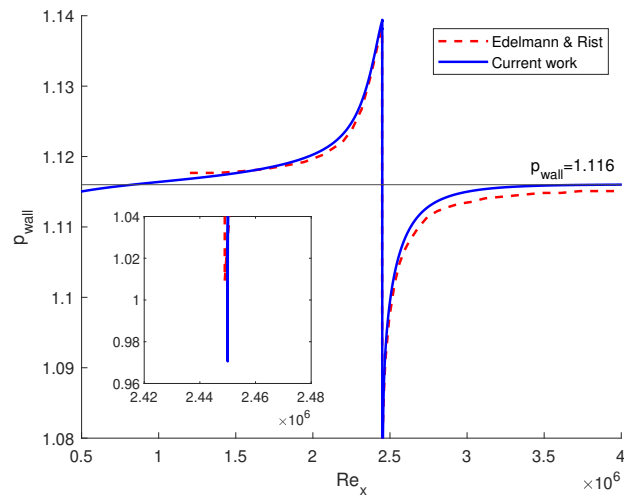


Figure 3.15: Wall pressure distribution comparison.

Chapter 4

Stable Riemann boundary condition for embedded DG compressible flow simulations

This chapter is reproduced and extended from the following publication. Since this work is developed by the author in collaboration with other researchers so that “we” rather than “I” is used.

- **G. Lyu**, C. Chen, X. Du, and S.J. Sherwin. Stable, entropy-pressure compatible subsonic Riemann boundary condition for embedded DG compressible flow simulations. *Journal of Computational Physics*, vol. 476, p. 111896, 2023. DOI: 10.1016/j.jcp.2022.111896.

4.1 Introduction

Laminar boundary layer transition and the following turbulence involve the generation, growth, stretch, and breakdown of tiny vortices inside the boundary layer. To numerically study these fine evolutions, high-fidelity methods such as implicit large-eddy simulation (LES) and direct numerical simulation (DNS) are more regularly being adopted. However, limited by current computational resources, full-scale simulations at realistic Reynolds numbers ($\sim 10^7$) are not currently available, even at the most optimistic scenario predicted by Moore’s law [79]. As a result, current efforts into simulating transitional mechanisms often use high fidelity simulation in a near-body, reduced domain which is embedded in a outer domain encompassing the whole geometry where a lower fidelity model is applied, as sketched in Fig.4.1(a). (See Ref. [75] [33, 108] [116, 117] [118] [119].)

Unlike in a large domain where the inflow and outflow boundaries are far away from the geometry of interest so that uniform freestream values can be enforced for the boundary conditions, simple boundary conditions are not available on the reduced domain. Hence, the distributions of the solution fields need to be specified in advance. For example, Wenzel [117] studied the high subsonic turbulent boundary layer in a rectangular reduced domain on the wing of Boeing 787 using DNS. To enforce the freestream boundary condition, a modelled velocity distribution was provided through an analytical expression, and the temperature and pressure distributions were calculated according to the one-dimensional isentropic relation. An al-

ternative approach at the boundaries is to use the results from a Reynolds-Averaged Navier–Stokes (RANS) simulation, which is carried in a larger or full domain. The RANS result can then be interpolated along the boundary of the reduced domain to provide appropriate distributions, e.g. Cooke [108], Tempelmann [75], and other references mentioned above. In these studies, the velocity distributions at the inflow boundary are interpolated. Since the inflow boundary is located upstream of the geometry, the fields are typically influenced little by the turbulence model in RANS. This is because the turbulence model modulates a RANS solution by adding additional “viscosity” (named as eddy viscosity), which mainly arise from the near-wall region and drastically decreases as a “probe” in the RANS field moves away from the wall [120–122]. In addition, if the region of interest is not close to the fuselage, there is little eddy viscosity transported from the upstream region of the computational domain when a low eddy viscosity ratio (i.e. eddy viscosity over molecular viscosity) is set as part of the inflow boundary condition of the RANS simulation. Compared with the distribution modelling which approximates field distributions along the boundary by analytical expressions, interpolating the distributions from a RANS simulation is more flexible. This enables the cases with more complex geometries to be studied, where the distributions are not typically well described by analytical expressions.

Having obtained the desired distributions on the boundary, they then need to be enforced on the boundary of the reduced domain through an appropriate implementation. The types of boundary conditions are usually related to the problem and the adopted numerical method. For the incompressible flows in continuous Galerkin (CG) formulations, they are often solved with strong boundary conditions which enforce the velocity and pressure through Dirichlet or Neumann boundary conditions. Therefore, the desired distributions of data from the outer simulations can be directly enforced. On the other hand, when discretized by Discontinuous Galerkin (DG) method, weak boundary conditions enforcements are adopted to solve both incompressible and compressible flows [97, 123]. For example, a DG based compressible flow solver uses a Riemann solution to infer a desired numerical flux to achieve better accuracy [124] and convergence [125, 126]. Compared with the strong enforcement, the flow quantity distributions are usually not directly set in the weak enforcement.

In addition, in the compressible flow regime, subsonic flows and supersonic flows behave differently due to the different sign of the hyperbolic characteristics, and therefore, different boundary conditions have to be specified. The most significant consequence lies in the number of conditions to well-pose the problem [127]. In a DG and Riemann-based solver, and for the inviscid fluxes of the governing equations, two conditions can be imposed in the inwards normal direction to the boundary for a subsonic inflow while three conditions can be imposed for a supersonic inflow. The choice of conditions naturally leads to the different quantities being enforced on the subsonic inflow boundary. A widely adopted subsonic inflow boundary condition in a DG solver is to enforce the incoming Riemann invariant and entropy, leading to a non-reflecting boundary. However, this does not directly enforce a compatible pressure condition with the outer RANS simulation. This incompatibility in the pressure distribution is undesirable in boundary layer transition prediction since the streamwise pressure gradient has a significant influence on the development of a transitional boundary layer flow. For example the Tollmien–Schlichting waves are

stabilized by a favorable pressure gradient and destabilized by an adverse pressure gradient while both pressure gradients destabilize the crossflow waves [26, 27]. Further the pressure load is usually well captured by the Euler or RANS simulation (at least for lift prediction) and the pressure distribution does not typically vary much over the boundary layer. The pressure distribution is therefore considered a reliable quantity of interest from the lower fidelity models and is an important property to be maintained in the reduced domain.

A similar example regards to the challenge of incompatible quantity at subsonic inflow is provided by the simulation of low-pressure turbine cascade in a jet engine. Since a full-scale simulation over the whole engine is also limited by the computational capacity, low-pressure turbine of certain stage is often studied separately or together with a few following stages. This separate stage(s) simulation also leads to a reduced domain as sketched in Fig.4.1(b), and leaves an artificial boundary condition at inflow to be specified. Since the turbine blades are designed to harvest the best efficiency at certain flow conditions, making it sensitive to the angle of attack (AoA) or alternately the ratio between the inflow velocity components. According to the multi-dimensional Riemann problem [96], the velocity component tangential to the inflow boundary can be directly enforced while the normal component is influenced by the reflected waves from downstream (for its subsonic working condition) if the standard Riemann inflow condition is adopted. This can cause incorrect AoA and fail the simulations. Therefore the normal velocity component, together with the tangential ones, is a desired quantity to be enforced in such subsonic compressible flow simulations. In this thesis, however, we will focus on the embedded simulations of wing sections (although the study in this chapter can well be used in the turbine simulations and etc.).

To achieve the pressure compatibility in the reduced domain, the corresponding subsonic inflow boundary condition needs to be constructed. However, although this construction can follow several approaches, not all of them are appropriate. The ideal boundary conditions enable the numerical simulation to converge in a stable way, inferring that the partial differential equation problem is well-posed and the numerical discretisation is stable with the adopted boundary conditions.

For the stability analysis, Giles [128] and Darmofal et al. [129] have developed one-dimensional (1D) linear analysis (or eigenmode analysis) to evaluate decay rates of the disturbances. Since the decay rates depend on the adopted boundary conditions, the performance of boundary conditions are therefore obtained. This method can also be used to check the well-posedness of the boundary condition enforcement. Nordström et al. [127, 130] used the energy method to analyze the linearized system in a control volume. This method can be used to understand the number of conditions to make the problem well-posed as well as examine suitability of certain combination of boundary conditions. These works provide insightful analysis and set up a useful framework, which are wildly used to establish boundary conditions for compressible flow simulations.

As for the boundary condition stability analysis of DG approximations, it is less studied compared with those based on the conventional finite difference discretisation. Hindenlang et al. [76] examined the linear stability of the wall boundary condition for the inviscid flows using the sufficient condition developed by Gassner et al. [131]. In addition, insights on the stability of wall boundary condition through penalization in the immersed boundary method using flux reconstruction are pro-

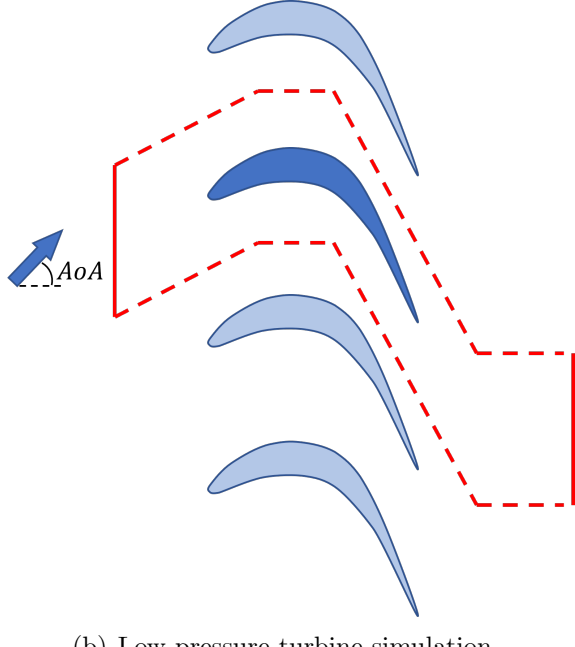
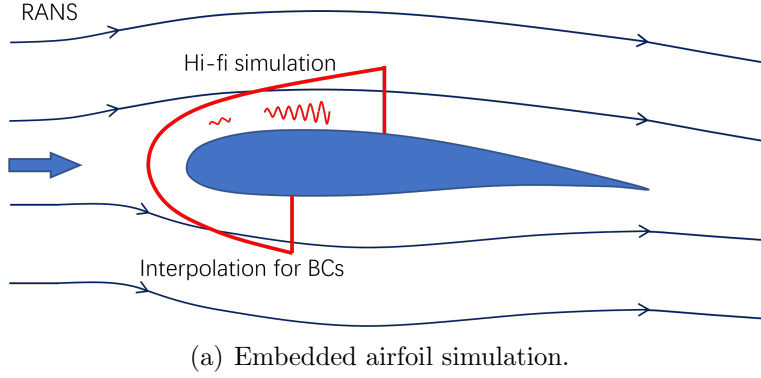


Figure 4.1: Illustrations of subsonic compressible flow simulations with specific physical quantities to be enforced at inflow boundary: (a) pressure along the inflow boundary is expected to be enforced; (b) the inflow velocity is to be enforced to guarantee the desired AoA. The dashed line in (b) denotes periodic boundary conditions.

vided by Kou et al. [132], where the stability condition for penalization parameter in the 1D scalar advection problem is given. These studies focused on the wall boundary condition while reasonably assumed the conditions on other boundaries are stable or periodic. However, since it is the combination of boundary conditions that determines the evolution of the system, the satisfaction of this condition on individual boundaries does not necessarily guarantee a non-singular system. To obtain a specific analysis within the conventional method, where the disturbance is introduced internally, a uniform baseflow is sometimes needed to compute the integration over the boundaries of the control volume. This can limit its application to problems with large gradient, and therefore an extension of this methodology is required.

In this chapter we therefore revisit the Riemann problem to see how best to enforce pressure compatibility at the subsonic inflow boundary. In Section 4.2, 1D Euler equations are linearized in a DG element, and the systems for the inflow

boundary conditions to be stable are derived. An entropy-pressure compatible inflow boundary condition is selected from the full range of possibilities in Section 4.3, and two other types of stable inflow boundary conditions are provided in Section 4.4. In Section 4.5 we show the entropy compatibility with the reference value at a Riemann inflow stabilizes the simulation. The applicability of the 1D stability model is further discussed regards to the local analysis versus the global analysis in Section 4.6. Section 4.7 extends the current analysis to multi-dimensions without assuming an uniform baseflow assumption. This method is then used to understand the instability issue in adopting a stale 1D entropy-pressure inflow in the region of a stagnation point flow. Finally, two transonic flows in reduced domains taken out of full three-dimensional (3D) RANS simulations are computed for validation.

4.2 Boundary conditions linear stability analysis

To analyze the applicability of weak boundary conditions, we now consider the stability of the linearized Euler system subject to a DG discretisation. A common practice for DG approximations of the compressible flow equations is to impose boundary conditions using 1D characteristic line theory. We therefore follow this practice and derive the linearized DG approximation for 1D Euler equations.

4.2.1 Linearized DG approximation for 1D Euler equations

The conservative form of the 1D Euler equations reads

$$\frac{\partial \mathbf{Q}}{\partial t} + \frac{\partial \mathbf{F}(\mathbf{Q})}{\partial x} = \mathbf{0}, \quad (4.1)$$

where \mathbf{Q} is the state vector of conservative variables, \mathbf{F} is vector for inviscid flux, that is

$$\mathbf{Q} = \begin{pmatrix} \rho \\ \rho u \\ E \end{pmatrix}, \quad \mathbf{F} = \begin{pmatrix} \rho u \\ p + \rho u^2 \\ u(E + p) \end{pmatrix}. \quad (4.2)$$

In the above ρ is the density, u is the velocity in the x -direction, p is the pressure and E is the total energy, which can be expressed under the assumption of a perfect gas law as

$$E = \frac{1}{\gamma - 1}p + \frac{1}{2}\rho u^2,$$

where γ is the specific heats ratio.

In the DG approach, the approximation in each element are independent and boundary conditions are enforced weakly in each element in the form of a numerical flux. Therefore, to derive the smallest linear system for stability analysis which preserves all the necessary boundary conditions, we consider the domain as consisting of a single element Ω , as shown in Fig.4.2. Eq. (4.1) is first multiplied by a test function ϕ and then integrated in the domain by part, which gives

$$\int_{\Omega} \phi \frac{\partial \mathbf{Q}}{\partial t} dx + [\phi \mathbf{F} \cdot \mathbf{n}]_{\partial\Omega} - \int_{\Omega} \nabla \phi \cdot \mathbf{F} = 0. \quad (4.3)$$

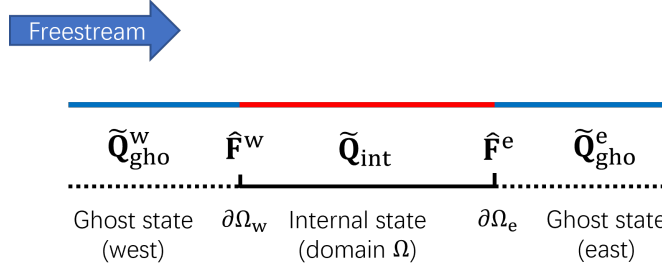


Figure 4.2: 1D solution domain and associated conservative states. The red region represents the inner state and blue regions represent the ghost state on each side where the solution domain boundaries are provided.

For simplicity we next consider a piecewise constant approximation in the element

$$\mathbf{Q} \simeq \tilde{\mathbf{Q}}(t)\phi(x), \quad \phi(x) = \begin{cases} 1, & x \in \Omega \\ 0, & x \notin \Omega \end{cases}. \quad (4.4)$$

Imposing this piecewise constant approximation to Eq. (4.3) allows us to analytically evaluate the first term and directly sets the third term to zero. Finally replacing the boundary flux \mathbf{F} by a numerical flux denoted by $\hat{\mathbf{F}}$, Eq. (4.3) becomes

$$\frac{d\tilde{\mathbf{Q}}}{dt}\Delta x = \hat{\mathbf{F}}^w - \hat{\mathbf{F}}^e, \quad (4.5)$$

where $\Delta x = x^e - x^w$ is the length of the 1D domain and the superscript “w” and “e” denote the west and east boundaries of the element.

Before going into more details of the numerical flux, for clarity we address the definitions of different states involved in the following analysis, and a summary is listed in Table 4.1.

Table 4.1: Definitions of different states.

States	Notion	Definition
Internal state	$(\cdot)_{\text{int}}$	The state inside the element.
External state	$(\cdot)_{\text{ext}}$	The state outside the element.
Boundary state	$(\cdot)_b$	The state at the boundary of the element.
Ghost state	$(\cdot)_{\text{gho}}$	The state used to replace the external state for a boundary element.
Reference state	$(\cdot)_{\text{ref}}$	The target state for the boundary state to reach, e.g. zero normal velocity on the wall. It can be the value prescribed from a known solution, e.g. the RANS field, which typically is a constant but we still can perturb it for mathematical analysis.

In Eq. (4.5) the numerical flux is typically computed through a Riemann solver, and takes the form

$$\hat{\mathbf{F}} = \hat{\mathbf{F}}(\tilde{\mathbf{Q}}_{\text{int}}, \tilde{\mathbf{Q}}_{\text{ext}}), \quad (4.6)$$

where at the interface between two adjacent elements $\tilde{\mathbf{Q}}_{\text{int}}$ and $\tilde{\mathbf{Q}}_{\text{ext}}$ represent the internal state and external states as listed in Table 4.1. For the numerical flux at the solution domain boundary, where there is no adjacent element, a ghost state $\tilde{\mathbf{Q}}_{\text{gho}}$ is introduced instead of the external state so that we have

$$\hat{\mathbf{F}} = \hat{\mathbf{F}}(\tilde{\mathbf{Q}}_{\text{int}}, \tilde{\mathbf{Q}}_{\text{gho}}). \quad (4.7)$$

In the standard use of a Riemann boundary condition the external or ghost state is independent of the internal state and the solution of the Riemann solver will provide a known boundary state $\tilde{\mathbf{Q}}_b$, i.e.

$$\tilde{\mathbf{Q}}_b(\tilde{\mathbf{Q}}_{\text{int}}, \tilde{\mathbf{Q}}_{\text{gho}}).$$

In this circumstances $\tilde{\mathbf{Q}}_b$ is not known explicitly but rather inferred through $\tilde{\mathbf{Q}}_{\text{int}}$ and $\tilde{\mathbf{Q}}_{\text{gho}}$ and the Riemann solution procedure [97]. Nevertheless it is also possible to explicitly impose as many conditions as there are incoming characteristics on the domain boundary, for example a prescribed freestream quantity such as pressure or a zero normal velocity at an inviscid wall. For this situation we introduce $\tilde{\mathbf{Q}}_{\text{ref}}$ to denote an external reference state which when provided as input to the Riemann solver in combination with the internal state it enforces the desired condition on $\tilde{\mathbf{Q}}_b$ and subsequently $\hat{\mathbf{F}}(\tilde{\mathbf{Q}}_b)$. Accordingly in this case the ghost state $\tilde{\mathbf{Q}}_{\text{gho}}$ is now dependent on $\tilde{\mathbf{Q}}_{\text{int}}$ and the desired conditions $\tilde{\mathbf{Q}}_{\text{ref}}$ we wish to impose such that

$$\begin{aligned} \hat{\mathbf{F}} &= \hat{\mathbf{F}}(\tilde{\mathbf{Q}}_{\text{int}}, \tilde{\mathbf{Q}}_{\text{gho}}(\tilde{\mathbf{Q}}_{\text{ref}}, \tilde{\mathbf{Q}}_{\text{int}})) \\ &= \hat{\mathbf{F}}(\tilde{\mathbf{Q}}_{\text{ref}}, \tilde{\mathbf{Q}}_{\text{int}}), \end{aligned} \quad (4.8)$$

or equivalently

$$\hat{\mathbf{F}} = \hat{\mathbf{F}}(\tilde{\mathbf{Q}}_b), \quad \tilde{\mathbf{Q}}_b = \tilde{\mathbf{Q}}_b(\tilde{\mathbf{Q}}_{\text{ref}}, \tilde{\mathbf{Q}}_{\text{int}}). \quad (4.9)$$

Since the numerical flux is constructed with the reference state and the internal state, the linearized system for stability analysis can be generated by introducing disturbances on both states, as is shown in Fig.4.2.1. The linearized form of Eq. (4.5) (see B.1 for full details), is given by

$$\frac{d(\delta\tilde{\mathbf{Q}}_{\text{int}})}{dt}\Delta x = \left(\frac{\partial\hat{\mathbf{F}}^w}{\partial\tilde{\mathbf{Q}}_{\text{int}}} - \frac{\partial\hat{\mathbf{F}}^e}{\partial\tilde{\mathbf{Q}}_{\text{int}}} \right) \delta\tilde{\mathbf{Q}}_{\text{int}} + \left(\frac{\partial\hat{\mathbf{F}}^w}{\partial\tilde{\mathbf{Q}}_{\text{ref}}^w} - \frac{\partial\hat{\mathbf{F}}^e}{\partial\tilde{\mathbf{Q}}_{\text{ref}}^e} \right) \delta\tilde{\mathbf{Q}}_{\text{ref}}, \quad (4.10)$$

where $\delta\hat{\mathbf{Q}}_{\text{int}}$ is the time-dependent disturbance on the internal state and $\delta\hat{\mathbf{Q}}_{\text{ref}}$ is the constant disturbance on the reference state. (The disturbance on the west boundary is assumed equal to that on the east boundary.)

Although the independent variables in Eq. (4.10) can be in any form for the 1D analysis it is convenient to use the characteristic variables which are

$$\mathbf{U} = \begin{pmatrix} R^+ \\ R^0 \\ R^- \end{pmatrix} = \begin{pmatrix} u + \frac{2}{\gamma-1}c \\ S \\ u - \frac{2}{\gamma-1}c \end{pmatrix}, \quad (4.11)$$

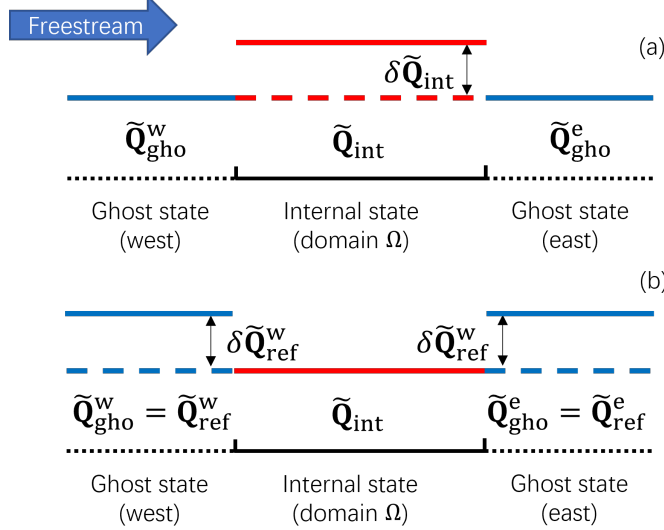


Figure 4.3: Steady state and perturbation in 1D cases: (a) Perturbation on the internal state; (b) perturbation on the reference state. The dashed lines represent the steady state.

where $c = \sqrt{\gamma p / \rho}$ is the speed of sound, S , which is the measure of entropy and takes the form

$$S = \frac{p}{\rho^\gamma}.$$

By assuming the baseflow is steady and therefore uniform because of one-dimensionality, the 1D linearized system in characteristic variables takes the form

$$\frac{d}{dt} (\delta \tilde{\mathbf{U}}_{int}) = \frac{1}{\Delta x} \mathbf{C}_{int} \delta \tilde{\mathbf{U}}_{int} + \frac{1}{\Delta x} \mathbf{C}_{ref} \delta \tilde{\mathbf{U}}_{ref}, \quad (4.12)$$

where the coefficient matrices are defined as

$$\mathbf{C}_{int} = \left(\frac{\partial \tilde{\mathbf{Q}}}{\partial \tilde{\mathbf{U}}} \right)^{-1} \frac{\partial \hat{\mathbf{F}}}{\partial \tilde{\mathbf{Q}}} \frac{\partial \tilde{\mathbf{Q}}}{\partial \tilde{\mathbf{U}}} \left(\frac{\partial \tilde{\mathbf{U}}_b^w}{\partial \tilde{\mathbf{U}}_{int}} - \frac{\partial \tilde{\mathbf{U}}_b^e}{\partial \tilde{\mathbf{U}}_{int}} \right) = \mathbf{C}_1 \mathbf{C}_{2,int}, \quad (4.13)$$

$$\mathbf{C}_{ref} = \left(\frac{\partial \tilde{\mathbf{Q}}}{\partial \tilde{\mathbf{U}}} \right)^{-1} \frac{\partial \hat{\mathbf{F}}}{\partial \tilde{\mathbf{Q}}} \frac{\partial \tilde{\mathbf{Q}}}{\partial \tilde{\mathbf{U}}} \left(\frac{\partial \tilde{\mathbf{U}}_b^w}{\partial \tilde{\mathbf{U}}_{ref}^w} - \frac{\partial \tilde{\mathbf{U}}_b^e}{\partial \tilde{\mathbf{U}}_{ref}^e} \right) = \mathbf{C}_1 \mathbf{C}_{2,ref}. \quad (4.14)$$

In the above, \mathbf{C}_1 relates to the uniform baseflow quantities and can be further evaluated as:

$$\mathbf{C}_1 = \left(\frac{\partial \tilde{\mathbf{Q}}}{\partial \tilde{\mathbf{U}}} \right)^{-1} \frac{\partial \hat{\mathbf{F}}}{\partial \tilde{\mathbf{Q}}} \frac{\partial \tilde{\mathbf{Q}}}{\partial \tilde{\mathbf{U}}} = \begin{pmatrix} u + c & -\frac{c^2}{\gamma(\gamma-1)S} & 0 \\ 0 & u & 0 \\ 0 & -\frac{c^2}{\gamma(\gamma-1)S} & u - c \end{pmatrix}, \quad (4.15)$$

which is similar to the Jacobian matrix $\partial \hat{\mathbf{F}} / \partial \tilde{\mathbf{Q}}$, and therefore the eigenvalues are the well-known $u + c$, u , and $u - c$. The remaining coefficient matrices are

$$\mathbf{C}_{2,int} = \frac{\partial \tilde{\mathbf{U}}_b^w}{\partial \tilde{\mathbf{U}}_{int}} - \frac{\partial \tilde{\mathbf{U}}_b^e}{\partial \tilde{\mathbf{U}}_{int}}, \quad (4.16)$$

$$\mathbf{C}_{2,\text{ref}} = \frac{\partial \tilde{\mathbf{U}}_{\text{b}}^{\text{w}}}{\partial \tilde{\mathbf{U}}_{\text{ref}}^{\text{w}}} - \frac{\partial \tilde{\mathbf{U}}_{\text{b}}^{\text{e}}}{\partial \tilde{\mathbf{U}}_{\text{ref}}^{\text{e}}}, \quad (4.17)$$

which contain the normalized coefficients about how the boundary condition will respond to the disturbance of the internal and reference states, respectively.

For the coefficient matrix \mathbf{C}_{int} , which originates from the hyperbolic conservation law system in Eq. (4.1), it can be diagonalised so that

$$\mathbf{C}_{\text{int}} = \mathbf{P}^{-1} \mathbf{\Lambda} \mathbf{P},$$

where $\mathbf{\Lambda} = \text{diag}(\lambda_i)$ ($i = 1, 2, 3$), and λ_i is its eigenvalue. If these eigenvalues are non-zero, the solution to Eq. (4.12) can be written as

$$\mathbf{P} \delta \tilde{\mathbf{U}}_{\text{int}}(t) = e^{\mathbf{\Lambda} t / \Delta x} \mathbf{P} \delta \tilde{\mathbf{U}}_{\text{int}}(0) + (\mathbf{I} - e^{\mathbf{\Lambda} t / \Delta x}) (-\mathbf{P} \mathbf{C}_{\text{int}}^{-1} \mathbf{C}_{\text{ref}}) \delta \tilde{\mathbf{U}}_{\text{ref}}. \quad (4.18)$$

For a stable solution to a well-posed problem, the initial disturbance on the internal state $\delta \tilde{\mathbf{U}}_{\text{int}}(0)$ in Eq. (4.18) should decay. Physically we understand that the disturbance waves will leave the domain through the boundaries without generating a stronger reflection, meanwhile the disturbance on the reference state enters the domain. The solution should exponentially converge to the reference value of the boundary conditions. This result is achieved if, and only if, the following conditions are satisfied

$$\begin{cases} \text{Re}(\lambda_i) < 0, \quad i = 1, 2, 3 \\ \mathbf{C}_{\text{ref}} = -\mathbf{C}_{\text{int}} \end{cases}. \quad (4.19)$$

The second condition is equivalent to a opposite relation for the second part of the coefficient matrices as

$$\mathbf{C}_{2,\text{ref}} = -\mathbf{C}_{2,\text{int}}. \quad (4.20)$$

If this condition is not satisfied, the solution will converge to

$$\delta \tilde{\mathbf{U}}_{\text{int}}(t \rightarrow \infty) = -\mathbf{C}_{2,\text{int}}^{-1} \mathbf{C}_{2,\text{ref}} \delta \tilde{\mathbf{U}}_{\text{ref}} \neq \delta \tilde{\mathbf{U}}_{\text{ref}}. \quad (4.21)$$

This solution fails to track the reference value, and therefore is not well-posed.

Another possible scenario is when \mathbf{C}_{int} is singular so that some eigenvalue is zero, e.g. $\lambda_i = 0$, the i -th component solution becomes

$$(\mathbf{P} \delta \tilde{\mathbf{U}}_{\text{int}}(t))_i = (\mathbf{P} \delta \tilde{\mathbf{U}}_{\text{int}}(0))_i + \left(\frac{1}{\Delta x} \mathbf{P} \mathbf{C}_{\text{ref}} \delta \tilde{\mathbf{U}}_{\text{ref}} \right)_i t. \quad (4.22)$$

This solution will grow or decay with time monotonously and finally diverge unless the entries in the i -th row of $\mathbf{P} \mathbf{C}_{\text{ref}}$ are all zero, inferring that \mathbf{C}_{ref} is also singular as \mathbf{P} has full rank. Under this condition the component solution is neutrally stable, which is accepted from the energy point of view since the disturbance will not further grow and thus the solution is bounded. However, its evolution is unrelated to the boundary conditions through the reference value. Since Eq. (4.12) is linearized from the discrete approximation given by Eq. (4.5), the failure to track the reference value further indicates the approximation is ill-posed through the boundary condition enforcement. Or alternatively, this neutral stability violates the uniqueness requirement for a well-posed steady state boundary value problem because both the steady state solution and the solution with the eigenfunction of the zero eigenvalue superimposed satisfy the boundary conditions.

According to the above analysis, the two requirements to form a stable system are provided by Eq. (4.19), based on the eigenvalue analysis of the coefficient matrices. We therefore next consider how the coefficient matrices are constructed for specific Riemann boundary conditions

4.2.2 Analysis for Riemann boundary condition

Having established the linear system, Eq. (4.12), relating the stability of the internal solution to the boundary conditions, we now need to construct the second part of coefficient matrices, $\mathbf{C}_{2,\text{int}}$ and $\mathbf{C}_{2,\text{ref}}$. Before doing so we first need to outline the characteristic treatment for Riemann boundary conditions.

To set up a Riemann boundary condition, a common practice is to construct the boundary state following the characteristic relations. Fig. 4.4 shows the characteristics (or characteristic curves) for the 1D Euler equations at a subsonic boundary ($x = 0$). For a subsonic inflow, the left state can be considered as the ghost state and two characteristics are pointing into the domain, indicating two conditions can be enforced, while the third conditions is provided by the solution within the domain (right state) related to the outwards-pointing characteristic. Since the Riemann invariants and entropy are constant along the characteristics, the following relations must be satisfied at the boundary

$$R_b^+ = R_l^+, \quad R_b^0 = R_l^0, \quad R_b^- = R_r^-, \quad (4.23)$$

where R^\pm denote the Riemann invariants, R^0 denotes the entropy, and subscript “l” and “r” denote the left (ghost) state and right (internal) state, respectively.

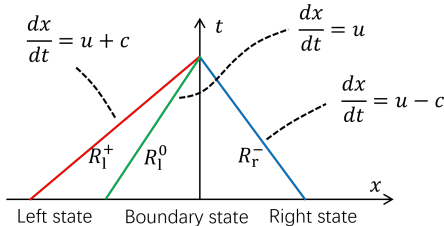


Figure 4.4: Characteristic lines for a subsonic boundary.

The simplest boundary condition one can enforce is to specify the reference state to be a given ghost state independent of the internal values (as is in Fig. 4.2.1) i.e.

$$\tilde{\mathbf{Q}}_{\text{ref}} = \tilde{\mathbf{Q}}_{\text{gho}}, \quad (4.24)$$

which leads to the so called Riemann inflow [129]. We will also refer to this boundary condition as an entropy-invariant compatible inflow in the current work since the entropy (as well as the other incoming Riemann invariant) are directly enforced on the boundary state by an exact Riemann solver.

Since this inflow boundary condition only enforces entropy and the incoming Riemann invariant, there is no guarantee for pressure compatibility with the outer solution. To complete the stability analysis, the boundary condition at the outflow also needs to be provided. In what follows we will enforce the invariant compatible

condition at the outflow in all of the following cases. This inflow-outflow combination, denoted by superscript SI , leads to the following coefficient matrices

$$\mathbf{C}_{2,int}^{SI} = \frac{\partial \tilde{\mathbf{U}}_b^w}{\partial \tilde{\mathbf{U}}_{int}} - \frac{\partial \tilde{\mathbf{U}}_b^e}{\partial \tilde{\mathbf{U}}_{int}} = \begin{pmatrix} 0 & 0 & 0 \\ 0 & 0 & 0 \\ 0 & 0 & 1 \end{pmatrix} - \begin{pmatrix} 1 & 0 & 0 \\ 0 & 1 & 0 \\ 0 & 0 & 0 \end{pmatrix} = \begin{pmatrix} -1 & 0 & 0 \\ 0 & -1 & 0 \\ 0 & 0 & 1 \end{pmatrix}, \quad (4.25)$$

$$\mathbf{C}_{2,ref}^{SI} = \frac{\partial \tilde{\mathbf{U}}_b^w}{\partial \tilde{\mathbf{U}}_{ref}} - \frac{\partial \tilde{\mathbf{U}}_b^e}{\partial \tilde{\mathbf{U}}_{ref}} = \begin{pmatrix} 1 & 0 & 0 \\ 0 & 1 & 0 \\ 0 & 0 & 0 \end{pmatrix} - \begin{pmatrix} 0 & 0 & 0 \\ 0 & 0 & 0 \\ 0 & 0 & 1 \end{pmatrix} = \begin{pmatrix} 1 & 0 & 0 \\ 0 & 1 & 0 \\ 0 & 0 & -1 \end{pmatrix}. \quad (4.26)$$

By substituting Eq. (4.25) and (4.26) into Eqs. (4.16) and (4.17), the coefficient matrices becomes

$$\mathbf{C}_{int}^{SI} = \mathbf{C}_1 \mathbf{C}_{2,int}^{SI} = \begin{pmatrix} -(c+u) & \frac{c^2}{\gamma(\gamma-1)S} & 0 \\ 0 & -u & 0 \\ 0 & \frac{c^2}{\gamma(\gamma-1)S} & -(c-u) \end{pmatrix} = -\mathbf{C}_{ref}^{SI}, \quad (4.27)$$

where the second condition in Eq. (4.19) is directly satisfied. The eigenvalues of \mathbf{C}_{int}^{SI} are $-(c+u)$, $-u$, and $-(c-u)$ while eigenvalues for \mathbf{C}_{ref}^{SI} are the same but negative values. The physical interpretation of these eigenvalues is that when the internal state is disturbed, the disturbance can be decomposed onto the three waves, which leave the domain at the speeds $c+u$, u , and $c-u$. The minus signs represent the decaying feature of the disturbances. On the other hand, if the reference state is disturbed, the disturbance can also be projected onto the waves that come into the domain at the positive speed $c+u$, u , and $c-u$. Since the eigenvalues for \mathbf{C}_{int}^{SI} are all negative, the first condition in Eq. (4.19) is also satisfied. Therefore, the solution to the linearized system in Eq. (4.12) is stable at the steady state using these boundary conditions.

Similarly, in the case where the baseflow is supersonic, $\mathbf{C}_{2,int}^{SI}$ and $\mathbf{C}_{2,ref}^{SI}$ read

$$\mathbf{C}_{2,int}^{SI} = \mathbf{0} - \mathbf{I} = -\mathbf{I}, \quad \mathbf{C}_{2,ref}^{SI} = \mathbf{I} - \mathbf{0} = \mathbf{I},$$

and therefore \mathbf{C}_{int}^{SI} has three negative the eigenvalues, i.e. $-(c+u)$, $-u$, and $-(u-c)$, inferring a stable boundary condition enforcement.

We note from inspecting Eqs. (4.25) and (4.26) that the following relations hold

$$\frac{\partial \tilde{\mathbf{U}}_b^w}{\partial \tilde{\mathbf{U}}_{int}} + \frac{\partial \tilde{\mathbf{U}}_b^w}{\partial \tilde{\mathbf{U}}_{ref}} = \mathbf{I}, \quad \frac{\partial \tilde{\mathbf{U}}_b^e}{\partial \tilde{\mathbf{U}}_{int}} + \frac{\partial \tilde{\mathbf{U}}_b^e}{\partial \tilde{\mathbf{U}}_{ref}} = \mathbf{I}, \quad (4.28)$$

and

$$\mathbf{C}_{2,int}^{SI} + \mathbf{C}_{2,ref}^{SI} = \mathbf{0}. \quad (4.29)$$

These relations are satisfied not only for the current boundary conditions but for all combinations including supersonic ones. This is because to construct the boundary state specific information should come from either internal state or reference state or both. The sum of the weight of contributions from both states should be one or zero depends on whether it is a diagonal entry, and form an identity matrix. Therefore the opposite condition in Eq. (4.19) (or (4.20)) is always satisfied by the Riemann boundary conditions, and the eigenvalues for $\mathbf{C}_{2,int}$ and $\mathbf{C}_{2,ref}$ are always equal and opposite numbers.

Although the opposite relation hold, we still distinguish \mathbf{C}_{int} and \mathbf{C}_{ref} since they are computed through different derivatives and this provides two different perspectives to examine if the boundary conditions enforcement leads to a stable system. In Eq. (4.12) if the disturbance on the reference state is not considered, it recovers the homogeneous dynamical system for conventional stability analysis

$$\frac{d}{dt} \left(\delta \tilde{\mathbf{U}}_{\text{int}} \right) = \frac{1}{\Delta x} \mathbf{C}_{\text{int}} \delta \tilde{\mathbf{U}}_{\text{int}}. \quad (4.30)$$

The stability of this system can be analyzed directly through the eigenvalues of \mathbf{C}_{int} . Alternatively, we can also examine the stability by constructing \mathbf{C}_{ref} and using the opposite relation.

A special case that is worth further discussion is when one or more eigenvalues in $\mathbf{C}_{2,\text{int}}$ (or equivalently in $\mathbf{C}_{2,\text{ref}}$) are zero. According to the analysis in the previous section, in this case the solution in Eq. (4.22) is neutrally stable but the original problem is ill-posed. The zero eigenvalues usually occur when the same reference quantity is enforced at both inflow and outflow boundaries. This quantity could then be over constrained and there will be some other quantify lacking a constraint. In the construction of the coefficient matrices, this appears in the form of cancellation of entries, leading to rank-deficiency. Further similar to this zero eigenvalue case is the situation where some eigenvalues are purely imaginary. The difference lies in that the zero eigenvalues arise from insufficient boundary conditions to a well-posed problem while the purely imaginary eigenvalues indicates that sufficient boundary conditions are enforced but in a neutrally stable manner. In addition, the zero eigenvalue may solely exist while the purely imaginary eigenvalues will naturally appear as a conjugate pair. In practice the neutrally stable solution will easily diverge as the numerical errors accumulate and the solution will drift even if restarted from a already converged steady state solution.

Similar to the analysis for strong boundary conditions by Darmofal et al. [129], the coefficient matrix $\mathbf{C}_{2,\text{int}}$ contains the reflection properties of the adopted boundary conditions. However, here, it is the component matrices $\partial \tilde{\mathbf{U}}_b^w / \partial \tilde{\mathbf{U}}_{\text{int}}$ and $\partial \tilde{\mathbf{U}}_b^e / \partial \tilde{\mathbf{U}}_{\text{int}}$ rather than $\mathbf{C}_{2,\text{int}}$ should be checked to avoid entry cancellations. The zeros of $(\partial \tilde{\mathbf{U}}_b^w / \partial \tilde{\mathbf{U}}_{\text{int}})_{13}$ and $(\partial \tilde{\mathbf{U}}_b^w / \partial \tilde{\mathbf{U}}_{\text{int}})_{23}$ show that the inflow boundary condition has no reflection to the internal disturbance, while the zeros at $(\partial \tilde{\mathbf{U}}_b^e / \partial \tilde{\mathbf{U}}_{\text{int}})_{31}$ and $(\partial \tilde{\mathbf{U}}_b^e / \partial \tilde{\mathbf{U}}_{\text{int}})_{32}$ indicate a non-reflective outflow. Therefore, the combination of entropy-invariant compatible inflow and invariant compatible outflow is fully non-reflective in the normal direction.

4.3 Stability analysis for pressure compatible sub-sonic Riemann inflow boundary conditions

We now analyzes the eigenvalues for \mathbf{C}_{int} to determine a stable pressure compatible inflow for the DG solver. Three possible candidates are constructed and their stability performances analyzed. We only examine the coefficient matrix \mathbf{C}_{int} since the opposite relation in Eq. (4.20) always holds.

4.3.1 Entropy-pressure compatible inflow

Neglecting the superscript “w”, the entropy-pressure compatible inflow at the west boundary in Fig. 4.2 is given by

$$p_b = p_{\text{ref}}, \quad S_b = S_{\text{ref}}, \quad (4.31)$$

which directly implies

$$\rho_b = \rho_{\text{ref}}, \quad c_b = c_{\text{ref}}. \quad (4.32)$$

The third condition which needs to be specified according to the characteristic relations in Eq. (4.23)

$$R_b^- = u_b - \frac{2}{\gamma - 1} c_b = R_{\text{int}}^-. \quad (4.33)$$

Then the boundary state velocity and right-propagating characteristic are computed as

$$u_b = R_{\text{int}}^- + \frac{2}{\gamma - 1} c_{\text{ref}}, \quad (4.34)$$

$$R_b^+ = u_b + \frac{2}{\gamma - 1} c_b = R_{\text{int}}^- + \frac{4}{\gamma - 1} c_{\text{ref}} = R_{\text{int}}^- + (R_{\text{ref}}^+ - R_{\text{ref}}^-). \quad (4.35)$$

Therefore, the boundary state Riemann variables take the form

$$\tilde{\mathbf{U}}_b = \begin{pmatrix} R_b^+ \\ R_b^0 \\ R_b^- \end{pmatrix} = \begin{pmatrix} R_{\text{int}}^- + R_{\text{ref}}^+ - R_{\text{ref}}^- \\ R_{\text{ref}}^0 \\ R_{\text{int}}^- \end{pmatrix}. \quad (4.36)$$

As mentioned earlier, using the invariant compatible Riemann outflow, the second part of coefficient matrix $\mathbf{C}_{\text{int}}^{SP}$ is

$$\mathbf{C}_{2,\text{int}}^{SP} = \frac{\partial \tilde{\mathbf{U}}_b^w}{\partial \tilde{\mathbf{U}}_{\text{int}}} - \frac{\partial \tilde{\mathbf{U}}_b^e}{\partial \tilde{\mathbf{U}}_{\text{int}}} = \begin{pmatrix} 0 & 0 & 1 \\ 0 & 0 & 0 \\ 0 & 0 & 1 \end{pmatrix} - \begin{pmatrix} 1 & 0 & 0 \\ 0 & 1 & 0 \\ 0 & 0 & 0 \end{pmatrix} = \begin{pmatrix} -1 & 0 & 1 \\ 0 & -1 & 0 \\ 0 & 0 & 1 \end{pmatrix}, \quad (4.37)$$

with which the eigenvalues for $\mathbf{C}_{\text{int}}^{SP}$ are

$$\lambda_1^{SP} = -(c + u), \quad \lambda_2^{SP} = -u, \quad \lambda_3^{SP} = -(c - u). \quad (4.38)$$

Since all of the eigenvalues are negative for subsonic flows, the combination of the entropy-pressure inflow and the invariable compatible outflow leads to a stable system.

It is worth noting that the entropy-pressure compatible inflow is able to enforce more conditions in multiple-dimensional cases, where the tangential velocity components are enforced by the reference state. The density compatibility in Eq. (4.34) makes the boundary state tangential momentum components also match the reference state.

4.3.2 Velocity-pressure compatible inflow

Following the same notation, the velocity-pressure compatible inflow satisfies

$$u_b = u_{\text{ref}}, \quad p_b = p_{\text{ref}}. \quad (4.39)$$

Then the boundary state density is computed using the left-pointing characteristic as

$$\rho_b = \gamma \left(\frac{2}{\gamma - 1} \right)^2 \frac{p_{\text{ref}}}{(u_{\text{ref}} - R_{\text{int}}^-)^2}. \quad (4.40)$$

Therefore, the boundary state characteristic variables are given by

$$R_b^+ = u_b + \frac{2}{\gamma - 1} c_b = 2u_{\text{ref}} - R_{\text{int}}^- = (R_{\text{ref}}^+ + R_{\text{ref}}^-) - R_{\text{int}}^-, \quad (4.41)$$

$$R_b^0 = \frac{p_b}{\rho_b^\gamma} = \left[\frac{(R_{\text{ref}}^+ + R_{\text{ref}}^-) - 2R_{\text{int}}^-}{R_{\text{ref}}^+ - R_{\text{ref}}^-} \right]^{2\gamma} R_{\text{ref}}^0, \quad (4.42)$$

which leads to

$$\begin{aligned} \mathbf{C}_{2,\text{int}}^{UP} &= \frac{\partial \tilde{\mathbf{U}}_b^w}{\partial \tilde{\mathbf{U}}_{\text{int}}} - \frac{\partial \tilde{\mathbf{U}}_b^e}{\partial \tilde{\mathbf{U}}_{\text{int}}} = \begin{pmatrix} 0 & 0 & -1 \\ 0 & 0 & -(\gamma - 1) \frac{c}{\rho^{\gamma-1}} \\ 0 & 0 & 1 \end{pmatrix} - \begin{pmatrix} 1 & 0 & 0 \\ 0 & 1 & 0 \\ 0 & 0 & 0 \end{pmatrix} \\ &= \begin{pmatrix} -1 & 0 & -1 \\ 0 & -1 & -(\gamma - 1) \frac{c}{\rho^{\gamma-1}} \\ 0 & 0 & 1 \end{pmatrix}, \end{aligned} \quad (4.43)$$

and the eigenvalues of $\mathbf{C}_{\text{int}}^{UP}$ are

$$\lambda_1^{UP} = -(c + u), \quad \lambda_{2,3}^{UP} = \pm \sqrt{-u(c - u)}, \quad (4.44)$$

where $\lambda_{2,3}^{UP}$ are purely imaginary for subsonic flows. The first order linear analysis, indicates that part of the internal disturbance will keep oscillating and therefore the velocity-pressure compatible inflow is not desirable for a steady state solution.

4.3.3 Momentum-pressure compatible inflow

Similarly, a momentum and velocity boundary state can be enforced by the conditions

$$\rho_b u_b = \rho_{\text{ref}} u_{\text{ref}}, \quad p_b = p_{\text{ref}}. \quad (4.45)$$

By introducing a auxiliary variable, η , the boundary state density, velocity, and speed of sound take the form

$$\rho_b = \eta^{-2} \rho_{\text{ref}}, \quad u_b = \eta^2 u_{\text{ref}}, \quad c_b = \eta c_{\text{ref}}, \quad (4.46)$$

where

$$\eta = \sqrt{\frac{u_b}{u_{\text{ref}}}} = \frac{1}{\gamma - 1} \frac{c_{\text{ref}}}{u_{\text{ref}}} - \sqrt{\left(\frac{1}{\gamma - 1} \frac{c_{\text{ref}}}{u_{\text{ref}}} \right)^2 + \frac{R_{\text{int}}^-}{u_{\text{ref}}}}. \quad (4.47)$$

Therefore, the boundary state characteristic variables are

$$R_b^+ = u_b + \frac{2}{\gamma - 1} c_b = \frac{\eta^2}{2} (R_{\text{ref}}^+ + R_{\text{ref}}^-) + \frac{\eta}{2} (R_{\text{ref}}^+ - R_{\text{ref}}^-), \quad (4.48)$$

$$R_b^0 = \eta^{2\gamma} R_{\text{ref}}^0. \quad (4.49)$$

The second part of coefficient matrix is therefore given by

$$\begin{aligned} \mathbf{C}_{2,\text{int}}^{MP} &= \frac{\partial \tilde{\mathbf{U}}_b^w}{\partial \tilde{\mathbf{U}}_{\text{int}}} - \frac{\partial \tilde{\mathbf{U}}_b^e}{\partial \tilde{\mathbf{U}}_{\text{int}}} = \begin{pmatrix} 0 & 0 & -2\frac{c+(\gamma-1)u}{c-(\gamma-1)u} \\ 0 & 0 & -2(\gamma-1)\frac{c^2}{\rho^{\gamma-1}[c-(\gamma-1)u]} \\ 0 & 0 & 1 \end{pmatrix} - \begin{pmatrix} 1 & 0 & 0 \\ 0 & 1 & 0 \\ 0 & 0 & 0 \end{pmatrix} \\ &= \begin{pmatrix} -1 & 0 & -2\frac{c+(\gamma-1)u}{c-(\gamma-1)u} \\ 0 & -1 & -2(\gamma-1)\frac{c^2}{\rho^{\gamma-1}[c-(\gamma-1)u]} \\ 0 & 0 & 1 \end{pmatrix}. \end{aligned} \quad (4.50)$$

Subsequently the eigenvalues of $\mathbf{C}_{\text{int}}^{MP}$ are

$$\lambda_1^{MP} = -(c+u), \quad \lambda_{2,3}^{MP} = \frac{\pm\sqrt{\sigma} - cu + c^2 + \gamma cu}{2(c+u-\gamma u)}, \quad (4.51)$$

where

$$\sigma = c^4 + 2(\gamma-3)c^3u + \gamma(\gamma+6)c^2u^2 - 3c^2u^2 + 4(1-\gamma^2)cu^3 + 4(\gamma-1)^2u^4. \quad (4.52)$$

Since the second and third eigenvalues have complicated expressions, their values are examined numerically at different subsonic Mach numbers Ma , as shown in Fig. 4.5. We observe that these two eigenvalues are always real and positive, leading to an unstable solution and so the adopted boundary conditions are unstable.

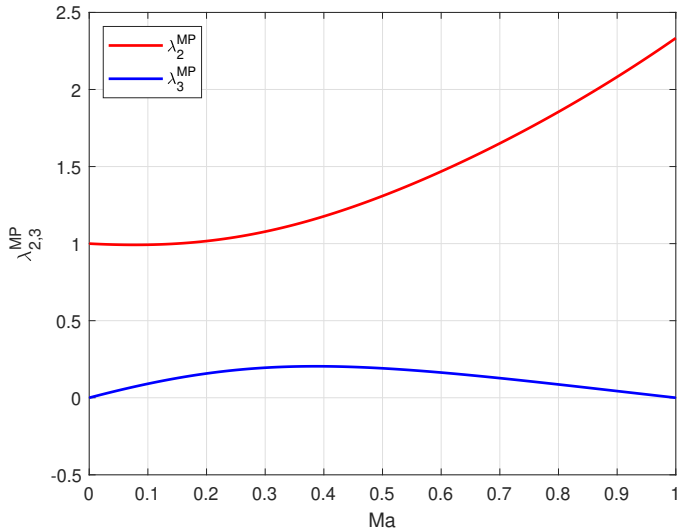


Figure 4.5: Variation of $\lambda_{2,3}^{MP}$ for subsonic flows.

4.4 Other types of stable subsonic inflows

In Section 4.3 we have constructed three types of inflow boundary condition where the pressure is compatible with the target reference state. However, we showed that only the entropy-pressure compatible one is stable. In this section, other two inflow boundary conditions, namely entropy-velocity compatible inflow and entropy-total enthalpy compatible inflow, are constructed with stability proved.

4.4.1 Entropy-velocity compatible inflow

The entropy-velocity compatible inflow enforces the corresponding quantities to the boundary states

$$S_b = S_{\text{ref}}, \quad u_b = u_{\text{ref}}. \quad (4.53)$$

Then using the $R_b^- = R_{\text{int}}^-$, the speed of sound at the boundary can be expressed by the characteristic variables as

$$c_b = \frac{\gamma - 1}{2} (u_b - R_{\text{int}}^-) = \frac{\gamma - 1}{4} (R_{\text{ref}}^+ + R_{\text{ref}}^- - 2R_{\text{int}}^-),$$

and the boundary state therefore reads

$$\tilde{\mathbf{U}}_b = \begin{pmatrix} R_b^+ \\ R_b^0 \\ R_b^- \end{pmatrix} = \begin{pmatrix} R_{\text{ref}}^+ + R_{\text{ref}}^- - R_{\text{int}}^- \\ R_{\text{ref}}^0 \\ R_{\text{int}}^- \end{pmatrix}. \quad (4.54)$$

We can use the above expression to obtain the second part of coefficient matrix

$$\mathbf{C}_{2,\text{int}}^{SV} = \frac{\partial \tilde{\mathbf{U}}_b^w}{\partial \tilde{\mathbf{U}}_{\text{int}}} - \frac{\partial \tilde{\mathbf{U}}_b^e}{\partial \tilde{\mathbf{U}}_{\text{int}}} = \begin{pmatrix} 0 & 0 & -1 \\ 0 & 0 & 0 \\ 0 & 0 & 1 \end{pmatrix} - \begin{pmatrix} 1 & 0 & 0 \\ 0 & 1 & 0 \\ 0 & 0 & 0 \end{pmatrix} = \begin{pmatrix} -1 & 0 & -1 \\ 0 & -1 & 0 \\ 0 & 0 & 1 \end{pmatrix}, \quad (4.55)$$

Subsequently the eigenvalues of $\mathbf{C}_{\text{int}}^{SV}$ are

$$\lambda_1^{SV} = -(c + u), \quad \lambda_2^{SV} = -u, \quad \lambda_3^{SV} = -(c - u) \quad (4.56)$$

which are all negative inferring a stable boundary condition enforcement.

4.4.2 Entropy-total enthalpy compatible inflow

The entropy-total enthalpy compatible inflow boundary condition is another stable condition enforcing reasonable quantities

$$S_b = S_{\text{ref}}, \quad H_b = H_{\text{ref}}. \quad (4.57)$$

where $H = \frac{\gamma}{\gamma-1} \frac{p}{\rho} + \frac{1}{2} u^2$ is the total enthalpy. Together with $R_b^- = R_{\text{int}}^-$, this solves the velocity and speed of sound on the boundary

$$\begin{aligned} u_b &= \frac{r-1}{r+1} R_{\text{int}}^- + \frac{\sqrt{2}}{r+1} \sqrt{(1-\gamma)R_{\text{int}} + (1+\gamma)\sigma}, \\ c_b &= -\frac{r-1}{r+1} R_{\text{int}}^- + \frac{r-1}{\sqrt{2}(r+1)} \sqrt{(1-\gamma)R_{\text{int}} + (1+\gamma)\sigma}, \end{aligned}$$

where

$$\sigma = u_{\text{ref}}^2 + \frac{2}{\gamma-1} c_{\text{ref}}^2 = \frac{\gamma+1}{8} (R_{\text{ref}}^+)^2 + \frac{\gamma+1}{8} (R_{\text{ref}}^-)^2 + \frac{3-\gamma}{4} R_{\text{ref}}^+ R_{\text{ref}}^-.$$

We then have the characteristic variable

$$R_b^+ = \frac{r-3}{r+1} R_{\text{int}}^- + \frac{2\sqrt{2}}{r+1} \sqrt{(1-\gamma)R_{\text{int}} + (1+\gamma)\sigma}. \quad (4.58)$$

and second part of coefficient matrix consequently calculated as

$$\mathbf{C}_{2,\text{int}}^{SH} = \frac{\partial \tilde{\mathbf{U}}_b^w}{\partial \tilde{\mathbf{U}}_{\text{int}}} - \frac{\partial \tilde{\mathbf{U}}_b^e}{\partial \tilde{\mathbf{U}}_{\text{int}}} = \begin{pmatrix} -1 & 0 & \frac{\gamma-3}{\gamma-1} - \frac{2}{\gamma+1} \frac{(\gamma-1)u-2c}{u+c} \\ 0 & -1 & 0 \\ 0 & 0 & 1 \end{pmatrix}, \quad (4.59)$$

$\mathbf{C}_{\text{int}}^{SH}$ finally has the eigenvalues

$$\lambda_1^{SH} = -(c+u), \quad \lambda_2^{SH} = -u, \quad \lambda_3^{SH} = -(c-u) \quad (4.60)$$

which are also as ideal as the Riemann boundary condition.

4.5 Stability analysis of inflow entropy modification

In Section 4.3 we demonstrated that the only stable inflow boundary condition among the three candidates is the entropy-pressure compatible one. The similarity it shared with the entropy-invariant compatible inflow is that the boundary state entropy is kept the same as the reference state value. Using the similar method, density-velocity, entropy-velocity, and entropy-total enthalpy compatible inflows are constructed and examined, as provided in Section 4.4 for the last two. The stability analysis result of these inflow boundary conditions are listed in Table. 4.5. Similarly, the entropy compatible conditions have negative eigenvalues for \mathbf{C}_{int} while the others suffer stability issues from non-negative eigenvalues. These observations imply the entropy is a essential quantity, and violating entropy compatibility is likely to cause problems. We therefore provide more detailed analysis for entropy modification at inflow.

Table 4.2: Stability for different inflow boundary conditions

	Inflow compatibility	Outflow compatibility	Stability
1	Entropy-invariant	Invariant	✓
2	Entropy-pressure	Invariant	✓
3	Velocity-pressure	Invariant	✗
4	Momentum-pressure	Invariant	✗
5	Entropy-velocity	Invariant	✓
6	Density-velocity	Invariant	✗
7	Entropy-total enthalpy	Invariant	✓

We continue to follow the setting in Fig. 4.2 where the west boundary is the inflow, and again the invariant compatible outflow at the east boundary is adopted. Since only the outward-propagating Riemann invariant may be used to construct the boundary state at the inflow, the second part coefficient matrix takes the form

$$\mathbf{C}_{2,\text{int}} = \frac{\partial \tilde{\mathbf{U}}_b^w}{\partial \tilde{\mathbf{U}}_{\text{int}}} - \frac{\partial \tilde{\mathbf{U}}_b^e}{\partial \tilde{\mathbf{U}}_{\text{int}}} = \begin{pmatrix} 0 & 0 & a \\ 0 & 0 & b \\ 0 & 0 & 1 \end{pmatrix} - \begin{pmatrix} 1 & 0 & 0 \\ 0 & 1 & 0 \\ 0 & 0 & 0 \end{pmatrix} = \begin{pmatrix} -1 & 0 & a \\ 0 & -1 & b \\ 0 & 0 & 1 \end{pmatrix}, \quad (4.61)$$

where a and b are entries representing the contribution of the internal state. Then the characteristic polynomial for the coefficient matrix is

$$[\lambda + (c + u)] \left\{ \lambda^2 + \left[c + \frac{c^2}{\gamma(\gamma - 1)S} b \right] \lambda + u(c - u) \right\} = 0, \quad (4.62)$$

where $\lambda_1 = -(c + u)$ is always negative and $\lambda_{2,3}$ normalized by speed of sound are given by

$$\bar{\lambda}_{2,3} = \frac{\lambda_{2,3}}{c} = \frac{-d \pm \sqrt{d^2 - \hat{\beta}}}{2}, \quad (4.63)$$

where $Ma = u/c$ is the Mach number, $\hat{\beta} = 4Ma(1 - Ma)$ is always a positive parameter for subsonic flows, d is a normalized parameter

$$d = 1 + \frac{c}{\gamma(\gamma - 1)S} b. \quad (4.64)$$

Eqs. (4.63) and (4.64) show that $\lambda_{2,3}$ are only related to the entry b while the entry a has nothing to do with stability. This allows the boundary state Riemann invariant R_b^+ to be modified as desired without introducing any singularity to the system. On the other hand, the modification of the boundary state entropy R_b^0 needs to follow some restrictions. From Eq. (4.63) we can tell that the normalized real part of $\lambda_{2,3}$ is always negative for subsonic flows at $d > 0$. This point is more clearly shown in Fig. 4.6 where $\lambda_{2,3}$ changes with d at different Mach numbers. The right branches of the curves lead to negative real parts, corresponding to

$$b > -\frac{\gamma(\gamma - 1)S}{c}, \quad (4.65)$$

which needs to be satisfied for the boundary state entropy modification. Since the boundary state entropy equals to the ghost state entropy for an inflow boundary condition, Eq. (4.65) is essentially the requirement to design the ghost state.

There are two special cases. If $b = 0$, the eigenvalues recover the ideal values as $\lambda_2 = -u$ and $\lambda_3 = -(c - u)$, which is the case for all the entropy compatible inflow. This indicates that as long as the entropy compatibility is satisfied at inflow, another inflow compatible quantity can be chosen whilst maintaining a stable system. The other case is when $b = -\gamma(\gamma - 1)S/c$, which is the case for the velocity-pressure compatible Riemann inflow, $\lambda_{2,3}$ are purely imaginary conjugates, leading to oscillating disturbances.

4.6 Further discussion

4.6.1 Physical explanation of unstable Riemann boundary condition

In the previous sections, several subsonic inflow boundary conditions have been constructed while some of them are unstable, and the entropy compatibility is proved to be critical for stability. It is then interesting to question the cause for the instability for the better understanding.

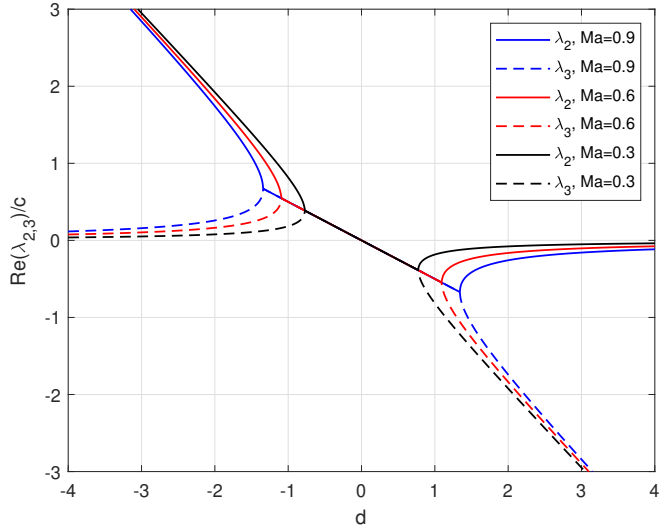


Figure 4.6: Normalized real part of $\lambda_{2,3}$ changing with parameter d at different three Mach numbers: $Ma = 0.3$ (black), 0.6 (red), and 0.9 (blue). The solid line represents λ_2 and the dashed line represents λ_3 .

We consider the instability arise from the Riemann solver, or equivalently the characteristic treatment. Here we provide an explanation beyond the clues in Section 4.2. When the boundary condition is enforced weakly through numerical flux based on the characteristic treatment, only the reverse-flow-direction propagating (i.e. outward-propagating for an inflow) characteristic from the internal state will be selected to construct the boundary state (or equivalently to construct the numerical flux) for whatever other quantities to be enforced on the boundary state. Therefore only the third column of the first matrix in Eq. (4.61) is non zero and its last entry is 1. Due to the complexity of the entropy expression, the flow quantity enforcement induced entropy modification must be restricted for a stable inflow.

Additionally, if the boundary state for numerical flux is not constructed based on characteristic treatment in the Weak-Prescribed approach, e.g. $\mathbf{R}_{\text{int}}^+$ and $\mathbf{R}_{\text{int}}^0$ are also used to obtain the boundary state, the previous unstable boundary conditions might be stable. This is could be the reason why different types of non-Riemann boundary conditions are stable, such as the mass flow rate-total temperature compatible inflow [133] and etc. However, further analysis is not performed since it is beyond the scope of current work. But it can be easily finished following exactly the same approach in this chapter by only modifying the expression of the boundary state.

4.6.2 Applicability: local analysis vs. global analysis

In the previous sections we have developed a linear stability analysis method for the boundary condition. Ideally this method can be applied for all numerical flux based discretisations although we have adopted the minimal system for simplicity and generality. However, the applicability of the method is worthy to be discussed.

In the analysis in Section 4.2 a single element is used with the Riemann invariant compatible outflow. This analysis studies the very first element in the upstream direction to examine the stability of the inflow boundary condition. It is therefore

a local analysis. The local stability is the necessary but not sufficient condition for the stable simulation, i.e. the global stability. Here we provide an example using a three-element system on the top of Fig. 4.6.2 with the entropy-pressure compatible inflow and pressure outflow adopted.

For Element 1 (E1), it has the entropy-pressure compatible inflow and Riemann invariant compatible outflow, and it is stable as proved in Section 4.3.1. Element 2 (E2) has Riemann inflow and outflow, and the combination of which also locally stabilize the solution. As for Element 3 (E3), the local boundary conditions are Riemann-invariant compatible inflow and pressure outflow. As mentioned in Section 2.5, the pressure outflow extrapolates the velocity and density and enforces the reference pressure on the ghost state

$$\mathbf{W}_{\text{gho}}^e = \begin{pmatrix} \rho_{\text{int}} \\ u_{\text{int}} \\ p_{\text{ref}} \end{pmatrix}, \quad (4.66)$$

where $\mathbf{W}_{\text{gho}}^e$ is the ghost state vector of primitive variables for the outflow boundary of Element 3. Then at this boundary the inward-propagating characteristic is calculated by

$$\begin{aligned} R_b^- = R_{\text{gho}}^- &= u_{\text{int}} - \frac{2}{\gamma - 1} \sqrt{\frac{\gamma p_{\text{ref}}}{\rho_{\text{int}}}} \\ &= \frac{1}{2} (R_{\text{int}}^+ + R_{\text{int}}^-) - \frac{2}{\gamma - 1} \sqrt{\gamma p_{\text{ref}}} \left[\left(\frac{\gamma - 1}{4} \right)^2 \frac{1}{\gamma} \right]^{-\frac{1}{2(\gamma-1)}} \left[\frac{(R_{\text{int}}^+ - R_{\text{int}}^-)^2}{R_{\text{int}}^0} \right]^{-\frac{1}{2(\gamma-1)}}, \end{aligned} \quad (4.67)$$

which leads to the following matrix

$$\frac{\partial \tilde{\mathbf{U}}_b^e}{\partial \tilde{\mathbf{U}}_{\text{int}}} \Big|^{P_o} = \begin{pmatrix} 1 & 0 & 0 \\ 0 & 1 & 0 \\ \frac{1}{2} + \frac{1}{2(\gamma-1)} & -\frac{1}{(\gamma-1)^2} \frac{c}{S} & \frac{1}{2} - \frac{1}{2(\gamma-1)} \end{pmatrix}, \quad (4.68)$$

where the superscript P_o denotes the pressure outflow. This matrix is used to construct the second part of the coefficient matrix which reads

$$\mathbf{C}_{2,\text{int}}^{E3} = \frac{\partial \tilde{\mathbf{U}}_b^w}{\partial \tilde{\mathbf{U}}_{\text{int}}} \Big|^{SI} - \frac{\partial \tilde{\mathbf{U}}_b^e}{\partial \tilde{\mathbf{U}}_{\text{int}}} \Big|^{P_o} = \begin{pmatrix} -1 & 0 & 0 \\ 0 & -1 & 0 \\ -\frac{1}{2} - \frac{1}{2(\gamma-1)} & \frac{1}{(\gamma-1)^2} \frac{c}{S} & \frac{1}{2} + \frac{1}{2(\gamma-1)} \end{pmatrix}. \quad (4.69)$$

We obtain the following eigenvalues of $\mathbf{C}_{\text{int}}^{E3}$

$$\lambda_1^{E3} = -(c + u), \quad \lambda_2^{E3} = -u, \quad \lambda_3^{E3} = -\frac{\gamma}{2(\gamma - 1)}(c - u). \quad (4.70)$$

Since all of the above eigenvalues are negative for subsonic flows, the local system for Element 3 is stable as well. Therefore the local analysis shows that all the elements have a stable solution inside. However, it is expected that the entropy-pressure compatible and pressure outflow cannot well-pose the simulation in 1D since the pressure is over-enforced while the velocity is out of constrain, which is demonstrated next from the global point of view.

The global linear system is constructed to have the similar form as Eq. (4.12)

$$\frac{d}{dt} \left(\delta \tilde{\mathbf{U}}_{\text{int}}^* \right) = \frac{1}{\Delta x} \mathbf{C}_{\text{int}}^* \delta \tilde{\mathbf{U}}_{\text{int}}^* + \frac{1}{\Delta x} \mathbf{C}_{\text{ref}}^* \delta \tilde{\mathbf{U}}_{\text{ref}}^* \quad (4.71)$$

where

$$\mathbf{U}_{\text{int}}^* = \begin{pmatrix} \mathbf{U}_{\text{int}}^1 \\ \mathbf{U}_{\text{int}}^2 \\ \mathbf{U}_{\text{int}}^3 \end{pmatrix}, \quad \mathbf{U}_{\text{ref}}^* = \begin{pmatrix} \mathbf{U}_{\text{ref}}^w \\ \mathbf{0} \\ \mathbf{U}_{\text{ref}}^e \end{pmatrix}, \quad (4.72)$$

$$\mathbf{C}_{\text{int}}^* = \begin{pmatrix} \mathbf{C}_{\text{int}}^{\text{E}1} & \mathbf{C}_{\text{ref}}^{\text{E}1,e} & \mathbf{0} \\ \mathbf{C}_{\text{ref}}^{\text{E}2,w} & \mathbf{C}_{\text{int}}^{\text{E}2} & \mathbf{C}_{\text{ref}}^{\text{E}2,e} \\ \mathbf{0} & \mathbf{C}_{\text{ref}}^{\text{E}3,w} & \mathbf{C}_{\text{int}}^{\text{E}3} \end{pmatrix}, \quad \mathbf{C}_{\text{ref}}^* = \begin{pmatrix} \mathbf{C}_{\text{ref}}^{\text{E}1,w} & \mathbf{0} & \mathbf{0} \\ \mathbf{0} & \mathbf{0} & \mathbf{0} \\ \mathbf{0} & \mathbf{0} & \mathbf{C}_{\text{int}}^{\text{E}3,e} \end{pmatrix}. \quad (4.73)$$

In the above, $\mathbf{C}_{\text{int}}^*$ is the 9×9 coefficient matrix and its eigenfunction reads

$$\lambda(\lambda - u)^3 \mathcal{P}^5(\lambda) = 0, \quad (4.74)$$

where $\mathcal{P}^5(\lambda)$ is a fifth-order polynomial of λ , and its detailed expression is given in B.3. It is clear there is an eigenvalue equal to zero while the rest have negative real parts as shown in Fig. 4.6.2, inferring the problem is ill-posed by the current boundary condition enforcement although the local analysis indicates a stable system in each of the elements. In contrast, in the three-element system if the Riemann inflow and outflow are adopted, one finds the ideal negative eigenvalues

$$\lambda_{1,2,3} = -u, \quad \lambda_{4,5,6} = -(c - u), \quad \lambda_{7,8,9} = -(c + u).$$

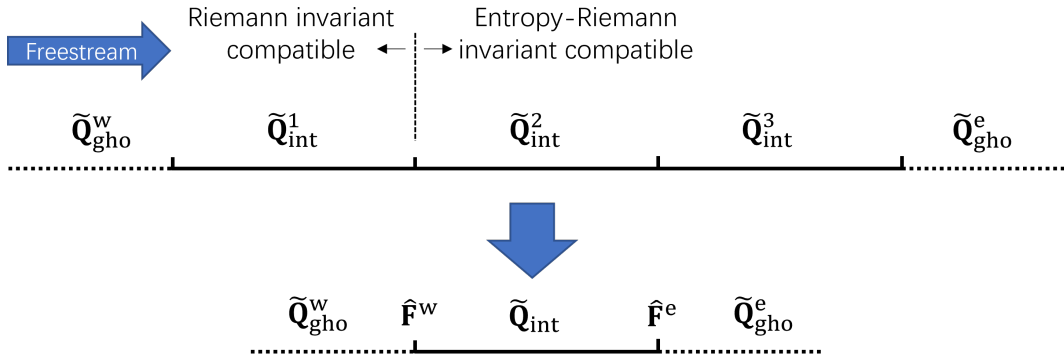


Figure 4.7: Global analysis and local analysis.

According to the above example we showed that the single element analysis examine the performance of a boundary condition locally. This kind of analysis seems only provides a useful necessary condition but the sufficiency for a good simulation is not guaranteed. However, the single element analysis is not necessarily performed locally but can also performed globally. We prove this by considering the system transformation shown in Fig. 4.6.2 where the whole computational domain is approximated by an single element with the entropy-pressure compatible inflow and pressure outflow boundary condition enforced on the west and east boundaries respectively.

In this case the second part of the coefficient matrix is constructed by

$$\mathbf{C}_{2,\text{int}} = \frac{\partial \tilde{\mathbf{U}}_{\text{b}}^w}{\partial \tilde{\mathbf{U}}_{\text{int}}} \Big|^{SP} - \frac{\partial \tilde{\mathbf{U}}_{\text{b}}^e}{\partial \tilde{\mathbf{U}}_{\text{int}}} \Big|^{Po} = \begin{pmatrix} -1 & | & 0 & | & 1 \\ 0 & | & -1 & | & 0 \\ -\frac{1}{2} - \frac{1}{2(\gamma-1)} & | & \frac{1}{(\gamma-1)^2} \frac{c}{S} & | & \frac{1}{2} + \frac{1}{2(\gamma-1)} \end{pmatrix}, \quad (4.75)$$

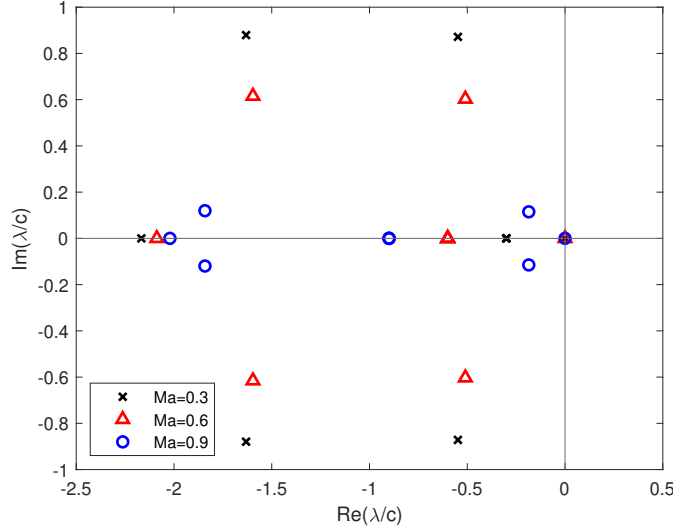


Figure 4.8: Eigenvalues at $Ma = 0.3, 0.6, 0.9$ for global analysis of the three-element system with entropy-pressure compatible inflow and pressure outflow.

where the rank-deficit is easily noticed. Therefore there must be a eigenvalue equal to zero for the coefficient matrix \mathbf{C}_{int} , and the system is ill-posed as is shown in the previous global analysis.

4.7 Ill-posedness for entropy-pressure inflow at the presence of a stagnation point

In the previous sections, the 1D eigenvalue analysis based on a steady and uniform baseflow shows that the entropy-pressure compatible inflow together with invariant compatible outflow leads to a stable system. However, multi-dimensional numerical tests highlight the emergence of a divergent solution for an inviscid simulations and strong oscillations appearing in viscous simulations. The divergence and oscillations are observed to initiate in the region of the stagnation point, for example at the leading edge of an aerofoil (see Section 4.8). To understand this issue, we analyse a standard 2D squared domain ($\Omega = (x_1, x_2) \in [-1, 1] \otimes [-1, 1]$), where wall boundary condition are imposed on one of the boundaries. Due to the presence of the wall, the baseflow of the linearized system can no longer be assumed uniform, which is obviously a key difference compared with the previous 1D analysis.

4.7.1 Linearized DG approximation for 2D Euler equations

Fig. 4.9 schematically shows a representative squared domain with associated boundary conditions in two cases with (a) and without (b) a stagnation point on the right wall. We next construct a 2D linearized system using the DG approximation of the 2D Euler equations, which take the conservation form

$$\frac{\partial \mathbf{Q}}{\partial t} + \frac{\partial \mathbf{F}_1(\mathbf{Q})}{\partial x_1} + \frac{\partial \mathbf{F}_2(\mathbf{Q})}{\partial x_2} = \mathbf{0}, \quad (4.76)$$

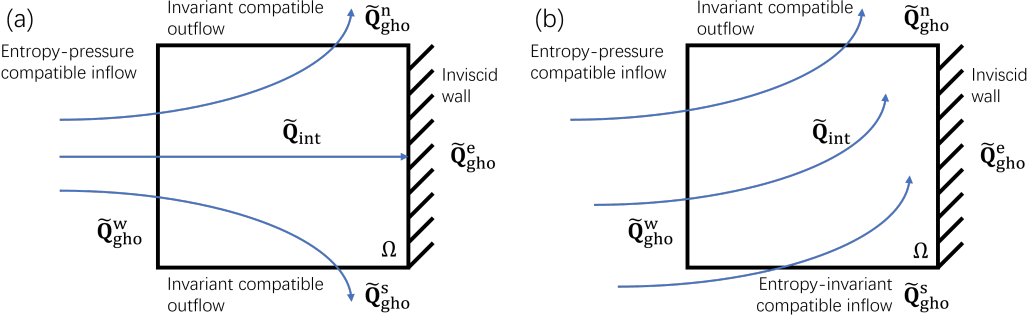


Figure 4.9: Baseflow and boundary conditions for 2D stability analysis near to a wall: (a) with a stagnation point and (b) without a stagnation point.

where \mathbf{Q} is the state vector of 2D conservative variables, \mathbf{F}_1 and \mathbf{F}_2 are the vectors of the inviscid flux

$$\mathbf{Q} = \begin{pmatrix} \rho \\ \rho u_1 \\ \rho u_2 \\ E \end{pmatrix}, \quad \mathbf{F}_1 = \begin{pmatrix} \rho u_1 \\ \rho u_1^2 + p \\ \rho u_1 u_2 \\ u_1(E + p) \end{pmatrix}, \quad \mathbf{F}_2 = \begin{pmatrix} \rho u_2 \\ \rho u_1 u_2 \\ \rho u_2^2 + p \\ u_2(E + p) \end{pmatrix}. \quad (4.77)$$

In the above, u_1 and u_2 are the velocity components in the x_1 and x_2 -directions, respectively, and $E = \frac{1}{\gamma-1}p + \frac{1}{2}\rho(u_1^2 + u_2^2)$. Others symbols are the same as in Eq. (4.1).

Following a similar analysis as performed in Section 4.2.1 and B.1, the domain Ω is approximated by a single quadrilateral DG element as

$$\int_{\Omega} \phi \frac{\partial \mathbf{Q}}{\partial t} d\Omega + \int_{\Gamma} \phi (\hat{\mathbf{F}} \cdot \mathbf{n}) d\Gamma - \int_{\Omega} \nabla \phi \cdot \mathbf{F} d\Omega = \mathbf{0}, \quad (4.78)$$

where $\Gamma = \partial\Omega$ is the boundary of the domain, $\mathbf{F} = (\mathbf{F}_1, \mathbf{F}_2)^T$ is the block vector for inviscid flux [76] while $\hat{\mathbf{F}} = (\hat{\mathbf{F}}_1, \hat{\mathbf{F}}_2)^T$ is the corresponding block vector of numerical inviscid fluxes.

The expanded form of Eq. (4.78) on the squared domain in Fig. 4.9(a) reads

$$\int_{\Omega} \phi \frac{\partial \mathbf{Q}}{\partial t} d\Omega = \int_{\Gamma^w} \phi \hat{\mathbf{F}}_1^w dx_2 - \int_{\Gamma^e} \phi \hat{\mathbf{F}}_1^e dx_2 + \int_{\Gamma^s} \phi \hat{\mathbf{F}}_2^s dx_1 - \int_{\Gamma^n} \phi \hat{\mathbf{F}}_2^n dx_1 + \int_{\Omega} \nabla \phi \cdot \mathbf{F} d\Omega, \quad (4.79)$$

where the subscript “n” and “s” denote north and south, respectively. Due to the presence of the wall the baseflow is no longer uniform so that a two-dimensional approximation of the following form is considered

$$\mathbf{Q} \simeq \sum_{p=0}^{N_{P_1}} \sum_{q=0}^{N_{P_2}} \hat{\mathbf{Q}}_{pq}(t) \phi_{pq}(x_1, x_2), \quad \phi_{pq}(x_1, x_2) = \phi_p(x_1) \phi_q(x_2), \quad (4.80)$$

where N_{P_1} and N_{P_2} are expansion order in the orthogonal directions, and typically are set to be equal to each other $N_{P_1} = N_{P_2} = N_P$. In the following analysis we choose to adopt a Lagrange nodal basis function for both ϕ_p and ϕ_q of the form

$$\phi_p(x) = \begin{cases} 1, & x = x_p, \\ \frac{(x - 1)(x + 1)L'_P(x)}{P(P + 1)L_P(x_p)(x_p - x)}, & \text{otherwise,} \end{cases} \quad 0 \leq p \leq N_P, \quad (4.81)$$

where x_p represents the Gauss-Lobatto-Legendre points including both end-points of the interval. For clarity, we use the semi-discrete form by only numerically integrating the boundary terms

$$\begin{aligned} \int_{\Omega} \phi \frac{\partial \mathbf{Q}_{\text{int}}}{\partial t} d\Omega &= \sum_{i=0}^{N_P} \phi w_i \widehat{\mathbf{F}}_{1,i}^w \left(\widetilde{\mathbf{Q}}_{\text{ref},i}^w, \widetilde{\mathbf{Q}}_{\text{int},i}^w \right) - \sum_{i=0}^{N_P} \phi w_i \widehat{\mathbf{F}}_{1,i}^e \left(\widetilde{\mathbf{Q}}_{\text{ref},i}^e, \widetilde{\mathbf{Q}}_{\text{int},i}^e \right) \\ &\quad + \sum_{i=0}^{N_P} \phi w_i \widehat{\mathbf{F}}_{2,i}^s \left(\widetilde{\mathbf{Q}}_{\text{ref},i}^s, \widetilde{\mathbf{Q}}_{\text{int},i}^s \right) - \sum_{i=0}^{N_P} \phi w_i \widehat{\mathbf{F}}_{2,i}^n \left(\widetilde{\mathbf{Q}}_{\text{ref},i}^n, \widetilde{\mathbf{Q}}_{\text{int},i}^n \right) \quad (4.82) \\ &\quad + \int_{\Omega} \nabla \phi \cdot \mathbf{F} d\Omega, \end{aligned}$$

where the numerical flux going through the wall, $\widehat{\mathbf{F}}_{1,i}^e$, is constructed using the internal state and no-penetration condition provided through the reference state $\widetilde{\mathbf{Q}}_{\text{ref},i}^e$. Since the no-penetration condition, or $\widetilde{\mathbf{Q}}_{\text{ref},i}^e$, is unrelated with the outer simulation, it is not disturbed and therefore in the linearized system the disturbance on the reference state for the east boundary is zero. Moreover, the last term in Eq. (4.82) is volumic flux integral where only the internal state is involved. The above leads to that the contribution by the reference state disturbances have two terms fewer than the contribution by the internal state disturbances.

To construct the 2D linearized system with normalized and neat coefficients, the following variables are introduced

$$\mathbf{V} = \left(\frac{2}{\gamma-1} c, \ u_1, \ u_2, \ S \right)^T, \quad (4.83)$$

which are referred to as quasi-characteristic variables since their linear combinations give the 1D characteristic variables in Eq. (4.11). The subsequent linear system for Fig. 4.9(a) takes the form (see B.2 for details)

$$\int_{\Omega} \phi \frac{\partial \mathbf{Q}}{\partial \mathbf{V}} \frac{\partial (\delta \mathbf{V}_{\text{int}})}{\partial t} d\Omega = RHS_{\text{int}} \left(\widehat{\mathbf{V}}, \delta \widehat{\mathbf{V}}_{\text{int}} \right) + RHS_{\text{ref}} \left(\widehat{\mathbf{V}}, \delta \widehat{\mathbf{V}}_{\text{ref}} \right), \quad (4.84)$$

where the contributions by internal state disturbances and reference state disturbances are respectively included in the right-hand side terms RHS_{int} and RHS_{ref} , are given by

$$\begin{aligned} RHS_{\text{int}} \left(\widehat{\mathbf{V}}, \delta \widehat{\mathbf{V}}_{\text{int}} \right) &= \\ &\sum_{i=0}^P \phi w_i \left[\frac{\partial \widehat{\mathbf{F}}_{1,i}^w}{\partial \widetilde{\mathbf{Q}}_{b,i}^w} \frac{\partial \widetilde{\mathbf{Q}}_{b,i}^w}{\partial \widetilde{\mathbf{V}}_{b,i}^w} \frac{\partial \widetilde{\mathbf{V}}_{b,i}^w}{\partial \widetilde{\mathbf{V}}_{\text{int},i}^w} \delta \widetilde{\mathbf{V}}_{\text{int},i}^w \right] - \sum_{i=0}^P \phi w_i \left[\frac{\partial \widehat{\mathbf{F}}_{1,i}^e}{\partial \widetilde{\mathbf{Q}}_{b,i}^e} \frac{\partial \widetilde{\mathbf{Q}}_{b,i}^e}{\partial \widetilde{\mathbf{V}}_{b,i}^e} \frac{\partial \widetilde{\mathbf{V}}_{b,i}^e}{\partial \widetilde{\mathbf{V}}_{\text{int},i}^e} \delta \widetilde{\mathbf{V}}_{\text{int},i}^e \right] \\ &\quad + \sum_{i=0}^P \phi w_i \left[\frac{\partial \widehat{\mathbf{F}}_{1,i}^s}{\partial \widetilde{\mathbf{Q}}_{b,i}^s} \frac{\partial \widetilde{\mathbf{Q}}_{b,i}^s}{\partial \widetilde{\mathbf{V}}_{b,i}^s} \frac{\partial \widetilde{\mathbf{V}}_{b,i}^s}{\partial \widetilde{\mathbf{V}}_{\text{int},i}^s} \delta \widetilde{\mathbf{V}}_{\text{int},i}^s \right] - \sum_{i=0}^P \phi w_i \left[\frac{\partial \widehat{\mathbf{F}}_{1,i}^n}{\partial \widetilde{\mathbf{Q}}_{b,i}^n} \frac{\partial \widetilde{\mathbf{Q}}_{b,i}^n}{\partial \widetilde{\mathbf{V}}_{b,i}^n} \frac{\partial \widetilde{\mathbf{V}}_{b,i}^n}{\partial \widetilde{\mathbf{V}}_{\text{int},i}^n} \delta \widetilde{\mathbf{V}}_{\text{int},i}^n \right] \\ &\quad + \int_{\Omega} \nabla \phi \cdot \frac{\partial \mathbf{F}}{\partial \mathbf{Q}} \frac{\partial \mathbf{Q}}{\partial \mathbf{V}} \delta \mathbf{V}_{\text{int}} d\Omega, \quad (4.85) \end{aligned}$$

and

$$\begin{aligned}
RHS_{\text{ref}} \left(\tilde{\mathbf{V}}, \delta \tilde{\mathbf{V}}_{\text{ref}} \right) = & \\
\sum_{i=0}^P \phi w_i \left[\frac{\partial \widehat{\mathbf{F}}_{1,i}^w}{\partial \tilde{\mathbf{Q}}_{b,i}^w} \frac{\partial \tilde{\mathbf{Q}}_{b,i}^w}{\partial \tilde{\mathbf{V}}_{b,i}^w} \frac{\partial \tilde{\mathbf{V}}_{b,i}^w}{\partial \tilde{\mathbf{V}}_{\text{ref},i}^w} \delta \tilde{\mathbf{V}}_{\text{ref},i}^w \right] + & \sum_{i=0}^P \phi w_i \left[\frac{\partial \widehat{\mathbf{F}}_{1,i}^s}{\partial \tilde{\mathbf{Q}}_{b,i}^s} \frac{\partial \tilde{\mathbf{Q}}_{b,i}^s}{\partial \tilde{\mathbf{V}}_{b,i}^s} \frac{\partial \tilde{\mathbf{V}}_{b,i}^s}{\partial \tilde{\mathbf{V}}_{\text{ref},i}^s} \delta \tilde{\mathbf{V}}_{\text{ref},i}^s \right] \\
- \sum_{i=0}^P \phi w_i \left[\frac{\partial \widehat{\mathbf{F}}_{1,i}^n}{\partial \tilde{\mathbf{Q}}_{b,i}^n} \frac{\partial \tilde{\mathbf{Q}}_{b,i}^n}{\partial \tilde{\mathbf{V}}_{b,i}^n} \frac{\partial \tilde{\mathbf{V}}_{b,i}^n}{\partial \tilde{\mathbf{V}}_{\text{ref},i}^n} \delta \tilde{\mathbf{V}}_{\text{ref},i}^n \right]. &
\end{aligned} \tag{4.86}$$

In the above, due to the presence of the wall, neither the baseflow nor the disturbances have a uniform distribution. Therefore the right-hand side terms cannot be further simplified to form two coefficient matrices as we have derived in the 1D analysis. So from the conventional point of view, the eigenvalue analysis for the coefficient matrix only with respect to the internal disturbance cannot be applied to this system. However, the instability issue can be shown by checking the responses to the reference state disturbances through the derivative matrix, i.e. $\partial \tilde{\mathbf{V}}_{b,i}^l / \partial \tilde{\mathbf{V}}_{\text{ref},i}^l$ ($l = w, s, n$) which arises in each term of RHS_{ref} .

4.7.2 Analysis in the stagnation point region

Considering the boundary conditions adopted, the boundary states for the east, north, and south boundaries are given by

$$\tilde{\mathbf{V}}_b^w = \begin{pmatrix} \frac{2}{\gamma-1} c_{\text{ref}}^w \\ u_{1,\text{int}}^w - \frac{2}{\gamma-1} c_{\text{int}}^w + \frac{2}{\gamma-1} c_{\text{ref}}^w \\ u_{2,\text{ref}}^w \\ S_{\text{ref}}^w \end{pmatrix}, \tag{4.87}$$

and

$$\tilde{\mathbf{V}}_b^{n/s} = \begin{pmatrix} \frac{1}{2} \left[\left(u_{2,\text{int}}^{n/s} + \frac{2}{\gamma-1} c_{\text{int}}^{n/s} \right) - \left(u_{2,\text{ref}}^{n/s} - \frac{2}{\gamma-1} c_{\text{ref}}^{n/s} \right) \right] \\ u_{1,\text{int}}^{n/s} \\ \frac{1}{2} \left[\left(u_{2,\text{int}}^{n/s} + \frac{2}{\gamma-1} c_{\text{int}}^{n/s} \right) + \left(u_{2,\text{ref}}^{n/s} - \frac{2}{\gamma-1} c_{\text{ref}}^{n/s} \right) \right] \\ S_{\text{int}}^{n/s} \end{pmatrix}, \tag{4.88}$$

where the subscript “n/s” denotes either north or south boundary, and the velocity tangential to the boundary is enforced to be the upstream value according to the feature of split Riemann problem [96]. The respective derivative matrices of boundary state with respect to the internal and reference states are

$$\frac{\partial \tilde{\mathbf{V}}_b^w}{\partial \tilde{\mathbf{V}}_{\text{int}}^w} = \begin{pmatrix} 0 & 0 & 0 & 0 \\ -1 & 1 & 0 & 0 \\ 0 & 0 & 0 & 0 \\ 0 & 0 & 0 & 0 \end{pmatrix}, \quad \frac{\partial \tilde{\mathbf{V}}_b^w}{\partial \tilde{\mathbf{V}}_{\text{ref}}^w} = \begin{pmatrix} 1 & 0 & 0 & 0 \\ 1 & 0 & 0 & 0 \\ 0 & 0 & 1 & 0 \\ 0 & 0 & 0 & 1 \end{pmatrix}, \tag{4.89}$$

$$\frac{\partial \tilde{\mathbf{V}}_b^{n/s}}{\partial \tilde{\mathbf{V}}_{\text{int}}^{n/s}} = \begin{pmatrix} \frac{1}{2} & 0 & \frac{1}{2} & 0 \\ 0 & 1 & 0 & 0 \\ \frac{1}{2} & 0 & \frac{1}{2} & 0 \\ 0 & 0 & 0 & 1 \end{pmatrix}, \quad \frac{\partial \tilde{\mathbf{V}}_b^{n/s}}{\partial \tilde{\mathbf{V}}_{\text{ref}}^{n/s}} = \begin{pmatrix} \frac{1}{2} & 0 & -\frac{1}{2} & 0 \\ 0 & 0 & 0 & 0 \\ -\frac{1}{2} & 0 & \frac{1}{2} & 0 \\ 0 & 0 & 0 & 0 \end{pmatrix}. \tag{4.90}$$

We notice that the entries in the second column in $\partial\tilde{\mathbf{V}}_b^w/\partial\tilde{\mathbf{V}}_{ref}^w$ and $\partial\tilde{\mathbf{V}}_b^{n/s}/\partial\tilde{\mathbf{V}}_{ref}^{n/s}$ are all zero. Since the disturbances of u_1 on the reference states are introduced into the domain through these entries, the zeros infer that the linearized system will not be influenced by the disturbance of u_1 from any of the boundaries. This non-physical condition leaves an under-determined u_1 -field, and therefore the boundary condition we have adopted are ill-posed for this problem.

Although the influence of the wall and stagnation point can hardly be analyzed in a 1D case (otherwise there is no inflow for the steady baseflow), this issue can still be understood in a 1D perspective. For simplicity, the velocity, speed of sound, and entropy are chosen as the independent variables. For the weakly imposed wall boundary condition, the ghost state velocity is specified as the opposite value of the internal state velocity while the ghost state density and energy are set equal to the internal state counterparts [97]. In such a manner, the boundary state velocity is zero and the speed of sound equals to the internal state value, which makes the inward-propagating Riemann invariant equal to the internal state speed of sound times $2/(\gamma - 1)$. At the inflow boundary, when the entropy-invariant compatible inflow is adopted, the entropy and the linear combination of velocity and speed of sound are specified. This boundary conditions combination leads to a solvable problem for each field. However, when adopting the entropy-pressure compatible inflow, the entropy and pressure provide the speed of sound at the inflow boundary but leaves a free velocity, which is not influenced by the speed of sound reflected back from the wall.

The ill-posedness issue in Fig. 4.9(a) can be addressed by introducing a boundary condition where the u_1 velocity component can be imposed on the solution. This leads to the scenario in Fig. 4.9(b), where the south boundary is set as an inflow and therefore there is no stagnation point on the wall. If the entropy-invariant inflow is present for the south boundary, the derivative matrix takes the form

$$\frac{\partial\tilde{\mathbf{V}}_b^s}{\partial\tilde{\mathbf{V}}_{ref}^s} = \begin{pmatrix} \frac{1}{2} & 0 & \frac{1}{2} & 0 \\ 0 & 1 & 0 & 0 \\ \frac{1}{2} & 0 & \frac{1}{2} & 0 \\ 0 & 0 & 0 & 1 \end{pmatrix}. \quad (4.91)$$

In this case the non-zero entry in the second column enables the disturbance on the reference state u_1 -velocity component go into the domain to determine the field and therefore the problem becomes well-posed.

4.8 Results

Having identified out the stable entropy-pressure compatible inflow and understood its potential singularity issue around a stagnation point, we next provide two examples for pressure compatible simulation in the reduced domain on the CRM-NLF model [134] and the DLR-F5 model [135]. The Navier-Stokes equations are solved using the open-source spectral/ hp framework *Nektar++* [106, 107].

4.8.1 CRM-NLF

To generate the background fields, a transonic RANS simulation over the full wing-fuselage geometry is first carried out under the conditions provided in Table. 4.3,

where α is the angle of attack, L is the reference length (i.e. the selected chord). Fig. 4.10 shows the pressure distribution on the surface where two shocks on the wing can be observed. We therefore set the outflow boundary of the reduced domain at the upstream of the shock. The reduced domain is obtained on the slice in the wall-normal direction passing the leading-edge of section D of the CRM-NLF model [134]. Fig. 4.11 shows the reduced domain together with the boundary condition strategy for advection terms. To avoid the stagnation-induced ill-posedness issue discussed in Section 4.7, the entropy-invariant compatible inflow is applied at the nose region of the domain, covering the streamline that passes the stagnation point. The pressure outflow (see Section 2.5) rather than the invariant compatible outflow is adopted since the pressure interpolated from the outer RANS simulation is considered a more reliable quantity inside the boundary layer. We compare the results using the entropy-pressure compatible inflow and results using the standard Riemann-invariant inflow boundary conditions, where a single inflow boundary condition is applied over the full inflow boundary. To carry out a quasi-3D simulation, the periodic boundary condition is enforced in the x_3 -direction. The boundary condition treatments for viscous fluxes are the same as those in Section 2.5.

Table 4.3: Freestream conditions for the RANS simulation of the CRM-NLF model.

Ma	Re_L	α [deg]	T_∞ [K]	U_∞ [m/s]	ρ_∞ [kg/m ³]	L [m]
0.856	8.5×10^6	1.5	277.1	285.7	3.343	0.154678

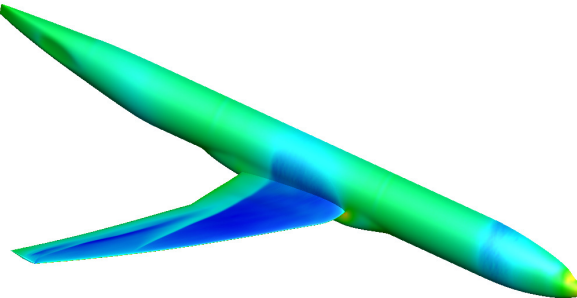


Figure 4.10: Pressure distribution in the RANS simulation over the full CRM-NLF model.

In Fig. 4.12 we compare the pressure distributions when using different inflow boundary conditions. The result for entropy-pressure compatible inflow is given in Fig. 4.12(b) where the contour lines perfectly match the pressure contours of the RANS field. Fig. 4.12(c) and Fig. 4.12(d) provide the pressure distributions without pressure compatibility enforced. Significant mismatching in contour lines is observed in the result for the entropy-invariant compatible inflow in Fig. 4.12(c), where the invariant compatible outflow rather than pressure outflow needs to be adopted for a stable simulation because of the large pressure incompatibility. Fig. 4.12(d) shows the pressure distribution for using the entropy-enthalpy compatible inflow. This result is better than that for entropy-invariant compatible inflow but some contour lines still unable to match the RANS data.

Fig. 4.13 provides more quantitative comparisons for pressure coefficient (C_p) distributions on both upper and lower surfaces of the wing section. In Fig. 4.13(a)

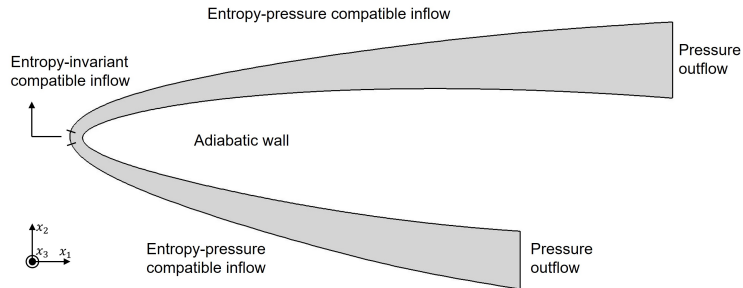


Figure 4.11: Boundary conditions for the reduced domain in the CRM-NLF simulation. The periodic boundary condition is adopted in the x_3 -direction for the 3D simulation.

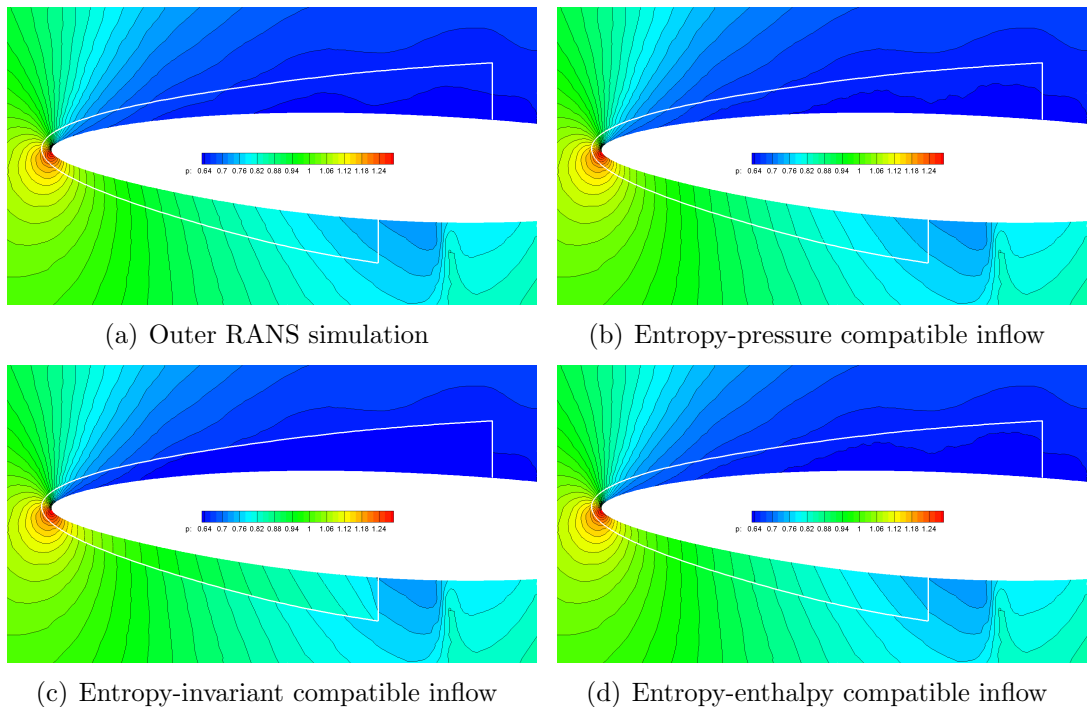
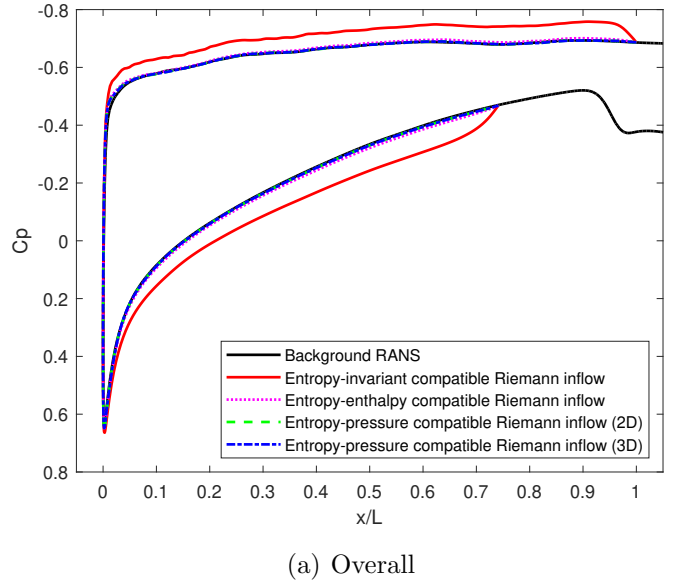
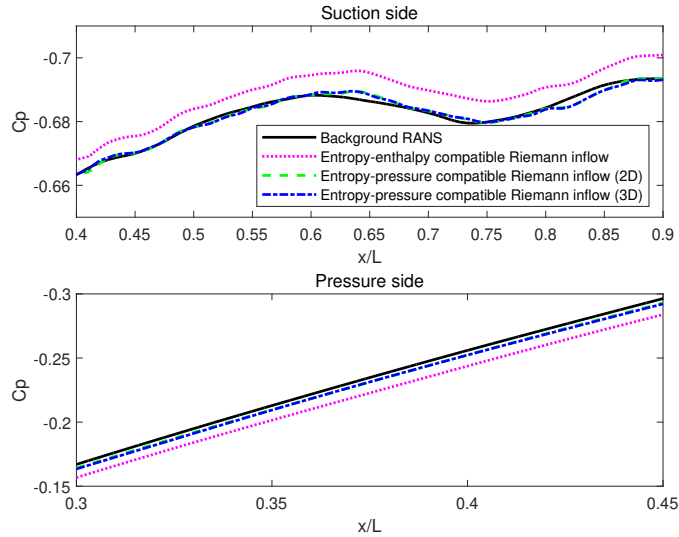


Figure 4.12: Pressure contours comparison for using different boundary conditions.

the discrepancy in the curve by entropy-invariant compatible inflow is readdressed, and the results by entropy-enthalpy compatible inflow and entropy-pressure compatible inflow are closer to each other. However, the zoomed-in comparison in Fig. 4.13(b) shows superiority of the entropy-pressure compatible inflow. To have a more well-rounded comparison, a quasi-3D simulation is also carried out using the entropy-pressure compatible inflow and the C_p distribution is provided. Excellent agreements with the RANS data are observed for both 2D and quasi-3D results in the comparison, indicating the effectiveness of the entropy-pressure compatible inflow.



(a) Overall



(b) Zoomed in

Figure 4.13: Comparison for C_p distributions of the CRM-NLF case. The result by entropy-invariant compatible inflow is not plotted in (b) for its significant deviation as indicated in (a).

4.8.2 DLR-F5

To further validate the performance of the entropy-pressure compatible inflow boundary condition, an embedded transonic simulation on the DLR-F5 model [136] is performed. In contrast to the CRM-NLF simulation, the DLR-F5 simulation has larger pressure variation over vast region on the suction side, which is closer to the real condition.

In Table 4.4 we show the flow conditions of the outer RANS simulation, and the pressure distribution on the surface is given in Fig. 4.14. As for the embedded simulation, the settings are similar to the CRM-NLF simulation in the previous section, and a wing section normal to the leading-edge of section 5 of the geometry [135] is used.

Table 4.4: Freestream conditions for the RANS simulation of the DLR-F5 model [136].

Ma	Re_L	Re/m	α [deg]	T_∞ [K]	L [m]
0.82	1.04184×10^6	1×10^7	2	273.25	0.10418395

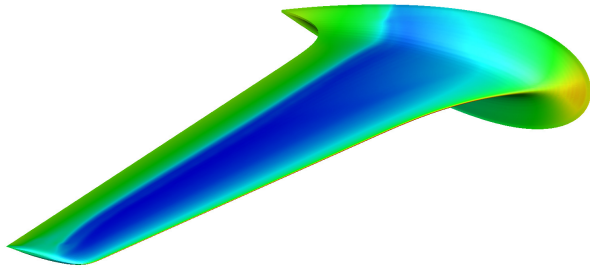


Figure 4.14: Pressure distribution in the RANS simulation over the DLR-F5 model.

In this case we only show the performance of the entropy-pressure compatible inflow condition while both 2D and quasi-3D simulations are performed. Fig. 4.15 provides the comparison of pressure and density fields, where the white solid line indicates the boundary of the embedded domain, and on the outside is the RANS field. In the above Figs. 4.15(b) and 4.15(c) compare the pressure field and Fig. 4.15(d) compares the density field respectively. It shows that all contour lines agree well with the RANS simulation, inferring the good performance of the boundary condition enforcement and a successful embedded simulation.

We also compare the C_p distributions in Fig. 4.16. Both results for 2D and quasi-3D simulations are on top of the RANS data as desired. Moreover, it is observed that the wiggles in the RANS data are get rid of in the two embedded simulations. This further proves an embedded simulation can be based on a computationally cheaper outer simulation, and will enable better studies on the growth of disturbances inside the boundary layer.

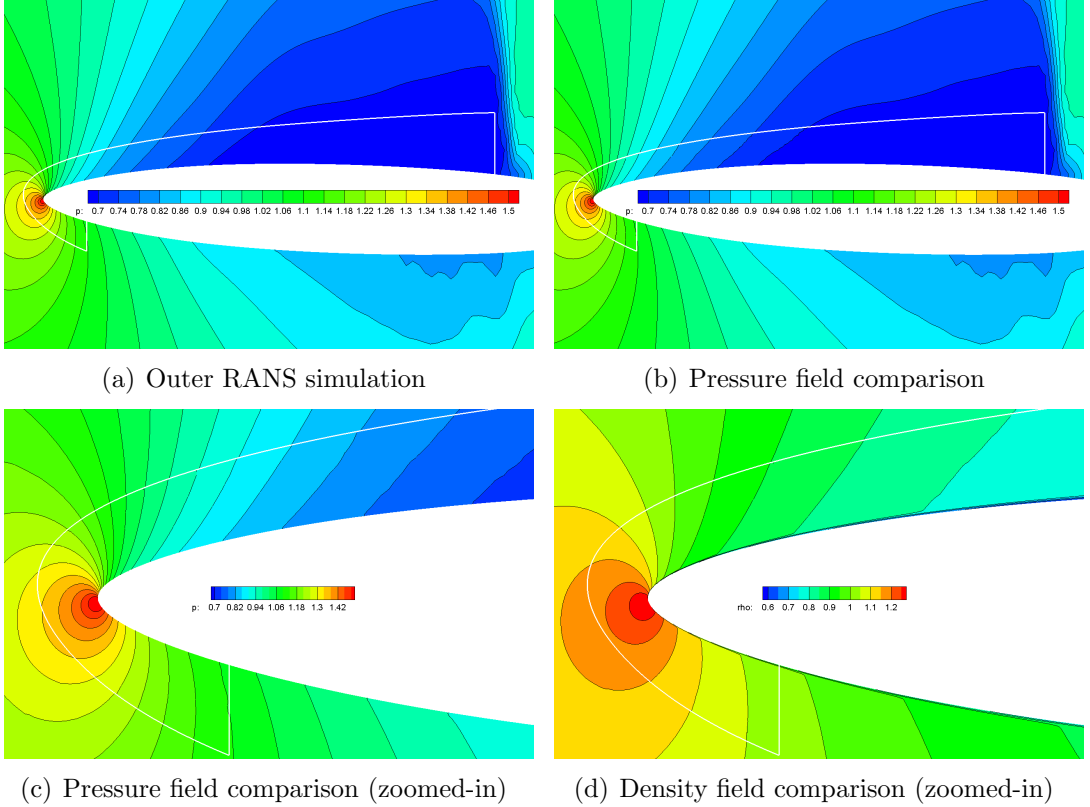


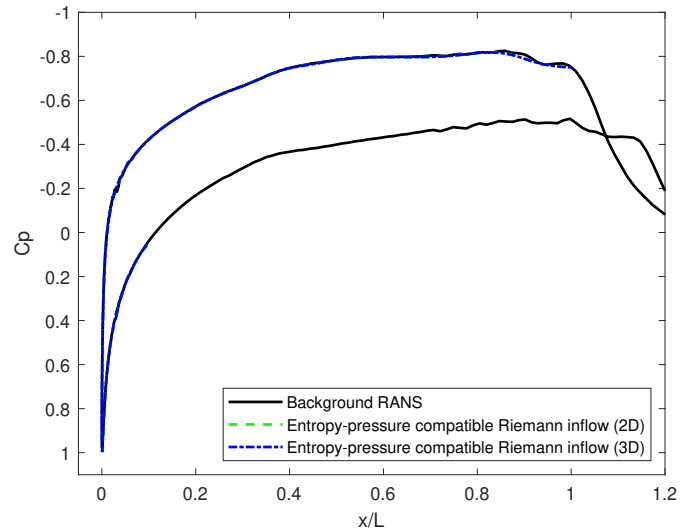
Figure 4.15: Pressure and density contours comparisons for using the entropy-pressure compatible inflow boundary condition.

4.9 Conclusion

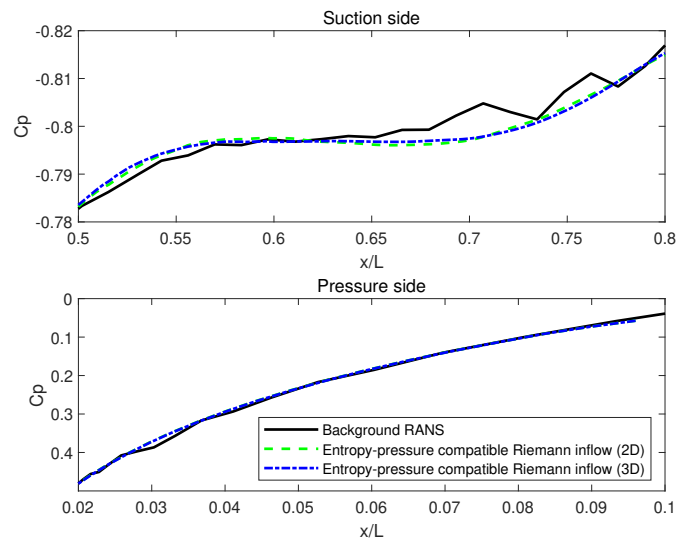
To carry out high fidelity simulation in a reduced domain which is embedded in a outer domain where a lower fidelity model such as RANS is applied, appropriate boundary condition enforcement is required. This is particularly the case when the high fidelity simulation is compressible but subsonic, since not all the data interpolated from the outer simulation can be enforced at the inflow boundary of the reduced domain. Since the pressure load is typically well predicted by the low fidelity model and does not vary much over the boundary layer, the pressure is considered a reliable quantity to maintain in the reduced domain. We have therefore determined the stable enforcement to achieve pressure compatibility at subsonic inflow boundary for DG compressible flow simulations.

Initially we derived the linearized DG approximation of 1D Euler equations using piecewise constant assumptions. The linearized system is considered in a single element since in DG simulations the boundary conditions are enforced in an individual element in form of numerical flux and the inflow boundary condition is enforced at the most upstream boundaries of the inflow boundary elements. To complete the analysis the invariant compatible outflow were considered as it is the implicit outflow condition for internal boundaries between the elements (e.g. the very upstream element and the adjacent downstream element) when the numerical flux is the solution from an exact Riemann solver.

The construction of numerical flux depends on the internal state (inside the element) and the reference state (which is usually the desired state) and so the



(a) Overall



(b) Zoomed in

Figure 4.16: Comparison for Cp distributions of the DLR-F5 case. (b) shows the zoomed-in view of (a).

linearized system can be derived from these two perspectives by introducing disturbance on either the internal state or the reference state, generating two different matrix problems. Introducing disturbance on the internal state is a standard approach, which finally leads to a linear dynamic system. Similarly from the reference state disturbance point of view, the derived coefficient matrix essentially represents how the reference state disturbance are received by the internal state. In the 1D analysis, these two perspectives have a complementary relation. Therefore the stability of the boundary conditions can be obtained by computing the eigenvalues of either of the matrices. For the coefficient matrix derived from the perturbed internal state, a stable boundary condition requires the three eigenvalues of the linearised matrix to have negative real parts. A representative example is the entropy-invariant compatible inflow, which leads to the eigenvalues of well-known $-(c + u)$, $-u$, and $-(c - u)$. A special case is when some eigenvalues are zero, indicating the coefficient matrix is rank-deficit. This usually implies that the boundary conditions is no well-posed, and therefore are inappropriate.

To achieve pressure compatibility at the inflow, three types inflow conditions were constructed and examined, namely entropy-pressure, velocity-pressure and momentum pressure compatible conditiions. It can be shown that only the entropy-pressure compatible inflow is stable while velocity-pressure compatible inflow is neutrally stable and the momentum-pressure compatible inflow is unstable. It is further possible to prove that the entropy is an important quantity to maintain in order to be compatible with the outer simulation. However, as long as the entropy compatibility is maintained, any other quantity can be chosen to be enforced at the inflow.

With the understanding for 1D stability analysis, the stable entropy-pressure compatible inflow is applied to the 2D simulations. However, the simulations were observed to easily diverge, which initiates around the region of a stagnation point. To understand this instability, a similar method was derived for the 2D Euler equations in a squared domain. Due to the presence of the stagnation point, the baseflow is no longer uniform and the distribution is unknown. The assumption that the disturbances introduced to different boundaries are equal is also dropped. The significant consequence is that the boundary integration term cannot be combined to form a single matrix for eigenvalues analysis. From the perspective of disturbance introduced on to the internal state, the instability issue cannot easily be further analyzed. However, the other perspective where the disturbance is introduced on to the reference state reveals that a rank deficient matrix problem related to the boundary interior coupling in the final linearized system. This therefore demonstrate that the instability is arising from the ill-posedness of the adopted boundary conditions.

The solution to this numerical instability issue is to locally replace the entropy-pressure compatible inflow by some other stable inflow, which enforces the normal velocity either explicitly or implicitly, in the boundary region related to the streamline related to the stagnation point. In this work we use the entropy-invariant compatible inflow to avoid this issue. We perform a numerical test based on the CRM-NLF model. A RANS simulation over the full wing-fuselage geometry is performed, and a high fidelity simulation in the reduced domain on the slice passing the leading-edge was generated. With the updated boundary conditions strategy, the simulation is stable and the C_p distribution agrees well with the RANS data.

Part III

Laminar boundary layer natural transition studies

Chapter 5

Transitional analysis on the wing section of CRM-NLF model

5.1 Introduction

As we have briefly introduced in Section 1.2.3, real wing geometries of airliners are not perfectly clean as in ideal CAD models but contain surface irregularities which are typically in form of quasi-3D steps or gaps as illustrated in Fig. 1.3. These small sized surface irregularities can destabilize the laminar boundary layer and cause early transition to turbulence, increasing the fuel consumption and waste emission. Therefore further investigations on their influence are of our interest.

In this chapter we analyze the transition related performance on both clean and gapped wing sections of the CRM-NLF model using the embedded DG simulation and e^N method as outlined in Chapter 3 and using the entropy-pressure compatible subsonic Riemann inflow boundary condition developed in Chapter 4. After obtaining the RANS results on the full wing-fuselage configuration, we first perform a two-dimensional analysis on both clean and gapped geometries. Results by using different wall boundary conditions are also compared. The three-dimensional analysis is then performed, where self-sustained oscillations inside the gap is observed.

We also remark that the NLF wing geometry is designed to have a low pressure gradient on the surface and therefore the disturbance in the boundary layer is less amplified than on widely adopted wing sections. The DLR-F5 model has also been tested, where a more conventional pressure gradient presents on the surface. However, although the DLR-F5 model was investigated at a transonic Mach number of interest, its low chord-based Reynolds number provides an N -factor approximately equal to 1 based on our preliminary LST analysis. This low N -factor indicates that the transition is driven by the shock and corresponding separation. Therefore only the CRM-NLF case is further studied in this work.

5.2 Geometries and conditions for simulations

5.2.1 Sizes of surface irregularities on the wings

To figure out the irregularity size of steps and gaps, a survey over several widely employed commercial airliners is performed. However, it is found that detailed descriptions are rarely available in the open reports and literature, particularly for the

irregularities near the leading edge which have more influence on the flow transition. Considering the irregularities are caused by imperfect skin junctions and slits at the slat trailing edge, the sizes (depth/height) of the quasi-3D irregularities should have the same order of the skin thickness. Data with regards to the skin thickness as well as the spoiler gap are provided as references.

Table 5.1 shows the skin thickness of four typical airplanes. By comparing the thickness data on high-lift surfaces of A320 and A340, Jabbal et al. [137] summarized that the skin thickness is not linearly scaled with the airplane size but is determined by other factors, where the thicker skin up to 5 mm on the flap does not come from local structure design but as additional protection from bird strike, while the thicker skin on the outboard/inboard flap helps the structure to bear the jet load by the engines. Therefore we can conclude that typical values of skin thickness are in the range of 1–2 mm except for additional considerations.

Table 5.1: Skin thickness of airplanes. Unit [mm].

Type	Fuselage	Slat	Outboard flap	Inboard flap
Boeing B737 [138]	1.02	—	—	—
Boeing B757 [139]	0.99	—	—	—
Airbus A320 [137]	—	2	2	5
Airbus A340 [137]	—	1	2 – 5	2

Boeing has developed a Performance Improvement Package (PIP) to improve the aerodynamic performance of the Next-Generation 737 [140], the geometrical improvements on the trailing-edge thickness and spoiler gap are listed in Tables 5.2 and 5.3, respectively. It reconfirms that these irregularities are in the order of millimeters even with the PIP adopted.

Table 5.2: Trailing-edge thickness reduction using PIP [140]. Unit [mm].

Trailing edge	Without PIP	With PIP
Slat	1.524	0.5
Spoiler	3.556	1.4478

Table 5.3: Spoiler trailing edge gap reduction using PIP [141]. Unit [mm].

Spoiler panel ID	Previous gap	New gap
1, 12	1.8	2.0
2, 11	8.1	2.5
3, 10	6.9	1.65
4, 9	6.9	1.65
5, 8	1.5	1.65
6, 7	1.3	2.0

5.2.2 CRM-NLF geometry, scaling, and settings

The influence of the quasi-3D gap type surface irregularities on the laminar boundary layer transition will be studied on the NASA Common Research Model with natural laminar flow wing (CRM-NLF). The CRM project is set up to enhance cross-organizational collaborations for aeronautic research, and several sets of experimental data are available in Ref. [142].

As mentioned in Section 5.2.1, the skin thickness on the wing is not linearly scaled with the airplane size, and neither is the size of the gap. In other words, a type of the airplane needs to be selected before the realistic sized gap can be scaled to the CRM model. In Table 5.4 the mean aerodynamic chords (MACs) of three major commercial airplanes and the CRM-NLF model are provided. In this work we consider a realistic quasi-3D gap of $2\text{mm} \times 8\text{mm}$ (depth \times length) on a widely equipped Boeing-737 airplane, and scale the geometry by MAC leads to the CRM-NLF model as listed in Table 5.5. Such a gap is then introduced to a section normal to the leading edge of section D of the geometry. The distance from the leading edge of the wing to that of the gap is 38.67 mm, and the selected chord length of 0.116009 m. On the simulation side, as listed in Table 5.6 we use the freestream conditions in the experiment # 2524 of the CRM-NLF model [142], where the Mach number is 0.856 and the Reynolds number per meter is 4.1×10^7 .

Table 5.4: Mean aerodynamic chords of typical commercial airplanes. Unit [m].

Geometry/model	MAC
CRM-NLF [114]	0.36429
Boeing B737-800 [143, 144]	3.96 ¹
Boeing B777-200 [145, 146]	7.08
Boeing B787-8 [147]	6.27126

Table 5.5: Scaled gap on the CRM-NLF model. Unit [m].

Depth	Length
1.8398×10^{-4}	7.3594×10^{-4}

Table 5.6: Freestream conditions for experiment #2524 of CRM-NLF model.

Ma	Re/m	α [deg]	T_∞ [K]	L [m]
0.856	4.1×10^7	1.98	241.9	0.116009

In this chapter we will perform compressible flow simulations on both clean and gapped geometries. Two sets of 2D 4-th order computational meshes (Mesh 1, Mesh 2) are generated as shown in Figs. 5.1(a) and 5.1(b). For each case, the origin of the global coordinate system (x, y, z) is set at the leading edge, and the mesh

¹Different MAC values for B737 and B777 are found in Ref. [148] but only the data provided by the official documents are listed here.

is non-dimensionalized by the selected chord length L . The outflow boundaries are therefore located at $x = 1$. In the gapped case, the leading edge of the gap is located at $x = 0.33$. When the boundary-layer profiles are extracted for comparisons, they will be provided in the wall-normal direction y^{loc} of a body-fitted, local coordinate system $(x^{\text{loc}}, y^{\text{loc}}, z^{\text{loc}})$ as sketched in Fig. 5.1(a). In addition, to perform a quasi-3D simulation, the corresponding 2D mesh is extruded in the spanwise (z) direction for three layers to generate a quasi-3D mesh. Fig. 5.1(c) depicts another mesh (Mesh 3) for the gapped case. It is generated in the reduced domain ($x \in [0.23, 0.55]$) with mesh refinement to study the quasi-3D flow physics near the gap, which will be discussed in Section 5.7. However, the settings of the global coordinate system are kept the same as the two cases above.

The 2D high-order mesh for the clean case (Mesh 1) is directly generated by NekMesh [149]. As for the gapped cases, 2D linear meshes are first generated and then projected onto the CAD model by NekMesh to generate high-order meshes (Mesh 2, Mesh 3) [150]. All meshes have the same non-dimensional first layer (i.e. the layer next to the wall) thickness of 2×10^{-5} . The total number of elements and degrees of freedom (DoF) for using 3-rd order modal expansions (P3) are summarized in Table 5.7. In addition, the boundary condition enforcement follows the strategy in Fig. 4.11 for all simulations.

Table 5.7: Types of boundary conditions.

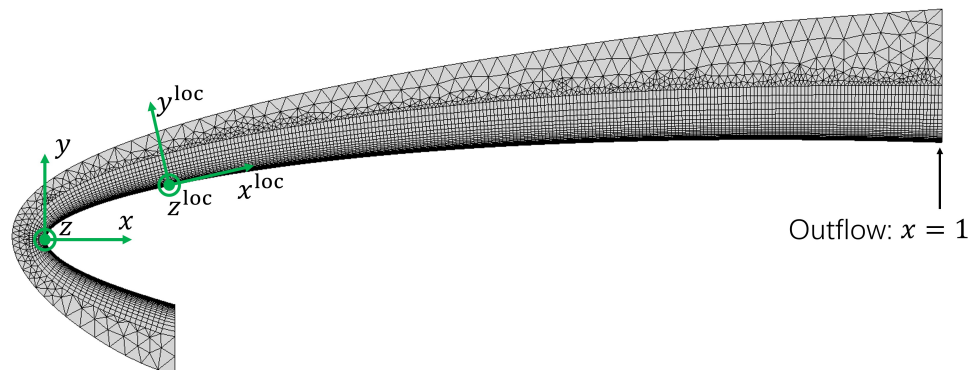
	2D		3D	
	Elements	DoF (P3)	Elements	DoF (P3)
Mesh 1 (clean)	13565	217040	40695	2604480
Mesh 2 (gap)	20525	328400	61575	3940800
Mesh 3 (gap, reduced domain)	–	–	51174	3275136

5.3 Challenges in baseflow computation

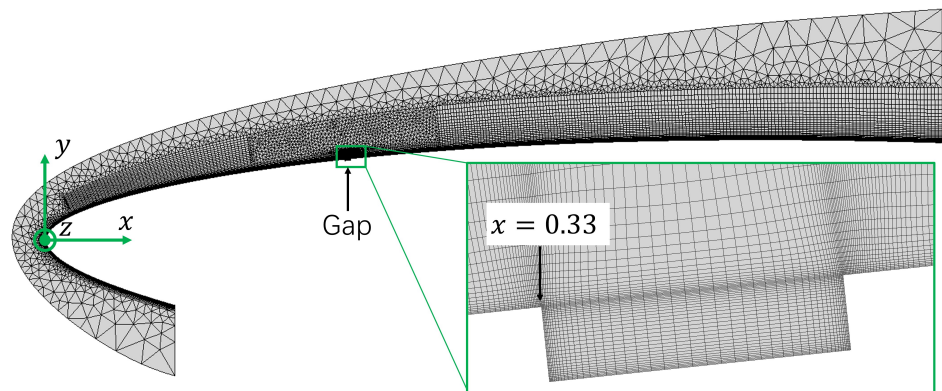
The baseflow computation in the near-wall reduced domain suffers from numerical instability, particularly in the initial stages when shocks form and hit the inflow/outflow boundaries. We use artificial viscosity to stabilize the simulation. Moreover, the standard Riemann inflow boundary condition is adopted to let the shock leave the domain with minimum reflection in the beginning of the simulation and then it is switched back to the entropy-pressure compatible inflow to achieve the desired pressure distribution.

Since the artificial viscosity leads to a nonphysical boundary profile, the artificial viscosity is therefore turned off after the main field is stabilized. Note that a boundary layer sensor such as the one proposed in Ref. [151] is not used to only apply the artificial viscosity outside the boundary layer. This is because when predicting the growth of disturbances, the region influenced by the disturbances is not limited within the boundary layer. The additional viscosity outside the boundary layer may still decrease the accuracy of prediction. In this work the artificial viscosity is used for 1st and 2nd order expansions to initialize the field.

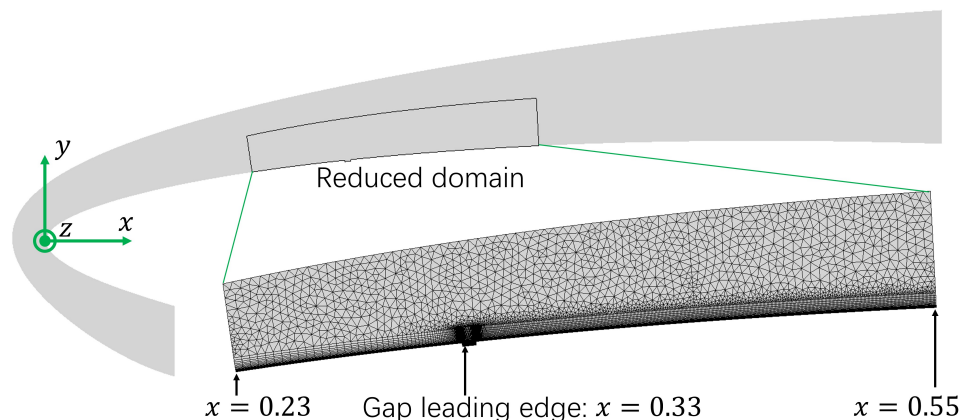
The turning off of artificial viscosity can also be challenging. After the turning off, the sudden drop of viscous force breaks the balance of inertia and viscous



(a) Mesh 1: clean geometry



(b) Mesh 2: gapped geometry



(c) Mesh 3: gapped geometry in a reduced domain

Figure 5.1: Coordinate systems and computational meshes in the $x - y$ plane.

forces inside the boundary layer, and a new balance is gradually established with a decreased boundary layer thickness. In this transient process, disturbances are generated due to the numerical effect. These disturbances typically grow as they travel downstream. This is particularly the case for high-order simulations due to their low numerical diffusion. Fig. 5.2(a) provides an example of the development of the disturbances arising from the gap, where from top to bottom are three snapshots in time order. The snapshots are dumped from 2D simulations while they are displayed in 3D for better visualization purposes. The vertical axis in the 3D visualization shows the density ρ , which is also used to color the snapshots. It is observed from the undamped development in Fig. 5.2(a) that the disturbances are weak in the beginning but they grow significantly before they arrive at the outflow boundary. These disturbances become so strong that they can directly cause under-resolution instability since the mesh is generated to capture a laminar boundary layer, or cause significant numerical oscillation when they hit the outflow boundary. To stabilize the simulations different possible approaches are tested, among which we find the sponge region and SFD work effectively. The results of these two approaches are shown in Fig. 5.2(b) and 5.2(c), respectively. The sponge region damps the disturbances smoothly due to the adopted coefficient profile. However, the SFD kills off the disturbances from the beginning when they are weak in amplitude and therefore has a better performance. We note another possible solution to avoid having strong disturbances in the boundary layer is to gradually decrease the artificial viscosity. However, since this needs a time-dependent coefficient in the settings or several human interventions during the simulations, this approach has not been tested in this thesis.

5.4 Baseline for two-dimensional analysis

Following the above procedures, we first compute the two-dimensional baseflow using a high-order method in the reduced domain. Since the RANS simulation is three-dimensional, the two-dimensional simulation is performed by removing the spanwise velocity and its contribution in the kinetic energy from the boundary data provided at the inflow boundary. Adiabatic wall is adopted for the temperature field. This successfully preserves the pressure coefficient (C_p) distribution on the surface as the RANS data by using the entropy-pressure compatible Riemann inflow and the pressure outflow boundary conditions, which is shown in Fig. 5.3. Note that the flow conditions are different from those in Section 4.8 and the C_p distributions are not identical. We also notice that the nonphysical oscillations near the leading edge are removed in the embedded simulation, enabling better e^N analysis of disturbances for the next step.

The convergence of the baseflow is also examined. The baseflow is solved by both 3rd-order expansion (4th-order accuracy, denoted by P3) and 4th-order expansion (5th-order accuracy, denoted by P4), as well as by the boundary layer equation solver *CoBL* [62, 152] using the C_p distribution provided by the embedded simulation. The boundary profiles for velocity components in the body-fitted coordinate system and for temperature are compared, and the comparisons at $x = 0.2$ and $x = 0.6$ are presented in Fig. 5.4. The convergence is confirmed for the excellent agreements of the data.

To perform the e^N analysis the disturbance fields for different frequencies are

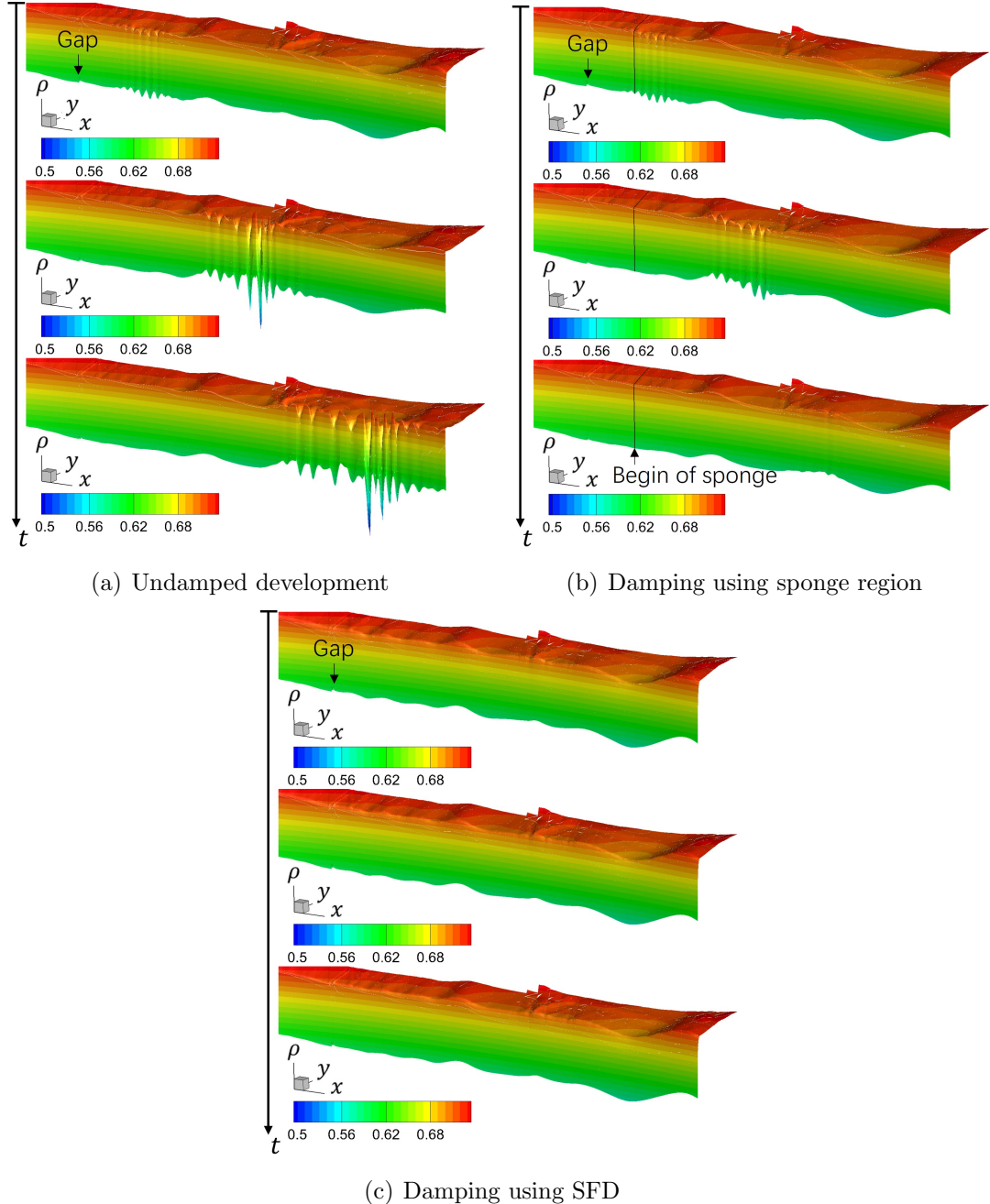


Figure 5.2: Density fields ρ showing the development of disturbances after turning-off the artificial viscosity, and effects of different damping methods. The flow travels from left to right. From top to bottom in each subfigure shows three representative snapshots in time order. The snapshots are dumped from 2D simulations but are visualized in 3D where the vertical axis also shows the density.

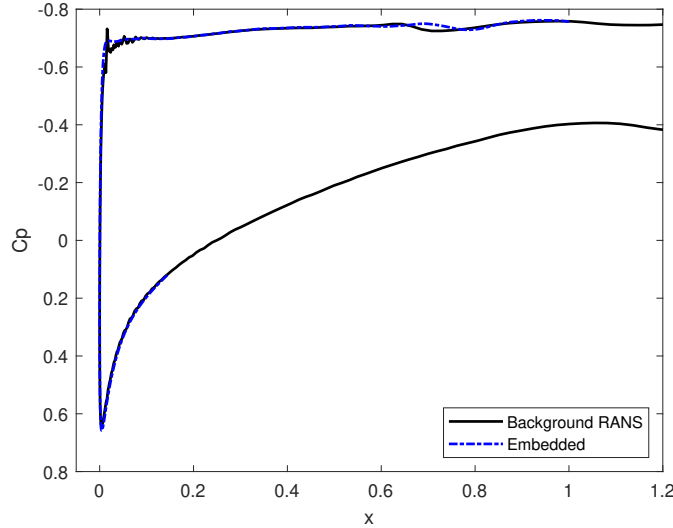


Figure 5.3: Cp comparison of the background RANS data and 2D embedded simulation.

computed. Since we are using the DNS solver to obtain the disturbances, it is not the disturbance fields themselves that are computed but the superposition of disturbance fields and the baseflow as a whole, namely the disturbed fields. The baseflow is then subtracted from the disturbed fields to obtain the disturbance fields. In contrast to the steady baseflow, the unsteady disturbed fields are excited by the artificial blowing-suction at $x = 0.05$ near the leading edge, and the reflected waves are damped using a sponge region. In 2D cases the disturbances are in the form of TS waves. The development of TS waves of four representative frequencies of 30, 40, 50, and 60 kHz are shown in Fig. 5.5, where the TS waves are clearly resolved in the reduced domain with wave contamination being successfully prevented.

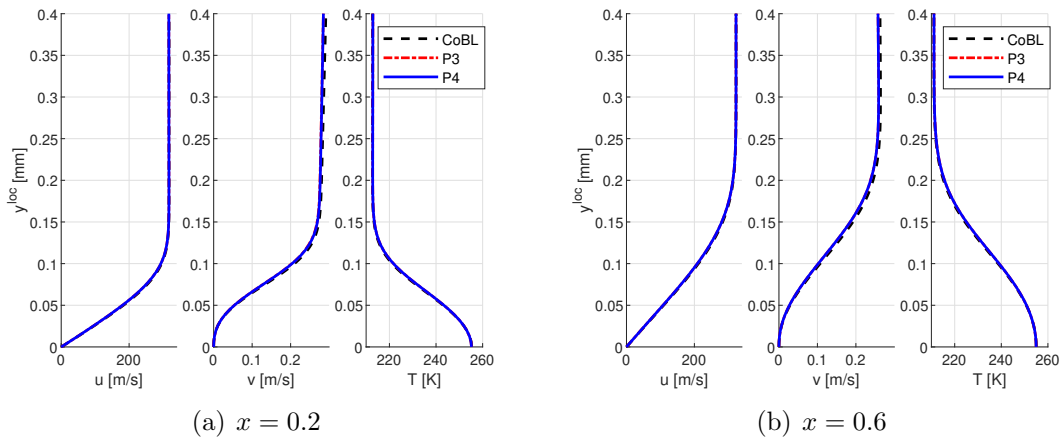


Figure 5.4: Boundary layer profile comparisons of using a 3rd-order expansion (P3), a 4th-order expansion (P4), and the CoBL solver for the 2D clean CRM-NLF case.

Considering the eigenfunctions of the TS waves or other types of flow instabilities have more variations in shape than the laminar boundary layer profile, the convergence of the disturbance fields should also be checked in addition to the baseflow

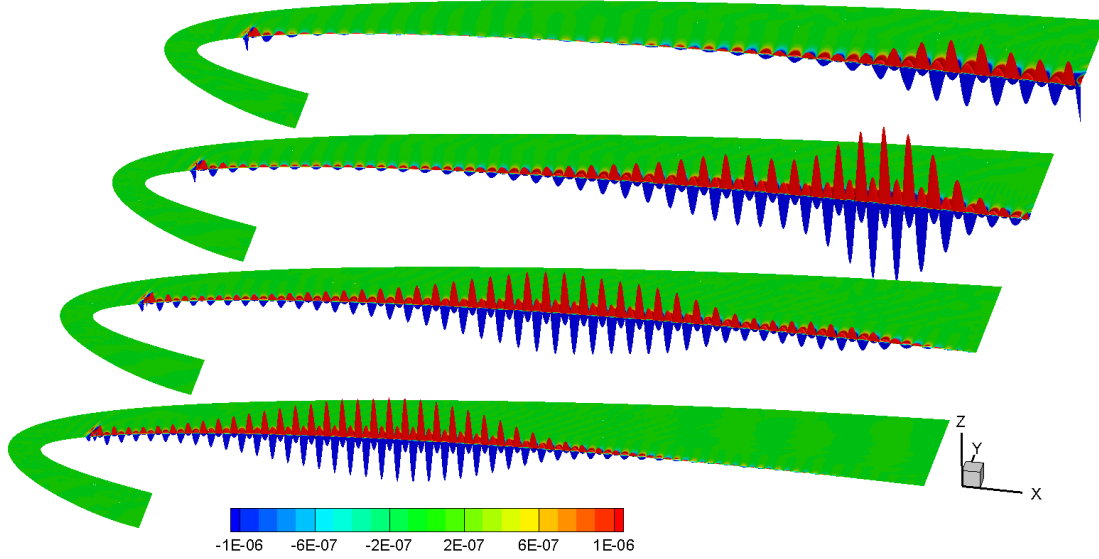


Figure 5.5: Streamwise component of the velocity disturbance fields u' of fully developed TS waves over the 2D clean CRM-NLF case. The four snapshots from top to bottom show the disturbance fields with frequencies $f = 30, 40, 50$, and 60 kHz.

convergence to confirm the mesh resolution and flow accuracy are appropriate. We have verified this point by comparing the P3 and P4 simulations. For instance, in Fig. 5.6 we compare for the disturbance amplitudes for velocity components and temperature of the TS wave of 50 kHz frequency, and the profiles at $x = 0.2$ and $x = 0.6$ are provided. The disturbance amplitudes for the P3 and P4 simulations coincide for all fields, confirming the convergence.

As the baseline case, we finally compute the growth of TS waves with frequencies from 30 kHz to 100 kHz. P3 simulations are used for efficiency. The generated envelope N -factor curve is shown in Fig. 5.7, where the N -factor initially slowly increases and significantly raises from 0.72 to 0.85, and the maximum reaches 4.

5.5 Effect of different wall boundary conditions

In the baseline case outlined in Section 5.4 we used an adiabatic wall boundary condition for temperature field. The adoption of an adiabatic wall is natural for the baseflow if we assume zero heat exchange between the wall and fluid. However, when it comes to the disturbance fields more careful consideration is needed. Mack assumed that the wall temperature can hardly be influenced by the disturbances unless they are stationary [42]. The boundary condition for temperature disturbances is therefore zero on the wall for traveling disturbances. Malik further explained this point as the temperature disturbances cannot influence deep into the solid due to the high disturbance frequencies and thermal inertia of the solid [48]. However, for solids with high thermal inertia, although the temperature fluctuations cannot penetrate deep into the solid, it is the surface temperature that is used as the boundary condition. The thermal inertia for certain materials/structures may also possibly be low. In addition, to the best of our knowledge the vanishing temperature disturbance

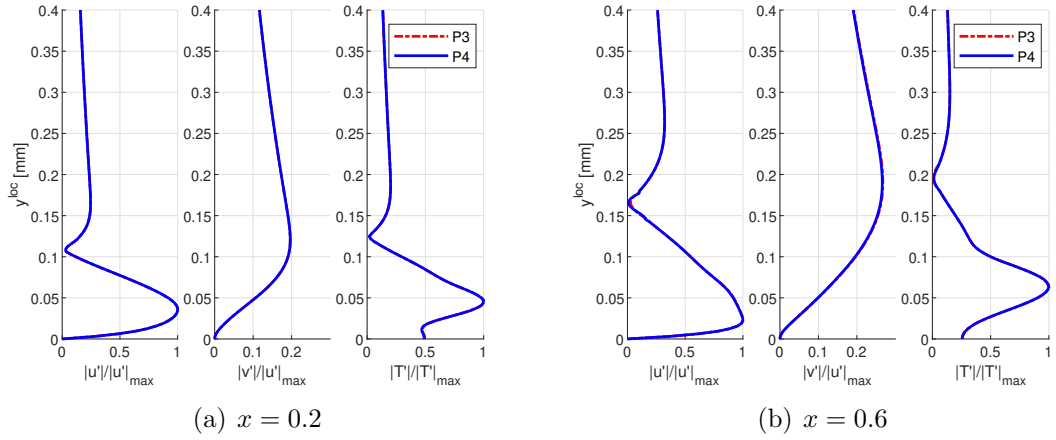


Figure 5.6: Disturbance amplitude profile comparisons of using 3rd-order (P3) and 4th-order (P4) expansions. The frequency of the disturbance is 50 kHz. The profiles for velocity disturbance amplitudes $|u'|$ and $|v'|$ are scaled by the maximum on the streamwise velocity disturbance amplitude profile $|u'|_{max}$, and the temperature disturbance amplitude profile $|T'|$ is scaled by its maximum.

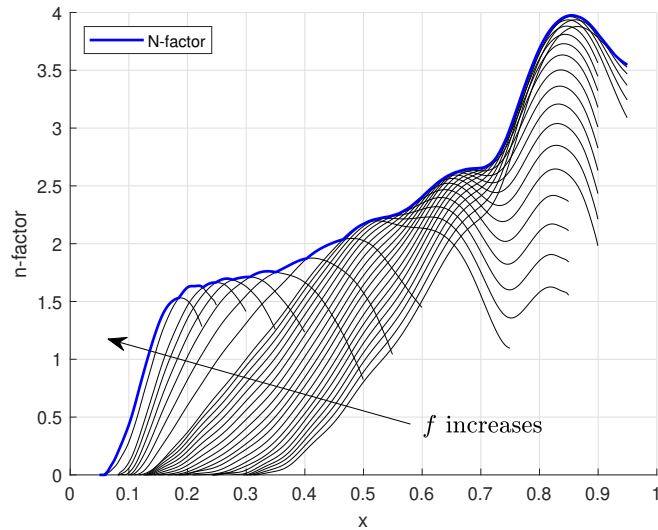


Figure 5.7: N -factor of the 2D clean CRM-NLF case. The component n -factors correspond to the highest frequency of 100 kHz and the lowest frequency of 30 kHz.

assumption is not yet validated by experiments due to the practical difficulties of making measurements near the wall. There are many papers such as Ref. [153–157] focused on controlling the growth of the disturbances by changing the wall temperature while the opposite influence on the wall temperature by the disturbances is rarely found. Therefore, in this section we further discuss the influence of different temperature boundary condition on the growth of disturbances.

We consider both adiabatic and isothermal walls for the temperature field. The results for using the adiabatic wall condition are already provided in the baseline case. To generate comparable results using the isothermal wall, the wall temperature is set pseudo-adiabatically [158], namely by not imposing the theoretical temperature but the wall temperature from the adiabatic baseline case, which is approximately 255 K. The resulting baseflow boundary layer profiles are compared in Fig. 5.8 at $x = 0.2$ and $x = 0.6$. The baseflow boundary layer profiles show agreement for both velocity and temperature, and meaningful comparisons for disturbances under different temperature boundary conditions can be performed.

We only analyze the growth of the representative disturbances with frequencies 30, 40, 50, and 60 kHz. The amplitude profiles for streamwise velocity disturbance (u'), wall-normal velocity disturbance (v'), and temperature disturbance (T') of the 50 kHz disturbance are provided in Fig. 5.9. It shows that different temperature boundary conditions do not influence the

amplitude profiles for velocity disturbances and even the top region of the temperature disturbances. The only difference lies in the foot region of the temperature disturbance amplitude profile, which agrees with the statement for the DNS turbulent study that the difference of using different boundary condition is limited within the viscous sublayer as cited by Wenzel [158].

In the next step we generate the n -factors and compare the amplitudes as shown in Fig. 5.10(a). It is clear that by using the isothermal wall the n -factors are always larger in the current domain. The difference of the two n -factors (Δn) of the same frequency are also provided in Fig. 5.10(b), where the difference grows along the flow direction. In the selected domain all the four differences grow to be above 0.3 and will be larger if we extended the range. Since the difference can be interpreted by the integral of growth rate as

$$\Delta n(x) = \int_{x_0}^x -(\alpha_i^{isot} - \alpha_i^{adia}) dx^{\text{loc}}(x),$$

where the body-fitted local coordinate $x^{\text{loc}}(x)$ is a function of the global coordinate x , the growing Δn indicates the growth rate using isothermal wall is always larger than that using adiabatic wall for all four frequencies, even in the region where the disturbances are decaying.

5.6 The influence of a gap irregularity

We study the influence of a gap on the growth of TS waves on the 2D CRM-NLF model in this section. As mentioned in Section 5.2.2, a 2×8 mm gap on the Boeing-737 is scaled to the CRM-NLF model based on the MAC. The gap is introduced to wall at the position $x = 0.333$. In Fig. 5.1(b) we provide the 2D mesh for the simulations. Quadrilateral elements are used in the boundary layer region, and

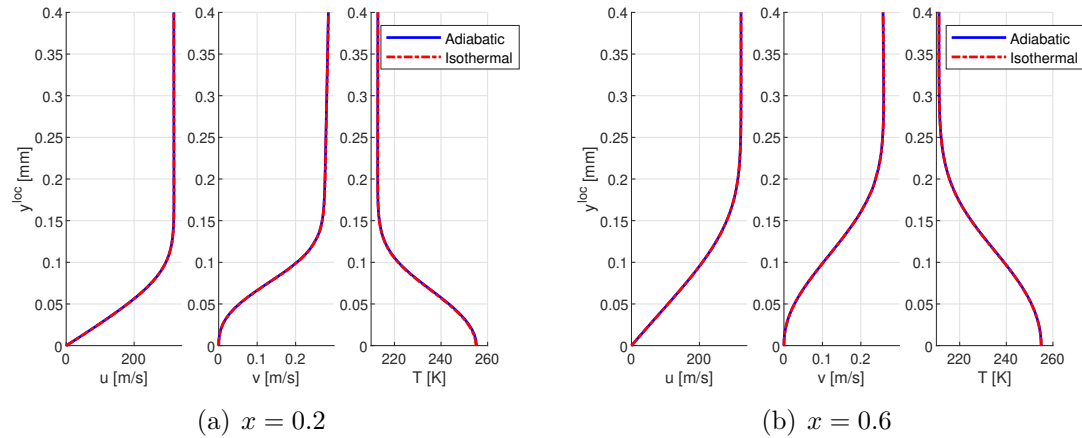


Figure 5.8: Boundary layer profile comparisons for using adiabatic and isothermal temperature boundary condition.

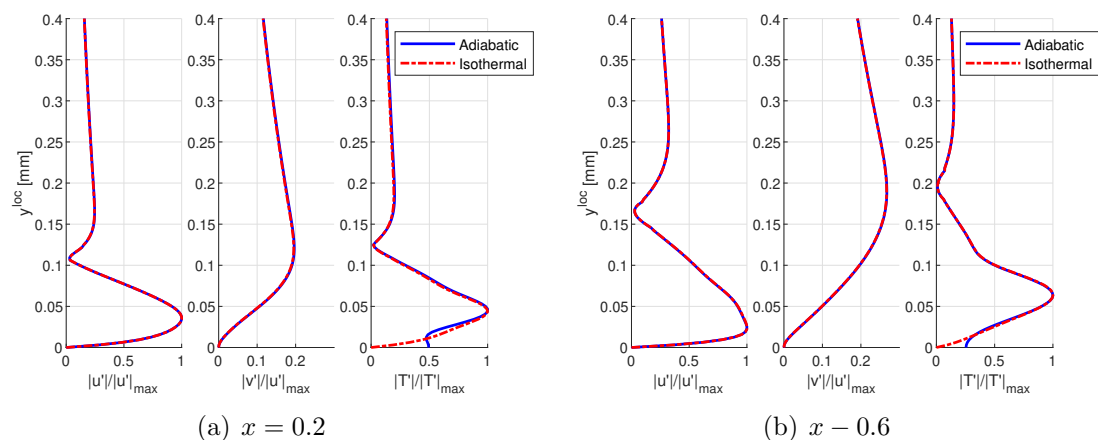
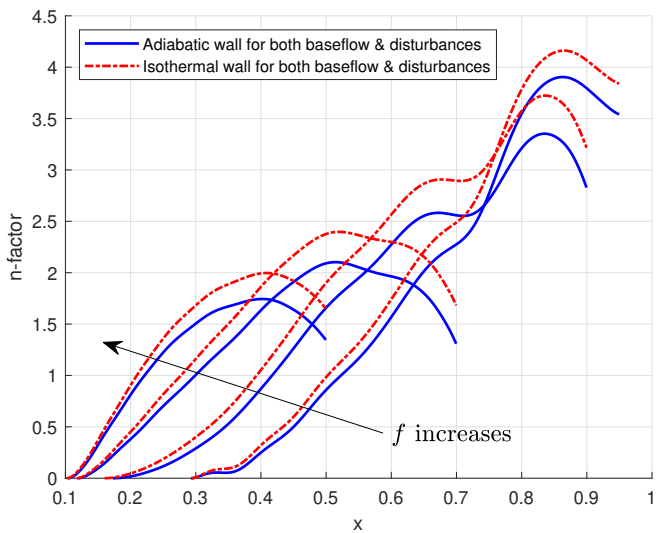
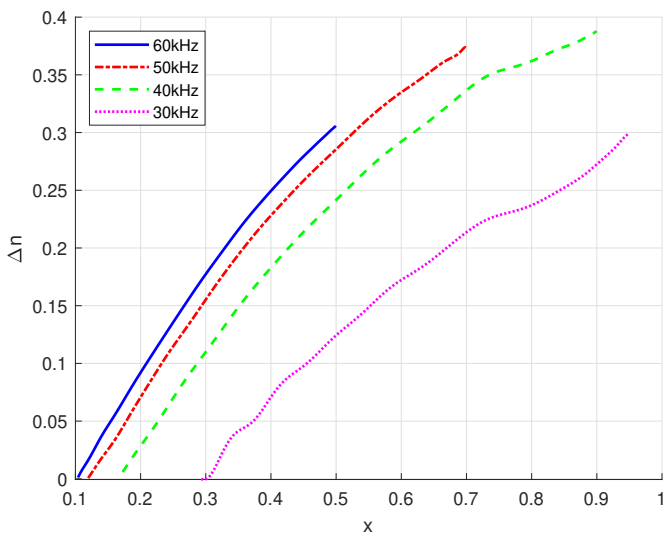


Figure 5.9: Disturbance amplitude profile comparisons of using adiabatic wall and isothermal wall boundary conditions. The frequency of the disturbance is 50 kHz.



(a) Absolute n -factors



(b) Differences in n -factors

Figure 5.10: N-factor comparisons for using adiabatic wall and isothermal wall boundary condition. The four curves in (a) from right to left correspond to disturbance frequencies $f = 30, 40, 50, 60$ kHz.

triangular elements are used to fill the outer region as well as to provide a better mesh distribution above the gap. The total number of spectral elements is 20 525 as shown in Table 5.7. The convergence check is also performed and shown in Appendix C.1.

Following the procedures in Section 5.3 we generate the baseflow with the help of artificial viscosity. In this case the baseflow computation is stopped after the residual is smaller than 1×10^{-10} , and the results are given in Fig. 5.11. The velocity contour in Fig. 5.11(a) shows that the flow adjacent to and above the gap is not significantly influenced by the gap. This is confirmed by the velocity profiles at $x = 0.34, 0.35, 0.36, 0.37, 0.38$, and 0.39 in Fig. 5.11(c), where we also notice that in the aft region inside the gap the velocity is much larger in magnitude than in the fore region. The vorticity arising from the velocity gradient is shown in Fig. 5.11(b), where a strong circulation is observed next to the rear wall of the gap. Additionally, from the velocity profile in Fig. 5.11(c) the ratio of the depth of the gap to the local boundary layer thickness is computed to be approximately 1.10. A region of strong vorticity is observed after the rear edge. This is the restart of the boundary layer after the gap as there is no recirculation according to Fig. 5.11(a).

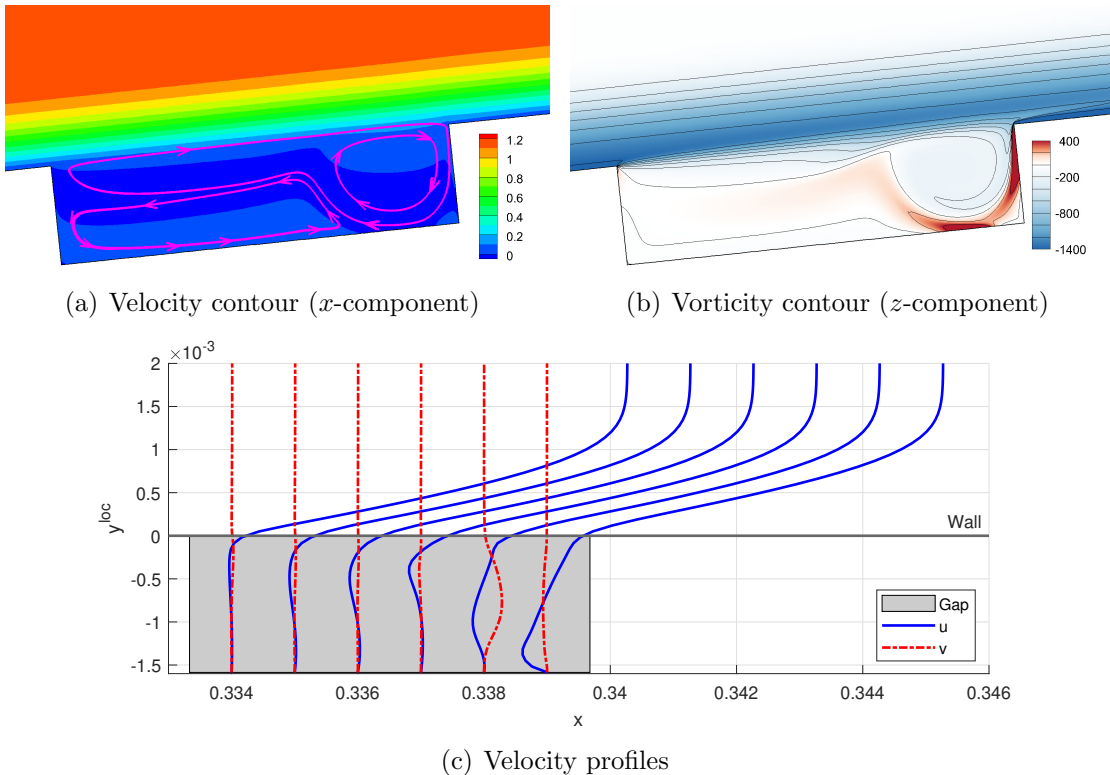


Figure 5.11: Baseflow in the gap region.

The disturbed fields are computed and the baseflow is subtracted to obtain the disturbance fields of TS waves. In the gap region of interest the TS waves of 60 kHz frequency are compared with those in the clean case in Fig. 5.12. Fig. 5.12(b) shows that the incident TS waves are reflected at both the leading and trailing edges of the gap. These waves ideally should have the same frequency as the incident TS waves, and are propagating in the direction of roughly 30 degrees with respect to the wall normal. Compared with the TS waves, these reflected waves are short in width in the flow direction as indicated by the dense contour lines. The two

arrays of reflected waves will merge as they travel away from the gap and can be unphysically reflected back at the inflow boundary of the reduced domain, causing data contamination. An additional sponge region is therefore necessary to absorb the original reflected waves. The field in Fig. 5.12(b) depicts the decontaminated results.

We record the local maximum of the amplitude field of the disturbances. Fig. 5.13 plots the distribution of the disturbance amplitude of tangential and normal velocity components in the body-fitted coordinate system (shown in Fig. 5.1(a)) of the 60 kHz TS waves. The blue region indicates low amplitude of disturbances while the red region is more energetic, and the two sub-figures have the same scale. According to Fig. 5.13(a) it is evident that the presence of the gap modulates the TS waves, leading to much larger amplitude of the tangential component near the leading edge of the gap. A local maximum in the boundary layer near the trailing-edge is also observed. Moreover, a ring shaped oscillation inside the gap is found on top of the high vorticity region in Fig. 5.11(b). This could infer to a flow instability. As for the normal component in Fig. 5.13(b), the maximum is found at the top corner of the trailing edge, which is significantly larger than the amplitude in the vicinity. Therefore if the n -factor is computed based on the normal velocity component, a much higher spike would be found compared with the n -factor based on the tangential velocity component. However, we keep the convention to generate the n -factor curves based on the tangential component of the disturbance velocity,

The n -factors obtained for 60, 50, 40, and 30 kHz TS waves are shown in Fig. 5.14(a) with the baseline results as reference. It shows that in general the n -factors have significant jumps near the gap while they converge to the baseline results downstream, inferring this gap has a regional influence to the growth of the TS waves. However, before the jump the n -factors first experience a drop, which is clearer in Fig. 5.14(b) for the difference of n -factors of the gapped case and baseline in Fig. 5.14(b). In addition, we observe that the larger the baseline n -factor is at the gap region, the larger the jump is in the corresponding gapped result.

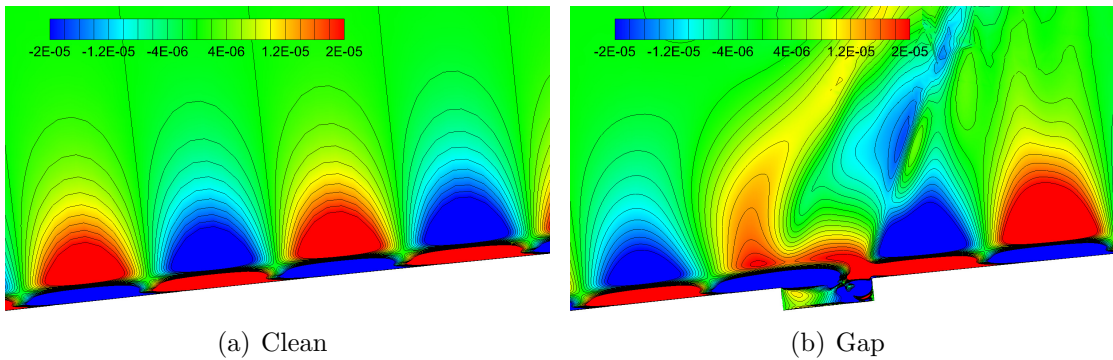


Figure 5.12: Comparison of TS waves of 60 kHz frequency in the gap region.

5.7 Effects of three-dimensionality and swept geometry

Having studied the influence of the 2D gap on the disturbance growth, we next focus on the 3D case. The computational mesh for the 3D simulations is generated

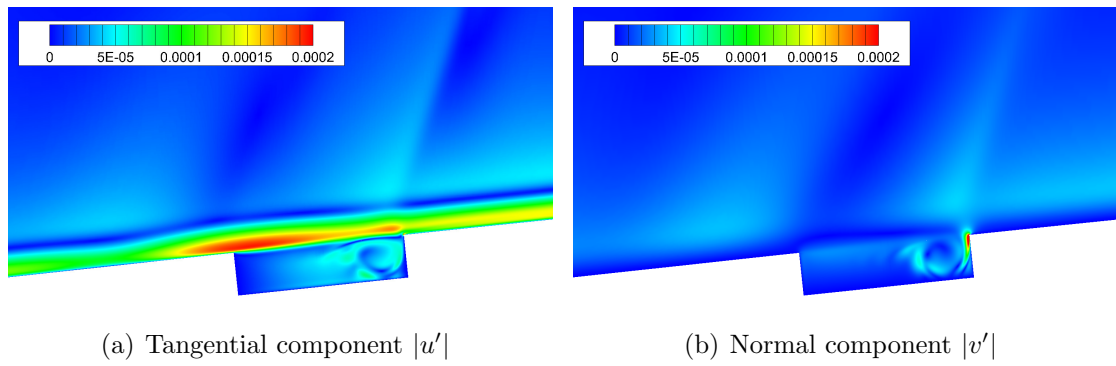


Figure 5.13: Amplitude of velocity components.

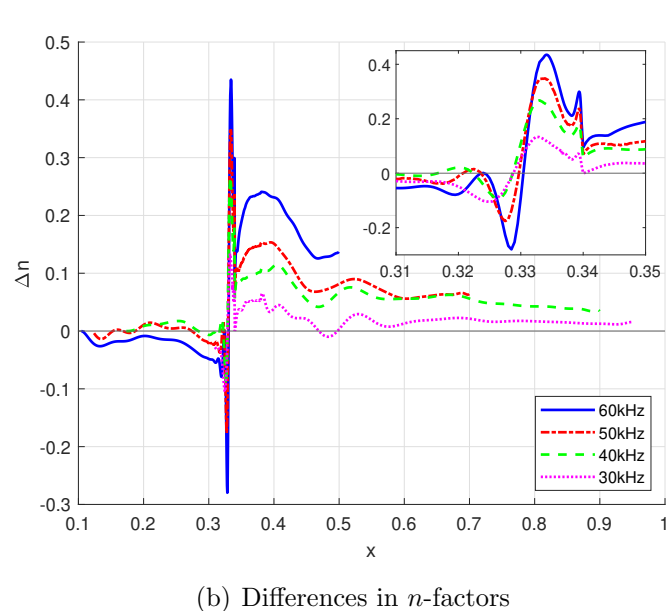
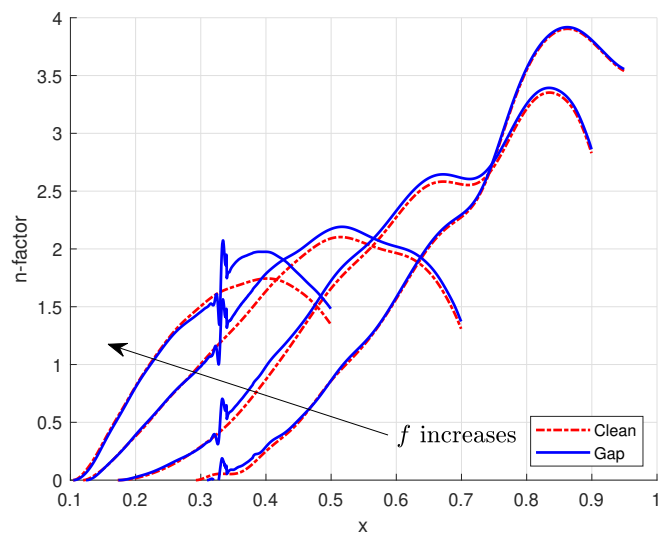


Figure 5.14: N -factor comparisons of the clean case and the gapped case.

by extruding the 2D mesh in the spanwise direction. Three layers are used for the extrusion, which has been tested to well resolve a single spanwise wave with P3 expansion. The spanwise wavenumber $\beta = 1.2 \times 10^4 \text{ m}^{-1}$ is first considered. This spanwise wavenumber corresponds to a ratio of the length of gap to the width of extrusion of 8.83.

The steady baseflow computation for the clean case is successful, where the SFD residual drops below the tolerance of 10^{-10}). However, in the gapped case we remark that when using the SFD to accelerate damping the disturbances in the baseflow, the residual fails to drop below that desired threshold tolerance, and if the SFD parameters are not particularly adjusted. Conversely, the residual periodically oscillates at certain level. This abnormal behavior has not occurred in the clean cases whether 2D or 3D. The snapshot of the instantaneous flow field is therefore of our interest. Since the SFD numerically suppresses the time-dependent variations, the current flow field is unphysical. The SFD is therefore turned off and the field is marched in time for three additional convective time scales, which is sufficient for the slowest waves to propagate over the computational domain in this case. To obtain the snapshot of the disturbances, the current flow field is time averaged and the average field subtracted. A slice in the $x - y$ plane is shown in Fig. 5.15. We observe that the flow inside the gap experiences oscillation without any disturbances introduced upstream. This oscillation causes the undamped SFD residual. The oscillation inside the gap excites the boundary layer above and adjacent downstream, shedding travelling crossflow waves. This receptivity-like process will be referred to as gap induced receptivity.

The excited crossflow waves have very short wavelength compared with the general crossflow wavelength, i.e. 3–6 times the local boundary layer thickness. This indicates a more refined mesh is necessary to simulate the downstream development of the waves. To save the computational resources, a new set of mesh embedded in the initial simulation is used as illustrated in Fig. 5.1(c), where the boundary layer mesh is refined in the streamwise direction. This domain sits in the interval of 0.23–0.55 of the original mesh in Fig. 5.1(b). Therefore boundary data are provided by the initial embedded simulation. After re-computing the baseflow, the boundary layer velocity and temperature profiles outside the gap in the initial and further reduced domain are compared and the results at $x = 0.3$ and $x = 0.5$ are given in Fig. 5.16. For the boundary layer profiles of major fields, i.e. streamwise and spanwise velocity components and temperature, good agreements are achieved as shown in the comparisons. Discrepancies are observed for the normal velocity components. However, apart from the fact that the normal velocity only weakly influence the growth of disturbances in a laminar boundary layer without separation, the relative differences in magnitude are $O(10^{-4})$ of the streamwise velocity magnitude. Such a difference is therefore well tolerated. Fig. 5.17 provides the comparison of Cp distributions, where the results are on top of each other and further shows the successful boundary condition enforcement.

As for the gap region, it is first discovered that two waves present in the spanwise direction at the current settings, where three layers of P3 element provide insufficient spanwise resolution. Therefore the previous spanwise wavenumber is doubled, leading to $\beta = 2.4 \times 10^4 \text{ m}^{-1}$ to be simulated. The disturbance field at this new spanwise wavenumber in the gap region is shown in Fig. 5.18(a). As expected, the flow in the gap keeps oscillating, and excites crossflow waves downstream. Only one

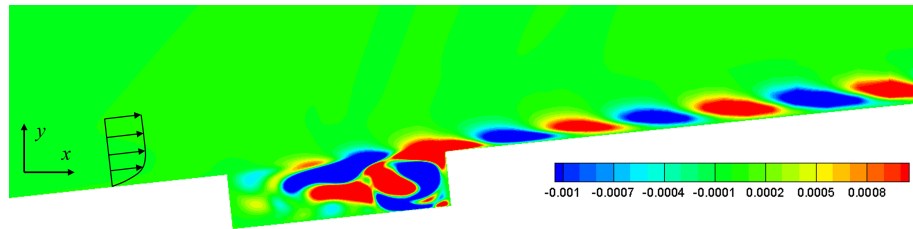


Figure 5.15: Gap induced oscillations of the velocity in the x -direction.

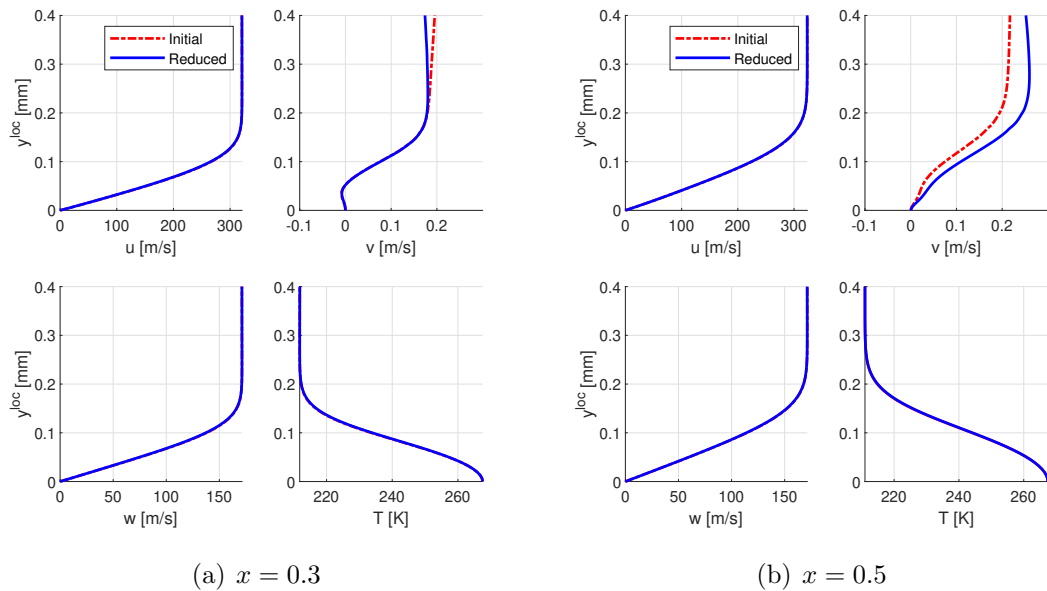


Figure 5.16: 3D boundary layer profile comparisons of the initial and reduced simulations.

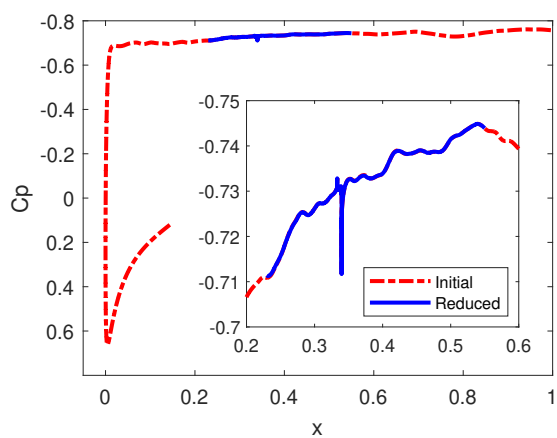
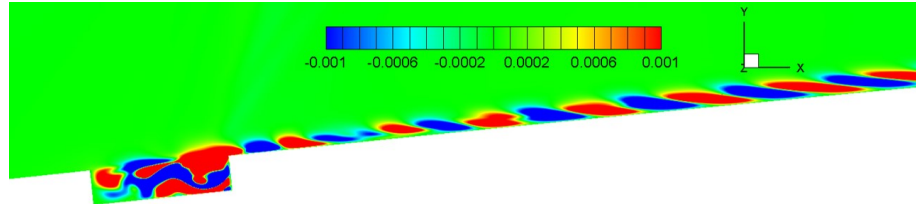


Figure 5.17: Pressure distribution comparison of the initial (Mesh 2 in Fig. 5.1(b)) and reduced (Mesh 3 in Fig. 5.1(c)) simulations.

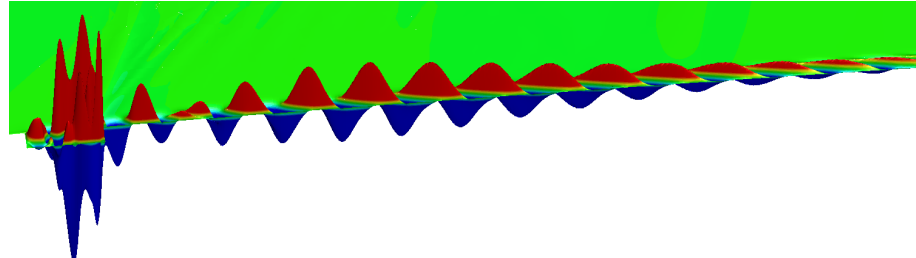
wave is checked to be present in the spanwise direction, showing sufficient resolution. An enlarged view in Fig. 5.18(b) shows that these crossflow waves finally decay in the selected domain. However, there is a critical difference compared with the field in Fig. 5.15. In the new case, the disturbance field is not as clean as the previous one since the excited waves have more than one streamwise wavenumber, which can be determined from the deficit in the waves. A bottom view of temperature disturbances on the wall is shown in Fig. 5.18(c). The disturbances (waves) extend not in the x -direction but in the streamwise direction.

To further confirm the excitation of multiple waves, a few sampling points are set both inside and downstream of the gap to record the time history of disturbances. Fig. 5.19(a) displays the disturbances on the momentum components ρu , ρv , and ρw at sampling points $(0.339, 0.0895, 0)$ (inside) and $(0.355, 0.0928, 0)$ (outside). It has been recorded for twelve convective time scales, but for clarity only the first two are shown. In the time history of the $(\rho u)'$ signal it is observed that the disturbances inside and outside have a synchronized oscillation, inferring the same main oscillation frequency. This is further confirmed in Fig. 5.19(b), where the fast Fourier transform (FFT) is performed to obtain the single-sided amplitude spectrum versus frequency. The main oscillation frequency is approximately 9.5 while the high-order harmonics are present in both signals. Moreover, the $(\rho v)'$ signal inside the gap in Fig. 5.19(a) also shows a typical pattern of wave superposition, inferring a complicated oscillation inside the gap.

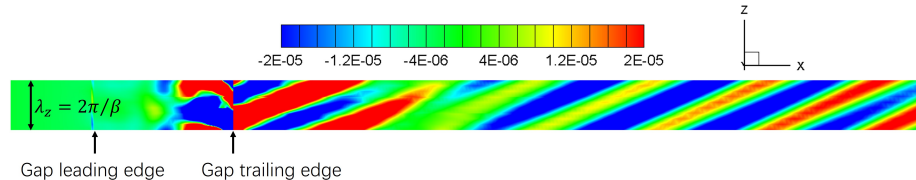
In the current simulation, as a preliminary study the disturbances of $\beta = 2.4 \times 10^4$ m^{-1} are self-excited due to the constrained spanwise width of the computational domain. However, for a wider quasi-3D gap, disturbances of spectra of spanwise wavenumbers may be generated due to the instability inside the gap. The e^N analysis will shed more insight only if better understanding of the flow mechanisms are further provided. For instance, in the classical e^N analysis the amplitude of the disturbances does not influence the results as long as the disturbances experience a linear growth. However, due to the gap-induced receptivity, excited crossflow waves are travelling, and have fixed amplitudes (which in this case are greater than 0.4% of the freestream velocity and close to the linear growth limit). Therefore the amplitudes of the artificially introduced disturbances for the e^N analysis may matter due to their potential interactions with the gap-induced travelling crossflow waves.



(a) Disturbance of the x -component velocity

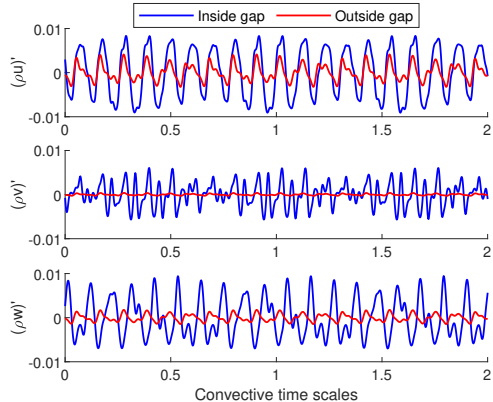


(b) Disturbance of the x -component velocity (enlarged view)

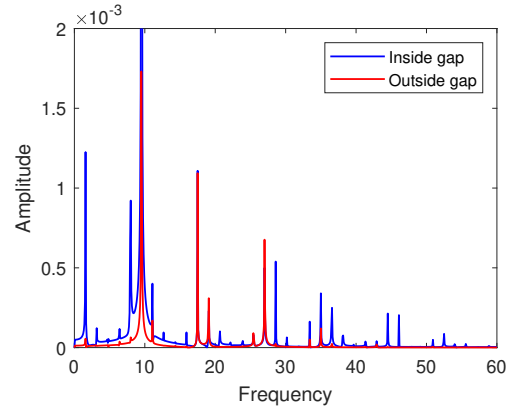


(c) Disturbance of the temperature on the wall (bottom view)

Figure 5.18: Gap induced receptivity at $\beta = 2.4 \times 10^4 \text{ m}^{-1}$. Flow from left to right. (b) shows the $z = 0$ plane in 3D, where the additional axis represents the disturbance of the x -component of the velocity.



(a) Disturbance signals



(b) FFT of the $(\rho u)'$ signals

Figure 5.19: Time history and FFT analysis results inside and outside the gap at sampling points $(0.339, 0.0895, 0)$ and $(0.355, 0.0928, 0)$, respectively. In (a) the first two convective time scales out of twelve are shown for clarity. The maximum single-sided amplitude in (b) reaches 6×10^{-3} but it is not shown for clarity. The symbol $(\cdot)'$ denotes the disturbance of the corresponding field.

Chapter 6

Incompressible laminar boundary layer flow over a quasi-3D gapped swept plate

6.1 Introduction

In Section 5.7 we illustrated the laminar boundary layer flow over a gap irregularity on a CRM-NLF swept wing section can experience self-sustained oscillations inside the gap, provided the transonic flow and the Reynolds number are close to realistic cruise conditions. According to our preliminary study, such oscillations not only excite crossflow waves in the vicinity of the gap but also produce a full spectrum of temporal frequencies. Since the underlying fluid mechanisms are not fully understood, in this chapter we will zoom in to the vicinity of the gap to better understand of the self-sustained oscillations at the presence of crossflow.

The boundary layer flow over the gap is more widely known as open cavity flow in the literature. The subtle difference between open cavity and gap may be the size [159], where the majority of the studies have focused on open cavities with large geometry deficits compared with the local boundary layer thickness. In the current work, we keep using the term “gap” for both the consistency with the previous chapters and highlighting the small-sized geometry of interest.

The study of the gaps was initiated as a beneficial approach for boundary layer tripping in wind tunnel experiments [160]. Gap effects on laminar flow transition were investigated no later than the mid-60s [161]. In recent years, Beguet et al. [160] summarized a series of works carried out at ONERA in the past decades. The gap effects were modelled in terms of variation in N -factor curves. Crouch et al. [161] performed experimental studies on the gap effect on the natural transition dominated by TS instability. The shifting on the transition location and on type of transition (from TS to bypass) was categorized for gaps of different sizes, and a variable N-factor model was developed. As for the computational works, in 2D compressible flow simulations by Zahn and Rist [36], a steady baseflow was obtained over a deep short gap (comparable with local boundary layer thickness). The steadiness was attributed from the observations that shear-layer mode instability was not excited for this short gap [36]. This agrees with our 2D results in Section 5.6.

Although started earlier, regarding transitional analysis gaps are much less well documented compared with those for forward-facing and backward-facing steps, and

most simulations are limited to 2D flows. One reason is that even a simple gap has several geometrical parameters [45], i.e. depth, length, and width (in the spanwise direction). The rich geometry variation typically leads to different recirculation patterns inside the gap as discussed by Sinha et al. [162], and the subsequent complicated instability behaviors [160]. The three main types of instabilities in a compressible flow are shear mode, wake mode, and three-dimensional mode.

The shear-layer mode instability originates from the interaction of the shear layer over the cavity and acoustics emitted at the downstream corner of the cavity (where it is mostly studied). The acoustic waves propagating upstream excite the shear layer while the shear layer selects the modes to be energized [163], which distinguishes the shear-layer mode from the pure acoustic resonance [164]. For the visualisation of the shear-layer mode related acoustic emission, Krishnamurty [165] provided clear Schlieren images for both subsonic and supersonic flows. Schlieren images were also shown in the vicinity of the cavity by Cattafesta et al. [166], where they observed three shear-layer modes' structures have much larger scale than the boundary layer thickness at the leading edge of the cavity. This provides additional evidence that shear-layer modes develop more easily in large cavities than in small gaps. As for the numerical side, Brès performed compressible DNS systematically in the cavity and informative animations are offered along with his thesis [164, 167]. Since the shear-layer mode involves acoustic feedback, compressibility plays a significant role and is therefore necessary to include in the simulations. This was further numerically tested by Martin et al. [168]. The shear mode is also known as a Rossiter mode [169]. Rossiter developed a semi-empirical formula to predict the resonance [169], which reasonably agrees with experiments. However, this formula predicts a series of potential modes while the particular excited modes are not identified [164].

The wake mode is another type of major instabilities in a cavity. It is a pure hydrodynamic instability that presents when large scale vortices shedding from the leading-edge of the cavity, typically leading to violent changes in the flow field. Both shear-layer mode and wake mode do not rely on the three-dimensionality while both of them can be modulated in the spanwise direction in 3D flows [168, 170], where Mathias & Medeiros reported the modulated shear-layer modes typically have larger spanwise wave lengths than the 3D mode introduced below [170]. In contrast, the three-dimensionality can stabilize the wake mode [164]. Suponitsky et al. [171] demonstrated that a random 3D disturbances would shift the wake mode to the shear-layer mode regardless of the strength of the disturbances.

Finally, for the 3D flows in the cavity (or gap) a three-dimensionality mode instability not present in 2D flows comes into existence. The 3D mode (also known as centrifugal or Görtler mode) instabilities arise from centrifugal effects in the recirculation region next to the trailing edge of the cavity. The presence of a similar instability has been previously reported in lid-driven cavity flows, Couette flows, and flows over backward-facing steps. Brès and Colonius [73] argued that since a forward-facing wall sets up a recirculation region, the corresponding flow would experience a centrifugal instability from the inviscid point view. The viscosity has a stabilization effect on such flows. Faure et al. [172] and Vicente et al. [74] both provided good visualizations and comparisons of the experiment and simulation results. The patterns of their computed 3D mode agree well with the experimental results, showing the improved understanding of such instability. Further reviews and studies of the 3D mode are provided in Refs. [74, 159, 164, 173]

Returning to the small gap case of interest discussed in Section 5.7, both shear-layer mode and wake mode are not likely to play a significant role since the wake can hardly develop in the shallow gap and the short chordwise length prevents the shear-layer mode oscillation, as addressed by Zahn and Rist [36]. Moreover, in Chapter 5 the observed oscillations in the gap are characterised by a high spanwise wavenumber (e.g. $\beta = 2.4 \times 10^4 \text{ m}^{-1}$), which typically suppresses the development of the shear-layer mode according to the study by Mathias and Medeiros [170]. The oscillations are therefore considered a special form of 3D instability in the presence of crossflow. To better understand such a flow and instability, particularly the most energized frequency and spanwise wavenumber, we set up quasi-3D incompressible flow simulations on a swept plate with a spanwise gap, as illustrated in Fig. 6.1. Calling that in the 3D compressible flow simulation of the previous chapter, the Mach number is below 0.3 in the gap, this study therefore includes all the underlying hydrodynamic mechanisms and reasonably reduces the computational cost, as well as taking full advantage of our simulation tool Nektar++ to use Fourier expansions in the spanwise direction.

6.2 Quasi-3D boundary layer flow over a swept plate with gap

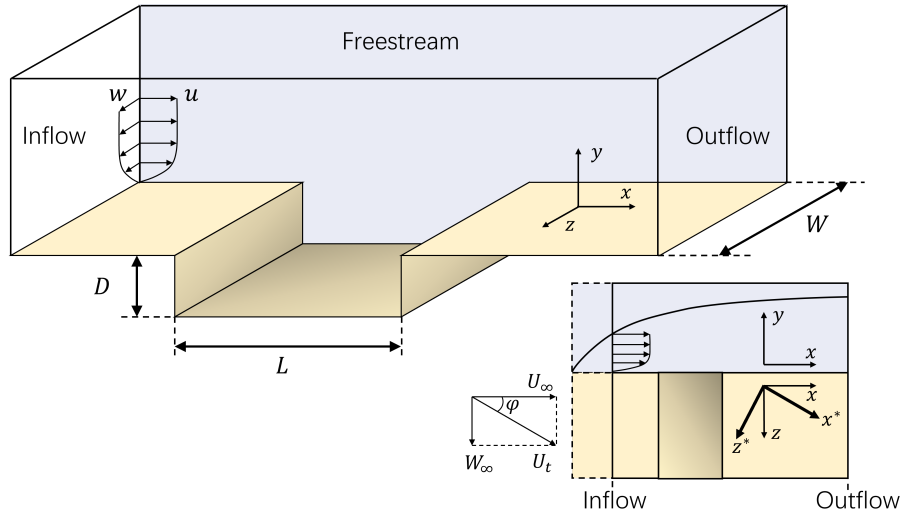


Figure 6.1: Configuration of the computational domain over the swept plate.

The configuration of the swept plate simulation is shown in Fig. 6.1, where the depth, length, and width of the gap are denoted by D , L , and W , respectively. This model problem is set according to the flow conditions in the gap region in Section 5.7. The aspect ratio (L/D) of 4 is therefore preserved. The spanwise ratio (W/D) of 2 is applied to allow modes of different harmonic spanwise wavenumbers to develop. As for the freestream, the velocity component in the x -direction (U_∞) is twice of that in the z -direction (W_∞), leading to a swept angle $\phi = 26.57$ deg of the plate. This velocity direction reproduces similar local flow conditions at the gap in the 3D CRM-NLF case. In the $x - z$ plane another Cartesian coordinate system (x^*, z^*) is set, where x^* is in the same direction as the freestream velocity U_t . The Reynolds

numbers at four key positions in the x -direction are listed in Table 6.1, where the local Reynolds number is based on the freestream total velocity, U_t , namely

$$Re_x = \frac{U_t x}{\nu}.$$

Accordingly, the depth based Reynolds number is $Re_D = 7500$.

Table 6.1: Re_x at key positions.

Positions	Inflow	Leading-edge	Trailing-edge	Outflow
x	0.0	0.2	0.4	1.0
$Re_x/10^6$	1.57	1.6	1.63	1.72

As for the boundary conditions, since the leading-edge of the swept plate is not included in the domain to avoid the fine mesh at the beginning of the boundary layer and to focus on the gap region, a rotated Blasius velocity profile is enforced at the inflow boundary near the wall. The Blasius profile can be obtained following the governing equations and solving approach in Appendix D.2, where the Hartree parameter should be set zero. In this case the zero pressure gradient (ZPG) is considered in this problem. The relative pressure at the freestream is therefore zero, and the high-order convective boundary condition [174] is adopted at outflow. In the z -direction, the periodic boundary condition is set.

A hybrid spectral/ hp -Fourier simulation is carried out [175]. In the $x - y$ plane a 2D mesh is generated and within each element the field is approximated by the spectral/ hp method. The z -direction is selected as the homogeneous direction, where the variations of the fields are expressed in form of Fourier expansions [176], such that periodicity is automatically enforced. An description of the 2D spectral/ hp element and the Fourier expansion is available in Ref. [177, 178]. The homogeneity in the z -direction leads to the base spanwise wavenumber $\beta_0 = 2\pi/W$ ($\lambda_0 = W$). As mentioned above, we consider the incompressible flow for solving efficiency while keeping all the physics of interest. The incompressible Navier-Stokes equations are solved by the velocity correction scheme [179] in Nektar++. To stabilize the high-order simulations, we adopt the classical spectral vanishing viscosity (SVV) [180, 181] with exponential kernel for both in-plane spectral/ hp expansion and Fourier expansion. By including high-frequency diffusion, the SVV function acts as a sink of energy for high-frequency components while having little influence on the low-frequency components.

Fig. 6.2 shows the computational mesh in the $x - y$ plane. The number of elements on this plane is 4133. The simulations are performed with 5th order expansion for velocity fields and 4th order expansion for pressure field. This setting follows the Taylor-Hood approach, where pressure expansion is one order lower than the velocity expansion to satisfy the inf-sup condition [176]. In the z -direction, 64 planes are used corresponding to 32 full Fourier modes. The above setting leads to a total degrees of freedom of 8 183 232. Since simulations are unsteady in nature due to the self-sustained oscillation, a statistically stationary base state is sought. The stationary state is achieved when the time-averaged modal energy of each Fourier mode does not change. The modal energy of the k -th Fourier mode is defined by

[176]

$$E_k(t) = \frac{1}{2} \int_{\Omega} ||\tilde{\mathbf{u}}_k^2|| d\Omega, \quad (6.1)$$

where $\tilde{\mathbf{u}}_k$ is the Fourier coefficient of the k -th mode of the velocity. The time histories of modal energy are recorded and averaged over 160 convective time scales. The averaged values are plotted in Fig. 6.3 in form of a spectra. The 0th mode is the mean mode, and the drop at the 25th mode is because the SVV cutoff eliminates higher Fourier modes. This plot shows that the modal energy for the first mode drops to the level of $O(10^{-8})$ with respect to the mean mode, which is $O(10^{-1})$, while the modal energy for the last undamped mode is two orders lower, indicating a sufficient resolution in the Fourier direction since the higher frequency modes are relatively insignificant as suggested by Slaughter et al. [176].

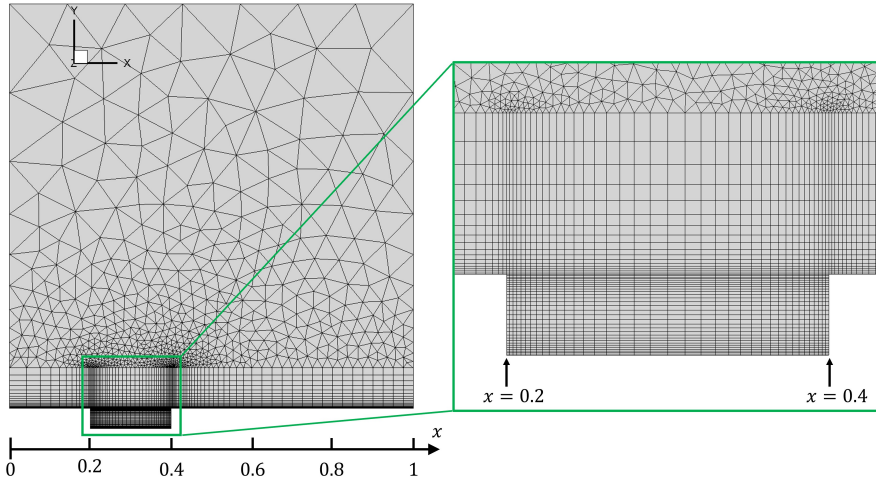


Figure 6.2: Computational mesh and expanded view in the gap region.

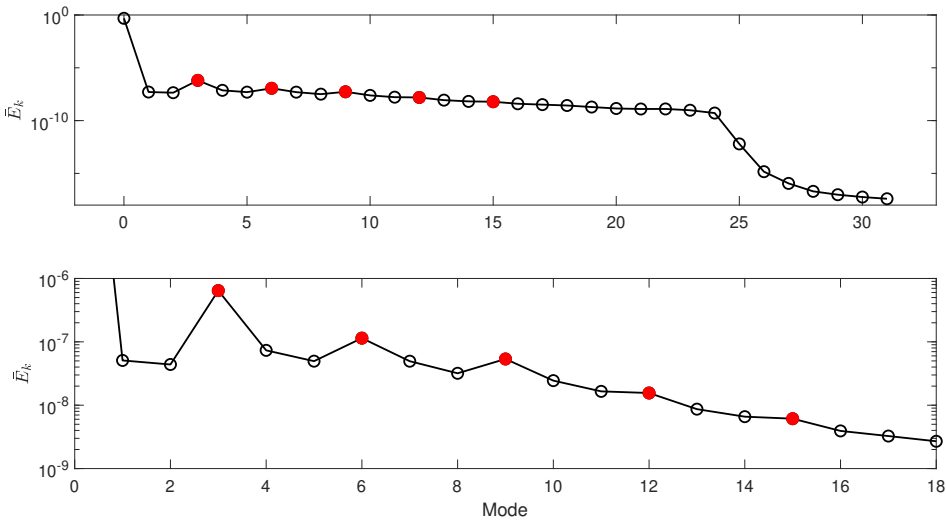


Figure 6.3: Averaged modal energy of the Fourier modes. The bottom subplot shows the expanded view of the top subplot. Local peaks are highlighted by red dots.

In addition, we remark that the energy distribution in the spectrum is not monotonically decreasing but has several peaks. This feature is better shown in subplot

on the bottom of Fig. 6.3, where the 3rd, 6th, 9th, 12th, and 15th modes are more energized than the adjacent modes. To better understand the underlying flow behavior, the transient field is decomposed into different Fourier modes (corresponding to different spanwise wavenumber β), and the first ten modes are shown in Fig. 6.4 at the same scale. The flow field for each Fourier mode is oscillating in the gap region. This infers a hydrodynamic instability inside the gap and a complex superposition of a series of unstable modes with different spanwise wavenumbers. Moreover, Fig. 6.4(c) clearly shows that the 3rd Fourier mode is significantly more energetic than the others, which agrees with the peak at the 3rd mode in Fig. 6.3. The 3rd mode not only experiences stronger self-sustained oscillation inside the gap but also includes crossflow mode-like waves downstream of the gap. In the x -direction, these waves have a wavenumber of approximately 6.5 times the depth of the gap. The origin of these waves will be discussed in the next section. On the other hand, flow fields corresponding to the other Fourier modes also include downstream waves while the wavenumbers are shorter in the x -direction and weaker in strength, e.g. the 7th mode in Fig. 6.4(g).

Fig. 6.5 displays a snapshot of the wall shear stress magnitude from the top view. The white arrows show the freestream direction from top left to bottom right. The large light region is the gap, showing the wall shear stress in the gap is much lower than outside. Inside the gap, the wall shear stress magnitude is larger near the trailing edge than near the leading edge. In this figure a streaky pattern is observed after the gap while the field is uniform before the gap. The direction of the streaks are almost aligned with the freestream. Three major peaks are shown as the yellow contours outline, which corresponds to the modulation by the dominate waves in the 3rd Fourier mode. The streaky pattern gets diffused as it progresses downstream.

6.3 Discussion on the origin of the downstream waves

In the previous section, we have shown the presence of a self-sustained oscillation inside the gap using the incompressible flow simulation. Due to the lack of large scale structures in the mean mode, such oscillation is considered to stem from the centrifugal instability in the recirculation region next to the trailing edge of the gap as shown in Fig. 6.6. Brès [164] first demonstrated this point at the inviscid limit by applying Rayleigh discriminant (used determine the presence of a centrifugal instability) in a cavity inspired by the analysis by Barkley et al. [182] on a forward-facing step, while the viscosity was shown to have a stabilizing effect [164].

Previous research mainly focused on the instability mechanism inside the gap. However, in the current work we adopt a larger domain (compared with the depth of the gap) including part of the downstream region, where we observed crossflow mode-like waves, e.g. those in Fig. 6.4(c). Note that these waves are not only present in the most energetic 3rd mode but also in all modes. To the best of our knowledge, these crossflow mode-like waves after the gap have not been reported in other studies.

Two reasonable assumptions can be made for the generation of these waves. The first one is that they are inherent convective instability modes of the boundary layer, and are excited by the oscillations in the gap. Otherwise, similar to the oscillation

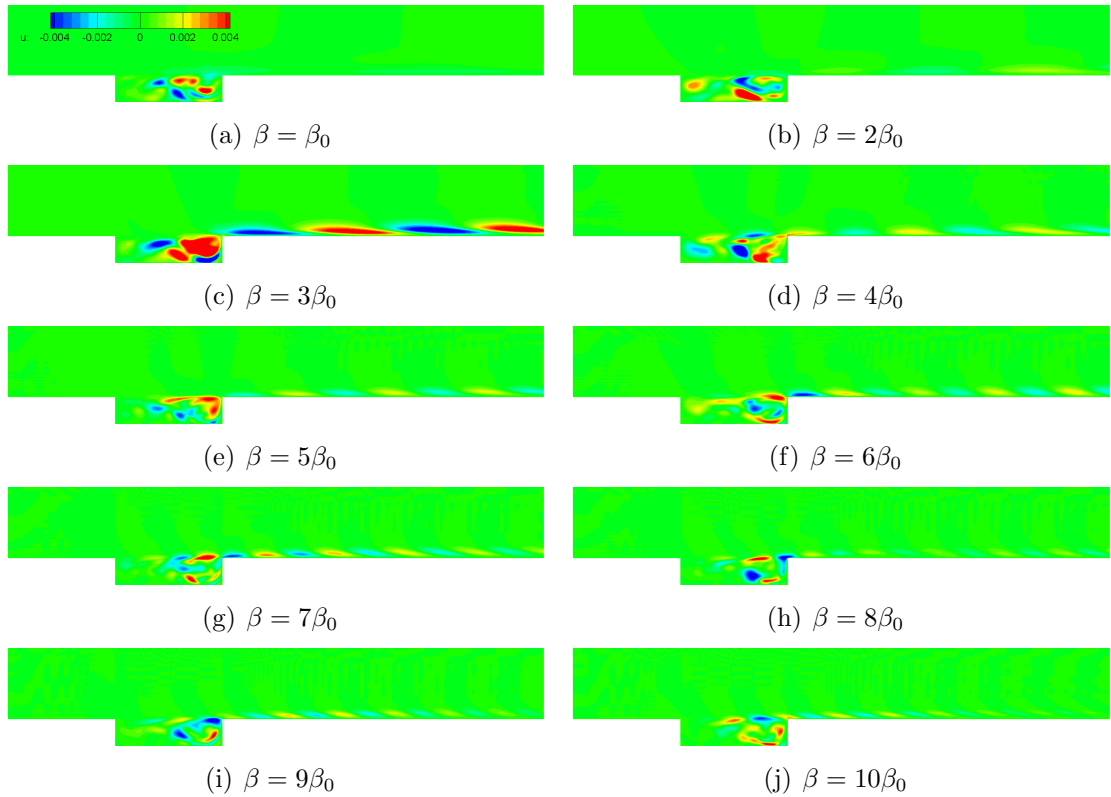


Figure 6.4: Chordwise velocity (u) contours of the self-sustained oscillation of the first ten Fourier modes. All the plots use the same scale.

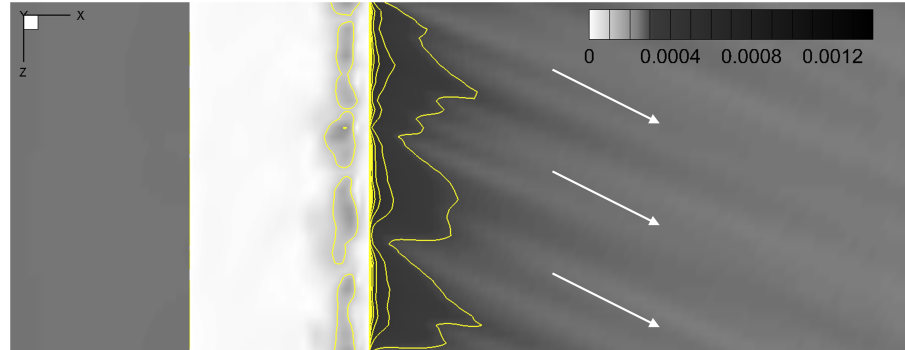


Figure 6.5: Top view of the wall shear stress magnitude. The write arrows show the freestream direction. The color is adjusted to better visualize the streaks.

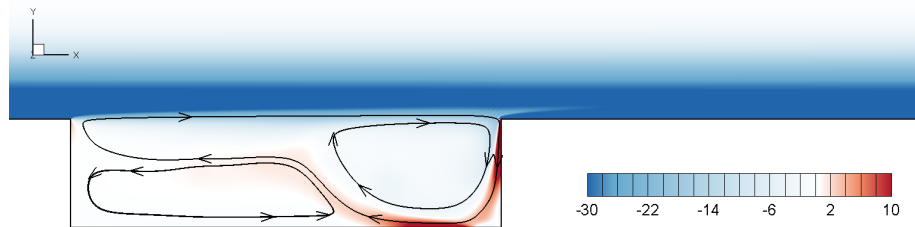


Figure 6.6: Vorticity field (z -component) and streamlines in the gap. Freestream comes from left to right.

inside of the gap, these waves also raise from a global instability mode. In the first assumption, however, for a swept plate without pressure gradient, the boundary layer velocity profile is the ideal rotated Blasius profile, where no inflection point exists while the inflection point is a necessary condition for crossflow instability. Fig. 6.7 depicts the wall pressure distribution in the x -direction. It shows the gap modulates the pressure near its trailing edge, and an adverse pressure gradient is formed after the gap. The effect of this pressure gradient on the crossflow direction (denoted by z^* in Fig. 6.1, perpendicular to the plane spanned by the freestream direction x^* and wall normal direction y) can lead to a crossflow component as a secondary flow.

This is confirmed by the boundary layer velocity profile in Fig. 6.8(a) at $x = 0.45$ (after the gap), where the velocity components are projected on to the (x^*, y, z^*) coordinate system and their components are denoted by $(\cdot)^*$. It clearly shows the presence of the crossflow component w^* near the bottom of the boundary layer. However, the crossflow component is much smaller compared with the freestream velocity and it is therefore scaled by 100 for better visualisation. The 3D profile is also provided in Fig. 6.8(c). Since the crossflow component vanishes at both ends of the boundary layer, such a profile brings the existence of an inflection point as a source of crossflow instability [26]. To better evaluate the velocity profile modulation by the gap, the differences with respect to the rotated Blasius profile at $x = 0.45$ and 0.9 are computed as shown in Fig. 6.8(b). At $x = 0.45$, although the difference on the crossflow velocity component is still smaller than that on the streamwise velocity component, the differences are of the same order. As the flow moves downstream to $x = 0.9$, the velocity modulation gets smaller and the profile becomes closer to the rotated Blasius profile, which infers the influenced region by the gap is local. In general, the modulation is more significant near the bottom of the boundary layer. This can be related with the restart of boundary layer after the trailing edge of the gap, which is noticed by the larger vorticity amplitude in Fig. 6.6.

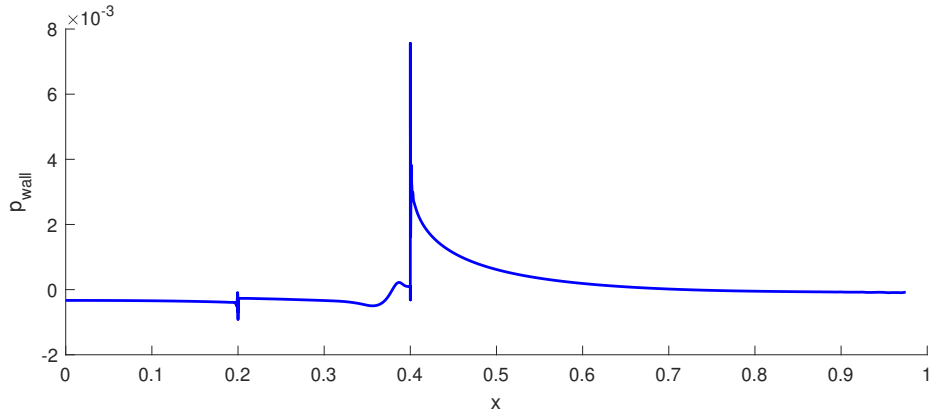


Figure 6.7: Wall pressure in the x -direction.

Sectional (1D) stability analysis is a suitable tool to examine whether the observed waves arise from crossflow instability. To perform the analysis, a spanwise wavenumber of $3\beta_0$ is used while the key parameter frequency remains to be determined. We therefore set a series of sampling points on the $z = 0$ plane of the field and record the time history of fluctuations to find out the dominant frequency of interest. The detailed positions of the sampling are listed in Table 6.2 and are

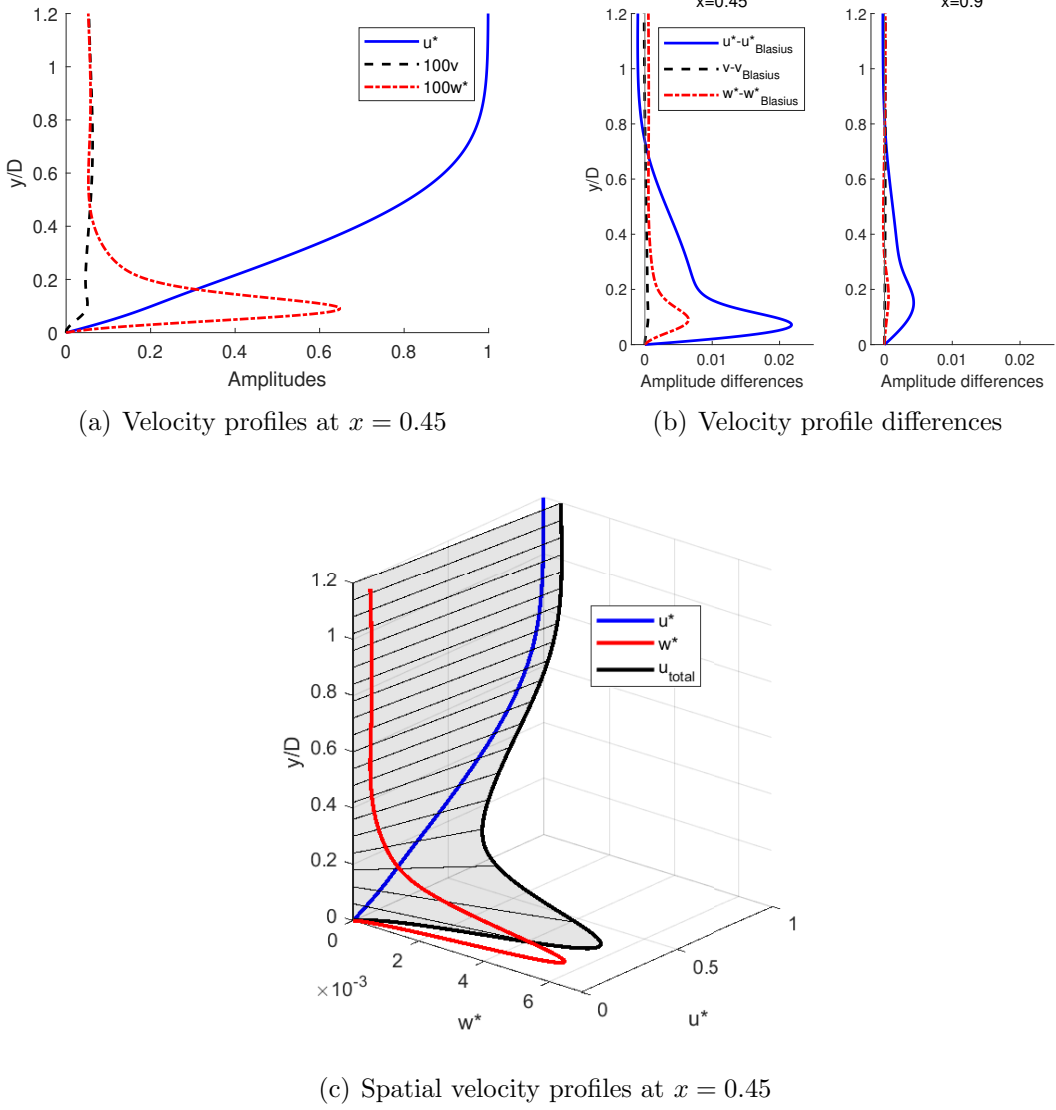
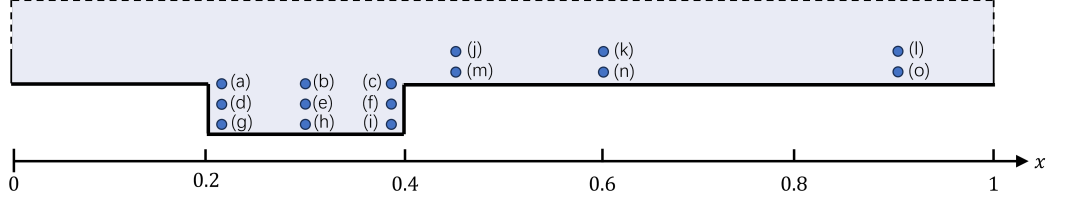


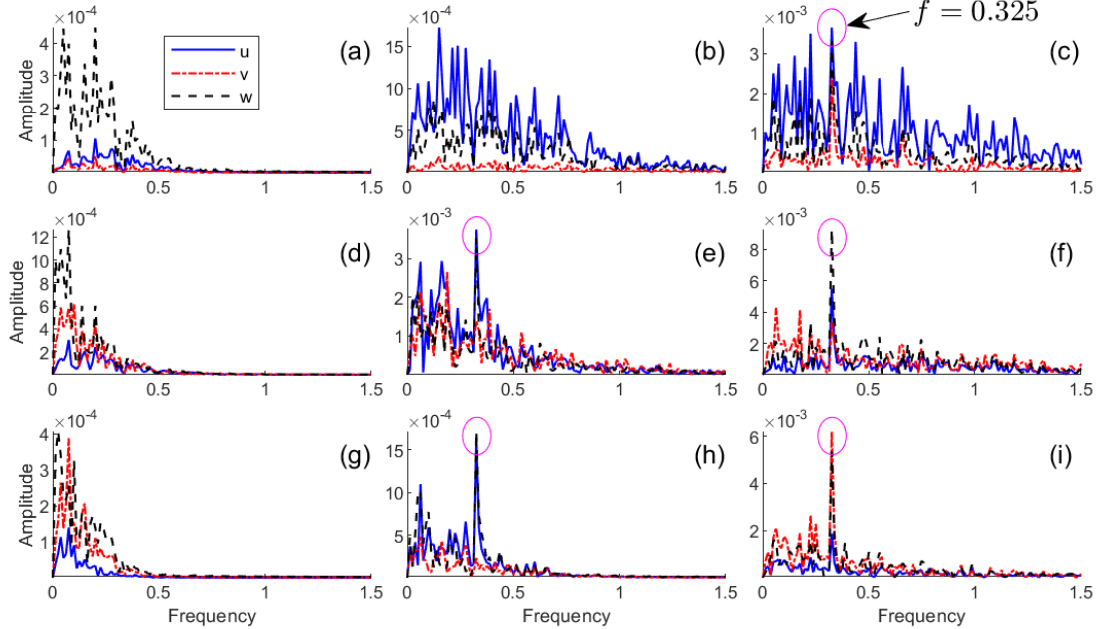
Figure 6.8: Boundary layer velocity profiles and differences with respect to the rotated Blaius profile.

also highlighted in Fig. 6.9(a) for clarity. A fast Fourier transform (FFT) is used to convert the recorded signals from time domain to frequency domain, and the spectra for u , v , and w signals are all shown in Fig. 6.9(b) for the points inside the gap (from (a) to (i)) and in Fig. 6.9(c) for the points outside the gap (from (j) to (o)). Sampling points (a), (d), and (g) are next to the leading edge of the gap, and (d) and (g) are associate with the weaker recirculation on the bottom left in Fig. 6.6. This figure shows that their oscillations have a much narrower spectrum compared with the rest of the points on the main recirculation on the right in Fig. 6.6. Additionally, frequency spectra at points (b) and (c) are particularly wide, possibly because of the strong shear at the interface of the gap and boundary layer. In the frequency spectra of points (c), (e), (h) and (i) significant peaks are observed at the same non-dimensional frequency of 0.325. This also agrees with the outstanding peaks in all sub-plots of Fig. 6.9(c) for the fluctuations outside of the gap, which suggests the frequency of the crossflow-like waves of the 3rd mode in Fig. 6.4(c).

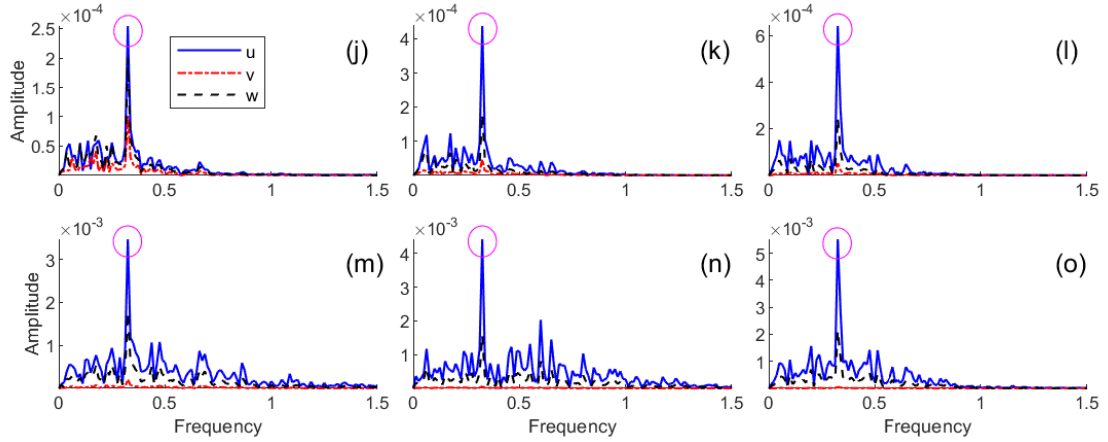
Sectional stability analysis is then performed with the obtained non-dimensional



(a) Distribution of sampling points



(b) Inside of the gap



(c) Outside of the gap

Figure 6.9: Disturbance frequency spectra (frequency vs. amplitude) at different sampling locations. The spectra are computed by FFT. The highest peak in each sub-plot except (a)(b)(d)(g) corresponds to a non-dimensional frequency of 0.325.

frequency 0.325 at $x = 0.45$ and 0.9 using the CoPSE3d package integrated in Nektar++ [49]. Since the package solves the 1D linear stability equations for compressible flows, we pick the hydrodynamic modes artificially by checking whether the density eigenfunction is negligible compared with the velocity eigenfunctions.

Table 6.2: Locations of the sampling points on the $z = 0$ plane.

Inside gap		
(a) – (0.205, 0)	(b) – (0.3, 0)	(c) – (0.395, 0)
(d) – (0.205, –0.02)	(e) – (0.3, –0.02)	(f) – (0.395, –0.02)
(g) – (0.205, –0.04)	(h) – (0.3, –0.04)	(i) – (0.395, –0.04)
Outside gap		
(j) – (0.45, 0, 03)	(k) – (0.6, 0, 03)	(l) – (0.9, 0, 03)
(m) – (0.45, 0.01)	(n) – (0.6, 0, 01)	(o) – (0.9, 0.01)

Fig. 6.10 shows the eigenspectra at the two positions, and the modes of interest are highlighted by red crosses. It is noticed two more discrete modes appear at $x = 0.9$ than 0.45. These eigenvalues are further refined using inverse Rayleigh iteration [49] to get a highly accurate eigenvalues and eigenfunctions. As listed in Table 6.3 the wave angles of these modes are all around –95 degrees. These wave angles suggest the corresponding modes come from the crossflow instability [52], which confirms effect of having the inflection point. We remark that however, since these eigenmodes have negative growth rates (i.e. α_i in Fig. 6.10 and Table 6.3), they are all decaying modes after excitation, and are unlikely to generate the waves we observed after the gap.

We next extract the waves from the DNS and eigenfunctions from the sectional stability analysis, and the profiles are compared in Fig. 6.11. It shows at $x = 0.45$ the DNS wave we observed in the simulation reach the maximum at a lower vertical position. As for $x = 0.9$ the vertical position for the DNS wave to reach the maximum is approximately the same as the LST mode 1. However, the shapes of the wave and eigenfunction are quite different particularly at lower vertical position near the wall. This difference in the comparison infers the crossflow-like waves observed in Fig. 6.4(c) are not real crossflow waves but could be a BiGlobal mode whose the eigenfunction is not a 1D function of vertical coordinate y but a 2D field in the $x - y$ plane.

To better understand this, a BiGlobal analysis in the $x - y$ plane as introduced in Section 1.3.1 is then performed by solving the linearized (incompressible) NS equations:

$$\begin{aligned} \frac{\partial \tilde{\mathbf{u}}}{\partial t} + (\mathbf{U} \cdot \nabla) \tilde{\mathbf{u}} + \tilde{\mathbf{u}} \cdot \nabla \mathbf{U} &= -\nabla p + \frac{1}{Re} \nabla^2 \tilde{\mathbf{u}}, \\ \nabla \cdot \tilde{\mathbf{u}} &= 0, \end{aligned} \quad (6.2)$$

where $\tilde{\mathbf{u}}$ is the linearized velocity, \mathbf{U} is the baseflow velocity. The baseflow is computed using the same settings as the DNS simulation except only 2 Fourier planes are used, leading to constant field distributions in the z -direction. Eq. (6.2) is solved after being transformed into an eigenvalue problem. More details are available in Ref. [183]. The BiGlobal results show that the most unstable mode is found to have the non-dimensional frequency of 0.355, with 9% relative difference to the dominate DNS frequency. As shown in Fig. 6.12, the spatial structure of this mode is also close to the DNS result for both inside the gap and in the downstream region. Fig. 6.12 also confirms that the absolute instability mode inside the gap basically sits on the main recirculation region near the trailing edge of the gap. Detailed eigenfunc-

tions at $x = 0.45$ and 0.9 are also compared in Fig. 6.13, where good agreements are achieved. The agreements finally indicate that the dominate waves downstream of the gap in the DNS result is a BiGlobal mode.

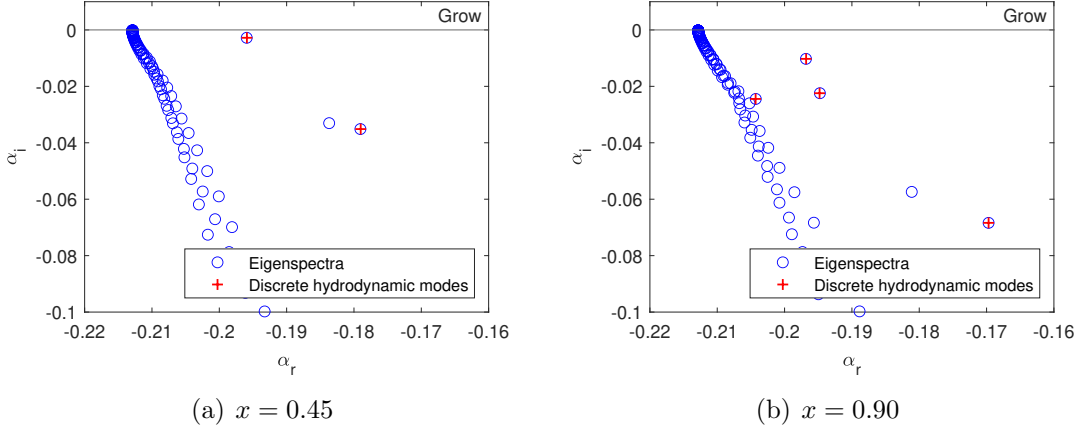


Figure 6.10: Eigenspectrum of the LST at different locations.

Table 6.3: Eigenvalues and wave angles from sectional stability analysis.

x	#	α_r	α_i	Orientation [deg]
0.45	1	-0.1790353	-0.03518669	-95.7723
	2	-0.1959312	-0.00278662	-93.9988
0.9	1	-0.1695965	-0.06856673	-96.7763
	2	-0.1948252	-0.02241802	-94.1081
	3	-0.1968162	-0.01026088	-93.9016
	4	-0.2041783	-0.02462411	-93.1437

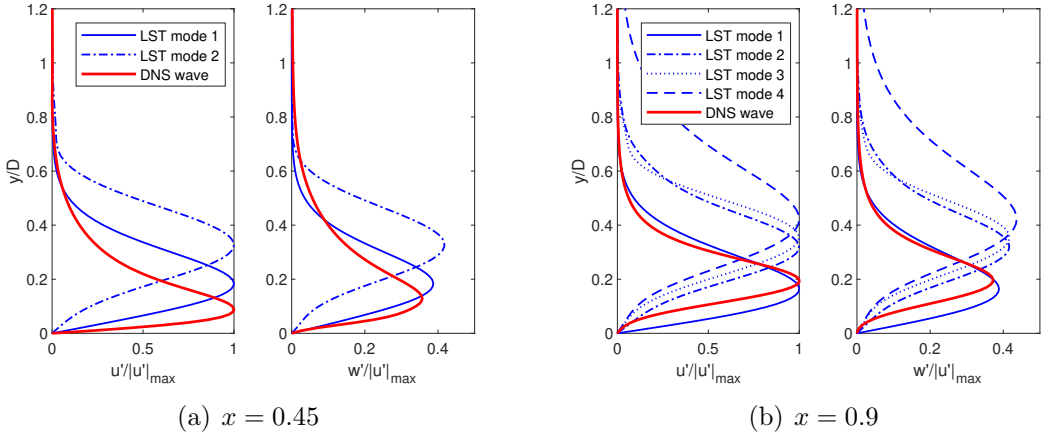
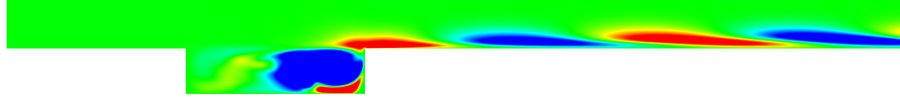
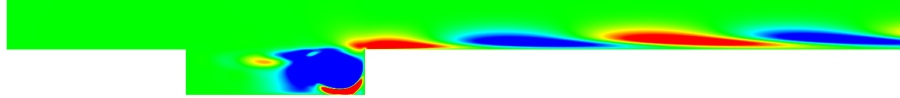


Figure 6.11: Comparisons of the LST eigenfunctions and shape of DNS waves at different locations.

After confirming the downstream waves arise from a BiGlobal mode, however, their physical nature in terms of the instability type is still left to be investigated.



(a) DNS wave



(b) BiGlobal mode

Figure 6.12: Chordwise component of velocity comparison of the DNS wave and BiGlobal mode.

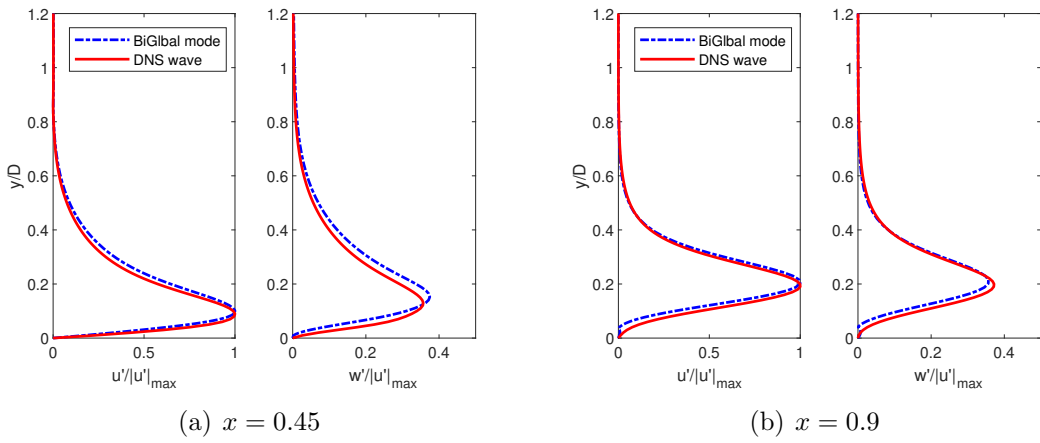


Figure 6.13: Comparisons of the BiGlobal mode and shape of DNS waves at different locations.

Providing the oscillations inside the gap arise from absolute instability, the downstream waves can either be the waves excited by the upstream oscillation and travelling downstream, showing a convective nature, or directly arise from the absolute instability intrinsic in the local boundary layer modulated by the gap. We perform the analysis by adopting the tool of structural sensitivity which is first introduced by Giannetti and Luchini [184]. The idea of structural sensitivity is to compute sensitivity of the leading eigenvalue with respect to the local eigenfunction amplitude in the linearized system, making the structural sensitivity an indicator of receptivity to localized feedback [185]. If the linear system is perturbed by an impulse function at \mathbf{x}_0 and proportional to the velocity perturbation, the drift of the eigenvalue takes the form [185]

$$\delta\lambda(\mathbf{x}) = \frac{|\int_{\Omega} \tilde{\mathbf{u}} \cdot \mathbf{C}(\mathbf{x}) \cdot \tilde{\mathbf{u}}^* d\Omega|}{|\int_{\Omega} \tilde{\mathbf{u}} \cdot \tilde{\mathbf{u}}^* d\Omega|} \leq \frac{\|\mathbf{C}_0\|}{|\int_{\Omega} \tilde{\mathbf{u}} \cdot \tilde{\mathbf{u}}^* d\Omega|} s(\mathbf{x}_0), \quad (6.3)$$

where \mathbf{C} is the proportionality coefficient, $\tilde{\mathbf{u}}$ and $\tilde{\mathbf{u}}^*$ are the velocity vectors of the BiGlobal and adjoint modes respectively [186] from the adjoint equations (Eq. (6.4)),

$$\begin{aligned} -\frac{\partial \tilde{\mathbf{u}}^*}{\partial t} + (\mathbf{U} \cdot \nabla) \tilde{\mathbf{u}}^* + (\nabla \mathbf{U})^T \cdot \tilde{\mathbf{u}}^* &= -\nabla p^* + \frac{1}{Re} \nabla^2 \tilde{\mathbf{u}}^*, \\ \nabla \cdot \tilde{\mathbf{u}}^* &= 0, \end{aligned} \quad (6.4)$$

where \mathbf{U} is the baseflow velocity vector. In Eq. (6.3), the structural sensitivity is measured by $s = \|\tilde{\mathbf{u}}\| \|\tilde{\mathbf{u}}^*\|$, which is a distributed function that bounds the drift of eigenvalue.

According to the above definitions, the adjoint equations are solved as an eigenvalue problem for the adjoint mode. Together with the BiGlobal mode, the structural sensitivity, s , is computed, which is finally provided in Fig. 6.14. We observe that inside the gap, particularly in the recirculation region, the structural sensitivity has a large amplitude, which reaches the maximum near the center of the recirculation region. This further shows the oscillation inside the gap is driven by the global instability. On the other hand, the structural sensitivity is approximately zero outside the gap, indicating the receptivity to localized feedback does not exist. This further infers the lack of self-sustaining mechanism, and therefore the waves downstream of the gap have a convective nature.

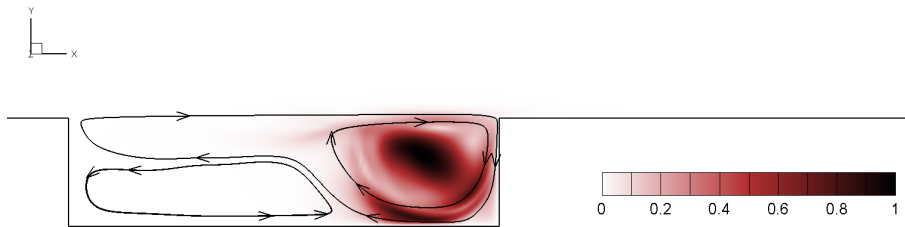


Figure 6.14: Scaled structural sensitivity, s , of the swept plate with a gap.

6.4 Conclusion

This chapter has reviewed three main types of instabilities in a gap or cavity. The self-sustained oscillation inside a gap considered in Section 5.7 originates from a centrifugal instability (3D instability). To further verify this and have a better understanding of the underlying physics, a swept plate flow with zero pressure gradient is designed, where the gap depth-based Reynolds number is 7500 and the gap is placed at $Re_x = 1.6 \times 10^6$ to 1.63×10^6 . The gap geometry and flow parameters are set to be close to the gapped 3D CRM-NLF case but an incompressible flow is considered since the centrifugal instability is purely of a hydrodynamic nature.

A DNS simulation is then performed using the spectral/ hp -Fourier method. By taking advantage of the numerical method, the flow field is decomposed into different Fourier modes. We observe the 3rd Fourier harmonic, as well as its high-order harmonics, are more energetic than other modes. The presence of the gap modulates the wall pressure and forms a favourable pressure gradient after the gap. Additionally, the boundary layer velocity profile is also modulated by the gap, bringing a crossflow velocity component into existence as well as an inflection point, which could be the origin of the crossflow instability.

In order to examine whether the observed waves after the gap are crossflow waves, we perform sectional stability analysis at $x = 0.45$ and 0.9 . The analysis shows that a few crossflow modes exist in the modulated boundary layer but are all decaying at the given positions. This prevents the disturbances from developing into crossflow waves. This is also confirmed by the eigenfunction comparison where

the profiles from the sectional stability analysis are different to the most energetic waves in DNS results.

BiGlobal analysis is then performed and the most unstable mode is found to have a non-dimensional frequency of 0.355 close to the dominant DNS frequency of 0.325. The comparisons of the spatial structure and eigenfunction show good agreement with the DNS results, indicating the waves downstream of the gap come from the BiGlobal mode.

The last remaining question is whether these waves possess a self-sustained or convective nature. We computed the structural sensitivity to show the receptivity to localized feedback. It is observed that the structural sensitivity is approximately zero outside the gap, indicating the lack of self-sustaining mechanism and therefore the waves have a convective nature.

Part IV

Conclusions and future works

Chapter 7

Conclusions and future works

7.1 Conclusions

Laminar flow transition to turbulence for external boundary layer is of particular interest for aerospace industry as the accurate prediction of transition onset can provide suggestive guidance for aerodynamic design, e.g. drag estimation and reduction, and therefore is still under intensive study in academia for the complex underlying flow physics. The laminar boundary layer flow transition at low environmental disturbance level, e.g. the one an airliner experiences during cruise, is often analyzed using the e^N method. The adoption of the e^N transition analysis involves two major steps: the computation of baseflow and disturbance field. Linear stability analysis of disturbances is preferred to target the parametric space of interest for the disturbance frequency and spanwise wavenumber, with which the linear growth of certain disturbances dominates the computational domain and finally supports the N -factor curve. The steps in the above workflow involve different kinds of simulations, and different computational tools are therefore used particularly when the geometries are complex. The resultant data conversion issue causes not only precision losses of data but also extra workload for researchers and engineers. In the current work an open-source and unified framework for laminar boundary layer natural transition analysis is introduced to better facilitate researchers and engineers. We also successfully extended the applicability of the e^N transition analysis from simple boundary layer flows over clean geometry to transonic compressible flows over complex geometries. The major challenges in the workflow are discussed and solutions are provided.

For the first major step, we compute the baseflow in a near-wall reduced domain to lower the computational cost. The computation in the reduced domain relies the boundary data interpolated from a pre-generated RANS simulation, where the pressure distribution is considered well predicted as examined by many experiments. A successful baseflow therefore needs to have pressure compatibility with the background RANS result. However, because of the hyperbolic nature for compressible flows, the pressure compatibility is not automatically guaranteed in the standard Riemann inflow boundary condition enforcement, and significant deviation can be caused for complex geometries. In addition, there are more than one type of pressure compatible inflow whereas not all of them are numerically stable. To figure out the best practice for the pressure compatible inflow, we revisit the basic settings for Riemann boundary condition enforcement for DG based simulations. We

construct entropy-pressure, velocity-pressure, and momentum-pressure compatible inflows, and develop a simple yet instructive 1D stability analysis approach based on single element approximation. Our analysis shows that maintaining entropy compatibility at inflow is critical for a stable simulation. Therefore the appropriate pressure compatible subsonic inflow should have entropy-pressure compatibility. Additional benefits from using this boundary condition include maintaining the compatibility of the speed of sound and density, as well as tangential momentum components in multi-dimensional simulations. According to this analysis, the other two types of pressure compatible inflow, i.e. velocity-pressure, and momentum-pressure compatible inflows are proven to be neutral stable or unstable. The above results agree with our numerical tests. Simulations on both CRM-NLF and DLR-F5 models show that the entropy-pressure compatible inflow condition leads to excellent agreement on pressure distributions with the outer RANS results. Further detailed study of the above stability analysis approach is also performed, showing the single element approximation can well reveal the global behavior of a multiple element system. Further, this stability analysis has been extended to 2D cases with non-uniform baseflow. We are able to explain the ill-posedness issue we observed near the leading-edge stagnation point using this approach. To conclude, in this step we have developed an approach to analyse the stability of boundary condition enforcement for DG compressible flow simulations. This approach helps us design an inflow boundary condition with pressure compatibility. The adoption of this boundary condition successfully generates a baseflow with the pressure distribution requested at the wall.

In the second major step to predict the growth of disturbances, data contamination caused by wave reflection is the main problem. The wave reflection stems from the adoption of blowing-suction to excite the disturbances developing in the boundary layer and the reflective inflow boundary condition for the truncated computational domain, particularly when the domain is reduced. A sponge region can suppress the reflected waves to a desired level (more than 2 orders smaller than the amplitude of the target boundary layer disturbance). Another source for wave reflection is the potential interaction between disturbances and surface irregularities on the wall, such as a small step embedded in the boundary layer. In this case the reflected waves would have the same frequency as the incident wave and therefore the separation of signals is difficult. Since limited analysis have been reported [111], signal separation through wave modelling is not applicable at the moment. We choose to reduce the contamination through filtering as a more user-friendly approach. However, wave reflection features at surface irregularities is under further study, which may bring us better solution in the future.

The above workflow is then verified through a Mach 0.8 flat plate case with both clean and stepped geometries. The generated N -factors for the TS waves well agree with the reference results [110]. The applicability of the framework is evaluated through the precision study and the linear growth limit of TS waves are also reported.

Having developed this workflow, the transitional performances over a wing section of the CRM-NLF model are studied going through the full workflow. In 2D cases the disturbances in the boundary layer develop in form of TS waves. The clean geometry is used as the baseline where the N -factor for the clean case reaches a maximum amplitude of 4 in the selected domain. We first study the the influ-

ence of different wall temperature boundary conditions, i.e. isothermal wall and adiabatic wall. It is found that the different temperature conditions do not change the TS wave velocity eigenfunction for both tangential and normal components but slightly influences the temperature eigenfunction in a limited region near the wall. However, the growth rate of disturbances is noticeably influenced as the isothermal wall condition always gives larger n -factor in this case. Next a gap is introduced to 33.3% of the selected chord. This gap is scaled from a real sized 2×8 mm gap on a Boeing-737 airliner, which models the irregularity at the trailing edge of the slat. In the 2D case it is discovered the gap causes local jumps in the amplitude of n -factors to approximately 0.5 or smaller depending on the disturbance frequency. However, as the disturbances travel pass the gap their amplitudes gradually recover the corresponding disturbances on the clean case.

Next, the 3D transition analysis is performed over the gapped geometry. However, in the baseflow computation we observe self-sustained oscillation inside the gap, which prevents the SFD tolerance decaying to a low level as prescribed if the SFD parameters are not specifically tuned. Since the acoustic emission is low, the observed self-sustained oscillation is unlikely caused by the acoustic related shear-layer instability. Considering the current simulation includes a narrow spectrum of spanwise wavenumbers, to better understand the self-sustained oscillation a wider swept plate with zero pressure gradient is designed as a model problem to study. The depth, length, and width of the gap has the ratio of 1 : 4 : 8, producing a depth-based Reynolds number of 7500. Other flow conditions are set to be similar to those for the 3D CRM-NLF case except for the incomprehensibility since the Mach number inside the CRM gap is lower than 0.1. This incompressible flow is simulated by a quasi-3D approach, where the Fourier expansion is adopted in the spanwise direction, providing the convenience of inherent modal decomposition regards to different spanwise wavenumbers. We discover the 3rd Fourier harmonic is significantly more energetic than other modes, and crossflow-like waves are generated after the gap. This confirms that the oscillation inside the gap raises from a centrifugal mode, which is a hydrodynamic mode unrelated to compressibility. It is not a wake mode as the mean flow is almost steady. Further analysis shows that the gap modulates the boundary layer velocity profile and generates a crossflow velocity component with inflection point, where crossflow instability may raise. In addition, the presence of the gap also generates a favourable pressure gradient downstream which can destabilize the crossflow instability. To figure out the details of these waves, we perform sectional LST analysis at two positions after the gap. However, although a few crossflow modes are successfully found their eigenfunctions are different to the shapes of the leading DNS waves we observe. The following BiGlobal analysis suggests the DNS waves arise from a BiGlobal instability mode. The final structural sensitivity indicates the lack of self-sustaining mechanism downstream of the gap. These waves are therefore considered being excited in the boundary layer above the gap region and traveling downstream, showing their convective nature.

In summary, in this thesis we have developed a transition prediction framework over wing sections with surface irregularities, and at transonic flow conditions and high Reynolds numbers. A variety of numerical methods/tools and strategies to adopt them have been explored to obtain well-resolved results. Those effective tools, such as the LST and SFD have been implemented and integrated into a framework as open-source software. This framework is then applied to study the influence of a

realistic sized gap, where self-sustained oscillations inside the gap are observed and further investigated.

Further, the development of boundary condition stability analysis has been driven by the numerous failures in the embedded simulations in trying to achieve agreement on wall pressure distribution. This analysis permits to examine in advance whether a boundary condition enforcement for a DG simulation is appropriate. This approach is characterised by its consistency, completeness, and simplicity, where some insights by Giles [128] and by Nordström et al. [127] are referenced. It has proven to be a success since it has not only solved our problems to match pressure but also has been used to design inflow boundary conditions in other projects, such as turbine cascade simulations [187].

7.2 Future works

In addition to the positive aspects mentioned above, during our study we realized there are a plenty of unsolved challenges, which we also would like to summarized for future works.

7.2.1 Operator speedup in Nektar++

Simulation efficiency is always a concern, particularly when high-order methods are adopted. In this thesis we have run both 2D (FFS, CRM-NLF) and 3D (CRM-NLF, swept plate) simulations. The 2D simulations are typically run on clusters of 5–50 CPU cores and the results can be obtained in a few hours or within a day. However, 3D simulations are much more computationally demanding as we need 300–1200 CPU cores to get the results in one day or two. These simulations demand better software implementation to speedup the operators in Nektar++.

In recent years, modern computational hardware has been advanced rapidly and exascale platforms are coming. These platforms typically adopt CPUs supporting Advanced Vector Extensions SIMD instructions (AVX series) or are equipped with Graphics Processing Units (GPUs), enabling powerful floating-point operations (FLOPS). We therefore have launched a re-design project for Nektar++ to fully take advantage of the modern hardware and speedup the main operators at the library level. This work is expected to effectively reduce the time and power cost for each simulation and will benefit the flow simulation community.

7.2.2 Gapped swept plate flow at medium Reynolds numbers

In the last chapter we have demonstrated that the flow in the gap on a swept plate experiences self-sustained oscillations. Such oscillations in the gap region raise from the centrifugal instability in the recirculation. More detailed analysis regards to gap flow to resolve the detailed centrifugal mode is of interest. In the current work we consider the realistic sizes of the gap irregularity on the wing surface of an airliner. This setting complicates the flow since several instability modes are energized simultaneously. In order to have a better resolution and convergence lower Reynolds number might be considered in the future works, where the influence of the crossflow velocity component on the centrifugal instability mode will be investigated.

Moreover, the oscillations in the gap also excite boundary layer waves that travel downstream of the gap. Since the excitation is unavoidable, its interaction with coming TS waves or crossflow waves from upstream could also play an significant role in flow transition and its prediction.

Bibliography

- [1] T. Appel, “Boundary layer instabilities due to surface irregularities: A harmonic navier-stokes approach,” Ph.D. dissertation, Imperial College London, 2020. DOI: 10.25560/88722.
- [2] A. Kharina and D. Rutherford, “Fuel efficiency trends for new commercial jet aircraft: 1960 to 2014,” Tech. Rep., 2015.
- [3] S. R. Department, *Total fuel consumption of commercial airlines worldwide between 2005 and 2021, with a forecast until 2023 (in billion gallons)*, 2023. [Online]. Available: www.statista.com/statistics/655057/fuel-consumption-of-airlines-worldwide/.
- [4] D. S. Lee *et al.*, “The contribution of global aviation to anthropogenic climate forcing for 2000 to 2018,” *Atmospheric Environment*, vol. 244, p. 117834, 2021. DOI: 10.1016/j.atmosenv.2020.117834.
- [5] I. A. T. A. (IATA), *Airline profitability outlook strengthens*, 2023. [Online]. Available: www.iata.org/en/pressroom/2023-releases/2023-06-05-01/.
- [6] E. Cabrera and J. M. M. de Sousa, “Use of sustainable fuels in aviation—a review,” *Energies*, vol. 15, no. 7, p. 2440, 2022. DOI: 10.3390/en15072440.
- [7] J. Holladay, Z. Abdullah, and J. Heyne, “Sustainable aviation fuel: Review of technical pathways,” Tech. Rep., 2020. DOI: 10.2172/1660415.
- [8] J. Huete, D. Nalianda, and P. Pilidis, “Propulsion system integration for a first-generation hydrogen civil airliner,” *The Aeronautical Journal*, vol. 125, no. 1291, pp. 1654–1665, 2021. DOI: 10.1017/aer.2021.36.
- [9] A. Bauen, N. Bitossi, L. German, A. Harris, and K. Leow, “Sustainable aviation fuels: Status, challenges and prospects of drop-in liquid fuels, hydrogen and electrification in aviation,” *Johnson Matthey Technology Review*, vol. 64, no. 3, pp. 263–278, 2020. DOI: 10.1595/205651320X15816756012040.
- [10] T. Yusaf *et al.*, “Sustainable aviation—hydrogen is the future,” *Sustainability*, vol. 14, no. 1, p. 548, 2022. DOI: 10.3390/su14010548.
- [11] S. Das, J. Warren, D. West, and S. M. Schexnayder, “Global carbon fiber composites supply chain competitiveness analysis,” Oak Ridge National Lab.(ORNL), Oak Ridge, TN (United States); The University, Tech. Rep., 2016. DOI: 10.2172/1333049.
- [12] J.-P. Marec, “Drag reduction: A major task for research,” in *Aerodynamic Drag Reduction Technologies: Proceedings of the CEAS/DragNet European Drag Reduction Conference, 19–21 June 2000, Potsdam, Germany*, Springer, 2001, pp. 17–27. DOI: 10.1007/978-3-540-45359-8_3.

- [13] G. Schrauf, “Status and perspectives of laminar flow,” *The aeronautical journal*, vol. 109, no. 1102, pp. 639–644, 2005. DOI: 10.1017/S00019240000097X.
- [14] N. Beck, T. Landa, A. Seitz, L. Boermans, Y. Liu, and R. Radespiel, “Drag reduction by laminar flow control,” *Energies*, vol. 11, no. 1, p. 252, 2018.
- [15] W. S. Saric, H. L. Reed, and E. J. Kerschen, “Boundary-layer receptivity to freestream disturbances,” *Annual review of fluid mechanics*, vol. 34, no. 1, pp. 291–319, 2002.
- [16] A. Ruban, S. Keshari, and M. Kravtsova, “On boundary-layer receptivity to entropy waves,” *Journal of Fluid Mechanics*, vol. 929, 2021.
- [17] X. Zhong and X. Wang, “Direct numerical simulation on the receptivity, instability, and transition of hypersonic boundary layers,” *Annual Review of Fluid Mechanics*, vol. 44, pp. 527–561, 2012.
- [18] L. S. Kovasznay, “Turbulence in supersonic flow,” *Journal of the Aeronautical Sciences*, vol. 20, no. 10, pp. 657–674, 1953.
- [19] J. Fanning, “In-flight measurements of freestream atmospheric turbulence intensities,” M.S. thesis, Texas A&M University, 2012. [Online]. Available: <https://hdl.handle.net/1969.1/148376>.
- [20] L. Brandt, P. Schlatter, and D. S. Henningson, “Transition in boundary layers subject to free-stream turbulence,” *Journal of Fluid Mechanics*, vol. 517, pp. 167–198, 2004. DOI: 10.1017/S0022112004000941.
- [21] G. B. Schubauer and H. K. Skramstad, “Laminar-boundary-layer oscillations and transition on a flat plate,” Tech. Rep. NACA-TR-909, 1943.
- [22] F. Charru, *Hydrodynamic instabilities*. Cambridge University Press, 2011, vol. 37.
- [23] H. Schlichting and K. Gersten, *Boundary-layer theory*, 9th ed. Springer Science & Business Media, 2017.
- [24] F. M. White and J. Majdalani, *Viscous fluid flow*, 4th ed. McGraw-Hill New York, 2021.
- [25] A. V. Boiko, G. R. Grek, A. V. Dovgal, and V. V. Kozlov, *The origin of turbulence in near-wall flows*. Springer Science & Business Media, 2002.
- [26] W. S. Saric, H. L. Reed, and E. B. White, “Stability and transition of three-dimensional boundary layers,” *Annual review of fluid mechanics*, vol. 35, no. 1, pp. 413–440, 2003.
- [27] H. L. Reed, W. S. Saric, and D. Arnal, “Linear stability theory applied to boundary layers,” *Annual review of fluid mechanics*, vol. 28, no. 1, pp. 389–428, 1996.
- [28] H. Zhou and G. Zhao, *Hydrodynamic Stability*. National Defense Industry Press, 2004.
- [29] J. Serpieri, “Cross-flow instability: Flow diagnostics and control of swept wing boundary layers,” Ph.D. dissertation, Delft University of Technology, 2018.
- [30] E. R. Gowree, “Influence of attachment line flow on form drag,” Ph.D. dissertation, City University London, 2014.

- [31] W. S. Saric, “Görtler vortices,” *Annual Review of Fluid Mechanics*, vol. 26, no. 1, pp. 379–409, 1994.
- [32] C. A. Edelmann and U. Rist, “Impact of forward-facing steps on laminar-turbulent transition in transonic flows,” *AIAA Journal*, vol. 53, no. 9, pp. 2504–2511, 2015.
- [33] E. E. Cooke, M. S. Mughal, S. Sherwin, R. Ashworth, and S. Rolston, “Destabilisation of stationary and travelling crossflow disturbances due to steps over a swept wing,” in *AIAA Aviation 2019 Forum*, 2019, p. 3533. DOI: [10.2514/6.2019-3533](https://doi.org/10.2514/6.2019-3533).
- [34] A. F. Rius-Vidales and M. Kotsonis, “Influence of a forward-facing step surface irregularity on swept wing transition,” *AIAA Journal*, vol. 58, no. 12, pp. 5243–5253, 2020. DOI: [10.2514/1.J059566](https://doi.org/10.2514/1.J059566).
- [35] T. Appel, E. Cooke, S. Mughal, and R. Ashworth, “Biglobal stability analysis of swept-wing boundary layers with forward and backward facing steps,” in *IUTAM Laminar-Turbulent Transition: 9th IUTAM Symposium, London, UK, September 2–6, 2019*, Springer, 2022, pp. 347–358. DOI: [10.1007/978-3-030-67902-6_30](https://doi.org/10.1007/978-3-030-67902-6_30).
- [36] J. Zahn and U. Rist, “Impact of deep gaps on laminar–turbulent transition in compressible boundary-layer flow,” *AIAA Journal*, vol. 54, no. 1, pp. 66–76, 2016.
- [37] X. Wu and L. W. Hogg, “Acoustic radiation of tollmien–schlichting waves as they undergo rapid distortion,” *Journal of Fluid Mechanics*, vol. 550, pp. 307–347, 2006. DOI: [10.1017/S0022112005008220](https://doi.org/10.1017/S0022112005008220).
- [38] H. Xu, J.-E. W. Lombard, and S. J. Sherwin, “Influence of localised smooth steps on the instability of a boundary layer,” *Journal of Fluid Mechanics*, vol. 817, pp. 138–170, 2017. DOI: [10.1017/jfm.2017.113](https://doi.org/10.1017/jfm.2017.113).
- [39] H. Xu, S. M. Mughal, E. R. Gowree, C. J. Atkin, and S. J. Sherwin, “Destabilisation and modification of tollmien–schlichting disturbances by a three-dimensional surface indentation,” *Journal of Fluid Mechanics*, vol. 819, pp. 592–620, 2017. DOI: [10.1017/jfm.2017.193](https://doi.org/10.1017/jfm.2017.193).
- [40] J. Casacuberta, S. Hickel, S. Westerbeek, and M. Kotsonis, “Direct numerical simulation of interaction between a stationary crossflow instability and forward-facing steps,” *Journal of Fluid Mechanics*, vol. 943, A46, 2022. DOI: [10.1017/jfm.2022.456](https://doi.org/10.1017/jfm.2022.456).
- [41] A. F. Rius-Vidales and M. Kotsonis, “Impact of a forward-facing step on the development of crossflow instability,” *Journal of Fluid Mechanics*, vol. 924, A34, 2021. DOI: [10.1017/jfm.2021.497](https://doi.org/10.1017/jfm.2021.497).
- [42] L. M. Mack, “Boundary-layer linear stability theory,” Jet Propulsion Laboratory, California Institute of Technology, Tech. Rep. AGARD Report No. 709, Part 3, 1984.
- [43] P. J. Schmid and D. S. Henningson, *Stability and Transition in Shear Flows* (Applied Mathematical Sciences 142). Springer New York, NY, 2001. DOI: [10.1007/978-1-4613-0185-1](https://doi.org/10.1007/978-1-4613-0185-1).

- [44] W. O. Criminale, T. L. Jackson, and R. D. Joslin, *Theory and computation in hydrodynamic stability*. Cambridge University Press, 2018.
- [45] V. Theofilis, “Global linear instability,” *Annual Review of Fluid Mechanics*, vol. 43, pp. 319–352, 2011. DOI: 10.1146/annurev-fluid-122109-160705.
- [46] H. M. Blackburn, D. Barkley, and S. J. Sherwin, “Convective instability and transient growth in flow over a backward-facing step,” *Journal of Fluid Mechanics*, vol. 603, pp. 271–304, 2008. DOI: 10.1017/S0022112008001109.
- [47] V. Theofilis, “Advances in global linear instability analysis of nonparallel and three-dimensional flows,” *Progress in aerospace sciences*, vol. 39, no. 4, pp. 249–315, 2003. DOI: 10.1016/S0376-0421(02)00030-1.
- [48] M. R. Malik, “Numerical methods for hypersonic boundary layer stability,” *Journal of computational physics*, vol. 86, no. 2, pp. 376–413, 1990. DOI: 10.1016/0021-9991(90)90106-B.
- [49] G. Lyu, C. Chen, X. Du, M. S. Mughal, and S. J. Sherwin, “Open-source framework for transonic boundary layer natural transition analysis over complex geometries in nektar++,” in *AIAA AVIATION 2022 Forum*, 2022, p. 4032. DOI: 10.2514/6.2022-4032.
- [50] A. Smith, D. A. Company, N. Gamberoni, A. R. C. F. M. Sub-Committee, and D. A. C. E. S. D. E. Department, *Transition, Pressure Gradient and Stability Theory* (ARC-19322). Douglas Aircraft Company, El Segundo Division, 1956. [Online]. Available: <https://books.google.co.uk/books?id=qXsxGwAACAAJ>.
- [51] J. van Ingen, “A suggested semi-empirical method for the calculation of the boundary layer transition region,” Faculty of Aerospace Engineering, Delft University of Technology, Tech. Rep., 1956.
- [52] D. Arnal, “Boundary layer transition: Predictions based on linear theory,” Tech. Rep., 1994.
- [53] G. Schrauf, J. Perraud, D. Vitiello, and F. Lam, “Comparison of boundary-layer transition predictions using flight test data,” *Journal of Aircraft*, vol. 35, no. 6, pp. 891–897, 1998. DOI: 10.2514/2.2409.
- [54] L. M. Mack, “Transition prediction and linear stability theory,” Tech. Rep., 1977.
- [55] J. Crouch and L. Ng, “Variable n-factor method for transition prediction in three-dimensional boundary layers,” *AIAA journal*, vol. 38, no. 2, pp. 211–216, 2000. DOI: 10.2514/2.973.
- [56] G. Schrauf, “Large-scale laminar flow tests evaluated with linear stability theory,” *Journal of Aircraft*, vol. 41, no. 2, pp. 224–230, 2004. DOI: 10.2514/1.9280.
- [57] L. Mack, “Stability of three-dimensional boundary layers on swept wings at transonic speeds,” in *Symposium Transsonicum III*, Springer, 1989, pp. 209–223.
- [58] R. Ashworth and S. Mughal, “Modeling three dimensional effects on cross flow instability from leading edge dimples,” *Procedia IUTAM*, vol. 14, pp. 201–210, 2015. DOI: 10.1016/j.piutam.2015.03.041.

- [59] P. Paredes, A. Hanifi, V. Theofilis, and D. S. Henningson, “The nonlinear pse-3d concept for transition prediction in flows with a single slowly-varying spatial direction,” *Procedia IUTAM*, vol. 14, pp. 36–44, 2015. DOI: 10.1016/j.piutam.2015.03.021.
- [60] H. Raposo, S. Mughal, and R. Ashworth, “Acoustic receptivity and transition modeling of tollmien-schlichting disturbances induced by distributed surface roughness,” *Physics of Fluids*, vol. 30, no. 4, 2018. DOI: 10.1063/1.5024909.
- [61] J. A. Franco Sumariva and S. J. Hein, “Adaptive harmonic linearized navier-stokes equations used for boundary layer instability analysis in the presence of large streamwise gradients,” in *2018 AIAA Aerospace Sciences Meeting*, 2018, p. 1548. DOI: 10.2514/6.2018-1548.
- [62] H. Raposo, S. Mughal, A. Bensalah, and R. Ashworth, “Acoustic-roughness receptivity in subsonic boundary-layer flows over aerofoils,” *Journal of Fluid Mechanics*, vol. 925, A7, 2021. DOI: 10.1017/jfm.2021.658.
- [63] S. Hein, F. Bertolotti, M. Simen, A. Hanifi, and D. Henningson, “Linear nonlocal instability analysis-the linear nolot code,” DLR, Tech. Rep., 1995. [Online]. Available: <https://elib.dlr.de/39000/>.
- [64] S. Hein, “Linear and nonlinear nonlocal instability analyses for two-dimensional laminar separation bubbles,” in *Laminar-Turbulent Transition: IUTAM Symposium, Sedona/AZ September 13–17, 1999*, Springer, 2000, pp. 681–686. DOI: 10.1007/978-3-662-03997-7_106.
- [65] R. Gross *et al.*, “Prediction of laminar/turbulent transition in an unstructured finite element navier stokes solver using a boundary layer code with emphasis on cross flow transition,” in *50th 3AF INTERNATIONAL CONFERENCE ON APPLIED AERODYNAMICS*, 2015.
- [66] H. L. Reed, A. S. U. T. D. O. MECHANICAL, and A. ENGINEERING, “Stability and transition analysis for reentry tool, star,” Department of Aerospace Engineering, Texas A&M University, Tech. Rep. FA9550-05-1-0273, 2005.
- [67] Y. Shi, R. Gross, C. A. Mader, and J. R. Martins, “Transition prediction in a rans solver based on linear stability theory for complex three-dimensional configurations,” in *2018 AIAA aerospace sciences meeting*, 2018, p. 0819. DOI: 10.2514/6.2018-0819.
- [68] M. Mughal, “Stability analysis of complex wing geometries: Parabolised stability equations in generalised non-orthogonal coordinates.,” in *36th AIAA Fluid Dynamics Conference and Exhibit*, 2006, p. 3222.
- [69] G. Lyu, C. Chen, X. Du, and S. J. Sherwin, “Stable, entropy-pressure compatible subsonic riemann boundary condition for embedded dg compressible flow simulations,” *Journal of Computational Physics*, vol. 476, p. 111896, 2023. DOI: 10.1016/j.jcp.2022.111896.
- [70] M. Mathias and M. F. Medeiros, “Global instability analysis of a boundary layer flow over a small cavity,” in *AIAA Aviation 2019 Forum*, 2019, p. 3535. DOI: 10.2514/6.2019-3535.

- [71] S. Westerbeek, J. A. Franco Sumariva, T. Michelis, S. Hein, and M. Kotsonis, “Linear and nonlinear stability analysis of a three-dimensional boundary layer over a hump,” in *AIAA SciTech 2023 Forum*, 2023, p. 0678. DOI: 10.2514/6.2023-0678.
- [72] T. Colonius, A. Basu, and C. Rowley, “Numerical investigation of the flow past a cavity,” in *5th AIAA/CEAS aeroacoustics conference and exhibit*, 1999, p. 1912. DOI: 10.2514/6.1999-1912.
- [73] G. A. Bres and T. Colonius, “Three-dimensional instabilities in compressible flow over open cavities,” *Journal of Fluid Mechanics*, vol. 599, pp. 309–339, 2008. DOI: 10.1017/S0022112007009925.
- [74] J. de Vicente, J. Basley, F. Meseguer-Garrido, J. Soria, and V. Theofilis, “Three-dimensional instabilities over a rectangular open cavity: From linear stability analysis to experimentation,” *Journal of Fluid Mechanics*, vol. 748, pp. 189–220, 2014. DOI: 10.1017/jfm.2014.126.
- [75] D. Tempelmann, L.-U. Schrader, A. Hanifi, L. Brandt, and D. S. Henningsson, “Swept wing boundary-layer receptivity to localized surface roughness,” *Journal of Fluid Mechanics*, vol. 711, pp. 516–544, 2012. DOI: 10.1017/jfm.2012.405.
- [76] F. J. Hindenlang, G. J. Gassner, and D. A. Kopriva, “Stability of wall boundary condition procedures for discontinuous galerkin spectral element approximations of the compressible euler equations,” in *Spectral and High Order Methods for Partial Differential Equations ICOSAHOM 2018*, Springer, 2020, pp. 3–19. DOI: 10.1007/978-3-030-39647-3_1.
- [77] T. Nazghelichi, F. Torabi, and V. Esfahanian, “Non-dimensional analysis of electrochemical governing equations of lead-acid batteries,” *Journal of Energy Storage*, vol. 27, p. 101120, 2020. DOI: 10.1016/j.est.2019.101120.
- [78] S. J. Sherwin, *Spectral/hp element discretisation*, <https://www.nektar.info/nektar-outline-videos-and-presentations/>, Accessed: 21-Nov-2021, 2021.
- [79] G. Mengaldo *et al.*, “Industry-relevant implicit large-eddy simulation of a high-performance road car via spectral/hp element methods,” *SIAM Review*, vol. 63, no. 4, pp. 723–755, 2021. DOI: 10.1137/20M1345359.
- [80] D. N. Arnold, F. Brezzi, B. Cockburn, and L. D. Marini, “Unified analysis of discontinuous galerkin methods for elliptic problems,” *SIAM journal on numerical analysis*, vol. 39, no. 5, pp. 1749–1779, 2002. DOI: 10.1137/S0036142901384162.
- [81] F. Bassi and S. Rebay, “A high-order accurate discontinuous finite element method for the numerical solution of the compressible navier–stokes equations,” *Journal of computational physics*, vol. 131, no. 2, pp. 267–279, 1997.
- [82] B. Cockburn and C.-W. Shu, “The local discontinuous galerkin method for time-dependent convection-diffusion systems,” *SIAM Journal on Numerical Analysis*, vol. 35, no. 6, pp. 2440–2463, 1998.

- [83] R. Hartmann and P. Houston, “Symmetric interior penalty dg methods for the compressible navier–stokes equations ii: Goal–oriented a posteriori error estimation,” *International Journal of Numerical Analysis & Modeling.*, vol. 3, no. 2, pp. 141–162, 2006.
- [84] R. Hartmann and P. Houston, “An optimal order interior penalty discontinuous galerkin discretization of the compressible navier–stokes equations,” *Journal of Computational Physics*, vol. 227, no. 22, pp. 9670–9685, 2008.
- [85] R. Hartmann, “Numerical analysis of higher order discontinuous galerkin finite element methods,” Von Karman Institute for Fluid Dynamics, Tech. Rep. VKI LS 2008-08, Oct. 2008, CFD - ADIGMA course on very high order discretization methods, Rhode Saint Genèse, Belgium. [Online]. Available: <https://elib.dlr.de/57074/1/Har08b.pdf>.
- [86] M. F. Wheeler, “An elliptic collocation-finite element method with interior penalties,” *SIAM Journal on Numerical Analysis*, vol. 15, no. 1, pp. 152–161, 1978. DOI: [10.1137/0715010](https://doi.org/10.1137/0715010).
- [87] D. N. Arnold, “An interior penalty finite element method with discontinuous elements,” Ph.D. dissertation, University of Chicago, 1979.
- [88] E. Ferrer, “A high order discontinuous galerkin-fourier incompressible 3d navier-stokes solver with rotating sliding meshes for simulating cross-flow turbines,” Ph.D. dissertation, Oxford University, UK, 2012.
- [89] K. Hillewaert, “Development of the discontinuous galerkin method for high-resolution, large scale cfd and acoustics in industrial geometries,” Ph.D. dissertation, Université Catholique de Louvain, 2013. [Online]. Available: <https://pul.uclouvain.be/book/?gcoi=29303100319670>.
- [90] Z. Dong and E. H. Georgoulis, “Robust interior penalty discontinuous galerkin methods,” *Journal of Scientific Computing*, vol. 92, no. 2, p. 57, 2022.
- [91] R. Hartmann, “Adjoint consistency analysis of discontinuous galerkin discretizations,” *SIAM Journal on Numerical Analysis*, vol. 45, no. 6, pp. 2671–2696, 2007. DOI: [10.1137/060665117](https://doi.org/10.1137/060665117).
- [92] V. Dolejší and M. Feistauer, *Discontinuous Galerkin Method, Analysis and Applications to Compressible Flow*. Springer, 2015, vol. 48, p. 481. DOI: [10.1007/978-3-319-19267-3](https://doi.org/10.1007/978-3-319-19267-3).
- [93] Z.-G. Yan *et al.*, “Nektar++: Design and implementation of an implicit, spectral/hp element, compressible flow solver using a jacobian-free newton krylov approach,” *Computers & Mathematics with Applications*, vol. 81, pp. 351–372, 2021. DOI: [10.1016/j.camwa.2020.03.009](https://doi.org/10.1016/j.camwa.2020.03.009).
- [94] S. K. Godunov and I. Bohachevsky, “Finite difference method for numerical computation of discontinuous solutions of the equations of fluid dynamics,” *Matematičeskij sbornik*, vol. 47, no. 3, pp. 271–306, 1959.
- [95] S. K. Godunov, A. Zabrodin, M. I. Ivanov, A. Kraiko, and G. Prokopov, “Numerical solution of multidimensional problems of gas dynamics,” *Moscow Izdatel Nauka*, 1976.
- [96] E. F. Toro, *Riemann Solvers and Numerical Methods for Fluid Dynamics: a practical introduction*, 3rd. Springer Science & Business Media, 2009. DOI: [10.1007/b79761](https://doi.org/10.1007/b79761).

- [97] G. Mengaldo *et al.*, “A guide to the implementation of boundary conditions in compact high-order methods for compressible aerodynamics,” in *7th AIAA Theoretical Fluid Mechanics Conference*, 2014, p. 2923. DOI: [10.2514/6.2014-2923](https://doi.org/10.2514/6.2014-2923).
- [98] D. De Grazia, “Three-dimensional discontinuous spectral/hp element methods for compressible flows,” Ph.D. dissertation, 2016. DOI: [10.25560/40416](https://doi.org/10.25560/40416).
- [99] G. E. Karniadakis and S. Sherwin, *Spectral/hp element methods for computational fluid dynamics*. Oxford University Press, 2005.
- [100] Z. Yan, “Efficient implicit spectral/hp element dg techniques for compressible flows,” Ph.D. dissertation, 2021. DOI: [10.25560/98366](https://doi.org/10.25560/98366).
- [101] Y. Pan, Z.-G. Yan, J. Peiró, and S. J. Sherwin, “Development of a balanced adaptive time-stepping strategy based on an implicit jfnk-dg compressible flow solver,” *Communications on Applied Mathematics and Computation*, vol. 4, no. 2, pp. 728–757, 2022.
- [102] Y. Saad and M. H. Schultz, “Gmres: A generalized minimal residual algorithm for solving nonsymmetric linear systems,” *SIAM Journal on scientific and statistical computing*, vol. 7, no. 3, pp. 856–869, 1986. DOI: [10.1137/0907058](https://doi.org/10.1137/0907058).
- [103] A. J. Wathen, “Preconditioning,” *Acta Numerica*, vol. 24, pp. 329–376, 2015. DOI: [10.1017/S0962492915000021](https://doi.org/10.1017/S0962492915000021).
- [104] B. E. Jordi, C. J. Cotter, and S. J. Sherwin, “Encapsulated formulation of the selective frequency damping method,” *Physics of Fluids*, vol. 26, no. 3, p. 034101, 2014.
- [105] D. J. Bodony, “Analysis of sponge zones for computational fluid mechanics,” *Journal of Computational Physics*, vol. 212, no. 2, pp. 681–702, 2006.
- [106] D. Moxey *et al.*, “Nektar++: Enhancing the capability and application of high-fidelity spectral/hp element methods,” *Computer Physics Communications*, vol. 249, p. 107110, 2020.
- [107] C. D. Cantwell *et al.*, “Nektar++: An open-source spectral/hp element framework,” *Computer physics communications*, vol. 192, pp. 205–219, 2015.
- [108] E. Cook, “Modelling the effect of step and roughness features on swept wing boundary layer instabilities,” Ph.D. dissertation, Imperial College London, UK, 2019. DOI: [10.25560/83744](https://doi.org/10.25560/83744).
- [109] M. Mughal, “Active control of wave instabilities in three-dimensional compressible flows,” *Theoretical and computational fluid dynamics*, vol. 12, no. 4, pp. 195–217, 1998.
- [110] C. A. Edelmann, “Influence of forward-facing steps on laminar–turbulent transition,” Ph.D. dissertation, Univ. of Stuttgart, Stuttgart, Germany, 2014.
- [111] M. Schopper, “Analysis of an existing on the interaction of acoustic waves with a laminar boundary layer,” Systems and Applied Sciences Corp, Tech. Rep. NASA-CR-3620, 1982.
- [112] J. P. Boyd, *Chebyshev and Fourier spectral methods*. Courier Corporation, 2001.

- [113] W. Mengmeng, H. Zhonghua, N. Han, S. Wenping, S. Le Clainche, and E. Ferrer, “A transition prediction method for flow over airfoils based on high-order dynamic mode decomposition,” *Chinese Journal of Aeronautics*, vol. 32, no. 11, pp. 2408–2421, 2019. DOI: [10.1016/j.cja.2019.03.020](https://doi.org/10.1016/j.cja.2019.03.020).
- [114] B. S. Venkatachari, P. Paredes, M. M. Choudhari, F. Li, and C.-L. Chang, “Transition analysis for the crm-nlf wind tunnel configuration using transport equation models and linear stability correlations,” in *AIAA SciTech 2022 Forum*, 2022, p. 1542. DOI: [10.2514/6.2022-1542](https://doi.org/10.2514/6.2022-1542).
- [115] N. Krimmelbein and A. Krumbein, “Transition prediction for the nasa crm-nlf with the en-method using incompressible and compressible linear stability analysis,” in *AIAA SciTech 2022 Forum*, 2022, p. 1953. DOI: [10.2514/6.2022-1953](https://doi.org/10.2514/6.2022-1953).
- [116] C. Wenzel, T. Gibis, M. Kloker, and U. Rist, “Self-similar compressible turbulent boundary layers with pressure gradients. part 1. direct numerical simulation and assessment of morkovin’s hypothesis,” *Journal of Fluid Mechanics*, vol. 880, pp. 239–283, 2019. DOI: [10.1017/jfm.2019.670](https://doi.org/10.1017/jfm.2019.670).
- [117] C. Wenzel, “DNS of compressible turbulent boundary layers: Pressure-gradient influence and self-similarity,” Ph.D. dissertation, University of Stuttgart, 2019. DOI: [10.13140/RG.2.2.28045.49121](https://doi.org/10.13140/RG.2.2.28045.49121).
- [118] R. Dadfar, A. Hanifi, and D. S. Henningson, “Control of instabilities in an unswept wing boundary layer,” *AIAA Journal*, vol. 56, no. 5, pp. 1750–1759, 2018. DOI: [10.2514/1.J056415](https://doi.org/10.2514/1.J056415).
- [119] S. M. Hosseini, R. Vinuesa, P. Schlatter, A. Hanifi, and D. S. Henningson, “Direct numerical simulation of the flow around a wing section at moderate reynolds number,” *International Journal of Heat and Fluid Flow*, vol. 61, pp. 117–128, 2016. DOI: [10.1016/j.ijheatfluidflow.2016.02.001](https://doi.org/10.1016/j.ijheatfluidflow.2016.02.001).
- [120] N. J. Georgiadis, C. L. Rumsey, and G. P. Huang, “Revisiting turbulence model validation for high-mach number axisymmetric compression corner flows,” in *53rd AIAA Aerospace Sciences Meeting*, 2015, p. 0316. DOI: [10.2514/6.2015-0316](https://doi.org/10.2514/6.2015-0316).
- [121] J. A. White, R. A. Baurle, B. J. Passe, S. C. Spiegel, and H. Nishikawa, “Geometrically flexible and efficient flow analysis of high speed vehicles via domain decomposition, part 1: Unstructured-grid solver for high speed flows,” in *2017 JANNAF-Interagency Propulsion Committee Meeting*, 2017.
- [122] P. Forooghi, B. Frohnappel, and F. Magagnato, “Simulation of a gaseous jet impinging on a convex heated surface—effect of inlet condition,” *Applied Thermal Engineering*, vol. 105, pp. 1076–1084, 2016. DOI: [10.1016/j.applthermaleng.2016.01.048](https://doi.org/10.1016/j.applthermaleng.2016.01.048).
- [123] E. Ferrer, “An interior penalty stabilised incompressible discontinuous galerkin-fourier solver for implicit large eddy simulations,” *Journal of Computational Physics*, vol. 348, pp. 754–775, 2017. DOI: [10.1016/j.jcp.2017.07.049](https://doi.org/10.1016/j.jcp.2017.07.049).
- [124] Q. Abbas and J. Nordström, “Weak versus strong no-slip boundary conditions for the navier-stokes equations,” *Engineering Applications of Computational Fluid Mechanics*, vol. 4, no. 1, pp. 29–38, 2010. DOI: [10.1080/19942060.2010.11015297](https://doi.org/10.1080/19942060.2010.11015297).

- [125] P. Eliasson, S. Eriksson, and J. Nordström, “Influence of weak and strong solid wall boundary conditions on the convergence to steady-state of the navier-stokes equations,” in *19th AIAA Computational Fluid Dynamics*, 2009, p. 3551. DOI: 10.2514/6.2009-3551.
- [126] J. Nordström, S. Eriksson, and P. Eliasson, “Weak and strong wall boundary procedures and convergence to steady-state of the navier–stokes equations,” *Journal of Computational Physics*, vol. 231, no. 14, pp. 4867–4884, 2012. DOI: 10.1016/j.jcp.2012.04.007.
- [127] J. Nordström and M. Svärd, “Well-posed boundary conditions for the navier–stokes equations,” *SIAM Journal on Numerical Analysis*, vol. 43, no. 3, pp. 1231–1255, 2005. DOI: 10.1137/040604972.
- [128] M. Giles, “Eigenmode analysis of unsteady one-dimensional euler equations,” NASA Langley Research Center, Tech. Rep. ICASE Report No. 83-47, 1983.
- [129] D. L. Darmofal, P. Moinier, and M. B. Giles, “Eigenmode analysis of boundary conditions for the one-dimensional preconditioned euler equations,” *Journal of Computational Physics*, vol. 160, no. 1, pp. 369–384, 2000. DOI: 10.1006/jcph.2000.6472.
- [130] J. Nordström, “A roadmap to well posed and stable problems in computational physics,” *Journal of Scientific Computing*, vol. 71, no. 1, pp. 365–385, 2017. DOI: 10.1007/s10915-016-0303-9.
- [131] G. J. Gassner, A. R. Winters, F. J. Hindenlang, and D. A. Kopriva, “The br1 scheme is stable for the compressible navier–stokes equations,” *Journal of Scientific Computing*, vol. 77, no. 1, pp. 154–200, 2018. DOI: 10.1007/s10915-018-0702-1.
- [132] J. Kou, A. Hurtado-de-Mendoza, S. Joshi, S. Le Clainche, and E. Ferrer, “Eigensolution analysis of immersed boundary method based on volume penalization: Applications to high-order schemes,” *Journal of Computational Physics*, vol. 449, p. 110817, 2022. DOI: 10.1016/j.jcp.2021.110817.
- [133] D. L. Rodriguez, M. J. Aftosmis, and M. Nemec, “Formulation and implementation of inflow/outflow boundary conditions to simulate propulsive effects,” in *2018 AIAA Aerospace Sciences Meeting*, 2018, p. 0334.
- [134] M. Lynde. “General information on the wind tunnel data from the crm-nlf test,” NASA. (Oct. 2021), [Online]. Available: https://commonresearchmodel.larc.nasa.gov/wp-content/uploads/sites/7/2020/02/CRM-NLF_Info_v2.pdf.
- [135] J. Schembri, “Three-dimensional laminar-turbulent transition simulations with the γ - re θ transition model,” 2016.
- [136] H. Sobieczky, “Dlr-f5: Test wing for cfd and applied aerodynamics,” 1994.
- [137] M. Jabbal, S. Liddle, J. Potts, and W. Crowther, “Development of design methodology for a synthetic jet actuator array for flow separation control applications,” *Proceedings of the Institution of Mechanical Engineers, Part G: Journal of Aerospace Engineering*, vol. 227, no. 1, pp. 110–124, 2013. DOI: 10.1177/0954410011428256.

- [138] N. Goldfine, D. Schlicker, and A. Washabaugh, “Surface-mounted eddy-current sensors for on-line monitoring of fatigue tests and for aircraft health monitoring,” in *Second Joint NASA/FAA/DoD Conference on Aging Aircraft*, 1998, pp. 1–16.
- [139] L. Werfelman, “Thin skinned,” *Aerosafety World*, vol. 1, pp. 18–20, Oct. 2011. [Online]. Available: https://flightsafety.org/wp-content/uploads/2016/10/asw_oct11_p18-20.pdf.
- [140] C. Brady, *737 ng performance improvement package*, University of Rhode Island. [Online]. Available: <http://www.b737.org.uk/737ng-pip.htm>.
- [141] D. Tesch, “Next-generation 737 performance improvement package,” *AERO*, vol. QTR_04, pp. 13–17, 2012. [Online]. Available: https://www.boeing.com/commercial/aeromagazine/articles/2012_q4/3/.
- [142] Rgwyatt. “Common research model,” NASA. (2012), [Online]. Available: <https://commonresearchmodel.larc.nasa.gov/>.
- [143] *Easa type-certificate data sheet no. easa.im.a.115 for boeing 737*, No. EASA.IM.A.115, European Aviation Safety Agency, Jul. 2012. [Online]. Available: [https://www.easa.europa.eu/sites/default/files/dfu/EASA-TCDS-A.120_\(IM\)_Boeing_737-09-12072012.pdf](https://www.easa.europa.eu/sites/default/files/dfu/EASA-TCDS-A.120_(IM)_Boeing_737-09-12072012.pdf).
- [144] *Type certificate data sheet A16WE*, No. A16WE, Federal Aviation Administration, Department of Transportation, Jun. 2014. [Online]. Available: [https://rgl.faa.gov/Regulatory_and_Guidance_Library/rgMakeModel.nsf/0/9c59427a20b3253686257d03004d8faa/\\$FILE/A16WE_Rev_53.pdf](https://rgl.faa.gov/Regulatory_and_Guidance_Library/rgMakeModel.nsf/0/9c59427a20b3253686257d03004d8faa/$FILE/A16WE_Rev_53.pdf).
- [145] *Easa type-certificate data sheet no. easa.im.a.003 for boeing 777*, No. EASA.IM.A.003, European Aviation Safety Agency, Aug. 2022. [Online]. Available: <https://www.easa.europa.eu/en/downloads/7521/en>.
- [146] Office of Aviation Research and Development, “Statistical loads data for the boeing 777-200er aircraft in commercial operations,” Federal Aviation Administration, U.S. Department of Transportation, Washington, DC 20591, Tech. Rep. DOT/FAA/AR-06/11, Nov. 2006. [Online]. Available: <http://www.tc.faa.gov/its/worldpac/techrpt/ar06-11.pdf>.
- [147] *Easa type-certificate data sheet no. easa.im.a.115 for boeing 787*, EASA.IM.A.115, European Aviation Safety Agency, Apr. 2022. [Online]. Available: <https://www.easa.europa.eu/en/downloads/7302/en>.
- [148] P. M. Sforza, *Commercial airplane design principles*. Elsevier, 2014.
- [149] M. Turner, D. Moxey, J. Peiró, M. Gammon, C. R. Pollard, and H. Bucklow, “A framework for the generation of high-order curvilinear hybrid meshes for cfd simulations,” *Procedia engineering*, vol. 203, pp. 206–218, 2017. DOI: [10.1016/j.proeng.2017.09.808](https://doi.org/10.1016/j.proeng.2017.09.808).
- [150] M. D. Green *et al.*, “Nekmesh: An open-source high-order mesh generation framework,” *Available at SSRN 4632754*, DOI: [10.2139/ssrn.4632754](https://doi.org/10.2139/ssrn.4632754).
- [151] P. Kalita and A. Dass, “A diffusion-regulated scheme for the compressible navier–stokes equations using a boundary-layer sensor,” *Computers & Fluids*, vol. 129, pp. 91–100, 2016. DOI: [10.1016/j.compfluid.2016.02.001](https://doi.org/10.1016/j.compfluid.2016.02.001).

- [152] C. Thomas, S. M. Mughal, M. Gipon, R. Ashworth, and A. Martinez-Cava, “Stability of an infinite swept wing boundary layer with surface waviness,” *AIAA Journal*, vol. 54, no. 10, pp. 3024–3038, 2016. DOI: 10.2514/1.J054755.
- [153] A. Fedorov *et al.*, “High-speed boundary-layer stability on a cone with localized wall heating or cooling,” *AIAA Journal*, vol. 53, no. 9, pp. 2512–2524, 2015. DOI: 10.2514/1.J053666.
- [154] P. Guo, Z. Gao, C. Jiang, and C.-H. Lee, “Linear stability analysis on the most unstable frequencies of supersonic flat-plate boundary layers,” *Computers & Fluids*, vol. 197, p. 104394, 2020. DOI: 10.1016/j.compfluid.2019.104394.
- [155] V. I. Lysenko and A. A. Maslov, “The effect of cooling on supersonic boundary-layer stability,” *Journal of Fluid Mechanics*, vol. 147, pp. 39–52, 1984. DOI: 10.1017/S002211208400197X.
- [156] R. Oddo *et al.*, “Effect of surface cooling on second-mode dominated hypersonic boundary layer transition,” *Experiments in Fluids*, vol. 62, no. 7, p. 144, 2021. DOI: 10.1007/s00348-021-03237-0.
- [157] B. Herman, C. Hader, and H. F. Fasel, “Numerical investigation of the effects of wall heating and cooling on the nonlinear transition stages for a sharp cone at mach 6,” in *AIAA Scitech 2022 Forum*, 2022, p. 0601. DOI: 10.2514/6.2022-0601.
- [158] C. Wenzel, B. Selent, M. Kloker, and U. Rist, “Dns of compressible turbulent boundary layers and assessment of data/scaling-law quality,” *Journal of Fluid Mechanics*, vol. 842, pp. 428–468, 2018. DOI: 10.1017/jfm.2018.179.
- [159] M. S. Mathias, “Computational study of the hydrodynamic stability of gaps and cavities in a subsonic compressible boundary layer,” Ph.D. dissertation, Universidade de São Paulo, 2021. DOI: 10.11606/T.18.2021.tde-29032022-085318.
- [160] S. Beguet, J. Perraud, M. Forte, and J.-P. Brazier, “Modeling of transverse gaps effects on boundary-layer transition,” *Journal of Aircraft*, vol. 54, no. 2, pp. 794–801, 2017. DOI: 10.2514/1.C033647.
- [161] J. Crouch, V. Kosorygin, M. Sutanto, and G. Miller, “Characterizing surface-gap effects on boundary-layer transition dominated by tollmien–schlichting instability,” *Flow*, vol. 2, E8, 2022. DOI: 10.1017/flo.2022.1.
- [162] S. Sinha, A. Gupta, and M. Oberai, “Laminar separating flow over backsteps and cavities. ii-cavities,” *AIAA journal*, vol. 20, no. 3, pp. 370–375, 1982.
- [163] M. Mathias and M. F. Medeiros, “The influence of the boundary layer thickness on the stability of the rossiter modes of a compressible rectangular cavity,” in *2018 Fluid Dynamics Conference*, 2018, p. 3386. DOI: 10.2514/6.2018-3386.
- [164] G. A. Bres, “Numerical simulations of three-dimensional instabilities in cavity flows,” Ph.D. dissertation, California Institute of Technology, 2007. DOI: 10.7907/Z96W988B.

- [165] K. Krishnamurty, “Acoustic radiation from two-dimensional rectangular cutouts in aerodynamic surfaces,” California Institute of Technology, Tech. Rep., 1955.
- [166] L. Cattafesta III, S. Garg, M. Kegerise, and G. Jones, “Experiments on compressible flow-induced cavity oscillations,” in *29th AIAA, Fluid Dynamics Conference*, 1998, p. 2912.
- [167] G. A. Bres, *Numerical simulations of three-dimensional instabilities in cavity flows*, Last accessed 16 August 2023, 2007. [Online]. Available: <https://thesis.library.caltech.edu/1515/>.
- [168] R. Martin, M. Soria, O. Lehmkuhl, A. Gorobets, and A. Duben, “Noise radiated by an open cavity at low mach number: Effect of the cavity oscillation mode,” *International Journal of Aeroacoustics*, vol. 18, no. 6-7, pp. 647–668, 2019. DOI: [10.1177/1475472X19871534](https://doi.org/10.1177/1475472X19871534).
- [169] J. Rossiter, “Wind-tunnel experiments on the flow over rectangular cavities at subsonic and transonic speeds,” 1964.
- [170] M. Mathias and M. Medeiros, “Interaction between rossiter and görler modes in the compressible flow in an open cavity,” in *AIAA AVIATION 2020 FORUM*, 2020, p. 3074. DOI: [10.2514/6.2020-3074](https://doi.org/10.2514/6.2020-3074).
- [171] V. Suponitsky, E. Avital, and M. Gaster, “On three-dimensionality and control of incompressible cavity flow,” *Physics of Fluids*, vol. 17, no. 10, p. 104 103, 2005.
- [172] T. M. Faure, L. Pastur, F. Lusseyran, Y. Fraigneau, and D. Bisch, “Three-dimensional centrifugal instabilities development inside a parallelepipedic open cavity of various shape,” *Experiments in Fluids*, vol. 47, pp. 395–410, 2009. DOI: [10.1007/s00348-009-0671-0](https://doi.org/10.1007/s00348-009-0671-0).
- [173] J. Basley, L. R. Pastur, N. Delprat, and F. Lusseyran, “Space-time aspects of a three-dimensional multi-modulated open cavity flow,” *Physics of Fluids*, vol. 25, no. 6, 2013.
- [174] S. Dong, G. E. Karniadakis, and C. Chryssostomidis, “A robust and accurate outflow boundary condition for incompressible flow simulations on severely-truncated unbounded domains,” *Journal of Computational Physics*, vol. 261, pp. 83–105, 2014. DOI: [10.1016/j.jcp.2013.12.042](https://doi.org/10.1016/j.jcp.2013.12.042).
- [175] H. M. Blackburn and S. J. Sherwin, “Formulation of a galerkin spectral element–fourier method for three-dimensional incompressible flows in cylindrical geometries,” *Journal of Computational Physics*, vol. 197, no. 2, pp. 759–778, 2004. DOI: [10.1016/j.jcp.2004.02.013](https://doi.org/10.1016/j.jcp.2004.02.013).
- [176] J. Slaughter, D. Moxey, and S. Sherwin, “Large eddy simulation of an inverted multi-element wing in ground effect,” *Flow, Turbulence and Combustion*, vol. 110, no. 4, pp. 917–944, 2023. DOI: [10.1007/s10494-023-00404-7](https://doi.org/10.1007/s10494-023-00404-7).
- [177] M. Lahooti, Y. Bao, D. Scott, R. Palacios, and S. J. Sherwin, “Les/dns fluid-structure interaction simulation of non-linear slender structures in nektar++ framework,” *Computer Physics Communications*, vol. 282, p. 108 528, 2023. DOI: [10.1016/j.cpc.2022.108528](https://doi.org/10.1016/j.cpc.2022.108528).

- [178] M. Z. Hossain, C. D. Cantwell, and S. J. Sherwin, “A spectral/hp element method for thermal convection,” *International Journal for Numerical Methods in Fluids*, vol. 93, no. 7, pp. 2380–2395, 2021.
- [179] J.-L. Guermond and J. Shen, “Velocity-correction projection methods for incompressible flows,” *SIAM Journal on Numerical Analysis*, vol. 41, no. 1, pp. 112–134, 2003. DOI: [10.1137/S0036142901395400](https://doi.org/10.1137/S0036142901395400).
- [180] E. Tadmor, “Convergence of spectral methods for nonlinear conservation laws,” *SIAM Journal on Numerical Analysis*, vol. 26, no. 1, pp. 30–44, 1989. DOI: [10.1137/0726003](https://doi.org/10.1137/0726003).
- [181] Y. Maday, S. M. O. Kaber, and E. Tadmor, “Legendre pseudospectral viscosity method for nonlinear conservation laws,” *SIAM Journal on Numerical Analysis*, vol. 30, no. 2, pp. 321–342, 1993. DOI: [10.1137/0730016](https://doi.org/10.1137/0730016).
- [182] D. Barkley, M. G. M. Gomes, and R. D. Henderson, “Three-dimensional instability in flow over a backward-facing step,” *Journal of fluid mechanics*, vol. 473, pp. 167–190, 2002.
- [183] N. team, “Nektar++: Spectral/hp element framework – user guide,” 2023.
- [184] F. Giannetti and P. Luchini, “Structural sensitivity of the first instability of the cylinder wake,” *Journal of Fluid Mechanics*, vol. 581, pp. 167–197, 2007. DOI: [10.1017/S0022112007005654](https://doi.org/10.1017/S0022112007005654).
- [185] G. Rocco, “Advanced instability methods using spectral/hp discretisations and their applications to complex geometries,” Ph.D. dissertation, Imperial College London, 2014. DOI: [10.25560/28686](https://doi.org/10.25560/28686).
- [186] O. Marquet, D. Sipp, and L. Jacquin, “Sensitivity analysis and passive control of cylinder flow,” *Journal of Fluid Mechanics*, vol. 615, pp. 221–252, 2008. DOI: [10.1017/S0022112008003662](https://doi.org/10.1017/S0022112008003662).
- [187] J. Isler, G. Vivarelli, F. Montomoli, S. Sherwin, P. Adami, and R. Vazquez, “High fidelity compressible and incompressible flow simulations of a turbomachinery geometrical configuration,” in *15th European Conference on Turbomachinery Fluid dynamics & Thermodynamics*, 2023. DOI: [10.29008/ETC2023-189](https://doi.org/10.29008/ETC2023-189).
- [188] C. A. Kennedy and T. B. Gatski, “Self-similar supersonic variable-density shear layers in binary systems,” *Physics of Fluids*, vol. 6, no. 2, pp. 662–673, 1994.
- [189] M. Höglberg and D. Henningson, “Secondary instability of cross-flow vortices in falkner–skan–cooke boundary layers,” *Journal of Fluid Mechanics*, vol. 368, pp. 339–357, 1998.
- [190] J. Cooke, “The boundary layer of a class of infinite yawed cylinders,” in *Mathematical proceedings of the Cambridge philosophical society*, Cambridge University Press, vol. 46, 1950, pp. 645–648.

Part V

Appendix

Appendix A

DG formulations

A.1 DG with different forms of interior penalty

Following Eq. (2.29) in Chapter 2, the global primal formulation takes the form

$$\begin{aligned} & \frac{\partial}{\partial t} \int_{\Omega} v u d\Omega - \int_{\Omega} \nabla v \cdot \mathbf{a} u d\Omega + \int_{\Gamma_I} \left(\llbracket \mathbf{a} \hat{u} \rrbracket \cdot \llbracket v \rrbracket + \llbracket \mathbf{a} \hat{u} \rrbracket \llbracket v \rrbracket \right) d\Gamma_I \\ & + \int_{\Omega} b \nabla u \cdot \nabla v d\Omega + \int_{\Gamma_I} b \left(\llbracket \nabla v \rrbracket \cdot \llbracket \hat{u} - u \rrbracket + \llbracket \nabla v \rrbracket \llbracket \hat{u} - u \rrbracket \right) d\Gamma_I \\ & - \int_{\Gamma_I} b \left(\llbracket \hat{\sigma} \rrbracket \cdot \llbracket v \rrbracket + \llbracket \hat{\sigma} \rrbracket \llbracket v \rrbracket \right) d\Gamma_I = \int_{\Omega} v f d\Omega, \end{aligned} \quad (\text{A.1})$$

where $\Gamma_I = \cup_{e=1}^{N_e} \Gamma_e$ is the non-repeated internal boundary set of all elements. With the assumption that the numerical fluxes are conservative [80, 85], their jumps of numerical fluxes are eliminated and the average operators are removed from the numerical fluxes in the Eq. (A.1)

$$\begin{aligned} & \frac{\partial}{\partial t} \int_{\Omega} v u d\Omega - \int_{\Omega} \nabla v \cdot \mathbf{a} u d\Omega + \int_{\Gamma_I} \left(\llbracket \mathbf{a} \hat{u} \rrbracket \cdot \llbracket v \rrbracket + \llbracket \mathbf{a} \hat{u} \rrbracket^0 \llbracket v \rrbracket \right) d\Gamma_I \\ & + \int_{\Omega} b \nabla u \cdot \nabla v d\Omega + \int_{\Gamma_I} b \left(\llbracket \nabla v \rrbracket^0 \cdot \llbracket \hat{u} - u \rrbracket + \llbracket \nabla v \rrbracket \llbracket \hat{u} - u \rrbracket \right) d\Gamma_I \\ & - \int_{\Gamma_I} b \left(\llbracket \hat{\sigma} \rrbracket^0 \cdot \llbracket v \rrbracket + \llbracket \hat{\sigma} \rrbracket^0 \llbracket v \rrbracket \right) d\Gamma_I = \int_{\Omega} v f d\Omega, \end{aligned} \quad (\text{A.2})$$

which is simplified as

$$\begin{aligned} & \frac{\partial}{\partial t} \int_{\Omega} v u d\Omega - \int_{\Omega} \nabla v \cdot \mathbf{a} u d\Omega + \int_{\Gamma_I} \left(\mathbf{a} \hat{u} \cdot \llbracket v \rrbracket \right) d\Gamma_I + \int_{\Omega} b \nabla u \cdot \nabla v d\Omega \\ & + \int_{\Gamma_I} b \left(-\llbracket \nabla v \rrbracket \cdot \llbracket u \rrbracket + \llbracket \nabla v \rrbracket \llbracket \hat{u} - u \rrbracket \right) d\Gamma_I - \int_{\Gamma_I} b \hat{\sigma} \cdot \llbracket v \rrbracket d\Gamma_I = \int_{\Omega} v f d\Omega. \end{aligned} \quad (\text{A.3})$$

In this work, we consider symmetric interior penalty Galerkin method (SIPG) for the diffusion operator. The form of its numerical fluxes, together with the numerical fluxes for nonsymmetric symmetric (NIPG) and incomplete interior penalty (IIPG) are listed in Table A.1, and the final expressions of these three schemes are provided in order in Eqs.A.4 A.5 A.6.

Table A.1: Interior penalty numerical diffusion fluxes.

Method	\hat{u}	$\hat{\sigma}$
SIPG	$\{u\}$	$\{\nabla u\} - \eta[u]$
NIPG	$\{u\} + \mathbf{n}[u]$	$\{\nabla u\} - \eta[u]$
IIPG	NA (\hat{u} does not present)	$\{\nabla u\} - \eta[u]$

$$\begin{aligned} & \frac{\partial}{\partial t} \int_{\Omega} vud\Omega - \int_{\Omega} \nabla v \cdot \mathbf{a}ud\Omega + \int_{\Gamma_I} (\{a\hat{u}\} \cdot [v]) d\Gamma_I \\ & + \int_{\Omega} b\nabla u \cdot \nabla vd\Omega + \int_{\Gamma_I} b(-\{\nabla u\} \cdot [v] - \{\nabla v\} \cdot [u] + \eta[u] \cdot [v]) d\Gamma_I = \int_{\Omega} vfd\Omega \end{aligned} \quad (\text{A.4})$$

$$\begin{aligned} & \frac{\partial}{\partial t} \int_{\Omega} vud\Omega - \int_{\Omega} \nabla v \cdot \mathbf{a}ud\Omega + \int_{\Gamma_I} (\{a\hat{u}\} \cdot [v]) d\Gamma_I \\ & + \int_{\Omega} b\nabla u \cdot \nabla vd\Omega + \int_{\Gamma_I} b(-\{\nabla u\} \cdot [v] + \{\nabla v\} \cdot [u] + \eta[u] \cdot [v]) d\Gamma_I = \int_{\Omega} vfd\Omega \end{aligned} \quad (\text{A.5})$$

$$\begin{aligned} & \frac{\partial}{\partial t} \int_{\Omega} vud\Omega - \int_{\Omega} \nabla v \cdot \mathbf{a}ud\Omega + \int_{\Gamma_I} (\{a\hat{u}\} \cdot [v]) d\Gamma_I \\ & + \int_{\Omega} b\nabla u \cdot \nabla vd\Omega + \int_{\Gamma_I} b(-\{\nabla u\} \cdot [v] + \eta[u] \cdot [v]) d\Gamma_I = \int_{\Omega} vfd\Omega \end{aligned} \quad (\text{A.6})$$

Conventionally, the NIPG and IIPG are derived by substituting different forms numerical flux in Table A.1 into Eq. (2.32). However, in this work we present an alternative approach of derivation. Recall that in 2.25a the fluxes in the interface integrals are changed to be numerical fluxes while in Eq. (2.26) the fluxes remains to be the internal values. We can change the order to introduce the numerical flux, where the bilinear form of the diffusion operator in Eq. (2.28) finally reads

$$\mathcal{B}_v^{NIPG}(u, v) = \int_{\Omega_e} b\nabla u \cdot \nabla vd\Omega_e + \int_{\Gamma_e} b(u - \hat{u})(\nabla v \cdot \mathbf{n})d\Gamma_e - \int_{\Gamma_e} v(b\hat{\sigma} \cdot n)d\Gamma_e \quad (\text{A.7})$$

where it is now $(u - \hat{u})$ rather than $(\hat{u} - u)$ that appears in the surface integral. Therefore its the global formulation we can still let the $\hat{u} = \{u\}$ as in SIPG, which directly leads to the NIPG scheme in Eq. (A.5).

Similarly, if in Eq.2.25a the interface fluxes are not replaced by numerical fluxes (or we replace the interface fluxes with numerical fluxes in Eq. (2.26)), $(u - u)$ (or $(\hat{u} - \hat{u})$) is eliminated and the diffusion operator takes the bilinear form

$$\mathcal{B}_v^{IIPG}(u, v) = \int_{\Omega_e} b\nabla u \cdot \nabla vd\Omega_e - \int_{\Gamma_e} v(b\hat{\sigma} \cdot n)d\Gamma_e \quad (\text{A.8})$$

where the symmetric term does not present, and the IIPG scheme in Eq. (A.6) is derived by sum all the element.

A.2 DG formulation of NS equations

In the derivation of DG formulation of the NS equations, key transformations include

$$\begin{aligned}\boldsymbol{\sigma} : \boldsymbol{\tau} &= \begin{pmatrix} \boldsymbol{\sigma}_1 \\ \boldsymbol{\sigma}_2 \\ \boldsymbol{\sigma}_3 \end{pmatrix} : \begin{pmatrix} \boldsymbol{\tau}_1 \\ \boldsymbol{\tau}_2 \\ \boldsymbol{\tau}_3 \end{pmatrix} = \boldsymbol{\sigma}_i \cdot \boldsymbol{\tau}_i = \left(\mathbf{K}_{ij} \frac{\partial \mathbf{Q}}{\partial x_j} \right) \cdot \boldsymbol{\tau}_i = \frac{\partial \mathbf{Q}}{\partial x_j} \cdot (\mathbf{K}_{ij}^T \boldsymbol{\tau}_i) \\ &= \begin{pmatrix} \partial \mathbf{Q} / \partial x_1 \\ \partial \mathbf{Q} / \partial x_2 \\ \partial \mathbf{Q} / \partial x_3 \end{pmatrix} : \begin{pmatrix} \mathbf{K}_{11}^T \boldsymbol{\tau}_1 + \mathbf{K}_{21}^T \boldsymbol{\tau}_2 + \mathbf{K}_{31}^T \boldsymbol{\tau}_3 \\ \mathbf{K}_{12}^T \boldsymbol{\tau}_1 + \mathbf{K}_{22}^T \boldsymbol{\tau}_2 + \mathbf{K}_{32}^T \boldsymbol{\tau}_3 \\ \mathbf{K}_{13}^T \boldsymbol{\tau}_1 + \mathbf{K}_{23}^T \boldsymbol{\tau}_2 + \mathbf{K}_{33}^T \boldsymbol{\tau}_3 \end{pmatrix} = \nabla \mathbf{Q} : (\mathbf{K}^T \boldsymbol{\tau})\end{aligned}\tag{A.9}$$

where $(\mathbf{K}^T)_{ij} = (\mathbf{K}_{ji})^T$. In the above the third identity is based on the transformation $\mathbf{c}^T \mathbf{A} \mathbf{b} = (\mathbf{c}^T \mathbf{A} \mathbf{b})^T = \mathbf{b}^T \mathbf{A}^T \mathbf{c}$ for a matrix \mathbf{A} and vectors \mathbf{b} and \mathbf{c} .

To obtain the vector form of integration by part we have adopted the following identities

$$\int_{\Omega_e} (\nabla \cdot \mathbf{F}) \cdot \mathbf{v} d\Omega_e = \int_{\Gamma_e} (\mathbf{F} \cdot \mathbf{n}) \cdot \mathbf{v} d\Gamma_e - \int_{\Omega_e} \mathbf{F} : \nabla \mathbf{v} d\Omega_e\tag{A.10a}$$

$$\int_{\Omega_e} (\nabla \cdot \boldsymbol{\sigma}) \cdot \mathbf{v} d\Omega_e = \int_{\Gamma_e} (\boldsymbol{\sigma} \cdot \mathbf{n}) \cdot \mathbf{v} d\Gamma_e - \int_{\Omega_e} \boldsymbol{\sigma} : \nabla \mathbf{v} d\Omega_e\tag{A.10b}$$

$$\int_{\Omega_e} \nabla \mathbf{Q} : (\mathbf{K}^T \boldsymbol{\tau}) d\Omega_e = \int_{\Gamma_e} \mathbf{Q} \cdot ((\mathbf{K}^T \boldsymbol{\tau}) \cdot \mathbf{n}) d\Gamma_e - \int_{\Omega_e} \mathbf{Q} \cdot (\nabla \cdot (\mathbf{K}^T \boldsymbol{\tau})) d\Omega\tag{A.10c}$$

Appendix B

Linearized DG approximation for Euler equations

B.1 Linearized DG approximation for 1D Euler equations

Considering the piecewise constant approximation the integration of 1D Euler equation in an element gives

$$\frac{d\tilde{\mathbf{Q}}}{dt}\Delta x = \hat{\mathbf{F}}^w - \hat{\mathbf{F}}^e, \quad (\text{B.1})$$

where $\hat{\mathbf{F}}^w$ and $\hat{\mathbf{F}}^e$ are numerical fluxes at west and east boundaries. Each of them is constructed by the internal state $\tilde{\mathbf{Q}}_{\text{int}}$ and a reference state $\tilde{\mathbf{Q}}_{\text{ref}}$. The linearized system can be derived by introducing perturbations to all of these states, leading to

$$\begin{aligned} \frac{d(\tilde{\mathbf{Q}} + \delta\tilde{\mathbf{Q}}_{\text{int}})}{dt}\Delta x &= \left(\hat{\mathbf{F}}^w + \frac{\partial\hat{\mathbf{F}}^w}{\partial\tilde{\mathbf{Q}}_{\text{int}}}\delta\tilde{\mathbf{Q}}_{\text{int}} + \frac{\partial\hat{\mathbf{F}}^w}{\partial\tilde{\mathbf{Q}}_{\text{ref}}^w}\delta\tilde{\mathbf{Q}}_{\text{ref}}^w \right) \\ &\quad - \left(\hat{\mathbf{F}}^e + \frac{\partial\hat{\mathbf{F}}^e}{\partial\tilde{\mathbf{Q}}_{\text{int}}}\delta\tilde{\mathbf{Q}}_{\text{int}} + \frac{\partial\hat{\mathbf{F}}^e}{\partial\tilde{\mathbf{Q}}_{\text{ref}}^e}\delta\tilde{\mathbf{Q}}_{\text{ref}}^e \right). \end{aligned} \quad (\text{B.2})$$

By substituting Eq. (B.1) from Eq. (B.2), and assuming the perturbation on both reference states are equal, $\delta\tilde{\mathbf{Q}}_{\text{ref}}^w = \delta\tilde{\mathbf{Q}}_{\text{ref}}^e = \tilde{\mathbf{Q}}_{\text{ref}}$, the 1D linearized systems is given by

$$\frac{d(\delta\tilde{\mathbf{Q}}_{\text{int}})}{dt}\Delta x = \left(\frac{\partial\hat{\mathbf{F}}^w}{\partial\tilde{\mathbf{Q}}_{\text{int}}} - \frac{\partial\hat{\mathbf{F}}^e}{\partial\tilde{\mathbf{Q}}_{\text{int}}} \right) \delta\tilde{\mathbf{Q}}_{\text{int}} + \left(\frac{\partial\hat{\mathbf{F}}^w}{\partial\tilde{\mathbf{Q}}_{\text{ref}}^w} - \frac{\partial\hat{\mathbf{F}}^e}{\partial\tilde{\mathbf{Q}}_{\text{ref}}^e} \right) \delta\tilde{\mathbf{Q}}_{\text{ref}}, \quad (\text{B.3})$$

which can then be transformed into characteristic variables as

$$\begin{aligned} \frac{d}{dt} \left(\frac{\partial\tilde{\mathbf{Q}}_{\text{int}}}{\partial\tilde{\mathbf{U}}_{\text{int}}} \delta\tilde{\mathbf{U}}_{\text{int}} \right) \Delta x &= \left(\frac{\partial\hat{\mathbf{F}}^w}{\partial\tilde{\mathbf{Q}}_b^w} \frac{\partial\tilde{\mathbf{Q}}_b^w}{\partial\tilde{\mathbf{U}}_b^w} \frac{\partial\tilde{\mathbf{U}}_b^w}{\partial\tilde{\mathbf{Q}}_{\text{int}}} - \frac{\partial\hat{\mathbf{F}}^e}{\partial\tilde{\mathbf{Q}}_b^e} \frac{\partial\tilde{\mathbf{Q}}_b^e}{\partial\tilde{\mathbf{U}}_b^e} \frac{\partial\tilde{\mathbf{U}}_b^e}{\partial\tilde{\mathbf{Q}}_{\text{int}}} \right) \frac{\partial\tilde{\mathbf{Q}}_{\text{int}}}{\partial\tilde{\mathbf{U}}_{\text{int}}} \delta\tilde{\mathbf{U}}_{\text{int}} \\ &\quad + \left(\frac{\partial\hat{\mathbf{f}}^w}{\partial\tilde{\mathbf{Q}}_b^w} \frac{\partial\tilde{\mathbf{Q}}_b^w}{\partial\tilde{\mathbf{U}}_b^w} \frac{\partial\tilde{\mathbf{U}}_b^w}{\partial\tilde{\mathbf{Q}}_{\text{ref}}^w} - \frac{\partial\hat{\mathbf{f}}^e}{\partial\tilde{\mathbf{Q}}_b^e} \frac{\partial\tilde{\mathbf{Q}}_b^e}{\partial\tilde{\mathbf{U}}_b^e} \frac{\partial\tilde{\mathbf{U}}_b^e}{\partial\tilde{\mathbf{Q}}_{\text{ref}}^e} \right) \frac{\partial\tilde{\mathbf{Q}}_{\text{ref}}^e}{\partial\tilde{\mathbf{U}}_b^e} \delta\tilde{\mathbf{U}}_{\text{ref}}. \end{aligned} \quad (\text{B.4})$$

Due to the assumption that the baseflow is constant, Eq. (B.4) is simplified as

$$\begin{aligned} \frac{d}{dt} (\delta \tilde{\mathbf{U}}_{\text{int}}) &= \frac{1}{\Delta x} \left(\frac{\partial \tilde{\mathbf{Q}}}{\partial \tilde{\mathbf{U}}} \right)^{-1} \frac{\partial \hat{\mathbf{F}}}{\partial \tilde{\mathbf{Q}}} \frac{\partial \tilde{\mathbf{Q}}}{\partial \tilde{\mathbf{U}}} \left(\frac{\partial \tilde{\mathbf{U}}_{\text{b}}^{\text{w}}}{\partial \tilde{\mathbf{U}}_{\text{int}}} - \frac{\partial \tilde{\mathbf{U}}_{\text{b}}^{\text{e}}}{\partial \tilde{\mathbf{U}}_{\text{int}}} \right) \delta \tilde{\mathbf{U}}_{\text{int}} \\ &\quad + \frac{1}{\Delta x} \left(\frac{\partial \tilde{\mathbf{Q}}}{\partial \tilde{\mathbf{U}}} \right)^{-1} \frac{\partial \hat{\mathbf{F}}}{\partial \tilde{\mathbf{Q}}} \frac{\partial \tilde{\mathbf{Q}}}{\partial \tilde{\mathbf{U}}} \left(\frac{\partial \tilde{\mathbf{U}}_{\text{b}}^{\text{w}}}{\partial \tilde{\mathbf{U}}_{\text{ref}}^{\text{w}}} - \frac{\partial \tilde{\mathbf{U}}_{\text{b}}^{\text{e}}}{\partial \tilde{\mathbf{U}}_{\text{ref}}^{\text{e}}} \right) \delta \tilde{\mathbf{U}}_{\text{ref}}, \end{aligned} \quad (\text{B.5})$$

or

$$\frac{d}{dt} (\delta \tilde{\mathbf{U}}_{\text{int}}) = \frac{1}{\Delta x} \mathbf{C}_{\text{int}} \delta \tilde{\mathbf{U}}_{\text{int}} + \frac{1}{\Delta x} \mathbf{C}_{\text{ref}} \delta \tilde{\mathbf{U}}_{\text{ref}}, \quad (\text{B.6})$$

where the state vectors and matrices without subscript or superscript denote the baseflow quantities which are uniform for the 1D analysis.

Note that the above linear system can also be directly obtained by considering $\mathbf{Q} = \mathbf{Q}(\mathbf{U} + \delta \mathbf{U})$, $\mathbf{F} = \mathbf{F}(\mathbf{Q}(\mathbf{U} + \delta \mathbf{U}))$.

B.2 Linearized DG approximation for 2D Euler equations

The DG approximation for 2D Euler equation at the presence of wall on the east boundary (Fig. 4.9) is derived from the integration form of 2D Euler equations

$$\int_{\Omega} \phi \frac{\partial \mathbf{Q}}{\partial t} d\Omega = \int_{\Gamma^{\text{w}}} \phi \hat{\mathbf{F}}_1^{\text{w}} dx_2 - \int_{\Gamma^{\text{e}}} \phi \hat{\mathbf{F}}_1^{\text{e}} dx_2 + \int_{\Gamma^{\text{s}}} \phi \hat{\mathbf{F}}_2^{\text{s}} dx_1 - \int_{\Gamma^{\text{n}}} \phi \hat{\mathbf{F}}_2^{\text{n}} dx_1 + \int_{\Omega} \nabla \phi \cdot \mathbf{F} d\Omega. \quad (\text{B.7})$$

We use the semi-discrete form by only numerically integrating the boundary terms, the DG approximation reads

$$\begin{aligned} \int_{\Omega} \phi \frac{\partial \mathbf{Q}_{\text{int}}}{\partial t} d\Omega &= \sum_{i=0}^P \phi w_i \hat{\mathbf{F}}_{1,i}^{\text{w}} \left(\tilde{\mathbf{Q}}_{\text{ref},i}^{\text{w}}, \tilde{\mathbf{Q}}_{\text{int},i}^{\text{w}} \right) - \sum_{i=0}^P \phi w_i \hat{\mathbf{F}}_{1,i}^{\text{e}} \left(\tilde{\mathbf{Q}}_{\text{ref},i}^{\text{e}}, \tilde{\mathbf{Q}}_{\text{int},i}^{\text{e}} \right) \\ &\quad + \sum_{i=0}^P \phi w_i \hat{\mathbf{F}}_{2,i}^{\text{s}} \left(\tilde{\mathbf{Q}}_{\text{ref},i}^{\text{s}}, \tilde{\mathbf{Q}}_{\text{int},i}^{\text{s}} \right) - \sum_{i=0}^P \phi w_i \hat{\mathbf{F}}_{2,i}^{\text{n}} \left(\tilde{\mathbf{Q}}_{\text{ref},i}^{\text{n}}, \tilde{\mathbf{Q}}_{\text{int},i}^{\text{n}} \right) \\ &\quad + \int_{\Omega} \nabla \phi \cdot \mathbf{F} d\Omega, \end{aligned} \quad (\text{B.8})$$

where in the reference state for the east boundary (wall), $\hat{\mathbf{Q}}_{\text{ref},i}^{\text{e}}$, the momentum in the normal direction is zero for no-penetration condition. Following the same procedures in B.1, the linearized system for introducing disturbances on all the

states leads to

$$\begin{aligned}
& \int_{\Omega} \phi \frac{\partial(\delta \mathbf{Q}_{\text{int}})}{\partial t} d\Omega = \\
& \sum_{i=0}^P \phi w_i \left[\frac{\partial \tilde{\mathbf{F}}_{1,i}^w}{\partial \tilde{\mathbf{Q}}_{\text{int},i}^w} \delta \tilde{\mathbf{Q}}_{\text{int},i}^w + \frac{\partial \tilde{\mathbf{F}}_{1,i}^w}{\partial \tilde{\mathbf{Q}}_{\text{ref},i}^w} \delta \tilde{\mathbf{Q}}_{\text{ref},i}^w \right] \\
& - \sum_{i=0}^P \phi w_i \left[\frac{\partial \tilde{\mathbf{F}}_{1,i}^e}{\partial \tilde{\mathbf{Q}}_{\text{int},i}^e} \delta \tilde{\mathbf{Q}}_{\text{int},i}^e + \frac{\partial \tilde{\mathbf{F}}_{1,i}^e}{\partial \tilde{\mathbf{Q}}_{\text{ref},i}^e} \delta \tilde{\mathbf{Q}}_{\text{ref},i}^e \right] \\
& + \sum_{i=0}^P \phi w_i \left[\frac{\partial \tilde{\mathbf{F}}_{1,i}^s}{\partial \tilde{\mathbf{Q}}_{\text{int},i}^s} \delta \tilde{\mathbf{Q}}_{\text{int},i}^s + \frac{\partial \tilde{\mathbf{F}}_{1,i}^s}{\partial \tilde{\mathbf{Q}}_{\text{ref},i}^s} \delta \tilde{\mathbf{Q}}_{\text{ref},i}^s \right] \\
& - \sum_{i=0}^P \phi w_i \left[\frac{\partial \tilde{\mathbf{F}}_{1,i}^n}{\partial \tilde{\mathbf{Q}}_{\text{int},i}^n} \delta \tilde{\mathbf{Q}}_{\text{int},i}^n + \frac{\partial \tilde{\mathbf{F}}_{1,i}^n}{\partial \tilde{\mathbf{Q}}_{\text{ref},i}^n} \delta \tilde{\mathbf{Q}}_{\text{ref},i}^n \right] + \int_{\Omega} \nabla \phi \cdot \frac{\partial \mathbf{F}}{\partial \mathbf{Q}} \delta \mathbf{Q}_{\text{int}} d\Omega.
\end{aligned} \tag{B.9}$$

Since the $\tilde{\mathbf{Q}}_{\text{ref},i}^e$ will not be influenced by the outer simulation, we have $\delta \tilde{\mathbf{Q}}_{\text{ref},i}^e = \mathbf{0}$. The consequent linearized system for Fig. 4.9(a) is derived as

$$\int_{\Omega} \phi \frac{\partial(\delta \mathbf{Q}_{\text{int}})}{\partial t} d\Omega = RHS_{\text{int}}(\tilde{\mathbf{Q}}, \delta \tilde{\mathbf{Q}}_{\text{int}}) + RHS_{\text{ref}}(\tilde{\mathbf{Q}}, \delta \tilde{\mathbf{Q}}_{\text{ref}}), \tag{B.10}$$

which is then transformed into quasi-characteristic variables (Eq. (4.83)) as

$$\int_{\Omega} \phi \frac{\partial \mathbf{Q}}{\partial \mathbf{V}} \frac{\partial(\delta \mathbf{V}_{\text{int}})}{\partial t} d\Omega = RHS_{\text{int}}(\tilde{\mathbf{V}}, \delta \tilde{\mathbf{V}}_{\text{int}}) + RHS_{\text{ref}}(\tilde{\mathbf{V}}, \delta \tilde{\mathbf{V}}_{\text{ref}}), \tag{B.11}$$

where the right-hand side terms take the form

$$\begin{aligned}
RHS_{\text{int}}(\tilde{\mathbf{V}}, \delta \tilde{\mathbf{V}}_{\text{int}}) = & \\
& \sum_{i=0}^P \phi w_i \left[\frac{\partial \hat{\mathbf{F}}_{1,i}^w}{\partial \tilde{\mathbf{Q}}_{\text{b},i}^w} \frac{\partial \tilde{\mathbf{Q}}_{\text{b},i}^w}{\partial \tilde{\mathbf{V}}_{\text{b},i}^w} \frac{\partial \tilde{\mathbf{V}}_{\text{b},i}^w}{\partial \tilde{\mathbf{V}}_{\text{int},i}^w} \delta \tilde{\mathbf{V}}_{\text{int},i}^w \right] - \sum_{i=0}^P \phi w_i \left[\frac{\partial \hat{\mathbf{F}}_{1,i}^e}{\partial \tilde{\mathbf{Q}}_{\text{b},i}^e} \frac{\partial \tilde{\mathbf{Q}}_{\text{b},i}^e}{\partial \tilde{\mathbf{V}}_{\text{b},i}^e} \frac{\partial \tilde{\mathbf{V}}_{\text{b},i}^e}{\partial \tilde{\mathbf{V}}_{\text{int},i}^e} \delta \tilde{\mathbf{V}}_{\text{int},i}^e \right] \\
& + \sum_{i=0}^P \phi w_i \left[\frac{\partial \hat{\mathbf{F}}_{1,i}^s}{\partial \tilde{\mathbf{Q}}_{\text{b},i}^s} \frac{\partial \tilde{\mathbf{Q}}_{\text{b},i}^s}{\partial \tilde{\mathbf{V}}_{\text{b},i}^s} \frac{\partial \tilde{\mathbf{V}}_{\text{b},i}^s}{\partial \tilde{\mathbf{V}}_{\text{int},i}^s} \delta \tilde{\mathbf{V}}_{\text{int},i}^s \right] - \sum_{i=0}^P \phi w_i \left[\frac{\partial \hat{\mathbf{F}}_{1,i}^n}{\partial \tilde{\mathbf{Q}}_{\text{b},i}^n} \frac{\partial \tilde{\mathbf{Q}}_{\text{b},i}^n}{\partial \tilde{\mathbf{V}}_{\text{b},i}^n} \frac{\partial \tilde{\mathbf{V}}_{\text{b},i}^n}{\partial \tilde{\mathbf{V}}_{\text{int},i}^n} \delta \tilde{\mathbf{V}}_{\text{int},i}^n \right] \\
& + \int_{\Omega} \nabla \phi \cdot \frac{\partial \mathbf{F}}{\partial \mathbf{Q}} \frac{\partial \mathbf{Q}}{\partial \mathbf{V}} \delta \mathbf{V}_{\text{int}} d\Omega,
\end{aligned} \tag{B.12}$$

and

$$\begin{aligned}
RHS_{\text{ref}}(\tilde{\mathbf{V}}, \delta \tilde{\mathbf{V}}_{\text{ref}}) = & \\
& \sum_{i=0}^P \phi w_i \left[\frac{\partial \hat{\mathbf{F}}_{1,i}^w}{\partial \tilde{\mathbf{Q}}_{\text{b},i}^w} \frac{\partial \tilde{\mathbf{Q}}_{\text{b},i}^w}{\partial \tilde{\mathbf{V}}_{\text{b},i}^w} \frac{\partial \tilde{\mathbf{V}}_{\text{b},i}^w}{\partial \tilde{\mathbf{V}}_{\text{ref},i}^w} \delta \tilde{\mathbf{V}}_{\text{ref},i}^w \right] + \sum_{i=0}^P \phi w_i \left[\frac{\partial \hat{\mathbf{F}}_{1,i}^s}{\partial \tilde{\mathbf{Q}}_{\text{b},i}^s} \frac{\partial \tilde{\mathbf{Q}}_{\text{b},i}^s}{\partial \tilde{\mathbf{V}}_{\text{b},i}^s} \frac{\partial \tilde{\mathbf{V}}_{\text{b},i}^s}{\partial \tilde{\mathbf{V}}_{\text{ref},i}^s} \delta \tilde{\mathbf{V}}_{\text{ref},i}^s \right] \\
& - \sum_{i=0}^P \phi w_i \left[\frac{\partial \hat{\mathbf{F}}_{1,i}^n}{\partial \tilde{\mathbf{Q}}_{\text{b},i}^n} \frac{\partial \tilde{\mathbf{Q}}_{\text{b},i}^n}{\partial \tilde{\mathbf{V}}_{\text{b},i}^n} \frac{\partial \tilde{\mathbf{V}}_{\text{b},i}^n}{\partial \tilde{\mathbf{V}}_{\text{ref},i}^n} \delta \tilde{\mathbf{V}}_{\text{ref},i}^n \right].
\end{aligned} \tag{B.13}$$

In the above RHS_{ref} has two less terms than RHS_{int} .

B.3 Global linear system for the three-element model problem

In the three-element system on the top of Fig. 4.6.2, the global system is linearized to have

$$\frac{d}{dt} \left(\delta \tilde{\mathbf{U}}_{\text{int}}^* \right) \Delta x = \begin{pmatrix} \mathbf{C}_{\text{int}}^{\text{E1}} & \mathbf{C}_{\text{ref}}^{\text{E1,e}} & \mathbf{0} \\ \mathbf{C}_{\text{ref}}^{\text{E2,w}} & \mathbf{C}_{\text{int}}^{\text{E2}} & \mathbf{C}_{\text{ref}}^{\text{E2,e}} \\ \mathbf{0} & \mathbf{C}_{\text{ref}}^{\text{E3,w}} & \mathbf{C}_{\text{int}}^{\text{E3}} \end{pmatrix} \delta \tilde{\mathbf{U}}_{\text{int}}^* + \begin{pmatrix} \mathbf{C}_{\text{ref}}^{\text{E1,w}} & \mathbf{0} & \mathbf{0} \\ \mathbf{0} & \mathbf{0} & \mathbf{0} \\ \mathbf{0} & \mathbf{0} & \mathbf{C}_{\text{int}}^{\text{E3,e}} \end{pmatrix} \delta \tilde{\mathbf{U}}_{\text{ref}}^*, \quad (\text{B.14})$$

or

$$\frac{d}{dt} \left(\delta \tilde{\mathbf{U}}_{\text{int}}^* \right) \Delta x = \mathbf{C}_{\text{int}}^* \delta \tilde{\mathbf{U}}_{\text{int}}^* + \mathbf{C}_{\text{ref}}^* \delta \tilde{\mathbf{U}}_{\text{ref}}^*. \quad (\text{B.15})$$

In the above $\mathbf{C}_{\text{int}}^*$ is a tridiagonal block matrix. When the entropy-pressure compatible inflow and pressure outflow is adopted, its eigenfunction takes the form

$$\lambda(\lambda - u)^3 \mathcal{P}^5(\lambda) = 0,$$

where $\mathcal{P}^5(\lambda)$ is a fifth-order eigenfunction

$$\mathcal{P}^5(\lambda) = \lambda^5 - c_1 \lambda^4 - c_2 \lambda^3 + c_3 \lambda^2 + c_4 \lambda + c_5,$$

and the coefficients are

$$\begin{aligned} c_1 &= \frac{1}{2(\gamma - 1)} (10c + 2u - 11\gamma c - \gamma u), \\ c_2 &= \frac{1}{2(\gamma - 1)} (8cu - 25\gamma c^2 + 5\gamma u^2 + 20c^2 - 4u^2 - 4\gamma cu), \\ c_3 &= \frac{1}{2(\gamma - 1)} (30\gamma c^3 + 12cu^2 - 12c^2u - 2\gamma u^3 - 20c^3 + 4u^3 - 18\gamma cu^2 + 6\gamma c^2u), \\ c_4 &= \frac{1}{2(\gamma - 1)} (20\gamma c^4 + 8cu^3 - 8c^3u + 4\gamma u^4 - 10c^4 - 2u^4 + 12c^2u^2 - 4\gamma cu^3 \\ &\quad + 4\gamma c^3u - 24\gamma c^2u^2), \\ c_5 &= \frac{1}{2(\gamma - 1)} (7\gamma c^5 - 2cu^4 - 2c^4u + \gamma u^5 - 2c^5 - 2u^5 + 4c^2u^3 + 4c^3u^2 + 7\gamma cu^4 \\ &\quad + \gamma c^4u - 2\gamma c^2u^3 - 14\gamma c^3u^2). \end{aligned}$$

Appendix C

CRM-NLF

C.1 Convergence check

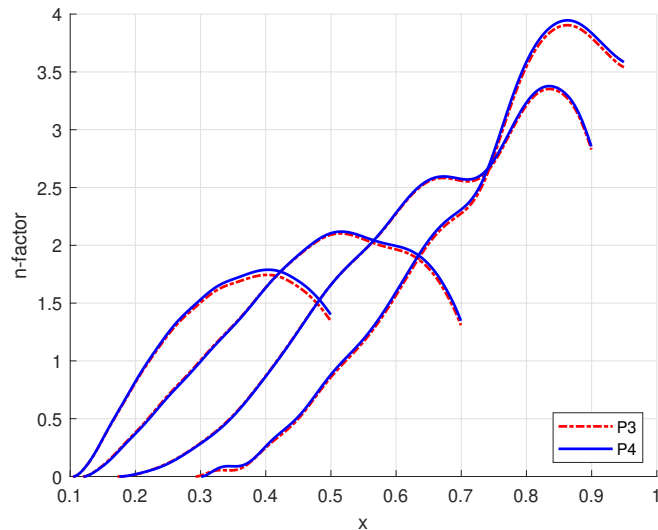
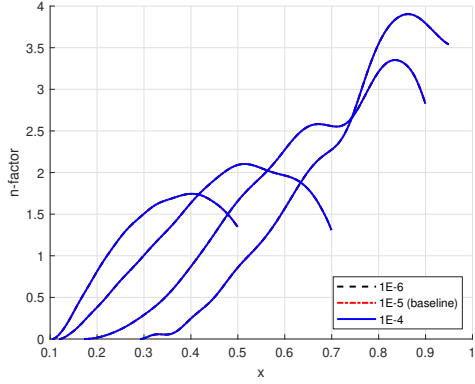
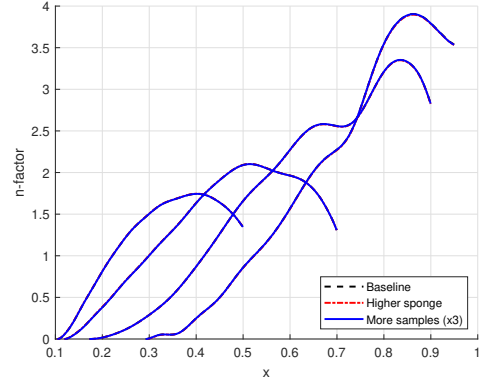


Figure C.1: N -factor comparisons for P3 and P4 expansions of the 2D clean CRM-NLF case. The four curves from right to left shows the disturbance frequencies $f = 30, 40, 50, 60$ kHz.



(a) Different disturbance amplitudes



(b) Different settings

Figure C.2: N -factor comparisons for using different parameters of the 2D clean CRM-NLF case. P3 expansion is used.

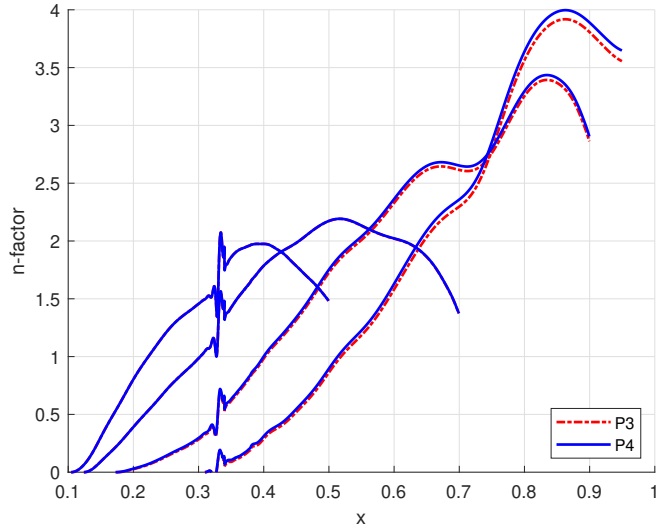


Figure C.3: N -factor comparisons for P3 and P4 expansions of the 2D gapped CRM-NLF case. The four curves from right to left shows the disturbance frequencies $f = 30, 40, 50, 60$ kHz.

Appendix D

Self-similar solution of boundary layer equations

D.1 2D compressible boundary layers

D.1.1 Governing equations

Two-dimensional steady compressible boundary layer flows are governed by the following equations [23]

$$\frac{\partial(\rho u)}{\partial x} + \frac{\partial(\rho v)}{\partial y} = 0 \quad (\text{D.1})$$

$$\rho \left(u \frac{\partial u}{\partial x} + v \frac{\partial v}{\partial y} \right) = -\rho g \sin \alpha - \frac{dp}{dx} + \frac{\partial}{\partial y} \left(\mu \frac{\partial u}{\partial y} \right) \quad (\text{D.2})$$

$$\rho c_p \left(u \frac{\partial T}{\partial x} + v \frac{\partial T}{\partial y} \right) = \frac{\partial}{\partial y} \left(\kappa \frac{\partial T}{\partial y} \right) + \beta T u \frac{dp}{dx} + \mu \left(\frac{\partial u}{\partial y} \right)^2 \quad (\text{D.3})$$

which can be solved after Levy–Lees transformation, which reads

$$\xi = \int_0^x \rho_e \mu_e u_e dx, \quad \eta = \frac{u_e}{\sqrt{2\xi}} \int_0^y \rho dy \quad (\text{D.4})$$

where the subscript "e" denotes the quantity at the edge of the boundary layer.

The transformed compressible boundary layer equations then take the form

$$(C f'')' + f f'' + \beta \left(\frac{\rho_e}{\rho} - f'^2 \right) = 2\xi \left(f' \frac{\partial f'}{\partial \xi} - f'' \frac{\partial f}{\partial \xi} \right) \quad (\text{D.5})$$

$$\left[\frac{C}{Pr} g' + C \frac{u_e^2}{h_{te}} \left(1 - \frac{1}{Pr} \right) f' f'' \right]' + f g' = 2\xi \left(f' \frac{\partial g}{\partial \xi} - g' \frac{\partial f}{\partial \xi} \right) \quad (\text{D.6})$$

where prime denotes the derivative with respect to the wall-normal coordinate, η , Pr is the Prandtl number, f and g are two non-dimensional functions representing the profiles

$$f'(\xi, \eta) = \frac{u}{u_e}, \quad g(\xi, \eta) = \frac{h_t - h_{te}}{h_{te}} \quad (\text{D.7})$$

The coefficients in Eqs. (D.5) and (D.6) are

$$\beta = \frac{2\xi}{u_e} \frac{du_e}{d\xi}, \quad C = \frac{\rho \mu}{\rho_e \mu_e} \quad (\text{D.8})$$

To solve Eqs. (D.5) and (D.6) the following boundary conditions need to be enforced

1. $\eta = 0: f = 0, f' = 0, g = g_w$ or $g' = 0$ (iso-thermal/adiabatic wall)
2. $\eta \rightarrow \infty: f' = 1, g = 0$

For a flat plate boundary layer flow with zero pressure gradient (ZPG), $\partial(\cdot)/\partial\xi = 0$. Therefore Eqs. (D.5) and (D.6) are simplified as

$$(Cf'')' + ff'' = 0 \quad (\text{D.9})$$

$$\left[Cg' + C \frac{u_e^2}{h_{te}} (Pr - 1) f' f'' \right]' + Pr f g' = 0 \quad (\text{D.10})$$

which are the equations to be solved in the current work to generate inflow profile.

Since in Eq. (D.9) g only appears in form of g' , the following expression is adopted in the rest of this work for simplicity

$$g(\eta) = \frac{h_t}{h_{te}} \quad (\text{D.11})$$

where the temperature and its derivative are derived as

$$T = \left(T_e + \frac{u_e^2}{2c_p} \right) g - \frac{u_e^2}{2c_p} f'^2 \quad (\text{D.12})$$

$$T' = \left(T_e + \frac{u_e^2}{2c_p} \right) g' - \frac{u_e^2}{c_p} f' f'' \quad (\text{D.13})$$

To compute the parameter C and its derivative, the viscosity is given by Sutherland's law, which reads

$$\mu = \mu_{ref} \left(\frac{T}{T_{ref}} \right)^{3/2} \frac{T_{ref} + S}{T + S} \quad (\text{D.14})$$

where μ_{ref} , T_{ref} , and S are parameters to calibrate Sutherland's law and thus are known. C is then expressed as

$$\begin{aligned} C &= \frac{\rho\mu}{\rho_e\mu_e} = \frac{1}{\rho_e\mu_e} \frac{p}{RT} \mu_{ref} \left(\frac{T}{T_{ref}} \right)^{3/2} \frac{T_{ref} + S}{T + S} \\ &\stackrel{p=p_e}{=} \frac{\mu_{ref}}{\mu_e} \frac{T_e}{T} \left(\frac{T}{T_{ref}} \right)^{3/2} \\ &= \frac{\mu_{ref}}{\mu_e} \frac{T_e T^{1/2}}{T_{ref}^{3/2}} \frac{T_{ref} + S}{T + S} \end{aligned} \quad (\text{D.15})$$

Therefore

$$C' = \left(\frac{1}{2T} - \frac{1}{T + S} \right) CT' \quad (\text{D.16})$$

According to Kennedy and Gatski [188] the expression for the vertical velocity v is given by

$$\begin{aligned} v &= \rho_e u_e \mu_e \sqrt{2\xi} \frac{\partial f}{\partial \eta} \left[\left(\frac{1}{2\xi} - \frac{1}{u_e} \frac{\partial u_e}{\partial \xi} \right) \int_0^\eta \frac{1}{\rho} d\eta^* - \int_0^\eta \frac{1}{\rho^2} \frac{\partial \rho}{\partial \xi} d\eta^* \right] \\ &\quad - \frac{\rho_e u_e \mu_e}{\rho} \left(\frac{f}{\sqrt{2\xi}} + \sqrt{2\xi} \frac{\partial f}{\partial \xi} \right) \end{aligned} \quad (\text{D.17})$$

Since $\partial(\cdot)/\partial\xi = 0$ for a flat plate boundary layer flow with ZPG, Eq. (D.17) is simplified as

$$\begin{aligned} v &= \frac{\rho_e u_e \mu_e}{\sqrt{2\xi}} \left[f' \int_0^\eta \frac{1}{\rho(\eta^*)} d\eta^* - \frac{f}{\rho} \right] \\ &= \sqrt{\frac{\mu_e u_e}{2\rho_e x}} \left[f' \int_0^\eta \frac{\rho_e}{\rho(\eta^*)} d\eta^* - f \frac{\rho_e}{\rho} \right] \end{aligned} \quad (\text{D.18})$$

As for $y = y(\eta)$, by computing the derivative of η with respect to y we obtain

$$\frac{d\eta}{dy} = \sqrt{\frac{\rho_e u_e}{2\mu_e x}} \frac{\rho}{\rho_e} \quad (\text{D.19})$$

Therefore

$$y = \sqrt{\frac{2\mu_e x}{\rho_e u_e}} \int_0^\eta \frac{\rho_e}{\rho} d\eta = \sqrt{\frac{2\mu_e x}{\rho_e u_e}} h(\eta) \quad (\text{D.20})$$

Eqs. (D.18) and (D.20) can be used for polynomial approximation as input for *Nektar++* session file after $f'(\eta)$ and $g(\eta)$ are solved. In this work the 8th order polynomials are used.

D.1.2 Solving

Since the boundary conditions at $\eta \rightarrow \infty$ are given, the above Eqs. (D.8) and (D.9) can be solved using the shooting method to obtain the unknown boundary conditions for $f''(0)$ and $g(0)$ or $g'(0)$ that leads to $f'(\eta \rightarrow \infty) = 1$, $g(\eta \rightarrow \infty) = 0$. For each shoot, the profiles are solved using the 4th order Runge-Kutta method (RK4), where the derivatives are given by

$$\begin{aligned} (f)' &= f' \\ (f')' &= f'' \\ (f'')' &= -\frac{C'}{C} f'' - \frac{1}{C} f f'' \\ (g)' &= g' \\ (g')' &= -\frac{C'}{C} g' - \frac{u_e^2}{h_{te}} (Pr - 1) f' f''' - \frac{u_e^2}{h_{te}} (Pr - 1) f''^2 \\ &\quad - \frac{C'}{C} \frac{u_e^2}{h_{te}} (Pr - 1) f' f'' - \frac{1}{C} Pr f g' \end{aligned} \quad (\text{D.21})$$

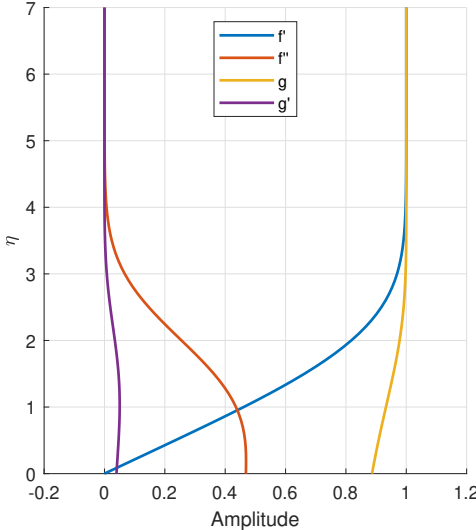
The detailed steps to solve the equations are provided in Algorithm 1. Because there are two unknown boundary conditions at $\eta = 0$, the shooting method is used twice for outer loop and inner loop, where $f''(0)$ is searched in the outer loop while $g(0)$ or $g'(0)$ is searched in the inner loop. The bisection method is used for both searches. Fig.D.1 shows the non-dimensional profiles for iso-thermal wall and adiabatic wall with $Pr = 0.71$.

Algorithm 1 Solve the compressible flat plate boundary layer profile with ZPG

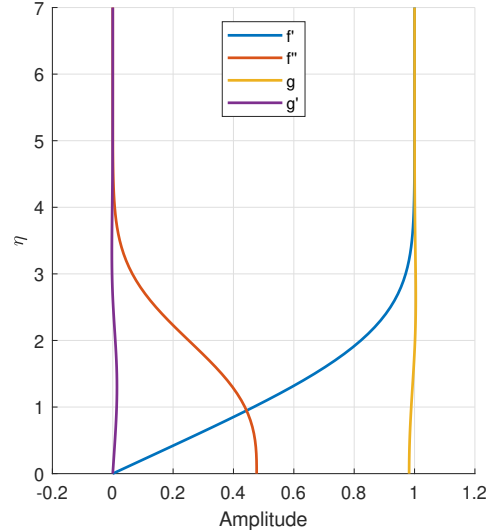
Require: $f(0)$, $f'(0)$, and $g'(0)$ or $g(0)$. Prescribed bisection intervals for $f''(0)$ and $g(0)$ or $g'(0)$

Ensure: $f'(\eta \rightarrow \infty) = 1$ and $g(\eta \rightarrow \infty) = 0$

- 1: **while** $f'(\eta \rightarrow \infty) \neq 1$ **do**
- 2: Reset the interval for $g(0)$ or $g'(0)$;
- 3: Get $f''(0)$ as the mid value of the interval;
- 4: **while** $g(\eta \rightarrow \infty) \neq 0$ **do**
- 5: Get $g(0)$ or $g'(0)$ as the mid value of the interval;
- 6: Set initial value vector $y_0 = (f(0), f'(0), f''(0), g(0), g'(0))$;
- 7: Solve $y(\eta \rightarrow \infty) = (f, f', f'', g, g')$ using RK4;
- 8: Update the interval head/tail for $g(0)$ or $g'(0)$;
- 9: Check convergence for $g(0)$ or $g'(0)$;
- 10: **end while**
- 11: Update the interval head/tail for $f''(0)$;
- 12: Check convergence for $f''(0)$;
- 13: **end while**



(a) Iso-thermal wall



(b) Adiabatic wall

Figure D.1: 2D compressible flat plate boundary layer self-similar profiles using the definition $g = h_t/h_{te}$. The Prandtl number $Pr = 0.71$. (a) uses iso-thermal wall where $T_{wall} = T_\infty$.

D.2 3D incompressible boundary layers with cross-flow

D.2.1 Governing equations

For a infinite flat plate geometry ($\partial(\cdot)/\partial z = 0$) where the inflow direction is not normal to its leading-edge, it is called infinite swept flat plate and the boundary layer flow also has a self-similar solution along the normal direction to the leading-edge but with an additional crossflow component. The boundary layer flow therefore

shows a three-dimensional feature.

The governing equations for this steady three-dimensional boundary layer flow are [23, 189]

$$\frac{\partial u}{\partial x} + \frac{\partial v}{\partial y} = 0 \quad (\text{D.22})$$

$$u \frac{\partial u}{\partial x} + v \frac{\partial u}{\partial y} = u_e \frac{du_e}{dx} + v \frac{d^2 u}{dy^2} \quad (\text{D.23})$$

$$u \frac{\partial w}{\partial x} + v \frac{\partial w}{\partial y} = v \frac{d^2 u}{dy^2} \quad (\text{D.24})$$

where the boundary conditions are

1. $y = 0: u = v = w = 0$
2. $y \rightarrow \infty: u \rightarrow u_e, w \rightarrow w_e$

where the subscript "e" denotes the quantity at the edge of the boundary layer. It is assumed that the variation of the chordwise velocity at the boundary layer edge obeys a power law $u_e(x) = U_\infty(x - x_0)^m$ and the spanwise velocity $w_e = \text{Constant}$. x_0 is a fixed streamwise position with known velocity state.

The self-similar solution is obtained by introducing the transformation

$$\eta = y \left(\frac{m+1}{2} \frac{u_e}{\nu x} \right)^{1/2}$$

and stream function

$$\psi = \left(\frac{2}{m+1} u_e \nu x \right)^{1/2} f(\eta)$$

then the transformed non-dimensional boundary layer equations read

$$f''' + f f'' + \beta_H (1 - f'^2) = 0 \quad (\text{D.25})$$

$$g'' + f g' = 0 \quad (\text{D.26})$$

where $\beta_H = 2m/(m+1)$ is the Hartree parameter, the prime denotes the derivative with respect to the wall-normal coordinate, η , f and g are two non-dimensional functions representing the profiles

$$f'(\eta) = \frac{u}{u_e}, \quad g(\eta) = \frac{w}{w_e} \quad (\text{D.27})$$

The expression for v takes the form

$$v = -\frac{\partial \psi}{\partial x} = \frac{1}{2} u_e \left(\frac{2}{m+1} \frac{\nu}{u_e x} \right)^{1/2} (\eta f' - f)$$

The boundary conditions for Eqs. (D.25) and (D.26) now become

1. $\eta = 0: f = 0, f' = 0, g = 0$
2. $\eta \rightarrow \infty: f' = 1, g = 1$

The solutions for the above equations are named as Falkner-Skan-Cooke (FSC) velocity profiles first proposed by Cooke [190]. For a flat plate boundary layer flow with zero pressure gradient (ZPG), $u_e(x)$ is constant along the x direction so $\beta_H(m=0) = 0$.

D.2.2 Solving

We follow similar method as in Section D.2 to solve the self-similar incompressible 3D boundary layer profile in Eqs. (D.25) and (D.26).

The shooting method is employed for the outer loop to obtain the unknown boundary condition $f''(0)$ and $g'(0)$ that leads to $f'(\eta \rightarrow \infty) = 1$ and $g(\eta \rightarrow \infty) = 1$ while the 4th order Runge-Kutta method (RK4) is used to solve for the profile within each boundary conditions guess. Since Eq. (D.25) does not contain g , the solution for f can be obtained first. The derivatives are given respectively by

$$\begin{aligned}(f)' &= f' \\ (f')' &= f'' \\ (f'')' &= -ff'' - \beta_H(1 - f'^2)\end{aligned}\tag{D.28}$$

and

$$\begin{aligned}(g)' &= g' \\ (g')' &= -fg'\end{aligned}\tag{D.29}$$

whose solution is shown in Fig. D.2 for $m = 0$ and 0.2 as examples.

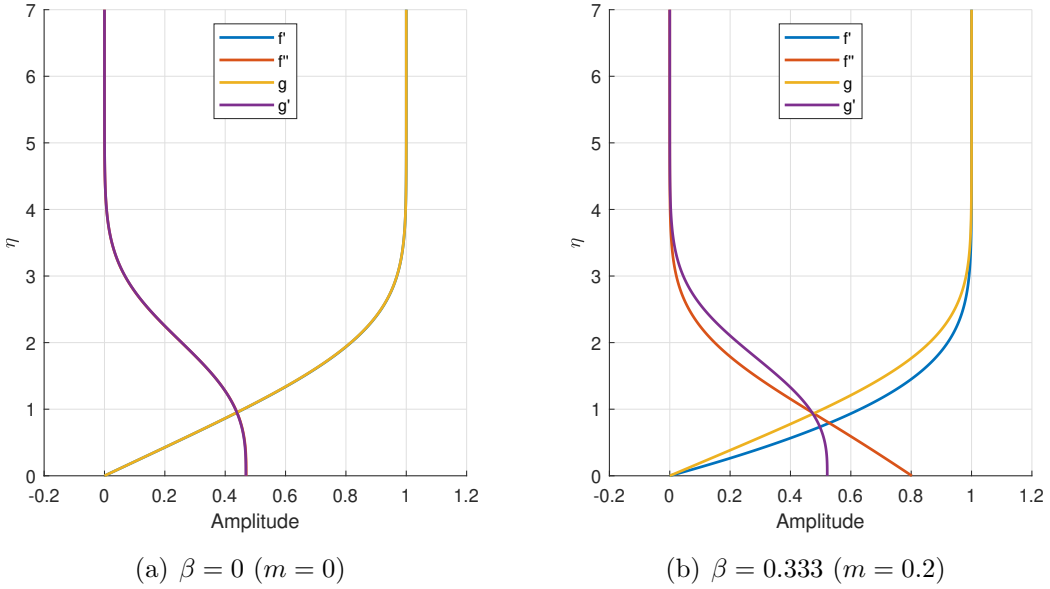


Figure D.2: 3D incompressible Falkner-Skan-Cooke (FSC) profiles.